

# UC Irvine

## UC Irvine Electronic Theses and Dissertations

### Title

Complex Mixtures of Terpenes Results in Highly Viscous Secondary Organic Aerosols

### Permalink

<https://escholarship.org/uc/item/6z05j94b>

### Author

Smith, Natalie Rose

### Publication Date

2022

### Copyright Information

This work is made available under the terms of a Creative Commons Attribution License, available at <https://creativecommons.org/licenses/by/4.0/>

Peer reviewed|Thesis/dissertation

UNIVERSITY OF CALIFORNIA,  
IRVINE

Complex Mixtures of Terpenes Results in Highly Viscous Secondary Organic Aerosols

DISSERTATION

submitted in partial satisfaction of the requirements  
for the degree of

DOCTOR OF PHILOSOPHY

in Chemistry

by

Natalie Rose Smith

Dissertation Committee:  
Professor Sergey A. Nizkorodov, Chair  
Professor Celia L. Faiola  
Professor Manabu Shiraiwa

2022

Chapter 2 © 2021 American Chemical Society

Chapter 3 © 2021 The Royal Society of Chemistry

All other material © 2022 Natalie Rose Smith

# TABLE OF CONTENTS

	Page
TABLE OF CONTENTS	ii
LIST OF FIGURES	iv
LIST OF TABLES	ix
ACKNOWLEDGEMENTS	x
VITA	xii
ABSTRACT OF THE DISSERTATION	xix
CHAPTER 1: INTRODUCTION	1
1.1 Atmospheric aerosols	1
1.2 Biogenic aerosols	2
1.3 Impact of chemical composition on physical properties of SOA	5
1.4 Summary of Goals	7
CHAPTER 2: HUMIDITY-DEPENDENT VISCOSITY OF SECONDARY ORGANIC AEROSOL FROM OZONOLYSIS OF B-CARYOPHYLLENE: MEASUREMENTS, PREDICTIONS, AND IMPLICATIONS	9
2.1 Introduction	10
2.2 Experimental methods	12
2.2.1 SOA Generation	12
2.2.2 Viscosity measurements	14
2.2.3 High-resolution mass spectrometry	21
2.2.4 Predictions of the Viscosity of SOA from measurements of the chemical composition of the SOA	23
2.2.5 Prediction of viscosity using a mole-fraction based Arrhenius mixing rule	25
2.3 Results and Discussion	26
2.3.1 Viscosity as a function of RH	27
2.3.2 Diffusion coefficients and mixing times of organic molecules within $\beta$ -caryophyllene SOA as a function of RH	29
2.3.3 Chemical composition of the SOA based on mass spectrometry	33
2.3.4 Viscosity predictions based on the measured chemical composition	38
2.3.5 Viscosity predictions based on mole-fraction based Arrhenius mixing rule	43
2.4 Conclusions	44
CHAPTER 3: VISCOSITY AND LIQUID-LIQUID PHASE SEPARATION IN HEALTHY AND STRESSED PLANT SOA	46
3.1 Introduction	48

3.2	Experimental methods	53
3.2.1	VOC mixtures	53
3.2.2	SOA generation	55
3.2.3	High-resolution mass spectrometry	58
3.2.4	Liquid-liquid phase separation	58
3.2.5	Viscosity measurements	59
3.2.6	Volatility predictions	67
3.2.7	Viscosity predictions	68
3.3	Results and Discussion	70
3.3.1	Molecular composition of SOA particles	70
3.3.2	LLPS	77
3.3.3	Experimental viscosity and mixing	78
3.3.4	Viscosity predictions	83
3.4	Conclusions	88
CHAPTER 4: VISCOSITY OF CANARY ISLAND PINE SECONDARY ORGANIC AEROSOL		90
4.1	INTRODUCTION	91
4.2	Experimental	94
4.2.1	Tree Enclosure	94
4.2.2	PTR-ToF-MS	94
4.2.3	TD-GC-MS	95
4.2.4	HR-ToF-MS	97
4.2.5	SOA Generation	97
4.2.6	SOA yield calculation	102
4.2.7	Experimental Viscosity	105
4.3	Results and Discussion	109
4.3.1	Gas-phase composition	109
4.3.2	Experimental Viscosity	112
4.3.3	Particle phase composition (AMS)	117
4.4	Conclusion	120
REFERENCES		122
APPENDIX A		151
APPENDIX B		154

## LIST OF FIGURES

Page

- Figure 2.1** Optical images of particles taken during poke-flow experiments at RH values of (a) 48, (b) 28, and (c) 0%. Images [a(1),b(1),c(1)] correspond to images taken before the particle was poked. Images [a(2),b(2),c(2)] are images taken immediately after poking. Images [a(3),b(3),c(3)] are taken during recovery and images [a(4),b(4),c(4)] are taken at  $\tau_{\text{exp,flow}}$  where the equivalent area diameter of the hole has decreased to 50% of its original size. The white scale bar in the prepoking images corresponds to 50  $\mu\text{m}$ . The circle in the center of the particle in [b(1)] is an optical effect due to the hemispherical shape. .... 17
- Figure 2.2** Viscosities as a function of particle conditioning time to the surrounding RH. Measurements were taken at RHs of (a) 48, (b) 28%, (c) 15%, and (d) 0%. .... 18
- Figure 2.3** Particle 2-D projected area as a function of time during exposure to dry nitrogen flow with a secondary y-axis showing the percent change in the projected particle area. The y-error bars correspond to the uncertainty in the measurement of the particle area in  $\mu\text{m}^2$ . The straight line is a linear fit to the data and the shaded regions are the 95% confidence intervals for that fit. .... 19
- Figure 2.4** Panel (a) shows the experimental flow time,  $\tau_{\text{exp,flow}}$ , for poked particles as a function of RH. Panel (b) shows measured viscosities and calculated diffusion coefficients and mixing times of organic molecules in a 200 nm particle. The x-error bars correspond to uncertainties in the RH measurements and in panel (b), the y-error bars represent the upper and lower limits of the measured viscosities at each RH. The dotted line corresponds to a mixing time of 1 h. Also included in panel (b) are literature viscosity values for toluene SOA.<sup>106</sup> Pictures of common substances have been added to panel (b) as points of reference per Koop et al. (2011).<sup>28</sup> The tar pitch image is from the tar pitch experiment (image courtesy of Wikimedia Commons, GNU Free Documentation License, University of Queensland, John Mainstone). Panels (c,d) show the RH and temperature frequency distributions in January (black line) and July (red line) in the global planetary boundary layer (i.e., the planetary boundary layer in both the northern and southern hemisphere) based on GEOS-Chem. RH and temperature conditions were only included if the monthly averaged concentration of organic aerosol were greater than 0.5  $\mu\text{g m}^{-3}$  at the surface based on the output of GEOS-Chem.<sup>100</sup> Conditions where the organic aerosol concentrations were  $<0.5 \mu\text{g m}^{-3}$  were excluded, as aerosols at low concentrations are expected to be of less importance to climate or visibility. .... 28
- Figure 2.5** Viscosities of  $\beta$ -caryophyllene SOA and calculated mixing times within a 450 nm  $\beta$ -caryophyllene SOA particle. The y-error bars correspond to the upper and lower limits of viscosity from the measurements. The x-error bars correspond to uncertainties in the RH measurements. The horizontal line corresponds to a mixing time of 1 hr. .... 33
- Figure 2.6** High-resolution mass spectrometry data taken with ESI, nano-ESI, and nano-DESI ionization sources in both positive and negative mode. The intensities were normalized to the largest peak within each ionization mode. .... 35
- Figure 2.7** Sum of intensities of all molecular formula assignments based on carbon number for three ionization techniques (ESI, nano-ESI, and nano-DESI), which are normalized to the maximum intensity peak in each respective spectrum. .... 36

**Figure 2.8** Nano-DESI mass spectrum taken in the positive mode (red spectrum) and negative mode (black spectrum). The signals were normalized to the highest intensity in each respective mode. The five most abundant peaks in each mode are labeled by the corresponding neutral (unionized) molecular formulas. .... 37

**Figure 2.9** Comparison of measured and predicted viscosities as a function of RH. The *x*-error bars correspond to uncertainties in the RH measurements, and the *y*-error bars correspond to the upper and lower limits of viscosity at each RH. Panel (a) shows the viscosity predictions using the averaged positive- and negative-ion mode mass spectrometry data where it was assumed that the weight fraction of the individual SOA species was proportional to the mass spectrum signal intensities (Equation 2.3). Panel (b) shows the viscosity predictions using the averaged mass spectrometry data assuming a relation between weight fraction and intensity given in Equation 2.14. .... 39

**Figure 2.10** Toluene SOA viscosity as a function of RH. The *y*-error bars correspond to the upper and lower limits of viscosity from the measurements. Shown in blue are the viscosity predictions based on nano-DESI positive mode mass spectrometry results from DeRieux et al.<sup>29</sup> where it was assumed that the weight fraction of individual compounds was proportional to the mass spectrum signal intensity (Equation 2.3). Shown in orange are the viscosity predictions from DeRieux et al.<sup>29</sup> where a relation between weight fraction and intensity given in Equation 2.14 of the main text was assumed. The shaded regions were calculated from nano-DESI mass spectrometry data collected at high and low RH separately.<sup>191</sup> ..... 41

**Figure 2.11** Diesel fuel vapour SOA viscosities as a function of RH. The *x*-error bars correspond to uncertainties in the RH measurements and the *y*-error bars correspond to the upper and lower limits of viscosity at each RH from Song et al.<sup>51</sup> Shown in blue are the viscosity predictions based on nano-DESI negative mode mass spectrometry results where it was assumed that the weight fraction of individual compounds was proportional to the mass spectrum signal intensity (Equation 2.3). Shown in orange are the viscosity predictions where a relation between weight fraction and intensity given in Equation 2.14 was assumed..... 42

**Figure 2.12** Measured viscosities and predicted viscosities using a mole-fraction based Arrhenius mixing rule. For the measurements, the *x*-error bars correspond to uncertainties in the RH and the *y*-error bars represent the upper and lower limits of the simulated viscosities at each RH. The uncertainties in the predictions are due to uncertainties in the hygroscopicity of the SOA. For the hygroscopicity, we used a range of CCN-derived kappa values of 0.04–0.001.<sup>158,159</sup> ..... 44

**Figure 3.1** Mixing ratio of each VOC after the injection into the environmental chamber. The relative VOC amounts (Table 3.1) were chosen to replicate the emission profile of healthy (green) and aphid-stressed (black) Scots Pine trees reported in Faiola et al. (2019). .... 55

**Figure 3.2** Measured spectral flux density in chamber compared to the solar spectral flux density calculated at a solar zenith angle of 0 degrees. .... 56

**Figure 3.3** Particle viscosity as a function of conditioning time in poke- flow cell at humidity of interest. Vertical bars represent the calculated lower and upper limits of viscosity (83% confidence interval) based on COMSOL simulations (see Table 3.2 for input parameters). .... 60

**Figure 3.4** Particle area as a function of exposure time to dry (< 0.5% RH) nitrogen gas flow, shaded red regions indicates the 95% confidence bands. The lack of change suggests that particles are stable with respect to evaporation over the experimental time scale..... 63

**Figure 3.5** Results from the poke-flow experiments for hp-SOA (green hexagons), sp-SOA (black hexagons) mixing times of water within a 50  $\mu\text{m}$  sized particle ( $\tau_{\text{mixing}}, 50 \mu\text{m}$ ). Error in the RH measurement was  $\pm 2.5\%$ . Upward arrows indicate lower limits. Vertical bars represent the calculated lower and upper limits of  $\tau_{\text{mixing}}, 50 \mu\text{m}$  (83% confidence interval) based on COMSOL simulations (see Table 3.2 for input parameters).  $\tau_{\text{mixing}}, 50 \mu\text{m}$  was also calculated using upper (A= 0.61, B= 2.08) and lower limits (A=0.85, B=1.50) for uncertainty in the fractional exponent ( $\xi$ ). ..... 66

**Figure 3.6** Nano-DESI mass spectra in a) negative mode and b) positive mode for healthy (green) and stressed (black) plant SOA as a function of the molecular weight of the detected neutral compound..... 71

**Figure 3.7** (a) viscosity of individual SOA compounds at 50% RH and 291 K as a function of  $C_0$  in healthy ( $\kappa = 0.15$ ) and stressed ( $\kappa = 0.07$ ) plant SOA. (b) Viscosity of individual SOA compounds at 50% RH and 291 K as a function of  $C_0$  with  $\kappa = 0.1$  applied to both healthy and stressed plant SOA. In each panel, the warmer the color, the higher the glass transition temperature. The larger the circle or square marker size, the larger the relative abundance of the species based on the HRMS analysis..... 76

**Figure 3.8** Optical images and illustrations of stressed and healthy plant SOA particles taken while decreasing relative humidity. The green represents the organic-rich phase and blue represents the aqueous-rich phase. The relative error of the SRH was obtained by using twice the standard deviation from the four measurement results plus an uncertainty of the hydrometer ( $\sim 2.5\%$ ). The diameter of the particles was between 50-80  $\mu\text{m}$ . ..... 77

**Figure 3.9** Optical images of SOA particles produced from photooxidation with VOCs from stressed trees during a poke-flow experiment at a) 50%, and b) 0% RH. Images a1), and b1) are pre-poking images. a4), and b4) are demonstrative diagrams of pre-poking. a2), and b2) are the first frame post-poking. a5), and b5) are demonstrative diagrams of the first frame post-poking. a3), and b3) are the post-poking images. a6), and b6) are demonstrative diagrams of post-poking. The white scale bars correspond to 50  $\mu\text{m}$ . ..... 79

**Figure 3.10** Optical images of SOA particles produced from photooxidation of VOCs from healthy trees during a poke-flow experiment at a) 50%, and b) 0% RH. Images a1) and b1) are pre-poking images. a4) and b4) are demonstrative diagrams of pre-poking. a2) and b2) are the first frame post-poking. a5) and b5) are demonstrative diagrams of the first frame post-poking. a3) and b3) are the post-poking images at 150 s and 6 hrs. a6) and b6) are demonstrative diagrams of post-poking at 150 s and 6 h. The white scale bars correspond to 50  $\mu\text{m}$ . ..... 80

**Figure 3.11** Results from the poke-flow experiments for hp-SOA (green diamonds), sp-SOA (black hexagons), and  $\alpha$ pin-SOA (red diamonds): (a) experimental flow time,  $\tau_{\text{exp, flow}}$ ; (b) viscosity; (c) mixing times of organic molecules within a 200 nm sized particle ( $\tau_{\text{mixing}}, 200 \text{ nm}$ ). In panel (a) error in the RH measurement was  $\pm 2.5\%$ . In panel (c), horizontal  $\tau_{\text{mixing}}$  bars correspond to the 1 h mixing band, which is roughly the mixing time assumed in chemical transport models. Upward arrows indicate lower limits. Vertical bars represent the calculated lower and upper limits of viscosity and  $\tau_{\text{mixing}}, 200 \text{ nm}$  (83% confidence interval) based on COMSOL simulations (see Table 3.2 for input parameters). ..... 81

**Figure 3.12** Experimentally determined viscosity of toluene photooxidation SOA reproduced from Song et al. (2016) compared to healthy and stressed photooxidation SOA over various relative



humidities determined by the poke-flow method. Vertical bars represent the calculated lower and upper limits of viscosity using the COMSOL simulations (see Table 3.2 for input parameters). Horizontal bars represent the uncertainty in the relative humidity measurement. The upward arrows indicate lower limits of viscosity. .... 82

**Figure 3.13** Predicted viscosity as a function of RH compared to the experimental values determined by the poke-flow method. Vertical bars represent the calculated lower and upper limits of viscosity using the COMSOL simulations (see Table 3.2 for input parameters). Horizontal bars represent the uncertainty in the relative humidity measurement. The upward arrows indicate lower limits of the viscosity. Predicted viscosities were calculated for healthy and stressed plant SOA using either scaled (solid lines) or unscaled (dashed lines) peak abundances in the mass spectra that combined both positive and negative ion mode peaks. .... 84

**Figure 3.14** Predicted viscosity as a function of RH using  $\kappa = 0.1$  calculated for both healthy and stressed plant SOA using either scaled (solid lines) or unscaled (dashed lines) peak abundances in the mass spectra that combined both positive and negative ion mode peaks. .... 87

**Figure 3.15** Glass transition temperature ( $T_g$ ) of hp-SOA and sp-SOA under dry conditions as a function of saturation mass concentration of individual compounds ( $C_0$ ).  $T_g$  is predicted according to DeRieux et al., (2018) and  $C_0$  is estimated according to Li et al., 2016. The warmer is the color, the higher is the O/C ratio. The larger the circle or square marker size, the larger the relative abundance of the species based on the HRMS analysis. .... 88

**Figure 4.1** Experimental Setup for SOA generation in a 5 m<sup>3</sup> environmental chamber with 2 m<sup>3</sup> Teflon pine enclosure used a source of VOCs containing a Canary Island pine (*Pinus Canariensis*). .... 98

**Figure 4.2** Example particle wall loss correction ( $K_w = 0.0028 \text{ s}^{-1}$ ) applied to healthy plant SOA trial ..... 99

**Figure 4.3** Particle formation as a function of time determined from SMPS data for SOA generated from HCIP1. .... 100

**Figure 4.4** a) picture of aphid-infested tree (SCIP4). b) Sample of aphid and aphid exuviae (exoskeleton) collected from pine needles onto a petri dish. C) Close up of collected aphid, identified as a light green pine needle aphid (*Eulachnus brevipilosus*). .... 102

**Figure 4.5** The dependence of viscosity on exposure time was monitored for all SOA types. A poke-flow experiment was performed at various exposure times up to 24 h at (a) 0%, (b) 25%, (c) 50%, and (d) 60% RH to ensure that the particles were at equilibrium. Black points correspond to those of healthy plant SOA and red points correspond to stressed plant SOA. .... 108

**Figure 4.6** Particle evaporation tests performed within the flow cell of a poke-flow experiment. The area of a SOA particle was monitored for each SOA type over the course of up to 27 h. The particles were exposed to (a)  $\approx 0\%$  RH and (b) 60% RH within the flow cell. Error bars correspond to the standard deviation of repeated measurements of the area of the particle at a given time point. Black points correspond to those of healthy plant SOA and red points correspond to stressed plant SOA. .... 109

**Figure 4.7** Average fraction of total initial VOC mixing ratio in the chamber at the start of the experiment for the healthy (HCIP1-3) and aphid-stressed (HCIP4-5) experiments. Other MT category refers to other monoterpenoids. The Oxy-T category refers to oxygenated monoterpenes.

The stress SQT category contains farnesene and germacrene. An asterisk (\*) denotes statistical significance ( $p \leq 0.01$ ) with a Student's t-test (reported in Table S3). Error bars are standard error of the mean. .... 112

**Figure 4.8** (a) Viscosity and (b) mixing times of organic molecules ( $\tau_{\text{mix},200\text{nm,org}}$ ) obtained from poke-flow measurements of healthy and stressed plant SOA as a function of relative humidity at room temperature (292 K). Error bars in the y-direction correspond to the upper and lower bounds of viscosity and mixing times, whereas error bars in the x-direction correspond to the error in relative humidity from the measurement of dewpoints using a chilled mirror hygrometer. Upwards arrows correspond to lower limits, and downwards arrows correspond to upper limits. Open black circles (mimic HCIP SOA) correspond to data from Smith et al. (2021) and Maclean et al. (2021)<sup>278,280</sup>, red open circles (mimic SCIP SOA) correspond to data from Smith et al. (2021).<sup>278</sup> ..... 113

**Figure 4.9** Experimental flow times ( $\tau_{\text{exp,flow}}$ ) as a function of relative humidity of poke-flow experiments obtained at room temperature (292 K). Panel (a) corresponds to those of healthy plant SOA (HCIP1-3) and panel (b) corresponds to those of stressed plant SOA (SCIP4-5). ..... 114

**Figure 4.10** Viscosity as a function of RH of poke-flow experiments obtained at room temperature (292 K). Panel (a) corresponds to those of healthy plant SOA (CIP1-3) and panel (b) corresponds to those of stressed plant SOA (TA3 and TB2). Green circles (hp-proxy SOA) correspond to data from Smith et al. (2021) and Maclean et al. (2021)<sup>305,306</sup>, green squares (sp-proxy SOA) correspond to data from Smith et al. (2021).<sup>305</sup> ..... 115

**Figure 4.11** High resolution mass spectra normalized to the sum of normalized intensities for HCIP2-3 (HCIP, black) and SCIP4-5 (SCIP, red) from AMS data. .... 117

**Figure 4.12** Sum of normalized intensities as a function of carbon number based on organic families for HCIP2-3 (HCIP, black) and SCIP 4-5 (SCIP, red) from AMS data. .... 118

**Figure 4.13** High resolution mass spectra normalized to the sum of normalized intensities for HCIP2-3 (HCIP, black) and SCIP4-5 (SCIP, red) from AMS data, with respect to chemical family CH ( $\text{C}_x\text{H}_y^+$ ), CHO ( $\text{C}_x\text{H}_y\text{O}^+$ ), CHO<sub>gt1</sub> ( $\text{C}_x\text{H}_y\text{O}_{z>1}^+$ ). .... 119

## LIST OF TABLES

	Page
<b>Table 2.1</b> Calculated mixing times of water within the SOA particles ( $\tau_{\text{mix,H}_2\text{O}}$ ) and experimental conditioning time for water vapor ( $t_{\text{exp,H}_2\text{O}}$ ), which corresponds to the time the SOA particles were exposed to a given relative humidity before the poke-flow experiments. Viscosities are based on the upper limits of viscosity shown in Figure 2.4 below. Diffusion coefficients were calculated using the relation between viscosity and diffusion coefficients in sucrose-water from Price et al., 2016. <sup>102</sup> The variable $d_p$ corresponds to the diameter of the SOA used in the poke-flow experiments. ....	16
<b>Table 2.2</b> COMSOL parameters used when simulating the viscosity of $\beta$ -caryophyllene SOA from poke-flow measurements. ....	21
<b>Table 3.1</b> Chemical composition of the VOC mixture used to produce SOA; purity and sources of commercially- available standards used to generate healthy and stressed VOC mixtures; and lifetimes with respect to oxidation in the chamber. Monoterpene is abbreviated as MT and sesquiterpene is abbreviated as SQT. The chemical structures of these VOCs are reported in Appendix A. ....	54
<b>Table 3.2</b> COMSOL parameters used for simulating the upper and lower limits of viscosity of the collected SOA by poke-flow. ....	61
<b>Table 3.3</b> The most abundant formulas detected by nano-DESI-HRMS. All of these compounds appear in both (+) and (-) ESI modes; the second column lists the ionization mode in which they have higher relative peak abundance. References for previously reported structures identified as a monoterpene oxidation product (MTOX) or sesquiterpene oxidation product (SQTOX) that have the same neutral molecular formula and mass as those found in this study are listed in the last column. ....	73
<b>Table 4.1</b> Purity and sources of commercially available standards used to generate calibration curves for TD-GC-MS quantification. ....	97
<b>Table 4.2</b> Experimental conditions for SOA particles generated in the chamber from different Canary Island pine trees (1-5). The VOC concentration used was the total VOC contribution from terpenes monoterpene ( $\text{MT}_i$ ), oxygenated monoterpene ( $\text{OMT}_i$ ), and sesquiterpenes ( $\text{SQT}_i$ ) identified using GC-MS. HCIP abbreviation designates healthy Canary Island pine trees and SCIP designates stressed Canary Island pine trees. ....	101
<b>Table 4.3</b> Percent of total VOC identified with TD-GC-MS for each experiment. P-values were determined using a two-tailed, Student's t-test for the comparison of the average healthy (HCIP1-3) and stressed (SCIP4-5) trees. ....	104
<b>Table 4.4</b> COMSOL parameters used for simulating the upper and lower limits of viscosity of the collected SOA by poke-flow at 292 K. ....	106

## ACKNOWLEDGEMENTS

I would like to thank everyone who has supported me over the years and encouraged me to pursue my goals against all odds, without you all this achievement would have not been possible.

To my two PIs, Professor Sergey Nizkorodov and Professor Celia Faiola thank you for your constant support and help throughout my time in graduate school. Working with both of you has expanded my perspective on collaborative science and I am thankful to have had the opportunity to be a part of two groups that are filled with amazing people. Sergey, you are truly a wonderful advisor, and I am so glad that I joined your lab back in 2017 along with Alex and Vahe. you have had such an enormous positive impact on my life. To my collaborators in the Bertram Group at UBC, Shiraiwa Group at UCI, Laskin Group at Purdue, and Dabdub group at UCI, it has been a pleasure working with you all and your groups and I am so glad we could do some awesome science together!

To Dr. Barkley Sive, I am so thankful that I got a chance to meet you at Appalachian State University's open house back in 2012, where I was a young High School student looking into Environmental Science programs. You introduced me to the idea of pursuing Environmental/Atmospheric Chemistry, something that I had not considered before. The opportunity you gave me as a freshman at App opened a world of opportunity for me within Atmospheric Chemistry and I will forever be grateful for your mentorship and constant support over the years. I am truly grateful to have met and worked with you, even a short period of time made a world of difference. To Dr. Brett Taubman, thank you for being a wonderful advisor and allowing me to continue on my Atmospheric Chemistry research journey through working in your lab. I truly enjoyed working with you my last three years at App.

A HUGE thank you to the other two-thirds of the "triplets" in the Nizkorodov Lab, Dr. Alex Klodt and Dr. Vahe Baboornian. You have made grad school so fun, and I am very grateful for our friendship, jokes, and good times. I will truly miss having coffee time with you all and going on lunch adventures to UTC and travelling to conferences together. Alex, you are such an amazing and caring person, and I am so glad that we have become such close friends. You have been a massive support system for me, and I will never forget how special both you and Igor are to me. I would also like to thank all former and current members of the Nizkorodov Lab. Especially Dr. Lauren Fleming and Dr. Julia Montoya- Aguilera for teaching me how to be a grad student and training me on all our lab's instrumentation and being wonderful people. Julia- I will forever be your hype-man and talk about how wonderful, exciting, novel, showstopping you and your research is. Alex Klodt, Cynthia Wong, and Lucia Liu thank you for being my climbing partners and keeping me physically active and being such supportive, sweet, and great people. You will truly be missed!

Thank you to my family for being so supportive and giving me advice when times get tough. Thank you to my mom who has always been my number one supporter and has even attended some of my research conferences over the years. I don't think I could have done it without your constant love and support. I would also like to thank my grandmother who taught me the value of a good education and how to be resilient regardless of the circumstances you are in.

My friends have been a massive encouragement and source of joy over the years. Thank you to my friends from back home in North Carolina: Nadine Lambert, Tayler Barnard, Rina Leonidas, William Davis, and Stefan Isaza for always making me laugh and reminding me that no matter what happens I will always have your love and support and to enjoy the beautiful things life has to offer.

Thank you to Lisa Wingen, Veronique Perraud, and Adam Thomas for being wonderful people and being people that I could always talk to about research issues. I will miss being an Orbitrap Instrument Overlord (IO) with you all. Setting up and maintaining a new instrument is already a challenge, but to do it during the COVID shutdown was quite the task! However, you are all superstars and we made it happen!!

Thank you to everyone in AIRUCI, you are the most supportive and friendly group of people that I have had the pleasure of working with. Thank you to Professor Don Blake for taking me on as a WAS mentor for SARP and being so supportive during graduate school. I am so thankful we got the chance to work together, and you are a wonderful human! Thank you to the NASA SARP 2022 program and all the wonderful people I got to meet and interact with. Being around you all has reminded me of the joy of doing science and the goal of making the world a better place.

I am grateful for the support the UC- Irvine Department of Chemistry has given me over the course of my graduate career through the F. Sherwood Rowland Fellowship which supported me during two quarters and for the Chemistry Dissertation Fellowship which supported me in the Spring quarter of my final year in graduate school. These two funding opportunities provided a great deal of support and gave me protected time which allowed me to focus solely on research and finish my last set of research projects regarding Real pine tree SOA. I would also like to thank the publishers of my research works within this dissertation.

The text of chapter 2 within this dissertation is a reprint of the material as it appears in Maclean et al., Humidity-dependent viscosity of secondary organic aerosol from ozonolysis of  $\beta$ -caryophyllene: Measurements, predictions, and implications, ACS Earth and Space Chemistry, 5 (2021) 305-318, used with permission from The American Chemical Society. The co-authors listed in this publication are Adrian M. Maclean, Natalie R. Smith, Ying Li, Yuanzhou Huang, Anusha P. S. Hettiyadura, Giuseppe V. Crescenzo, Manabu Shiraiwa, Alexander Laskin, Sergey A. Nizkorodov, and Allan K. Bertram.

The text of chapter 3 within this dissertation is a reprint of the material as it appears in Smith et al., Viscosity and liquid-liquid phase separation in healthy and stressed plant SOA, Environmental Science: Atmospheres, 1 (2021) 140-153, used with permission from The Royal Society of Chemistry. The co-authors listed in this publication are Natalie R. Smith, Giuseppe V. Crescenzo, Yuanzhou Huang, Anusha P. S. Hettiyadura, Kyla Siemens, Ying Li, Celia L. Faiola, Alexander Laskin, Manabu Shiraiwa, Allan K. Bertram, Sergey A. Nizkorodov.

## VITA

Natalie Rose Smith

### **Education**

---

**University of California, Irvine**

August 2022

Degree: Ph.D. Chemistry

Advanced to Ph.D. candidacy (January 2020)

**University of California, Irvine**

June 2020

Degree: M.S. Chemistry

**Appalachian State (AppState) University, Boone, NC**

September 2017

Degree: B.S. Chemistry

Minor: Physics

### **Academic Research Experience**

---

#### **Molecular Composition of Viscous SOA**

**(September 2017-September 2022)**

PI: Prof. Sergey Nizkorodov

Department of Chemistry, University of California, Irvine, Irvine, CA, USA

Laboratory generated secondary organic aerosols (SOA) from various volatile organic gasses are prepared in a photochemical smog chamber under varying sets of atmospherically relevant conditions and analyzed using a suite of instruments including a scanning mobility particle sizer, aerosol mass spectrometer, and proton transfer high resolution mass spectrometer, as well as several gas monitors. Viscosity measurements of the generated SOA are carried out at the University of British Columbia in Professor Allan Bertram's group using the poke-flow method. High resolution mass spectrometry measurements are taken at Purdue University in Professor Alexander Laskin's group using nano-desorption electrospray ionization high resolution mass spectrometry. The molecular composition data is then input into the Manabu Shiraiwa model for glass transition temperatures where viscosities of the SOA can be derived. The experimental viscosity data is then compared against the predicted viscosity of the SOA from the model to identify any missing parameters so that improvements to the model can be made. The information attained from this study will help to parameterize the impact particle composition has on SOA viscosity.

#### **Reactive Uptake of Amines and Ammonia onto Heterocyclic Nitrogen Containing SOA (February 2017- October 2021)**

PI: Prof. Sergey Nizkorodov and Prof. Donald Dabdub

Department of Chemistry, University of California, Irvine, Irvine, CA, USA

Various types of biogenic VOCs are oxidized in a photochemical smog chamber to form SOA, and the resulting particles are exposed to a 100 ppb pulse of one of the following vapors: dimethyl amine, butyl amine or ammonia. The decay of the injected ammonia or amines is used to determine the overall reactive uptake coefficient. An AMS is used to explicitly observe the formation of nitrogen containing organic compounds (NOC) in SOA, and further constrain the reactive uptake coefficient. Nicotinic acid seed particles are used to help SOA particles grow, as well as to provide a convenient internal standard for quantifying NOC in SOA particles by AMS. The chemical

composition of SOA particles is also analyzed by off-line methods to determine the types of NOC formed in the ammonia/amine + SOA reactions. The experimental results are incorporated into the University of California, Irvine - California Institute of Technology (UCI-CIT) regional airshed model to investigate the effect of the ammonia/amine + SOA chemistry on the amount of particulate matter produced under different scenarios.

**Chemical and Optical Properties of Aerosols in the Southeastern U.S.  
(Fall 2014-Spring 2017)**

PI: Prof. Brett Taubman

Department of Chemistry, Appalachian State University, Boone, NC, USA

This research employed a method to characterize chemical properties of aerosols collected on quartz fiber filters from a low-volume sampler connected to a particle soot absorption photometer (PSAP) located at the Appalachian Atmospheric Interdisciplinary Research (AppalAIR) facility located on the University's campus in Boone, NC. The chemical characterization of the aerosols involved the direct thermal desorption of quartz fiber filters onto a gas chromatography-mass spectrometer. The standards used to analyze the particulate matter collected on the filter included anthracene, fluoranthene, fluorene, levoglucosan, cis-pinonic acid, and methacrylic acid. These standards served as anthropogenic and biogenic markers for biomass burning, combustion of fossil fuels, and secondary organic aerosols formed from vegetation. The aim of this study was to identify the chemical composition of the particulate matter that was collected, so that optical properties of aerosols could be attributed to specific chemical signatures.

**Planetary Boundary Layer Height Determination from Radiosonde Data from Weather Balloon Launched  
(Fall 2013)**

PI: Prof. James Sherman

Department of Physics, Appalachian State University, Boone, NC, USA

In the summer of 2013, over 200 weather balloons were launched around the Appalachian State University campus. MatLab was used to develop scripts and functions to average vertical profiles and determine the boundary layer height using several methods based on radiosonde data from the weather balloon launches. This project provided planetary boundary layer height data over a three-month period in the region, giving insight into the diurnal and day-to-day boundary layer height variability in the area.

**Volatile Organic Compound Ambient Trace Gas Analysis  
(Fall 2013- Spring 2014)**

PI: Prof. Barkley Sive and Dr. Yong Zhou

Department of Chemistry, Appalachian State University, Boone, NC, USA

Ambient whole air samples were collected from the AppalAIR facility in Boone, NC. These air samples were analyzed on a custom-built VOC sample concentration system that was paired with Gas Chromatographs coupled to four different detectors (Flame Ionization Detector, Mass Spectrometer, Thermal Conductivity Detector, and Electron Capture Detector). This work provided daily background level concentrations for various gases in the Appalachian Mountain region, giving insight into the volatile organic gaseous concentrations in pristine forest environments.

## **Professional Work Experience**

---

### **NASA Student Airborne Research Program**

June 2022-August 2022

#### **Bay Area Environmental Research Institute-Irvine, CA**

PI: Professor Donald Blake

I was responsible for mentoring seven undergraduate student interns working in the Whole Air Sampling research group during the 8-week, NASA Student Airborne Research Program. I was responsible for training these students on how to collect whole air samples using stainless steel canisters onboard the DC-8 aircraft, in the field, and the lab. In the Rowland-Blake lab at UC Irvine, I trained the students to analyze the whole air samples using gas chromatography and mass spectrometry procedures developed for highly sensitive analysis of trace volatile organic compounds (VOCs) in the atmosphere. I had daily one-on-one meetings with the students where I provided detailed guidance on their research projects and make sure they remain on track to finish within the 8-week program. I also work alongside a coding mentor to help assist the students in processing large datasets.

### **U.S. Environmental Protection Agency GRO Fellow-Grantee**

May 2016- August 2016

#### **EPA Region 5 Air and Radiation Division - Chicago, IL**

PI: Michael Compher and Marta Fuoco

Performed data analysis for the continuous air monitors attached to the EPA Village Green monitoring station located in southeast Chicago, in addition to the mobile EPA Air Sensor Toolbox. Specific tasks included learning about the air program, identifying and prioritizing emission sources through data analysis, evaluating the quality of data being collected, and performing statistical analysis. Promoted citizen science through community outreach, teaching citizens how to use EPA's Air Sensor Toolbox created by the EPA Office of Research and Development.

### **Pathways Physical Science Research Intern**

June 2015 - December 2016

#### **EPA's National Risk Management Research Laboratory- Air Pollution Control Division Research Triangle Park, NC**

PI: Dr. Michael Hays and Dr. Ingrid George

Analyzed ambient whole air samples collected using summa canisters under EPA method TO-15 from near-road and forested sites. Also analyzed cartridge samples under EPA method TO-17 for samples collected under ambient conditions.

## **Teaching Experience**

---

### **Teaching Assistant, University of California, Irvine, Department of Chemistry**

Environmental chemistry lecture (CHEM 141)

Winter 2022

General chemistry lecture (CHEM 1A)

Fall 2020

General chemistry lecture (CHEM 1C)

Spring 2018, Spring 2020

Analytical chemistry lab (CHEM M3LC)

Spring 2019

General chemistry lab (CHEM 1LD)

Fall 2017, Winter 2018, Winter 2019

### **Teaching Assistant, Appalachian State University, Department of Physics**

Environmental Physics

Fall 2017



## Peer-Reviewed Papers

---

**N. R. Smith**, G. V Crescenzo, F. Marht, C. L. Faiola, A. K. Bertram, S. A. Nizkorodov, Insect infestation increases viscosity of biogenic secondary organic aerosol (**In preparation**).

G. V Crescenzo, V. J. Baboomian, **N. R. Smith**, S. A. Nizkorodov, A. K. Bertram, Viscosity of secondary organic aerosol: effects of composition and oxidation method (**In preparation**).

L. Peng, F. Marht, **N. R. Smith**, S. A. Nizkorodov, A. K. Bertram, Viscosity of isomers of sesquiterpenes - small changes in structure lead to big changes in viscosity (**In preparation**).

F. Marht, L. Peng, Y. Huang, J. Zaks, P. E. Ohno, **N. R. Smith**, Y. Qin, F. K. A. Gregson, C. L. Faiola, S. T. Martin, S. A. Nizkorodov, M. Ammann, A. K. Bertram, Not all types of secondary organic aerosol mix: two phases observed when mixing different secondary organic aerosol types, *ACP*, **in open discussion** (2022) DOI: 10.5194/acp-2022-331

K. J. Kiland, K. L. Marroquin, **N. R. Smith**, S. Xu, S. A. Nizkorodov, and A. K. Bertram, A new hot-stage microscopy technique for measuring temperature-dependent viscosities of aerosol particles and its application to farnesene secondary organic aerosol, *AMT*, **in accepted** (2022) DOI: 10.5194/amt-2022-151

A. M. Maclean, Y. Li, G. V. Crescenzo, **N. R. Smith**, V. A. Karydis, A. P. Tsimpidi, A. P. S. Hettiyadura, K. Siemens, C. L. Butenhoff, C. L. Faiola, J. L. Jimenez, A. Laskin, J. Lelieveld, S. A. Nizkorodov, M. Shiraiwa, A. K. Bertram, Global distribution of the phase state and mixing times within secondary organic aerosol particles in the troposphere based on room-temperature viscosity measurements, *ACS Earth Sp. Chem.*, **5** (2021) 3458-3473. DOI:10.1021/acsearthspacechem.1c00296

**N. R. Smith**, J. Montoya-Aguilera, D. Dabdub, Sergey A. Nizkorodov, Effect of humidity on the reactive uptake of ammonia and dimethylamine by nitrogen-containing secondary organic aerosol, *Atmosphere*, **12** (2021) 1502. DOI:10.3390/atmos12111502

**N. R. Smith**, G. V Crescenzo, Y. Huang, A. P. S. Hettiyadura, K. Siemens, Y. Li, C. L. Faiola, A. Laskin, M. Shiraiwa, A. K. Bertram and S. A. Nizkorodov, Viscosity and liquid-liquid phase separation in healthy and stressed plant SOA, *Environ. Sci.: Atmos.*, 2021, **1**, 140–153. DOI:10.1039/d0ea00020e

A. M. Maclean, **N. R. Smith**, Y. Li, Y. Huang, A. P. S. S. Hettiyadura, G. V. Crescenzo, M. Shiraiwa, A. Laskin, S. A. Nizkorodov and A. K. Bertram, Humidity-dependent viscosity of secondary organic aerosol from ozonolysis of  $\beta$ -caryophyllene: Measurements, predictions, and implications, *ACS Earth Sp. Chem.*, 2021, **5**, 305–318. DOI:10.1021/acsearthspacechem.0c00296

M. Song, A. M. Maclean, Y. Huang, **N. R. Smith**, S. L. Blair, J. Laskin, A. Laskin, W.-S. W. DeRieux, Y. Li, M. Shiraiwa, S. A. Nizkorodov and A. K. Bertram, Liquid-liquid phase separation and viscosity within secondary organic aerosol generated from diesel fuel vapors, *Atmos. Chem. Phys.*, 2019, **19**, 12515–12529. DOI:10.5194/acp-19-12515-2019

## **Oral Presentations**

---

**N. R. Smith**, G. V. Crescenzo, F. Mahrt, C. L. Faiola, A. K. Bertram, S. A. Nizkorodov, *Viscosity and liquid-liquid phase separation of Canary Island pine SOA*, 39th Annual American Association for Aerosol Research (AAAR) Conference, October 8, 2021 (Online Conference).

**N. R. Smith**, J. Montoya-Aguilera, D. Dabdub, S. A. Nizkorodov, Effect of humidity on the reactive uptake of ammonia and dimethylamine by nitrogen-containing secondary organic aerosol, The American Chemical Society (ACS) Fall National Meeting, August 24, 2021 (Online Conference).

**N. R. Smith**, G. V. Crescenzo, Y. Huang, A. P.S. Hettiyadura, K. Siemens, Y. Li, C. L. Faiola, A. Laskin, M. Shiraiwa, A. K. Bertram, S. A. Nizkorodov, *Viscosity and liquid-liquid phase separation in healthy and stressed pine tree SOA*, 37th Annual Informal Symposium on Kinetics and Photochemical Processes in the Atmosphere (ISKPPA), February 19, 2021 (Online Conference).

**N. R. Smith**, Y. Huang, G. V. Crescenzo, A. Hettiyadura, K. Siemens, C. L. Faiola, A. Laskin, A. K. Bertram, S. A. Nizkorodov, *Highly Viscous Secondary Organic Aerosol from Healthy and Stressed Pine Trees*, 38th Annual American Association for Aerosol Research (AAAR) Conference, October 8, 2020 (Online Conference).

**N. R. Smith**, Y. Huang, G. V. Crescenzo, A. Hettiyadura, K. Siemens, C. L. Faiola, A. Laskin, A. K. Bertram, S. A. Nizkorodov, *Viscosity and LLPS of SOA from Healthy and Stressed Pine Trees*, The American Chemical Society (ACS) National Meeting, August 28, 2019, San Diego, CA, USA.

**N. R. Smith**, D. Dabdub, J. Montoya-Aguilera, J. R. Horne, S. Zhu, and S. A. Nizkorodov, *The role of ammonia: Interactions with particles and impacts on air quality*, PM in a Changing World EPA STAR Program Meeting, November 28-29, 2018, Research Triangle Park, NC, USA.

**N. R. Smith**, A. Maclean, M. Song, Y. Huang, W. DeRieux, Y. Li, A. Laskin, A. Bertram, M. Shiraiwa, S. A. Nizkorodov, *An investigation of viscous SOA in the atmosphere*, AirUCI Retreat, September 24-26, 2018, Lake Arrowhead, CA, USA.

## **Poster Presentations**

---

**N. R. Smith**, G. V. Crescenzo, F. Mahrt, C. L. Faiola, A. K. Bertram, S. A. Nizkorodov, Viscosity of Canary Island pine tree SOA, International Chemical Congress of Pacific Basin Societies (PACIFICHEM), December 16, 2021, (Online Conference).

**N. R. Smith**, G. V. Crescenzo, Y. Huang, A. Hettiyadura, K. Siemens, C. L. Faiola, A. Laskin, A. K. Bertram, S. A. Nizkorodov, *Composition, Phase Separation, and Viscosity of Healthy and Stressed Pine Tree SOA*, The 37th Association of Atmospheric Aerosol Research (AAAR) Annual Conference, October 15, 2019, Portland, OR, USA.

**N. R. Smith**, M. Song, A. M. Mclean, Y. Huang, S. L. Blair, J. Laskin, A. Laskin, W. Wong-DeRieux, Y. Li, M. Shiraiwa, A. K. Bertram, S. A. Nizkorodov, *Liquid-liquid Phase Separation and Viscosity within Secondary Organic Aerosol Generated from Diesel Fuel Vapor*, 36th Annual Informal Symposium on Kinetics and Photochemical Processes in the Atmosphere (ISKPPA), May 10, 2019, Riverside, CA, USA.

**N. R. Smith**, N. Hall, T. Sink, B. F. Taubman, *Investigation of the Chemical and Optical Properties of Aerosols in the Southeastern U.S.*, National Conference on Undergraduate Research (NCUR), 2017, Memphis, TN, USA.

**N. R. Smith**, N. Hall, T. Sink, B. F. Taubman, *Investigation of the Chemical and Optical Properties of Aerosols in the Southeastern U.S.* North Carolina BREATHE Conference, 2016, Charlotte, NC, USA.

**N. R. Smith**, K. Noel, T. Tayler, B. F. Taubman, *Investigation of the Chemical and Optical Properties of Aerosols in the Southeastern U.S.*, State of North Carolina Undergraduate Research and Creativity Symposium (SNCURCS), 2016, High Point, NC, USA.

**N. R. Smith**, A. Merwin, B. F. Taubman, *Investigation of the Chemical and Optical Properties of Aerosols in the Southeastern U.S.* State of North Carolina Undergraduate Research and Creativity Symposium (SNCURCS), 2015, Asheville, NC, USA.

**N. R. Smith**, I. Krintz, J. Sherman, *Planetary boundary layer determination from meteorological radiosonde data*, State of North Carolina Undergraduate Research and Creativity Symposium (SNCURCS), 2013, Charlotte, NC, USA.

### **Awards & Certifications**

---

Graduate Dissertation Fellowship UCI Department of Chemistry	Spring 2022
AirUCI Michael E. Gebel Awardee	2021
2020 Graduate Student Awardee in Environmental Chemistry, American Chemical Society	2020
F. Sherwood Rowland Graduate Fellowship, UCI Department of Chemistry	2020-2021
UCI Chemistry Department Travel Grant	April 2020
Certified Orbitrap HRMS Instrument Operator at AIRUCI	March 2020
Student Poster Award Recipient, 37th Association of Atmospheric Aerosol Research (AAAR) Annual Conference	October 2019
Admitted/Participant in the EMSL/ARM Aerosol Summer School,	July 2019

Pacific Northwest National Lab

Mentoring Excellence Certification through the Graduate Resource Center (GRC) at UCI Winter 2019

Activate to Captivate Certification through the Graduate Resource Center (GRC) at UCI Winter 2019

AppState Office of Student Research Travel Grant Recipient (Travel to research conferences) Fall 2015, Fall 2016, Fall 2017

U.S. EPA - Greater Research Opportunity (GRO) Fellow Fall 2015- Spring 2017

AppState Office of Student Research Grant Recipient Spring 2015, Fall 2015, Fall 2016

AppState A.R. Smith Department of Chemistry Research Scholarship Recipient Spring 2015, Fall 2015

American Meteorological Society Student Grant Recipient Summer 2015  
(Awarded full registration fee for the AMS National Summer Community Meeting)

AppState University Academy of Science Scholarship Recipient Summer 2013 - Spring 2014  
(Supported by National Science Foundation)

### **Leadership & Mentorship**

---

Graduate Student Mentor in Nizkorodov Group at UCI Fall 2018- Fall 2020  
Mentees: Michael Olsen and Samantha Scott

Alumni Mentor for Undergraduate Student at AppState University in Academy of Science program Winter 2020-Spring 2020  
Mentee: Nick Mencis

AppState University Club of Environmental Sciences Vice President Fall 2016-Spring 2017

AppState University Club of Environmental Sciences Secretary Fall 2014-Spring 2016

### **Memberships**

---

American Chemical Society 2019-Present

The American Association for Aerosol Research 2018-Present

American Meteorological Society 2012-Present

Graduate Women in Science 2018-2019

Appalachian Chemical Society, AppState University Spring 2015-2017

National Collegiate Honors Society 2014-2017

Club of Environmental Science, AppState University 2013-2017

## ABSTRACT OF THE DISSERTATION

Complex Mixtures of Terpenes Results in Highly Viscous Secondary Organic Aerosols

by

Natalie Rose Smith

Doctor of Philosophy in Chemistry

University of California, Irvine, 2022

Professor Sergey A. Nizkorodov, Chair

A major fraction of secondary organic aerosol (SOA) in the atmosphere are generated from oxidation of volatile organic compounds (VOCs) emitted from pine trees. Because  $\alpha$ -pinene and limonene typically dominate the monoterpene emission profile in forested areas, they have commonly been used as representative monoterpenes in laboratory studies investigating biogenic SOA fundamental properties. However, pine trees emit a wide range of terpenes with different reactivities and structures including numerous isomers of monoterpenes ( $C_{10}H_{16}$ ) and sesquiterpenes ( $C_{15}H_{24}$ ), drastically altering the resulting properties of SOA particles such as chemical composition and viscosity. Viscosity is an important physical property of SOA and can lead to much slower diffusion rates within the particles, impacting particle growth and evaporation, gas-particle partitioning, and the ability of SOA particles to act as nuclei for liquid cloud droplets or ice particles.

The goal of this thesis is to compare chemical composition and viscosity of SOA particles generated from single terpenes as well as from a mixture of terpenes emitted by pine trees. This work will elucidate how single-terpene SOA compares to real biogenic SOA chemical composition and viscosity, and thus determine if a single-terpene SOA is a good proxy system to model

biogenic SOA. A second goal of this work is to identify the influence plant stress has on chemical composition and viscosity of SOA. This is important because plant stress (ex. insect-herbivory) leads to an increase in the emission rates of sesquiterpenes from pine trees. Due to climate change, plants are expected to endure longer periods of stress. However, the impact this change in VOC profile has on SOA properties compared to SOA from healthy trees is not well characterized.

Chapter 2 investigated the humidity-dependent viscosity of SOA from ozonolysis of  $\beta$ -caryophyllene, which is the most abundant sesquiterpene emitted by pine trees. In this study, we measured viscosity as a function of RH using a poke-flow technique and measured chemical composition using nano-desorption electrospray ionization mass spectrometry. We found that at an RH of 0 and 48%, the viscosity was between  $6.9 \times 10^5$  and  $2.4 \times 10^7$  Pa s, and between  $1.3 \times 10^3$  and  $5.6 \times 10^4$  Pa s, respectively. Based on these viscosities and the fractional Stokes–Einstein equation, we found that mixing times of organics within 200 nm  $\beta$ -caryophyllene SOA are fast ( $<1$  h) for RH and temperatures typically found in the planetary boundary layer.

Chapter 3, focused on characterizing the molecular composition, viscosity, and liquid–liquid phase separation (LLPS) for SOA derived from synthetic mixtures of terpenes representing emission profiles for Scots pine trees under healthy and aphid-herbivory stress conditions. This work revealed that at 40% and 50% RH, stressed plant SOA had the highest viscosity, followed by healthy plant SOA and then  $\alpha$ -pinene SOA in descending order. The stressed plant SOA had increased abundance of higher molecular weight species, reflecting a greater fraction of sesquiterpenes in the stressed VOC mixture compared to the healthy plant VOC mixture. These findings suggest that plant stress influences the physicochemical properties of biogenic SOA. Furthermore, a complex mixture of VOCs resulted in a higher SOA viscosity compared to SOA generated from  $\alpha$ -pinene alone, highlighting the importance of studying properties of SOA

generated from more realistic multi-component VOC mixtures. As a result of the high viscosity, the mixing time of organic molecules within a 200 nm SOA particle emitted by stressed or healthy tree takes hours, even, under conditions of ambient relative humidity <40%, which is greater than the mixing times for  $\alpha$ -pinene SOA.

As a follow-up study, we investigated the viscosity of real Canary Island pine secondary organic aerosol to confirm our previous results from synthetic mixtures of tree SOA, using real SOA samples (Chapter 4). We found that SOA generated from real healthy and aphid-stressed pine trees closely matches the viscosity results we found previously where aphid-stressed pine tree SOA consistently had higher SOA viscosity compared to healthy pine tree SOA over all relative humidities investigated. This increased viscosity for stressed SOA was attributed to an increase in terpenes (oxygenated monoterpenes and sesquiterpenes) emitted as a result of aphid-herbivory.

Overall, this work highlights the need for using mixtures of terpenes to study the fundamental properties of biogenic SOA and how plant stress leads to even more viscous SOA compared to healthy pine tree SOA.

# CHAPTER 1

## Introduction

### 1.1 Atmospheric aerosols

Aerosols are solid or liquid particles suspended in a gas. Atmospheric aerosols, sometimes referred to as particulate matter (PM), are ubiquitous throughout Earth's troposphere and lower stratosphere. These particles come from both anthropogenic and biogenic sources and are emitted into the atmosphere via primary (i.e., direct emission) or secondary (i.e., formed by atmospheric chemistry) processes. Examples of primary aerosols include pollen emitted from vegetation, suspended sea-spray particles from crashing oceanic waves, smoke from forest fires and vehicle exhaust from tailpipes. Secondary aerosol particles are produced when volatile inorganic or organic compounds react with common atmospheric oxidants such as  $\text{NO}_x$ ,  $\text{O}_3$ , or  $\text{OH}$ , which form low volatility products that partition into the condensed phase. Aerosols are also classified by particle size into ultrafine (<100 nm in diameter), fine (<2.5  $\mu\text{m}$  in diameter, also known as  $\text{PM}_{2.5}$ ) and coarse (< 10  $\mu\text{m}$  in diameter, often referred to as  $\text{PM}_{10}$ ). Primary particles are often found in the coarse mode, and secondary particles dominate the ultrafine and fine modes.

Secondary organic aerosol (SOA) is formed from the condensation of oxidation products of volatile organic compounds (VOCs), which leads to thousands of individual compounds within the particle. SOA particles dominate the total fine aerosol mass in the atmosphere.<sup>1</sup> It is estimated that up to 100,000 different VOCs are emitted into the atmosphere, resulting in the highly complex composition of SOA.<sup>2</sup> Because of the chemical complexity of ambient SOA, only 10% of the total mass of SOA has been speciated in terms of molecular composition.<sup>1</sup>

Newly formed SOA, sometimes referred to as fresh SOA, typically starts with ultrafine particles but can grow through coagulation with other particles and gas-particle partitioning to



larger particles making a sizable contribution to PM<sub>2.5</sub>. Due to their small size, SOA can penetrate deep into the lungs causing significant respiratory issues as well as various other negative health outcomes such as cardiovascular disease.<sup>3-4</sup> A number of health studies have shown significant correlation between poor air quality (resulting in a high PM<sub>2.5</sub> exposure) and negative health outcomes, prompting the U.S. Environmental Protection Agency to set limits on PM exposure under the Clean Air Act.<sup>5</sup>

These tiny aerosol particles also have a significant influence on the radiative forcing of Earth's atmosphere. Aerosol particles can directly absorb and scatter incoming solar radiation and also can act as seeds for cloud formation, which can indirectly impact climate.<sup>6</sup> Additionally, light scattering by aerosol particles can lead to decreased visibility.<sup>7</sup> These particles can remain suspended in the atmosphere for days to weeks and can experience long-range transport to regions far from their generation site.<sup>8-10</sup> The full extent to which aerosols affect air quality and climate remains uncertain,<sup>6</sup> therefore it is critical to study their fundamental properties. A comprehensive understanding of the formation, properties, and transformation of SOA is essential for evaluating their impact on atmospheric processes, climate, and human health.

## **1.2 Biogenic aerosols**

Approximately 90% of all of VOCs in the atmosphere come from biogenic sources<sup>1</sup> leading to the large abundance of biogenic SOA in the atmosphere.<sup>11</sup> For example, plants have high emission rates of terpenes.<sup>11,12</sup> Terpenes are hydrocarbons that are categorized by the number of isoprene units (C<sub>5</sub>H<sub>8</sub>), with the most common being monoterpenes and (C<sub>10</sub>H<sub>16</sub>) and sesquiterpenes (C<sub>15</sub>H<sub>24</sub>).<sup>11,12</sup> Terpenes constitute the essential oils of plants and are produced during plant metabolism and stored in resin ducts of plant leaves.<sup>13</sup>

Because  $\alpha$ -pinene and d-limonene typically dominate the monoterpene emission profile in forested areas,<sup>14,15</sup> they have commonly been used as representative monoterpenes in laboratory and modelling studies investigating biogenic SOA, to simplify data analysis and decrease computation time. In laboratory studies,<sup>16,17</sup> SOA generated from a single precursor is generally favored because these simpler systems allow for the investigation of their fundamental properties. Single precursor experimental studies provide parameterizations for models in which the impact of SOA on climate is evaluated. However, real atmospheric particles formed in the ambient environment are produced from a complex mixture of VOCs.

Isomeric species within a given terpene class can have a range of reactivities due to changes in structure and position of their carbon double bonds.<sup>18</sup> As a result, individual isomers react under a range of chemical pathways which produces SOA particles with drastically different molecular composition and physical properties.<sup>19</sup> Due to the prevalence of these terpene-derived SOA in the atmosphere, there have been numerous works investigating their fundamental properties such as their reactivity, chemical composition, and volatility of individual chemical constituents in the condensed particle phase.<sup>1,20,21</sup>

Plant health needs to be taken into consideration when deciding which VOCs to use to accurately mimic real biogenic SOA in the laboratory. Plants can become stressed due to biotic and abiotic stressors.<sup>22</sup> Some examples of abiotic stressors include changing environmental conditions such as increased temperature, drought, or low soil nutrient levels, whereas biotic stress in plants can be induced due to mechanical damage from defoliators or removal of sap from sap-sucking aphids, known as herbivory.<sup>22</sup> In addition, when plants become stressed it sets off their natural defense mechanism, which alters their VOC emission profiles in both quantity and types of compounds being emitted by the plant.<sup>23,19</sup> The emission of these VOCs allows plants to

communicate with each other and can provide stress relief.<sup>22</sup> In addition these VOCs can protect plants from further destruction by priming them for the next stress event they may experience which can lead to quicker recovery times.<sup>24,25</sup> When aphid-herbivory is induced in pine trees, typically monoterpene and sesquiterpene emissions increase.<sup>19</sup> Studying how the change in the emission profile of plants impacts SOA properties is important because plant stress is common in ecosystems, however, it is not considered in many laboratory studies. Moreover, the SOA formed from stressed plants could impact climate differently than SOA formed from healthy plants due to differences in composition and physical properties. Therefore, the chemical and physical properties of healthy and stressed plant SOA should be investigated to parse out if there is a significant difference between the two systems.

Using complex VOC systems can impact the oxidant reactivity and subsequent products formed when compared to single precursor systems.<sup>26</sup> The discrepancy between lab-generated SOA and real SOA in the atmosphere could lead to uncertainties in estimation of their impact in climate models, as well as their impact on human health. Studying SOA generated from a single VOC may not be an adequate representation of those found in the ambient environment. Therefore, it is critical to use chemically complex mixtures of VOCs to better represent the impact that ambient SOA has on health and climate.

There have been few studies of SOA generated from real tree emissions. Previous studies have used Scots Pine trees (*Pinus sylvestris*), an evergreen tree typically found in the boreal forest, to investigate SOA particle properties. For example, Ylisirniö et al. (2020) used an oxidation flow reactor to generate SOA from Scots pine tree emissions and investigated their mass yields, chemical composition, and volatility.<sup>27</sup> Faiola et al. (2018) investigated the volatility distributions and oxidation products of SOA produced from photooxidation of Scots pine tree volatiles before,

during, and after exposure to pine weevils.<sup>19</sup> Faiola et al. (2019) generated dark ozonolysis and photooxidation SOA in a batch chamber to investigate oxidation products and volatility distributions of SOA formed from healthy and aphid-stressed Scots pine emissions.<sup>23</sup> Each of these studies reported differences in the mixtures of the SOA produced from pine emissions versus single SOA precursor systems such as  $\alpha$ -pinene SOA. In addition, the SOA that had an increased fraction of sesquiterpenes produced different particle properties than those of the healthy counterpart systems.

### **1.3 Impact of chemical composition on physical properties of SOA**

Chemical composition of the resulting SOA species influences other physical properties such as phase separation, glass transition temperature, and viscosity.<sup>28,29</sup> The phase state of SOA can be characterized by a parameter called dynamic viscosity, referred to hereafter as simply viscosity, which is a measure of a fluid's resistance to flow in units of Pa s. SOA particles were commonly assumed to be liquid-like, permitting fast diffusion of molecules through the particle until the pioneering experiments by Virtanen et al. showed that SOA particles bounce from substrate as if they were solid.<sup>30</sup> Recent research has shown that some organic aerosols exist as highly viscous semi-solids or glassy solids under certain environmental conditions.<sup>31</sup> Studies of SOA material generated from the oxidation of single biogenic VOCs, including isoprene and various terpenes, have shown that SOA becomes highly viscous semi-solids or glassy solids under certain environmental conditions such as low temperature and low RH.<sup>16,28,32-43</sup> Moreover, the viscosity of the SOA is directly dependent on temperature and humidity.<sup>31,44,28</sup> Water acts as a plasticizer for SOA in which increasing relative humidity leads to a decrease in overall particle viscosity, due to the lower viscosity of water ( $10^{-3}$  Pa s) compared to most other organics.<sup>45</sup> Additionally, temperature has a similar effect on viscosity in which increasing temperature leads

to decreased resistance to flow and therefore lower viscosity.<sup>46</sup> Characterizing relative humidity and temperature effects on viscosity is also a key component to understanding how SOA change in response to different environments. It is important to parameterize viscosity as a function of easily measurable aerosol properties. For example, DeRieux et al. (2018) has provided parameterization for using chemical composition to predict viscosity.<sup>29</sup> Other techniques for determining viscosity include predicting the glass transition temperature and viscosity from volatility distributions of organic aerosols.<sup>47</sup>

Currently, viscosity and phase state are not directly included in climate models that are trying to investigate transport and dispersion of particulate matter in the atmosphere. However, changes in viscosity can dramatically impact physicochemical processes that determine atmospheric lifetimes and concentrations, such as particle growth, chemical reactivity, and ability to serve as a cloud or ice nuclei.<sup>31</sup> Furthermore, highly viscous materials will likely lead to slower diffusion rates and uptake coefficients within the SOA.<sup>31</sup> Few measurements have been made of these highly viscous SOA, and those that have been made were not systematic. As a result, we do not know the effect of environmental conditions on SOA formation, photochemical aging, or inorganic compounds, therefore it is difficult to generalize the effects of SOA viscosity for modeling applications.

In addition to phase state, SOA can take on many diverse types of morphologies including phase separation. Liquid-liquid phase separation (LLPS) is usually defined as a particle that has two distinct liquid phases, an inner aqueous-rich phase and an outer organic-rich phase. LLPS in SOA particles has been observed in particles containing organic and inorganic species.<sup>48,49</sup> This phase separation was thought to only occur in the presence of organic and inorganic species because the inorganic salts usually found in SOA are highly hygroscopic.<sup>48</sup> Contrary to this

notion, LLPS was later observed at high relative humidity ( $> 90\%$  RH) in purely organic,  $\alpha$ -pinene ozonolysis SOA particles.<sup>50</sup> Additionally, Song et al. (2018) reported that SOA produced from diesel fuel vapor, consisting of a wide range of VOCs, exhibited LLPS between 70-100 % RH.<sup>51</sup> It is predicted that as chemical complexity of SOA increases, such as SOA produced from a mixture of terpenes, LLPS could extend to lower relative humidities in purely organic systems.<sup>51</sup> The presence of LLPS in SOA particles can impact the extent to which gas-particle partitioning may occur,<sup>52-54</sup> the reactive uptake of gasses,<sup>55,56</sup> as well as their ability to act as ice nuclei,<sup>57</sup> making it an important property to study.

#### **1.4 Summary of Goals**

This dissertation focuses on the impact that chemical composition has on important physical properties of SOA particles, such as viscosity and liquid-liquid phase separation, for atmospherically relevant systems representing biogenic SOA formed from complex mixtures of VOCs. This work will delve into three case studies aimed at understanding the relationship between chemistry, viscosity, and phase separation of biogenic SOA.

The first goal of this thesis is to provide first data on viscosity for sesquiterpene SOA, for which the data were previously lacking. Chapter 2 will describe the chemical composition and relative humidity-dependent viscosity for SOA generated from the most abundant sesquiterpene in the atmosphere,  $\beta$ -caryophyllene. This study will help elucidate differences between the viscosity of monoterpene and sesquiterpene SOA and how chemical composition influences this property.

The second goal of this thesis is to identify physicochemical differences between complex mixtures of healthy and stressed plant SOA compared to SOA generated from a single precursor to see if a single component system, such as  $\alpha$ -pinene SOA, is a good proxy for biogenic SOA in

climate models and laboratory studies investigating their fundamental properties. Chapter 3 investigates SOA generated from synthetic mixtures of VOCs mimicking the emission profile of Scots pine (*Pinus sylvestris L.*) trees.<sup>23</sup> Pine trees (Pinaceae) have a wide spatial distribution<sup>58</sup> and are typically found in boreal forests which cover one-third of the global forest area<sup>59</sup> making them a good representative plant for studying SOA generated by emissions in boreal forests. This work will also help elucidate the impact herbivory-induced plant stress has on the chemical and physical properties of SOA.

The third goal of this thesis is to compare the viscosity of SOA generated from proxy mixtures of VOCs to those generated from *real* Canary Island pine trees, discussed in Chapter 4. This comparison provides insight into how laboratory experiments can best represent biogenic SOA with terpene mixtures and therefore laboratory experiments can more accurately represent more atmospherically representative SOA and investigate their fundamental properties. This research presents novel viscosity and composition measurements for SOA generated from complex mixtures of VOCs representing the emissions of healthy and aphid-stressed Canary Island pine trees.

## CHAPTER 2

### HUMIDITY-DEPENDENT VISCOSITY OF SECONDARY ORGANIC AEROSOL FROM OZONOLYSIS OF $\beta$ -CARYOPHYLLENE: MEASUREMENTS, PREDICTIONS, AND IMPLICATIONS

Reprinted (adapted) with permission from:

Maclean, A. M.; Smith, N. R.; Li, y.; Huang, Y.; Hettiyadura, A. P. S.; Crescenzo, G. V.; Shiraiwa, M.; Laskin, A.; Nizkorodov, S. A.; Bertram, A. K., Humidity-dependent viscosity of secondary organic aerosol from ozonolysis of  $\beta$ -caryophyllene: Measurements, predictions, and implications, *ACS Earth & Space Chemistry*, **5** (2021) 305-318. Copyright 2021. American Chemical Society.

#### **Abstract**

To predict important secondary organic aerosol (SOA) properties, information on viscosity or diffusion rates within SOA is needed. Ozonolysis of  $\beta$ -caryophyllene is an important SOA source; yet, very few viscosity or diffusion rate measurements have been performed for this SOA type, and none as a function of relative humidity (RH). In this study, we measured viscosity as a function of RH for SOA generated from the ozonolysis of  $\beta$ -caryophyllene using the poke-flow technique. At an RH of 0% and 48%, the viscosity was between  $6.9 \times 10^5$  -  $2.4 \times 10^7$  Pa s, and between  $1.3 \times 10^3$  -  $5.6 \times 10^4$  Pa s, respectively. Based on these viscosities and the fractional Stokes-Einstein equation, characteristic mixing timescales of organics within 200 nm  $\beta$ -caryophyllene SOA particles range from  $\sim 0.2$  h at 0% RH to  $< 3$  sec at 48% RH, suggesting that these particles should be well mixed under most conditions in the lower atmosphere. The chemical composition of the SOA was also determined using nano-desorption electrospray ionization mass spectrometry. The measured chemical composition and the method of DeRieux et al. (ACP, 2018) were used to predict the viscosity of  $\beta$ -caryophyllene SOA. If the mass spectra peak abundances were adjusted to account for the sensitivity of the electrospray ionization to larger molecular



weight components, the predicted viscosity overlapped with the measured viscosity at 0% RH, while the predicted viscosities at 15% to 48% RH were slightly higher than the measured viscosities. The measured viscosities also overlapped with viscosity predictions based on a simple mole-fraction based Arrhenius mixing rule.

## 2.1 Introduction

Secondary organic aerosol (SOA) is formed in the atmosphere when volatile organic compounds (VOCs) from biogenic and anthropogenic sources are oxidized followed by partitioning of the reaction products to the particle phase<sup>1</sup> or multiphase reactions of the oxidation products.<sup>60</sup> On a global scale, biogenic VOCs are the dominant contributors to SOA.<sup>1,61,62</sup> The three main classes of biogenic VOCs important for SOA formation are isoprene, monoterpenes, and sesquiterpenes.<sup>4</sup> A recent modeling study showed that the global burden of SOA increased by 48% relative to the base case when sesquiterpenes were included in the model.<sup>63</sup> Field measurements and modeling studies have also illustrated that sesquiterpenes can contribute significantly to atmospheric SOA.<sup>64–67</sup> Examples of atmospherically relevant sesquiterpenes include  $\beta$ -caryophyllene,  $\alpha$ -cedrene,  $\alpha$ -humulene, and longifolene.<sup>68,69</sup>

SOA is important because it can impact the Earth's climate directly, by scattering incoming solar radiation, and indirectly, by serving as nuclei for cloud droplets and ice crystals.<sup>70–73</sup> SOA can also impact air quality by reducing visibility and negatively impacting health.<sup>4,74,75</sup> To predict important properties of SOA in the atmosphere, information on the diffusion rates of organics within SOA is needed. For example, diffusion rates of organics within particles affect the mass and size distribution of SOA<sup>8,76–85</sup> and the long-range transport of pollutants such as polycyclic aromatic hydrocarbons in the atmosphere.<sup>8,9,84–86</sup> In addition, diffusion rates can affect rates and mechanisms of photochemical and multiphase reactions within SOA.<sup>37,76,87–95</sup> Diffusion

rates of organics within SOA or SOA proxies have been determined in some studies by tracking the diffusion of fluorescent probe molecules within SOA or their proxies<sup>96–100</sup> and by measuring the evaporation rates of organic molecules from SOA or SOA proxies.<sup>8,101–103</sup> In cases where diffusion rates of organics have not been measured, they can be estimated from viscosity measurements using the Stokes–Einstein equation<sup>97,102,104–106</sup> or the fractional Stokes–Einstein equation.<sup>97,98,102</sup> A challenging aspect of measuring diffusion rates and viscosity within SOA is the low amount of material available for experiments, which precludes the use of traditional methods.<sup>31</sup>

Recently, Shiraiwa et al.,<sup>107</sup> DeRieux et al.,<sup>29</sup> Gervasi et al.,<sup>108</sup> and Li et al.<sup>47</sup> developed methods for predicting the viscosities of SOA from its chemical composition, which can be used with chemical transport models to predict viscosity of atmospheric SOA.<sup>107,109</sup> These methods have been used to predict the viscosity and glass transition temperatures of several types of SOA (isoprene SOA,  $\alpha$ -pinene SOA, toluene SOA, and ambient SOA).<sup>29,43,83,108,110–115</sup> However, the accuracy of these methods for predicting the viscosity of SOA has only been tested in a few cases, and the accuracy of these methods has never been tested for sesquiterpene SOA.

The viscosity of SOA as a function of RH can also be predicted using mixing rules and measured viscosities of water and dry SOA.<sup>108,116–118</sup> Gervasi et al.<sup>108</sup> showed that a mole-fraction based mixing rule is the best choice among simple mixing rules for predicting viscosity in a binary aqueous system. However, the accuracy of mixing rules for predicting the viscosity of SOA as a function of RH has only been tested in a few cases.<sup>108,117,118</sup>

Only two studies have reported diffusion rates or viscosities within sesquiterpene SOA. Zhao et al.<sup>103</sup> measured a diffusion coefficient of  $3 \times 10^{-19} \text{ m}^2 \text{ s}^{-1}$  under dry conditions of 2-

ethylhexyl nitrate within SOA generated from  $\alpha$ -cedrene ozonolysis. Champion et al.<sup>34</sup> measured viscosities under dry conditions of SOA generated from  $\beta$ -caryophyllene photo-oxidation. What is currently missing are measurements of diffusion rates or viscosities within sesquiterpene SOA as a function of relative humidity (RH). Such RH-dependent measurements are critical since RH varies from 0 to over 100% in the atmosphere and viscosity and diffusion rates have a strong dependence on RH.<sup>28</sup>

To address the knowledge gaps mentioned above, we measured viscosity as a function of RH for SOA generated via ozonolysis of  $\beta$ -caryophyllene (see Appendix A for the chemical structure of  $\beta$ -caryophyllene). The measured viscosities and the fractional Stokes–Einstein relation were used to estimate characteristic mixing timescales of organic molecules within  $\beta$ -caryophyllene SOA for typical RH conditions found in the planetary boundary layer (the region of the atmosphere between the Earth’s surface and approximately 1 km in height). In addition to measuring viscosity, we also measured the chemical composition of the SOA using high-resolution mass spectrometry with three different types of direct-infusion ionization sources. The chemical composition and the measured RH-dependent viscosities for  $\beta$ -caryophyllene SOA were used to test the accuracy of the parameterization from DeRieux et al.<sup>29</sup> for predicting viscosities of  $\beta$ -caryophyllene SOA. Finally, we evaluated the ability of a simple mole-fraction based Arrhenius mixing rule to predict the viscosity of the  $\beta$ -caryophyllene SOA as a function of RH from knowledge of the viscosity of water and the dry SOA.

## **2.2 Experimental methods**

### **2.2.1 SOA Generation**

SOA was generated in an environmental chamber by our collaborators at the University of British Columbia via dark ozonolysis of  $\beta$ -caryophyllene. The chamber was based on the design by Parsons et al.<sup>119</sup> and consisted of a 1.8 m<sup>3</sup> Teflon bag (Ingeniven) housed in a reflective aluminum enclosure. The enclosure had 24 UV lights (40 W Sylvania black lights, peak UV wavelength of  $\sim$ 360 nm) mounted on the inside of the enclosure for photochemical studies; however, the lamps were not used in the current study except for cleaning the Teflon bag. The chamber bag was periodically cleaned by passing dry air, ozone (1.2 ppm), and water vapor through the chamber with the UV lights on. Particles were continuously generated and collected by running the environmental chamber in a continuous-flow mode, similar to other continuous-flow environmental chambers.<sup>120–123</sup> The flow rate into and out of the chamber was  $\sim$ 18.2 L min<sup>-1</sup>, resulting in a calculated residence time of 1.7 h, consistent with residence time measurements.

A zero-air generator (Aadco 737) provided dry and hydrocarbon-free air for SOA generation. The RH of the air from the generator was  $<1\%$  based on measurements with a humidity meter (Vaisala HMT 330). Ozone was generated externally to the chamber by flowing 0.5–1 L min<sup>-1</sup> of the dry air through an ozone generator (Jelight 600). A mixture of 2 wt %  $\beta$ -caryophyllene (Sigma-Aldrich,  $\geq 98\%$ ) was prepared in 2-butanol (Sigma-Aldrich,  $\geq 99\%$  purity) and the resulting solution was continuously added (flow rate of 25  $\mu$ L h<sup>-1</sup>) with a syringe pump (Cole-Parmer model 100) to a round-bottom flask heated to 110 °C. A flow of 17.2–17.7 L min<sup>-1</sup> of the dry air was passed through the heated flask and carried the  $\beta$ -caryophyllene and 2-butanol vapors into the chamber. The 2-butanol was added to the chamber as a scavenger of OH radicals, which can be produced during some reaction pathways for the ozonolysis of  $\beta$ -caryophyllene.<sup>124</sup> The 2-butanol was estimated to scavenge  $\sim 84\%$  of OH radicals produced in the chamber based on the reaction rates of OH with 2-butanol and  $\beta$ -caryophyllene.

Ozone and  $\beta$ -caryophyllene entered the chamber through two separate 0.63 cm (outer diameter) tubes that had exits  $\sim$ 0.2 cm apart within the chamber to facilitate mixing. The concentrations of ozone and  $\beta$ -caryophyllene flowing into the chamber were 400–1200 and 40 ppb, respectively. After SOA formation, aerosols exited the chamber through a 0.63 cm (outer diameter) tube  $\sim$ 1 m away from the chamber inlets. Part of the exit flow was sampled with an ozone detector (49i, Thermo Scientific, USA). The remaining flow passed through an ozone denuder (Ozone Solutions, ODS-1) and was sampled with either an impactor to collect material for the viscosity and mass spectrometry measurements or with a scanning mobility particle sizer (SMPS) (TSI 3080 DMA and 3782 CPC) to measure the number diameter distribution of the SOA. From the number-diameter distribution and an assumed SOA density of  $990 \text{ kg m}^{-3}$ ,<sup>124</sup> the mass concentration of the SOA in the chamber was  $50\text{--}60 \text{ }\mu\text{g m}^{-3}$ .

To collect SOA for viscosity or mass spectrometry measurements, the flow was sampled with a multiorifice single-stage impactor (MSP Corporation) operated at a constant flow rate of  $15 \text{ L min}^{-1}$  and a cut size below  $0.18 \text{ }\mu\text{m}$  (aerodynamic particle diameter). The sample collection time ranged from 16 to 24 h, resulting in  $0.7\text{--}1 \text{ mg}$  of SOA collected per sample, assuming 100% collection efficiency. For the viscosity measurements, SOA was collected on fluorinated glass coverslips coated with Trichloro (1H,1H,2H,2H-perfluorooctyl) silane or FluoroPel 800 (Cytonix USA). For mass spectrometry measurements, SOA was collected on PTFE filters (47 mm, Whatman).

### **2.2.2 Viscosity measurements**

The poke-flow technique developed by our collaborators at the University of British Columbia was used along with fluid simulations to determine the viscosity of the collected SOA

material at room temperature (292–294 K). This technique, which is based, in part, on early experiments by Murray et al.,<sup>125</sup> has been described and validated by Renbaum-Wolff et al.<sup>16</sup> and Grayson et al.<sup>32</sup> For these experiments, the slides containing the SOA from the environmental chamber were mounted in a flow cell coupled to an optical microscope (Appendix B). The RH within the flow cell was controlled with a humidified flow of ultrapure N<sub>2</sub> (0.25–0.80 L min<sup>-1</sup>). The RH was measured with a chilled mirror hygrometer (General Eastern model D-2), which was calibrated by measuring the deliquescence relative humidity of ammonium sulfate (80% RH based on Martin)<sup>126</sup> and potassium carbonate (43% RH based on Greenspan).<sup>127</sup>

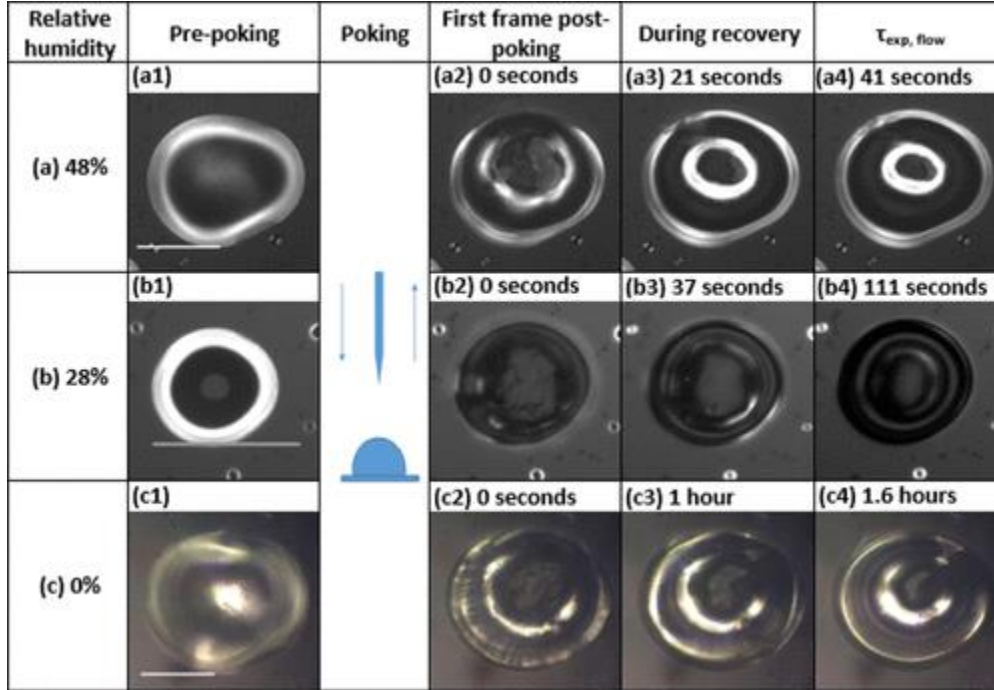
In the poke-flow experiments, the particles were poked with a needle (RS-6063, Roboz Surgical Store or 13561-20, Ted Pella Company) attached to a micromanipulator. The needle was coated with a hydrophobic film (Dursan coatings, SilcoTek USA or Oilslip 110, Cytonix) to prevent SOA material from sticking to the needle. The micromanipulator allowed the needle to be moved in the  $x$ ,  $y$ , and  $z$  direction. Prior to poking with the needle, the SOA particles had a spherical-cap geometry. After poking, the SOA material had a half-torus geometry and slowly flowed to reduce its total surface energy (e.g., Figure 2.1). From images recorded during the poke-flow experiments, we determined the experimental flow time,  $\tau_{\text{exp,flow}}$ , defined as the time taken for the equivalent area diameter of the hole in the half-torus geometry to decrease to 50% of its original diameter. The equivalent area diameter of the hole in the half-torus geometry was calculated using the following formula:<sup>128</sup>  $d = (4A/\pi)^{1/2}$ , where  $d$  is the equivalent area diameter of the hole with area  $A$ , determined from the images using Zen software (Zeiss) or ImageJ.<sup>129</sup>

Prior to poking the SOA particles, the particles were conditioned to the surrounding RH for 3–5, 5–25, 20, and 2–22 h for RH values of 48, 28, 15, and 0%, respectively (Table 2.1). These conditioning times were a factor of 0.18–22 greater than the estimated mixing times of water

within the SOA (Table 2.1). Viscosities were not dependent on the conditioning times used (Figure 2.2). Based on this information, we assume that the SOA was near equilibrium with the gas-phase water vapor prior to poking the particles for the viscosity measurements.

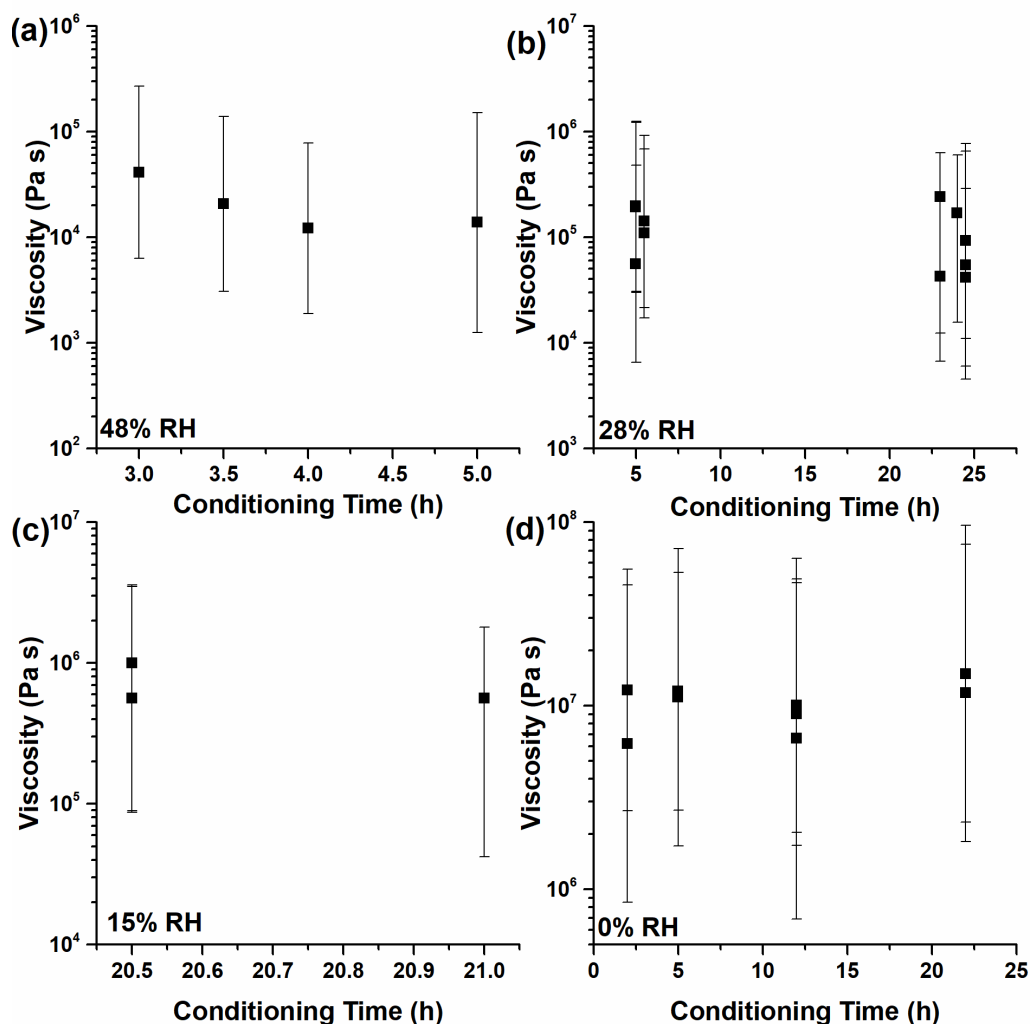
**Table 2.1** Calculated mixing times of water within the SOA particles ( $\tau_{\text{mix,H}_2\text{O}}$ ) and experimental conditioning time for water vapor ( $t_{\text{exp,H}_2\text{O}}$ ), which corresponds to the time the SOA particles were exposed to a given relative humidity before the poke-flow experiments. Viscosities are based on the upper limits of viscosity shown in Figure 2.4 below. Diffusion coefficients were calculated using the relation between viscosity and diffusion coefficients in sucrose-water from Price et al., 2016.<sup>102</sup> The variable  $d_p$  corresponds to the diameter of the SOA used in the poke-flow experiments.

RH	Upper limit of viscosity (Pa s)	Diffusion coefficient of water ( $\text{m}^2 \text{s}^{-1}$ )	$d_p$ ( $\mu\text{m}$ )	$\tau_{\text{mix,H}_2\text{O}}$ (hrs)	$t_{\text{exp,H}_2\text{O}}$ (hrs)	$t_{\text{exp,H}_2\text{O}}/\tau_{\text{mix,H}_2\text{O}}$
48	$5.63 \times 10^4$	$3.92 \times 10^{-14}$	61-91	0.7-1.5	3-5	2.3-6.5
28	$4.98 \times 10^5$	$1.13 \times 10^{-14}$	42-69	1.1-3.0	5-24.5	2.1-22
15	$9.13 \times 10^5$	$8.00 \times 10^{-15}$	45-78	1.8-5.4	20	3.9-11.6
0	$2.42 \times 10^7$	$1.24 \times 10^{-15}$	30-60	5.3-20.7	2-22	0.18-2.3



**Figure 2.1** Optical images of particles taken during poke-flow experiments at RH values of (a) 48, (b) 28, and (c) 0%. Images [a(1),b(1),c(1)] correspond to images taken before the particle was poked. Images [a(2),b(2),c(2)] are images taken immediately after poking. Images [a(3),b(3),c(3)] are taken during recovery and images [a(4),b(4),c(4)] are taken at  $\tau_{exp, flow}$  where the equivalent area diameter of the hole has decreased to 50% of its original size. The white scale bar in the prepoking images corresponds to 50  $\mu\text{m}$ . The circle in the center of the particle in [b(1)] is an optical effect due to the hemispherical shape.

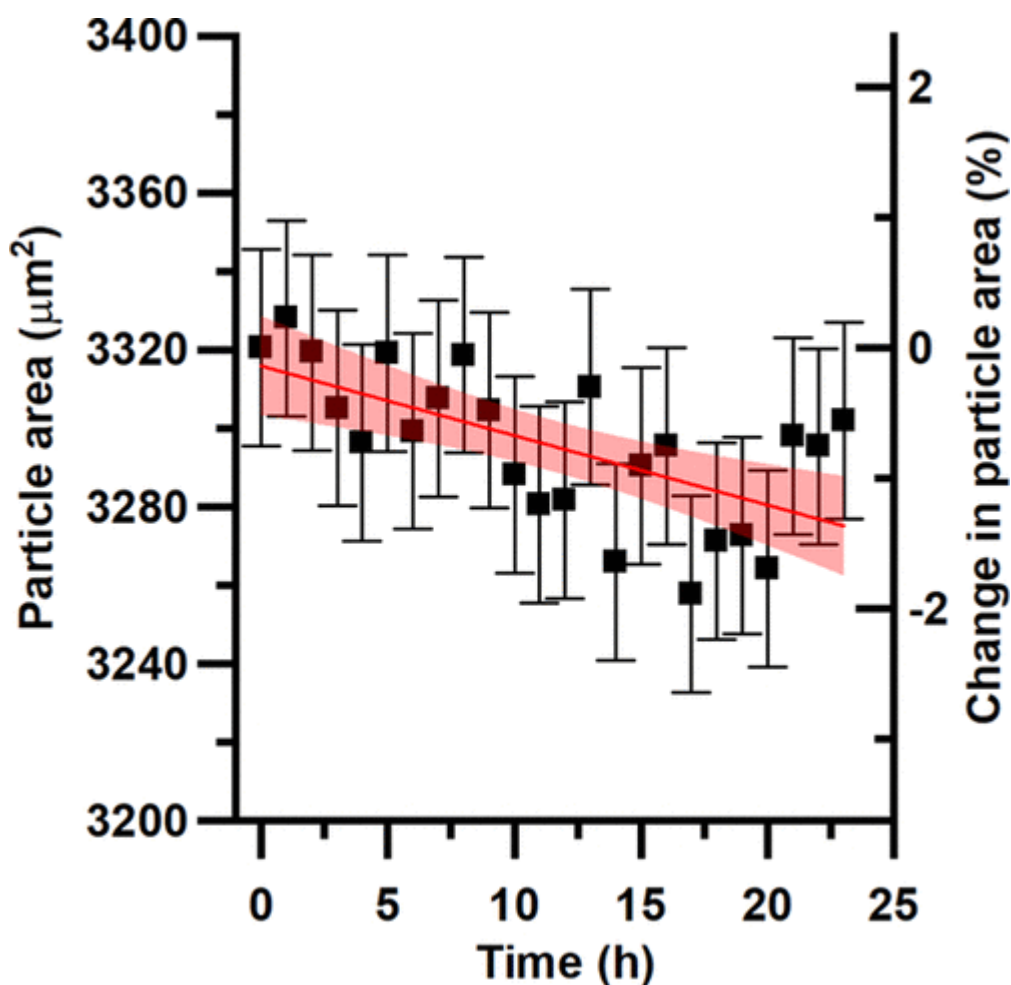




**Figure 2.2** Viscosities as a function of particle conditioning time to the surrounding RH. Measurements were taken at RHs of (a) 48, (b) 28%, (c) 15%, and (d) 0%.

When the particles were conditioning to the surrounding RH, semivolatile organic material could evaporate from the particles, potentially leading to a change in the viscosity of the particles.<sup>82,130,131</sup> To determine if evaporation of semivolatile organic material was important in the poke-flow experiments, a newly collected SOA sample was added to the flow cell discussed above and exposed to a dry flow of  $N_2$  gas ( $0.25 \text{ L min}^{-1}$ ) for 24 h, and images were recorded every hour to quantify evaporation of the SOA particles. In this experiment, the maximum change

in the 2-D projected area of the SOA particles was  $-1.4 \pm 0.4\%$  (Figure 2.3). We conclude that the composition change due to evaporation during the poke-flow experiments was minimal. This is consistent with expectations since the volume of  $N_2$  gas exposed to the particles in the poke-flow experiments ( $\leq 1.2 \times 10^3$  L) was small compared to the volume of air sampled from the environmental chamber when collecting SOA for the poke-flow experiments ( $1.6 \times 10^4$  to  $2.4 \times 10^4$  L).



**Figure 2.3** Particle 2-D projected area as a function of time during exposure to dry nitrogen flow with a secondary y-axis showing the percent change in the projected particle area. The y-error bars correspond to the uncertainty in the measurement of the particle area in  $\mu\text{m}^2$ . The straight line is a linear fit to the data and the shaded regions are the 95% confidence intervals for that fit.

The  $\tau_{\text{exp,flow}}$  values determined in the poke-flow experiments were converted to viscosities using fluid simulations of the SOA material. The fluid simulations were carried out with the Microfluidics Module (version 5.2a) within COMSOL. Details are described in Grayson et al.<sup>17</sup> In short, the flow of the SOA material was simulated using a laminar two-phase flow with a moving mesh consisting of  $\sim 5800$  elements. The simulations took into account the Navier–Stokes equation and the surface tension of the SOA. Flow occurred in the simulations to minimize the total surface energy of the system, similar to the experiments. The initial geometry in the simulations was a half-torus geometry, consistent with the experiments. In the simulations, conservative values for contact angle, surface tension of the SOA, slip length (a measure of the resistance to flow at the fluid–solid interface), and density of the SOA were used (Table 2.2). From each simulation, a modeled flow time,  $\tau_{\text{model,flow}}$ , was determined, which is the time taken for the diameter of the hole in the half-torus geometry to decrease to 50% of its original value (consistent with the definition of  $\tau_{\text{exp,flow}}$ ). To determine viscosities from  $\tau_{\text{exp,flow}}$ , the viscosity used in the simulation was varied until  $\tau_{\text{model,flow}}$  was within  $\sim 1\%$  of  $\tau_{\text{exp,flow}}$ .

**Table 2.2** COMSOL parameters used when simulating the viscosity of  $\beta$ -caryophyllene SOA from poke-flow measurements.

	Surface tension (mN m <sup>-1</sup> )	Slip length (m)	Density (kg m <sup>-3</sup> )	Contact angle (°)
Range of values	29.7 <sup>a</sup> -72.75 <sup>b</sup>	5x10 <sup>-9</sup> -1x10 <sup>-6</sup> <sup>c</sup>	990 <sup>d</sup>	30-100 <sup>e</sup>
Values for lower limit	29.7	5x10 <sup>-9</sup>	990	30-100
Values for upper limit	45	1x10 <sup>-6</sup>	990	30-100

<sup>a</sup>Lower limit of surface tension is the surface tension of liquid  $\beta$ -caryophyllene based on the model ACD/Labs Percepta Platform-PhysChem Module. Retrieved from Chemspider on May 15, 2019. <sup>b</sup>The upper limit is consistent with surface tension measurements of SOA at RH  $\leq$ 65% RH and surface tensions reported for alcohols, organic acids, esters, and ketones, as well as surface tension measurements of water solutions containing SOA products.<sup>132-135</sup> <sup>c</sup>Range is based on measurements of the slip length of organic compounds and water on hydrophobic surfaces.<sup>136-148</sup> <sup>d</sup>Densities is based on measurements from Tasoglou and Pandis.<sup>149</sup> <sup>e</sup>Contact angle range is based on ranges measured in other chamber generated SOA.<sup>32,106,150</sup> Note: the simulated viscosities depend only weakly on the contact angle. Changing the contact angle by  $\pm$ 10% changes the simulated viscosity on average by  $\pm$ 15%, which is small compared to the overall uncertainties associated with the simulated viscosities.

### 2.2.3 High-resolution mass spectrometry

High-resolution mass spectrometry data of the collected samples were obtained in the positive and negative ion mode separately using nano-desorption electrospray ionization (nano-DESI),<sup>151</sup> nano-electrospray ionization (nano-ESI), and electrospray ionization (ESI) sources attached to a Q-Exactive HF-X Orbitrap mass spectrometer (Thermo Scientific) with a mass resolution of  $\sim 1.7 \times 10^5$  at  $m/z$  400. Data were acquired from 80 to 1200  $m/z$  in the full scan mode. A low mass calibration was performed prior to analysis using commercial mass calibration solutions (Thermo scientific, PI-88323 and PI-88324) in both positive (+) and negative (-) ion modes, separately. A spray voltage of (+ or -) 3.5 kV, a funnel RF level of 80, and a capillary temperature of 250 °C were used in all ionization modes. Samples were delivered using a syringe pump at 1  $\mu\text{L min}^{-1}$  (nano-DESI), 2  $\mu\text{L min}^{-1}$  (nano-ESI), and 5  $\mu\text{L min}^{-1}$  (ESI). Nitrogen gas (99.995% purity) flow rates used in the ESI source include a sheath gas of 10–12 units and an

auxiliary gas of 0–1 units. For nano-DESI, half of the PTFE filter ( $1/2 \times 47$  mm, Whatman) of each sample was taped to a glass slide. A stable solvent droplet (1:1; acetonitrile/water) was formed at a juncture between the solvent capillary and spraying capillary. The substrate containing the SOA sample was brought in contact with the droplet using micromanipulators, and the droplet was dragged over the sample while acquiring mass spectra for approximately 2–3 min. In addition to the samples, a solvent blank consisting of a clean substrate was analyzed following the same procedure in both positive and negative modes.

For nano-ESI and regular ESI, the remaining filter halves were solvent-extracted with 2 mL of a 1:1 mixture of acetonitrile and water under sonication for 15 min. The extracted solution was then passed through a 0.45  $\mu\text{m}$ , PTFE membrane syringe filter (Fisherbrand) to remove any undissolved material. An additional 1 mL of solvent was passed through the PTFE membrane filter and collected with the filtered extracts to limit the loss of extracts on the filter surface. Data were acquired for approximately 2 min for nano-ESI and ESI. A solvent blank (a clean filter treated the same way as described above) was also analyzed for nano-ESI and ESI in the positive and negative mode.

The analysis procedure of the mass spectrometry data has been described previously.<sup>152</sup> Xcalibur was used to integrate portions of the scan and save the mass spectra as raw files. Then, the Decon2LS software program (<https://omics.pnl.gov/software/decontools-decon2ls>) was used to extract peak positions and intensities. Only peaks below  $m/z$  700 were considered in analysis because peaks at larger  $m/z$  values had negligibly small abundances. Peaks that were present in the solvent blank with a solvent/sample peak abundance ratio in an excess of 0.1 were considered impurities and excluded from further analysis. All positive ions were assigned to formulas  $\text{C}_{1-40}\text{H}_{2-80}\text{O}_{0-35}\text{N}_{0-3}\text{Na}_{0-1}^+$  with a  $m/z$  accuracy of 0.001. Protonation was the

most common ionization mechanism in the positive ion mode, although a small fraction of the ions were monosodium adducts. Sodium adducts can form during direct infusion electrospray ionization in the positive mode.<sup>153,154</sup> All negative ions were assigned to formulas  $C_{1-40}H_{2-80}O_{0-35}N_{0-3}^-$  assuming that deprotonation was the only ionization mechanism. Only closed-shell ions were permitted, and the elemental ratios were constrained to be  $0.30 < H/C < 2.25$  and  $0.00 < O/C < 2.30$  to ensure that elemental formula assignments were physically reasonable. Peaks that could not be assigned with the abovementioned constraints were assigned manually using the MIDAS molecular calculator (<https://nationalmaglab.org/user-facilities/icr/icr-software>). The  $^{13}C$  isotope and other obvious impurities, signified by unreasonably high mass defects, were examined and removed from the final dataset. The N-containing species made up a small portion (<1%) of the total signal and were therefore treated as impurities and excluded. The formulas of the assigned ions were converted to the neutral formulas by removing  $Na^+$ ,  $H^+$ , or  $NH_4^+$ , depending on the ionization mechanism in the positive mode and adding a H in the case of the negative mode. The assignments are reported in neutral mass of each species. The datasets for the positive and negative modes were aligned based on neutral mass and each mode was normalized so the sum of the intensities over all masses in a single mode would add up to one. Then the intensities were averaged between the modes for each mass for the combined dataset. All the peaks in the combined dataset were used to predict the viscosity.

#### **2.2.4 Predictions of the Viscosity of SOA from measurements of the chemical composition of the SOA**

To predict viscosity of the SOA from the mass spectra, we followed the approach of DeRieux et al.<sup>29</sup> First, the glass transition temperature ( $T_g$ ) of compound  $i$  was predicted from the mass spectra using the following equation:<sup>29</sup>

$$T_{g,i} = (n_C^0 + \ln(n_C))b_C + \ln(n_H) b_H + \ln(n_C) \ln(n_H) b_{CH} + \ln(n_O) b_O + \ln(n_C) \ln(n_O) b_{CO} \quad (2.1)$$

where  $n_C$ ,  $n_H$ , and  $n_O$  are the number of carbon, hydrogen, and oxygen atoms, respectively, of compound  $i$ . Values of the coefficients [ $n_C^0$ ,  $b_C$ ,  $b_H$ ,  $b_{CH}$ ,  $b_O$ , and  $b_{CO}$ ] were [1.96, 61.99, -113.33, 28.74, 0, and 0] for CH compounds and [12.13, 10.95, -41.82, 21.61, 118.96, and -24.38] for CHO compounds.

Next, the  $T_g$  of the SOA under dry conditions ( $T_{g,org}$ ) was estimated using the Gordon–Taylor equation assuming a Gordon–Taylor constant ( $k_{GT}$ ) of 1:<sup>28</sup>

$$T_{g,org} = \sum_i w_i T_{g,i} \quad (2.2)$$

where  $w_i$  is the mass fraction of compound  $i$ . Following DeRieux et al.,<sup>29</sup> we assumed that  $w_i$  values were proportional to the relative abundances in the combined mass spectra dataset,  $I_i$  (Equation 2.3), which is a known limitation of this approach:<sup>29,51</sup>

$$w_i = I_i \quad (2.3)$$

$T_g$  of organic–water mixtures ( $T_{g,mix}$ ) was then calculated using the Gordon–Taylor equation with a  $k_{GT}$  of 2.5:<sup>28,155</sup>

$$T_{g,mix} = \frac{(1-w_{org})T_{g,H_2O} + \frac{1}{k_{GT}}w_{org}T_{g,org}}{(1-w_{org}) + \frac{1}{k_{GT}}w_{org}} \quad (2.4)$$

where  $w_{org}$  is the mass fraction of the SOA and  $T_{g,H_2O}$  is the glass transition temperature of water (136 K).<sup>156</sup> The value of  $w_{org}$  can be calculated based on the mass concentration of water ( $m_{H_2O}$ ) and the organics ( $m_{org}$ ):

$$w_{org} = \frac{m_{org}}{m_{org} + m_{H_2O}} \quad (2.5)$$

Under humid conditions,  $m_{H_2O}$  was estimated using the effective hygroscopicity parameter ( $\kappa$ ) and Equation 2.6:<sup>157</sup>

$$m_{H_2O} = \frac{k\rho_w m_{SOA}}{\rho_{SOA} \left( \frac{1}{a_w} - 1 \right)} \quad (2.6)$$

where  $\rho_w$  and  $\rho_{org}$  are the densities of water and the SOA and  $a_w$  is the water activity, which corresponds to RH/100. The density of the SOA particles was assumed to be  $990 \text{ kg m}^{-3}$ <sup>149</sup> and the hygroscopicity parameter was assumed to be 0.04–0.001.<sup>158,159</sup>

Viscosity as a function of temperature ( $T$ ) was then calculated from  $T_{g,mix}$  using the Vogel–Tammann–Fulcher (VTF) equation:<sup>29</sup>

$$\eta = \eta_{\infty} e^{\frac{T_0 D_f}{T - T_0}} \quad (2.7)$$

where  $D_f$  represents the fragility parameter and  $\eta_{\infty}$  represents the viscosity at infinite temperature assumed to be  $10^{-5} \text{ Pa s}$ .<sup>160,161</sup>  $T_0$  is the Vogel temperature calculated as

$T_0 = \frac{39.17 T_{g,mix}}{D_f + 39.17}$ , which is deduced from an assumed viscosity of  $10^{12} \text{ Pa s}$  at the glass transition temperature.<sup>161</sup>  $D_f$ , which characterizes the deviation of the temperature dependence of viscosity from an Arrhenius behavior,<sup>160,162</sup> was assumed to be 10 based on our previous study.<sup>29</sup> The value of  $D_f$  is assumed to be independent of RH.<sup>29,107,163,164</sup> This assumption is consistent with previous studies that found that the value of  $D_f$  in sucrose and citric acid is independent of water content, except for anhydrous sucrose.<sup>161,165,166</sup>

## 2.2.5 Prediction of viscosity using a mole-fraction based Arrhenius mixing rule



The viscosities of SOA as a function of RH can also be estimated using the measured viscosities of pure water and dry SOA and mixing rules. In the following, we test a mole-fraction based Arrhenius mixing rule for predicting the viscosity of  $\beta$ -caryophyllene SOA as a function of RH. This mixing rule is expressed for our system using the following equation:<sup>167</sup>

$$\ln(\eta_{\text{org,wet}}) = x_{\text{org}} \ln(\eta_{\text{org,dry}}) + x_{\text{H}_2\text{O}} \ln(\eta_{\text{H}_2\text{O}}) \quad (2.8)$$

where  $\eta_{\text{org,wet}}$  is the viscosity of the SOA and water mixture,  $\eta_{\text{org,dry}}$  is the viscosity of the dry SOA,  $\eta_{\text{H}_2\text{O}}$  is the viscosity of pure water,  $x_{\text{org}}$  is the mole fraction of SOA in the SOA–water mixture, and  $x_{\text{H}_2\text{O}}$  is the mole fraction of water in the SOA–water mixture. For the viscosity of the dry SOA, we used  $4.6 \times 10^6$  Pa s (which is based on our experimental data), and for the viscosity of pure water, we used  $10^{-3}$  Pa s.<sup>168</sup> The mole fractions of SOA and water were calculated from the weight fractions of SOA and water using Equation 2.9:

$$x_{\text{SOA}} = \frac{\frac{w_{\text{org}}}{M_{\text{org}}}}{\frac{w_{\text{org}}}{M_{\text{org}}} + \frac{w_{\text{H}_2\text{O}}}{M_{\text{H}_2\text{O}}}} \quad (2.9)$$

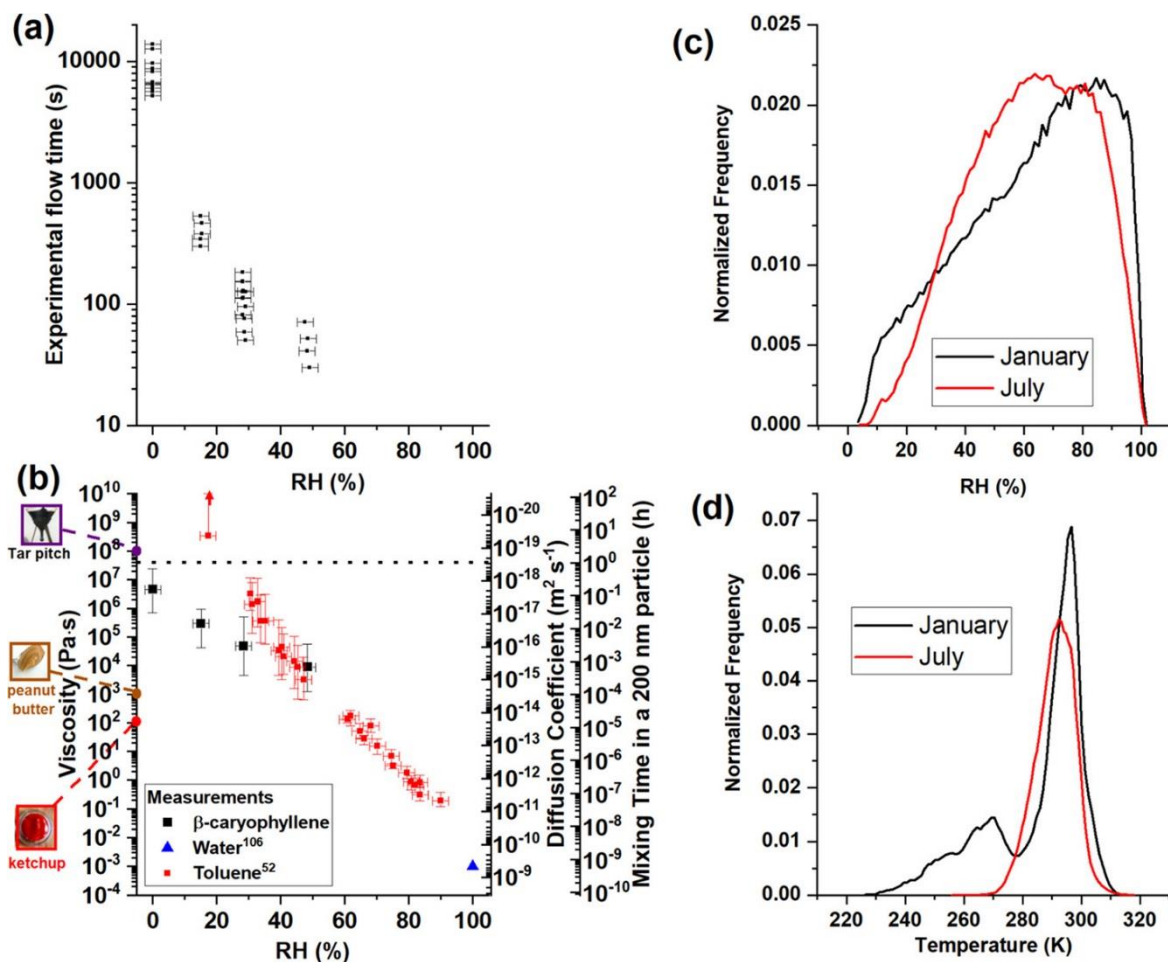
where  $w_{\text{org}}$  and  $w_{\text{H}_2\text{O}}$  are the weight fractions of the SOA and water, respectively, and  $M_{\text{org}}$  and  $M_{\text{H}_2\text{O}}$  are the molecular weights of the SOA and water, respectively. For the average molecular weight of the SOA, we used  $271.0$  g mol<sup>-1</sup> based on the mass spectra and Equation 2.14 (see below). The weight fraction of the SOA and water was estimated from the water activity using Equation 2.5 and 2.6, an SOA density of  $990$  kg m<sup>-3</sup>,<sup>149</sup> and CCN-derived kappa values of  $0.04$ – $0.001$  for SOA generated from the ozonolysis of  $\beta$ -caryophyllene in the presence of an OH scavenger.<sup>158,159</sup>

### 2.3 Results and Discussion

### 2.3.1 Viscosity as a function of RH

Values of  $\tau_{\text{exp,flow}}$  as a function of RH were determined from each of the poke-flow measurements (Figure 2.4a). The  $\tau_{\text{exp,flow}}$  values increased from  $\sim 48$  s at 48% RH to  $\sim 2.5$  h at 0% RH. Using the  $\tau_{\text{exp,flow}}$  values and the particle dimensions, upper and lower limits for the viscosities were determined from fluid-flow simulations (Figure 2.4b). At an RH of 0%, the viscosity was between  $6.9 \times 10^5$  and  $2.4 \times 10^7$  Pa s and at an RH of 48%, the viscosity was between  $1.3 \times 10^3$  and  $5.6 \times 10^4$  Pa s. Some other types of SOA previously investigated with the poke-flow technique were more sensitive to RH over the same RH range. For example, the viscosity of SOA generated by the photo-oxidation of toluene is  $>10^8$  Pa s at 17% RH but  $\sim 10^3$  to  $10^4$  Pa s at  $\sim 50\%$  RH (Figure 2.4b).<sup>106</sup> The weaker dependence on RH in the current experiments compared to toluene SOA is most likely because  $\beta$ -caryophyllene SOA has a lower hygroscopicity ( $\kappa = 0.04\text{--}0.001$ )<sup>158,159</sup> than toluene SOA ( $\kappa = 0.1\text{--}0.25$ ).<sup>169</sup> Water acts as a plasticizer for SOA (i.e., as water content increases, viscosity decreases)<sup>28</sup> and the smaller hygroscopicity of  $\beta$ -caryophyllene SOA likely translates into a weaker dependence of viscosity on RH over the range of RH values investigated.

A few previous studies investigated particle rebound as a function of RH for SOA from sesquiterpenes.<sup>37,40</sup> The rebound studies were used to infer whether the SOA was in a liquid (viscosity  $\lesssim 10^2$  Pa s) or a nonliquid state (viscosity  $\gtrsim 10^2$  Pa s). Li et al.<sup>37</sup> inferred that the nonliquid-to-liquid transition occurred at an RH  $> 90\%$  for SOA generated by the photo-oxidation of  $\beta$ -caryophyllene. Pajunoja et al.<sup>40</sup> inferred that the transition occurred at an RH of 70–90% for SOA from longifolene photo-oxidation, with an O/C-dependent transition RH. These studies are consistent with the current results.



**Figure 2.4** Panel (a) shows the experimental flow time,  $\tau_{\text{exp,flow}}$ , for poked particles as a function of RH. Panel (b) shows measured viscosities and calculated diffusion coefficients and mixing times of organic molecules in a 200 nm particle. The  $x$ -error bars correspond to uncertainties in the RH measurements and in panel (b), the  $y$ -error bars represent the upper and lower limits of the measured viscosities at each RH. The dotted line corresponds to a mixing time of 1 h. Also included in panel (b) are literature viscosity values for toluene SOA.<sup>106</sup> Pictures of common substances have been added to panel (b) as points of reference per Koop et al. (2011).<sup>28</sup> The tar pitch image is from the tar pitch experiment (image courtesy of Wikimedia Commons, GNU Free Documentation License, University of Queensland, John Mainstone). Panels (c,d) show the RH and temperature frequency distributions in January (black line) and July (red line) in the global planetary boundary layer (i.e., the planetary boundary layer in both the northern and southern hemisphere) based on GEOS-Chem. RH and temperature conditions were only included if the monthly averaged concentration of organic aerosol were greater than  $0.5 \mu\text{g m}^{-3}$  at the surface based on the output of GEOS-Chem.<sup>100</sup> Conditions where the organic aerosol concentrations were  $<0.5 \mu\text{g m}^{-3}$  were excluded, as aerosols at low concentrations are expected to be of less importance to climate or visibility.

### 2.3.2 Diffusion coefficients and mixing times of organic molecules within $\beta$ -caryophyllene SOA as a function of RH

Diffusion coefficients of organic molecules within SOA can be calculated from viscosity measurements using the Stokes–Einstein equation<sup>97,102</sup> or the fractional Stokes–Einstein equation.<sup>97,98,102</sup> A recent study showed that diffusion coefficients predicted with the Stokes–Einstein equation were in reasonable agreement with measured diffusion coefficients in most cases when the radius of the diffusing molecules ( $R_{\text{diff}}$ ) was greater than or equal to the radius of the matrix molecules ( $R_{\text{matrix}}$ ) and when the viscosities were between  $10^{-3}$  and  $10^6$  Pa s.<sup>44</sup> A more recent study showed that the fractional Stokes–Einstein equation was able to predict 98% of observed diffusion coefficients roughly within the uncertainty of the measurement for  $R_{\text{diff}}/R_{\text{matrix}}$  values ranging from 0.31 to 1.75 and viscosities ranging from  $10^{-3}$  to  $10^{10}$  Pa s. Based on these findings, we used the fractional Stokes–Einstein equation to predict diffusions of organic molecules within the SOA:<sup>170</sup>

$$D = D_o \times \left(\frac{\eta_0}{\eta}\right)^\xi \quad (2.10)$$

where  $\xi$  is the fractional exponent,  $\eta$  is the viscosity,  $\eta_0$  is the viscosity of pure water ( $10^{-3}$  Pa s at a temperature of 293 K), and  $D_o$  is the diffusion coefficient in pure water, calculated using the Stokes–Einstein equation:

$$D_o = \frac{k_B T}{6\pi\eta_0 R_{\text{diff}}} \quad (2.11)$$

where  $k_B$  is the Boltzmann constant,  $T$  is the temperature, and  $R_{\text{diff}}$  is the radius of the diffusing molecule. We assumed a radius of 0.47 nm for the diffusing molecule, based on a molecular weight of 254 g mol<sup>-1</sup> for some common first-generation  $\beta$ -caryophyllene ozonolysis

products,<sup>171</sup> a density of 990 kg m<sup>-3</sup>,<sup>149</sup> and an assumed spherical geometry of the diffusing molecule. The value of  $\xi$  was calculated using Equation 2.12:<sup>98</sup>

$$\xi = 1 - \left[ A \exp \left( -B \frac{R_{diff}}{R_{matrix}} \right) \right] \quad (2.12)$$

where  $A$  corresponds to 0.73 and  $B$  corresponds to 1.79.<sup>98</sup> A value of 1 was assumed for  $R_{diff}/R_{matrix}$ . Based on the fractional Stokes–Einstein equation, the diffusion coefficients ranged from  $\sim 4.1 \times 10^{-16} \text{ m}^2 \text{ s}^{-1}$  at 48% RH to  $\sim 1.8 \times 10^{-18} \text{ m}^2 \text{ s}^{-1}$  at 0% RH (Figure 2.4b, secondary  $Y$ -axis). The diffusion coefficients calculated using the fractional Stokes–Einstein equation correspond to bulk diffusion coefficients. These diffusion coefficients should be applicable to atmospheric particles that have diameters greater than  $\sim 0.1 \text{ }\mu\text{m}$ ,<sup>76,172</sup> which covers the majority of the mass of atmospheric particles. However, the diffusion coefficients may not apply to particles with diameters  $< 0.1 \text{ }\mu\text{m}$  as surface and confinement effects may become important for these particle diameters.<sup>172–174</sup>

Diffusion coefficients were converted into characteristic mixing timescales of organic molecules within 200 nm SOA particles using Equation 2.13:<sup>70</sup>

$$\tau_{mixing} = \frac{d_p^2}{4\pi^2 D} \quad (2.13)$$

where  $\tau_{mix}$  is the mixing time of the particle,  $d_p$  is the diameter the SOA particle used in the poke-flow experiments, and  $D$  is the diffusion coefficient of the diffusing molecule, calculated using Equation 2.10. The mixing time corresponds to the time it takes for the concentration of the diffusing molecules at the center of the SOA particle to differ from the equilibrium concentration by less than  $1/e$  for nonreactive partitioning. The SOA particle was assumed to have a diameter of 200 nm, which is within the range of SOA particle sizes found in the atmosphere.<sup>175–177</sup> The

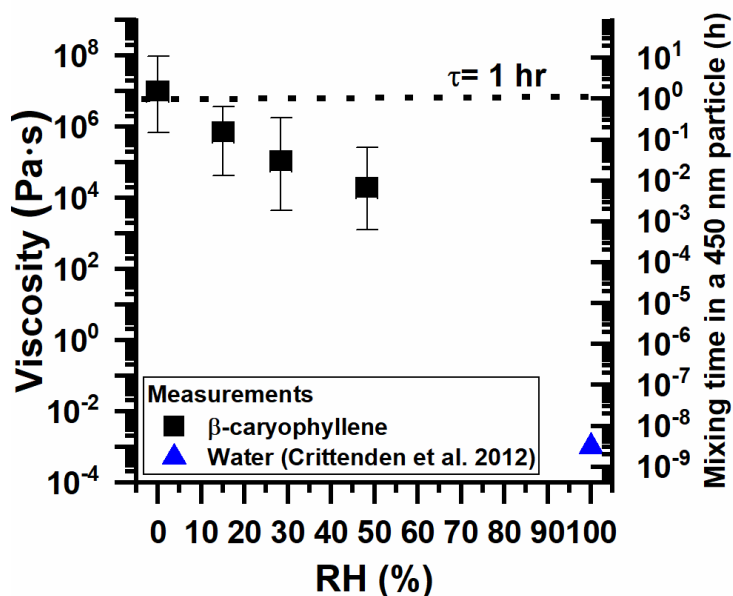
calculated mixing times ranged from  $\sim 0.2$  h at 0% RH to  $< 3$  s at 48% RH (Figure 2.4b, secondary Y-axis).

Mixing times of water within the SOA ( $\tau_{\text{mix,H}_2\text{O}}$ ) were also calculated using Equation 2.13, in which  $D$  refers to the diffusion coefficient of water ( $D_{\text{H}_2\text{O}}$ ) within the SOA. The  $\tau_{\text{mix,H}_2\text{O}}$  corresponds to the time it takes for the concentration of the water molecules at the center of the particle exposed to a change in RH to differ from the equilibrium concentration by less than  $1/e$ . To calculate  $\tau_{\text{mix,H}_2\text{O}}$  at each RH, we assumed that  $D_{\text{H}_2\text{O}}$  in the SOA was the same as  $D_{\text{H}_2\text{O}}$  in sucrose-water particles with an equivalent viscosity. For the viscosity of the SOA, we used the upper limit of the viscosity values shown in Figure 2.4b and listed in Table 2.1.  $D_{\text{H}_2\text{O}}$  was then calculated for the upper limits of the viscosity using the relationship between  $D_{\text{H}_2\text{O}}$  and viscosity for sucrose-water particles developed by Price et al.<sup>102</sup> (Fig. 7 in Price et al.); values for  $\tau_{\text{mix,H}_2\text{O}}$  determined using this approach are listed in Table 2.1.

Chemical transport models typically assume that the mixing times within SOA are less than  $\sim 1$  h.<sup>1</sup> Based on our results, the mixing time within a 200 nm  $\beta$ -caryophyllene SOA is  $< 1$  h at all RHs when the temperature is 292–294 K (Figure 2.4b). Based on previous calculations, the RH in the planetary boundary layer is nearly always  $\geq 10\%$  RH when the organic aerosol concentrations are  $> 0.5 \mu\text{g m}^{-3}$  at the surface (Figure 2.4c).<sup>178</sup> Furthermore, the temperature in the planetary boundary layer is most often 280–290 K when the organic aerosol concentrations are  $> 0.5 \mu\text{g m}^{-3}$  at the surface (Figure 2.4d).<sup>178</sup> Hence, the mixing times within  $\beta$ -caryophyllene SOA are  $< 1$  h for a large majority of RH and temperature conditions in the planetary boundary layer when the organic aerosol concentrations are  $> 0.5 \mu\text{g m}^{-3}$  at the surface. Conditions where the organic aerosol concentrations were  $< 0.5 \mu\text{g m}^{-3}$  were excluded, as aerosols at low concentrations are expected to be of less importance to climate or visibility.

One caveat to the discussion above is that the mass concentration of the SOA generated in the environmental chamber was 50–60  $\mu\text{g m}^{-3}$ , which is higher than typical mass concentrations of biogenic SOA in the atmosphere.<sup>61,179</sup> Previous studies have shown that for some types of SOA, the viscosity, and hence mixing times, increases with a decrease in mass concentration of SOA in the reactor.<sup>32,34,180</sup> Reducing the SOA mass concentration removes compounds with higher vapor pressures from the particles.<sup>181</sup> These higher vapor pressure compounds have lower glass transition temperatures.<sup>29,107</sup> Additional studies are needed to determine the effect of SOA mass concentration on the viscosity of  $\beta$ -caryophyllene SOA.

Related to the mixing times shown in Figure 2.4b, Ye et al.<sup>182</sup> investigated the mixing of semivolatile vapors from  $\alpha$ -pinene SOA and toluene SOA within  $\beta$ -caryophyllene SOA (formed by ozonolysis, as in the current experiments). In these experiments,  $\beta$ -caryophyllene SOA took up only a small amount of semivolatile vapors ( $\leq 10\%$  change in  $\beta$ -caryophyllene SOA mass) over a period of 2 h at 50% RH. The authors suggested two possible explanations for the limited uptake of the semivolatile vapors: (1) diffusion-limited uptake and (2) immiscibility (e.g., nonideality) of semivolatile vapors from  $\alpha$ -pinene SOA and toluene SOA within  $\beta$ -caryophyllene SOA.<sup>182</sup> The size of SOA particles studied by Ye et al.<sup>182</sup> ranged from 200 to 700 nm in diameter. Using the method discussed above, we calculated the mixing times of organic molecules within 450 nm  $\beta$ -caryophyllene SOA particles as a function of RH (Figure 2.5). Based on these calculations, the mixing times of organic molecules within a 450 nm  $\beta$ -caryophyllene SOA particle at 48% RH are 2.3–62 s.



**Figure 2.5** Viscosities of  $\beta$ -caryophyllene SOA and calculated mixing times within a 450 nm  $\beta$ -caryophyllene SOA particle. The y-error bars correspond to the upper and lower limits of viscosity from the measurements. The x-error bars correspond to uncertainties in the RH measurements. The horizontal line corresponds to a mixing time of 1 hr.

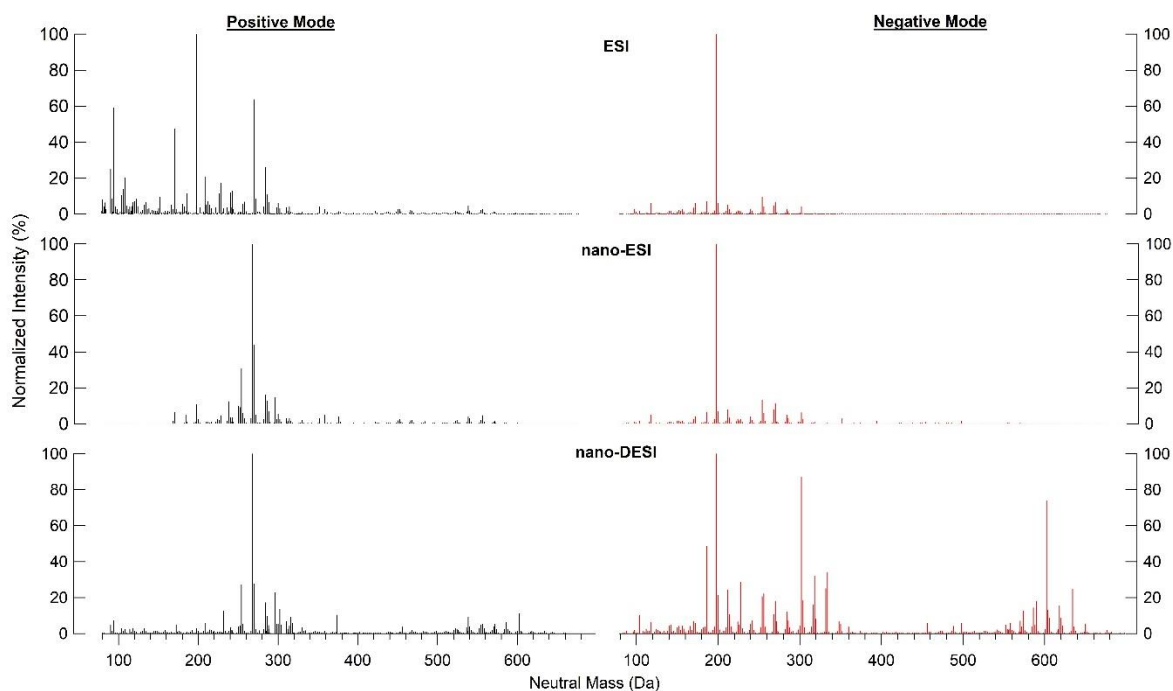
These calculations suggested that the limited uptake of semivolatile vapors from  $\alpha$ -pinene SOA and toluene SOA within  $\beta$ -caryophyllene SOA observed by Ye et al.<sup>182</sup> was due to immiscibility rather than diffusion-limited uptake. However, Ye et al.<sup>182</sup> used SOA generated with mass concentrations of 3.4–6.4  $\mu\text{g m}^{-3}$  compared to the mass loading of 50–60  $\mu\text{g m}^{-3}$  used in this study. Since viscosity can increase with a decrease in SOA mass concentration, the SOA studied by Ye et al.<sup>182</sup> may have been more viscous than the SOA in the current study, leading to longer mixing times than calculated from our data.

### 2.3.3 Chemical composition of the SOA based on mass spectrometry

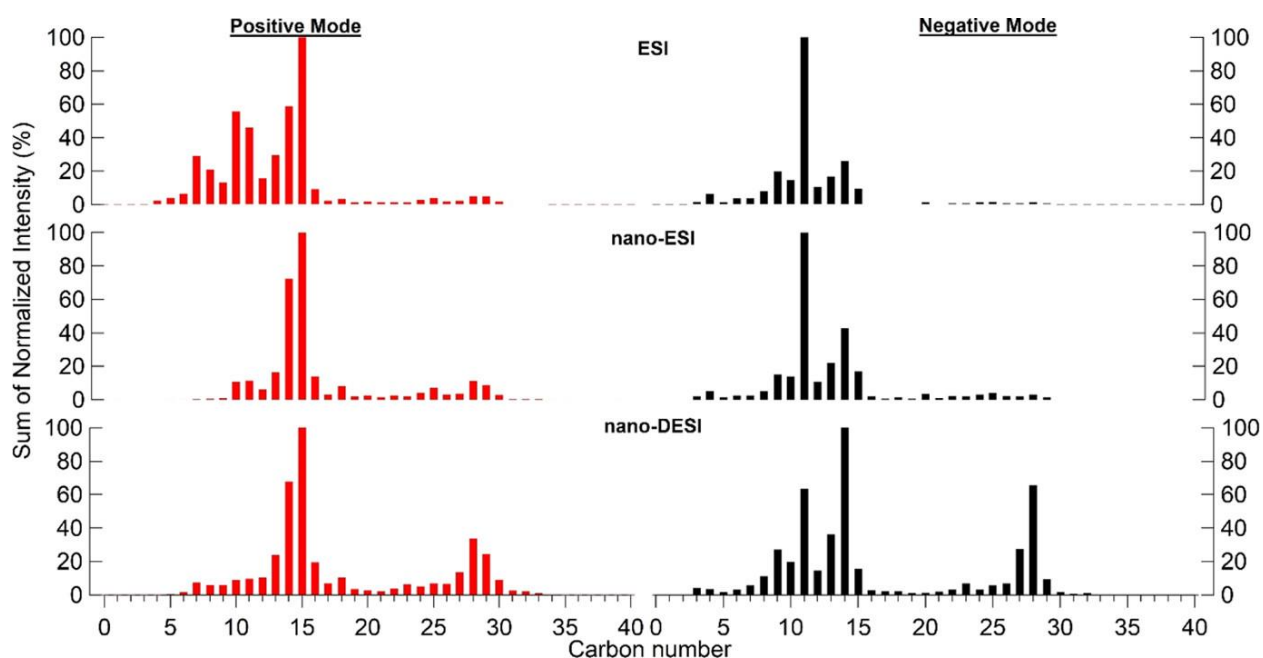
The full mass spectra are shown in Figure 2.6, and relative peak abundances from the mass spectra are shown in Figure 2.7 as a function of carbon number.  $\beta$ -Caryophyllene ( $\text{C}_{15}\text{H}_{24}$ ) is expected to produce mainly C14–C15 compounds during ozonolysis, but smaller compounds



resulting from more extensive backbone fragmentation and larger compounds resulting from oligomerization are also possible. We observed that ESI and nano-ESI favored the detection of smaller compounds compared to the nano-DESI. This effect is especially noticeable in the positive ion-mode ESI data, manifesting itself in unexpectedly high peak abundances in C5–C10 compounds. In the negative ion-mode spectra, the peak abundance is also shifted from the expected C14–C15 compounds in nano-DESI to smaller compounds in ESI and nano-ESI. Even though instrument conditions were optimized for each method, it is possible that fewer compounds experienced in-source fragmentation in nano-DESI than in other ionization modes. The ionization mechanism for nano-DESI has been shown to be better-suited for the detection of chemically labile compounds compared to ESI.<sup>183,184</sup> It has previously been found that chemically labile compounds may dissociate in solution during ESI-based analysis. Due to the shorter residence time of the sample in the solvent during nano-DESI, this dissociation is minimized.<sup>183</sup> Therefore, for the remainder of the document, we will focus on the nano-DESI results, which provide information on a broader range of SOA compounds.



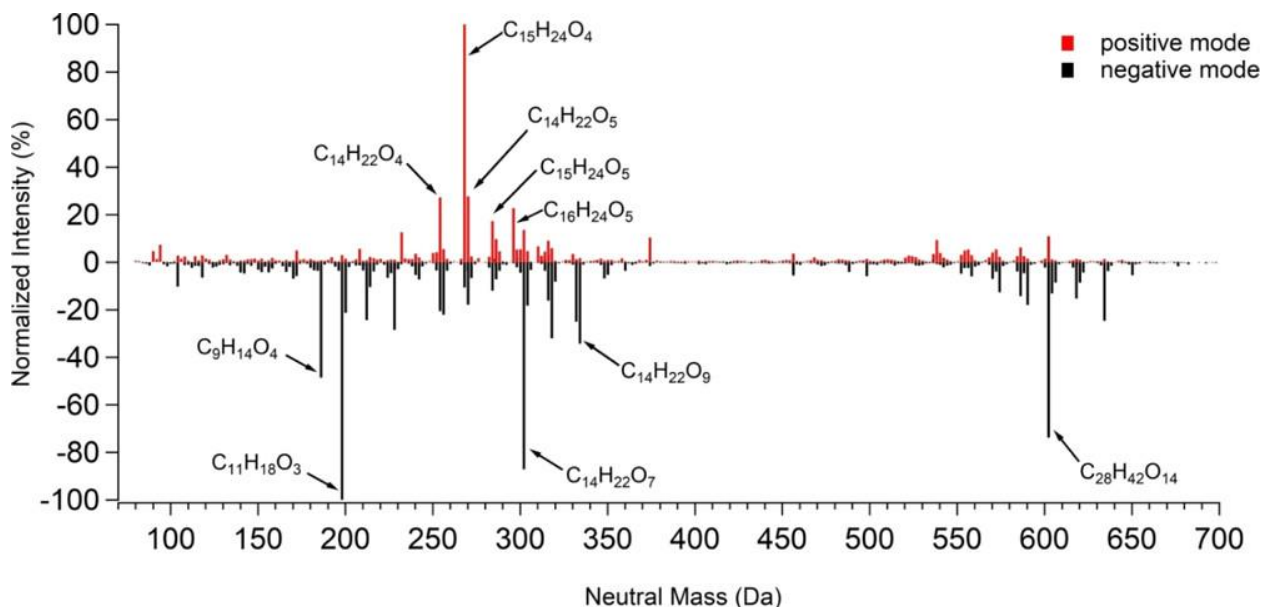
**Figure 2.6** High-resolution mass spectrometry data taken with ESI, nano-ESI, and nano-DESI ionization sources in both positive and negative mode. The intensities were normalized to the largest peak within each ionization mode.



**Figure 2.7** Sum of intensities of all molecular formula assignments based on carbon number for three ionization techniques (ESI, nano-ESI, and nano-DESI), which are normalized to the maximum intensity peak in each respective spectrum.

Shown in Figure 2.8 are nano-DESI mass spectra, with the five most abundant peaks in the positive and negative mode identified. Approximately 1000 peaks were observed in the positive mode compared to 700 peaks observed in the negative mode.  $\beta$ -Caryophyllene has two double bonds (Structure is reported in Appendix A) and attack by ozone on the more-reactive endocyclic double bond will generally lead to ring-opening products retaining the C15 carbon number. Attack on the less-reactive exocyclic double bond generally leads to C14 products. Indeed, the most-abundant peaks in the positive ion-mode mass spectra were C14 and C15 species. It is common to observe  $C_{15}H_{24}O_n$  products in mass spectra of oxidized sesquiterpenes.<sup>185,186</sup> The major C15 products identified include  $C_{15}H_{24}O_4$  and  $C_{15}H_{24}O_5$ , which have been reported as first-generation ozonolysis products.<sup>171,187</sup> Some of the major C14 products identified include  $C_{14}H_{22}O_4$ ,  $C_{14}H_{22}O_5$ , and  $C_{14}H_{22}O_7$ , which have been reported as second-

generation ozonolysis products.<sup>171,187</sup> The  $C_{14}H_{22}O_9$  product was previously reported in Richters et al.<sup>188</sup> as a highly oxidized reaction product of  $\beta$ -caryophyllene ozonolysis formed via an extended autoxidation pathway.



**Figure 2.8** Nano-DESI mass spectrum taken in the positive mode (red spectrum) and negative mode (black spectrum). The signals were normalized to the highest intensity in each respective mode. The five most abundant peaks in each mode are labeled by the corresponding neutral (unionized) molecular formulas.

In addition to C14 and C15 species, other carbon numbers were also observed, which result from fragmentation of Criegee intermediates during ozonolysis, other radical-driven secondary chemistry, and oligomerization processes occurring in the gas and particle phase. The C11 product  $C_{11}H_{18}O_3$  has been reported as a second-generation ozonolysis product of  $\beta$ -caryophyllene.<sup>171,187</sup> The C28 peak  $C_{28}H_{42}O_{14}$  has more carbon atoms than  $\beta$ -caryophyllene, indicating the formation of oligomers from  $\beta$ -caryophyllene oxidation products. Some other major peaks include  $C_9H_{14}O_4$  and  $C_{16}H_{24}O_5$ , which have not been reported previously and are likely second- or third-generation ozonolysis products of  $\beta$ -caryophyllene. These two compounds have O/C ratios of 0.44 and 0.31, respectively, which is consistent with O/C ratios of second-generation products.<sup>171</sup>

### 2.3.4 Viscosity predictions based on the measured chemical composition

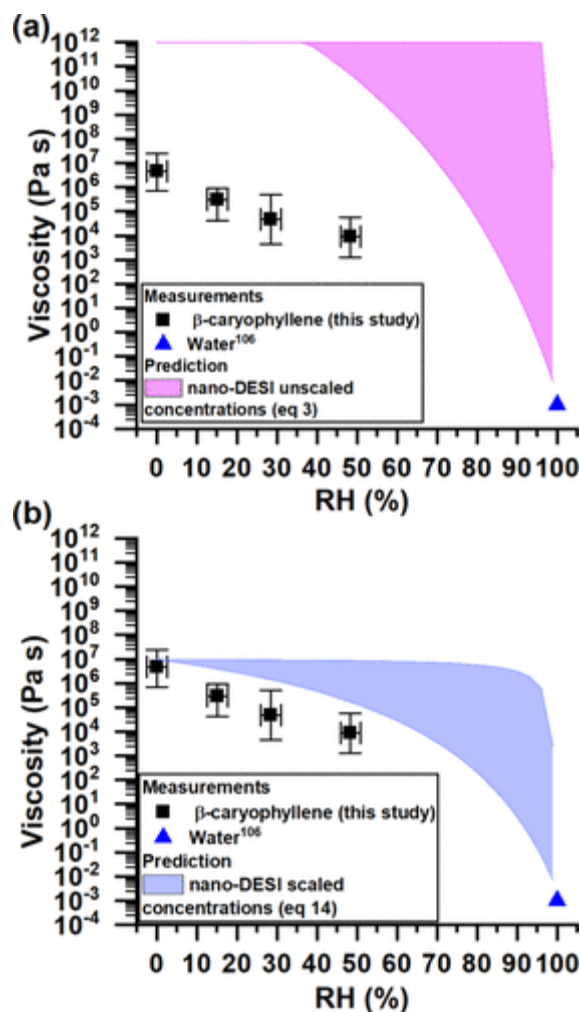
For viscosity predictions, we used the nano-DESI mass spectrometry results, since this method of ionization detected the widest spectrum of SOA compounds, based on Figure 2.7. As mentioned in Section 2.3.4, we assumed that the mass fraction of each compound was proportional to its relative peak abundance in the combined mass spectra dataset (Equation 2.3).<sup>29,51</sup> We found that predictions based on this assumption and the nano-DESI results drastically overpredicted the viscosity (Figure 2.9a). For example, under dry conditions, the predicted viscosities were up to 6 orders of magnitude larger than the measured viscosities.

ESI-based methods are known to be more sensitive to larger, oligomeric compounds,<sup>189,190</sup> and this may be the reason, at least in part, for the discrepancy between the measured viscosity and predicted viscosity. To investigate if this may be important to our studies, as a second step in our analysis, we used the adjusted mass approach based on the work of Nguyen et al.<sup>190</sup> to predict the mass fraction of each compound in the SOA:

$$w_i = \frac{I_i}{(H/C)_i \times M_i} \quad (2.14)$$

where  $M_i$  is the molecular weight of the compound,  $H/C_i$  is the hydrogen-to-carbon ratio of the compound, and  $H/C_i \times M_i$  is the adjusted mass. This scaling was used to approximately account for the impact of molecular weight and degree of unsaturation (represented by the H/C ratio) on the ionization efficiency of the individual compounds. This is the same relation developed by Nguyen et al.<sup>190</sup> based on the addition of calibration standards to a realistic SOA matrix, except Nguyen et al.<sup>190</sup> included a term to account for the limit of detection (LOD) of the compounds, which was found to inversely correlate with molecular weight and found to be small for compounds when the adjusted mass was  $>200$  Da. In the absence of better information, we

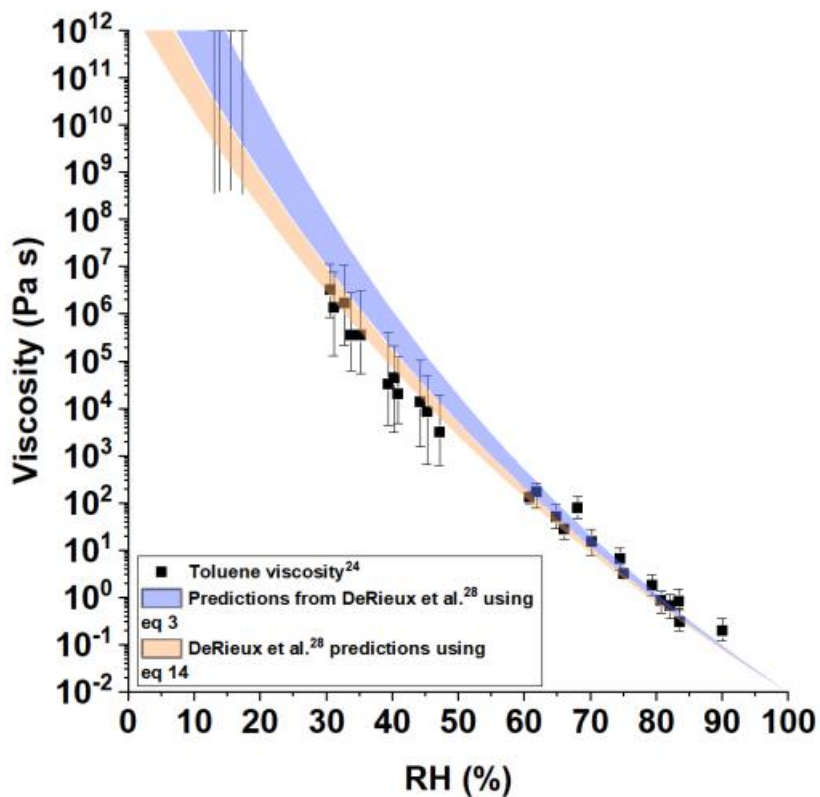
neglected the LOD term as more than 90% of the compounds detected via mass spectrometry have an adjusted mass >200 Da.



**Figure 2.9** Comparison of measured and predicted viscosities as a function of RH. The  $x$ -error bars correspond to uncertainties in the RH measurements, and the  $y$ -error bars correspond to the upper and lower limits of viscosity at each RH. Panel (a) shows the viscosity predictions using the averaged positive- and negative-ion mode mass spectrometry data where it was assumed that the weight fraction of the individual SOA species was proportional to the mass spectrum signal intensities (Equation 2.3). Panel (b) shows the viscosity predictions using the averaged mass spectrometry data assuming a relation between weight fraction and intensity given in Equation 2.14.

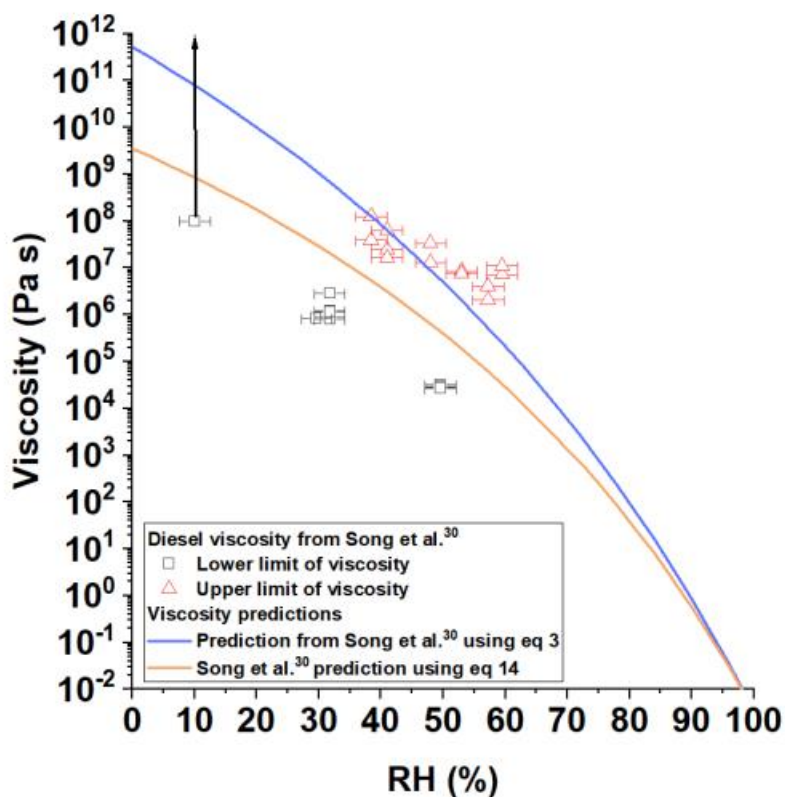
The viscosities predicted using Equation 2.14 better overlapped with the measured viscosities (Figure 2.9b). It is especially remarkable that the predicted viscosity matches with the

measured viscosity at 0% RH, indicating that the  $T_g$  parameterization and prediction method (Equations 2.1 and 2.2) work well. While ESI-based methods selectively ionize only oxidized species, the agreement implies that nano-DESI is capable of detecting the majority of the compounds present in  $\beta$ -caryophyllene SOA that contribute to its viscosity. It also suggests that the poor agreement between the measured viscosities and our initial predictions (assuming linearity between  $w_i$  and  $I_i$ ) may be, in part, due to the enhanced sensitivity of ESI methods to larger molecular weight compounds. At RH values of 15–48%, the predicted viscosities using Equation 2.14 are still larger than the measured viscosities, although the differences are much smaller than in Figure 2.9a. These differences may be due to uncertainties in the parameters or assumptions used to generate the predictions. Interestingly, in our previous studies using toluene SOA and diesel fuel SOA, we observed reasonable agreement between measured viscosities and predictions when we assumed a linear relation (i.e., Equation 2.3).<sup>29,51</sup> To investigate this further, we have redone these comparisons using Equations 2.3 and 2.14. The results show that using the relation in Equation 2.14 results in similar or improved predictions of the viscosity compared to Equation 2.14 for both the toluene SOA and diesel fuel SOA (Figure 2.10 and 2.11), consistent with the trend observed for  $\beta$ -caryophyllene SOA (although the difference in the predicted results is not nearly as dramatic as for  $\beta$ -caryophyllene SOA).



**Figure 2.10** Toluene SOA viscosity as a function of RH. The y-error bars correspond to the upper and lower limits of viscosity from the measurements. Shown in blue are the viscosity predictions based on nano-DESI positive mode mass spectrometry results from DeRieux et al.<sup>29</sup> where it was assumed that the weight fraction of individual compounds was proportional to the mass spectrum signal intensity (Equation 2.3). Shown in orange are the viscosity predictions from DeRieux et al.<sup>29</sup> where a relation between weight fraction and intensity given in Equation 2.14 of the main text was assumed. The shaded regions were calculated from nano-DESI mass spectrometry data collected at high and low RH separately.<sup>191</sup>





**Figure 2.11** Diesel fuel vapour SOA viscosities as a function of RH. The x-error bars correspond to uncertainties in the RH measurements and the y-error bars correspond to the upper and lower limits of viscosity at each RH from Song et al.<sup>51</sup> Shown in blue are the viscosity predictions based on nano-DESI negative mode mass spectrometry results where it was assumed that the weight fraction of individual compounds was proportional to the mass spectrum signal intensity (Equation 2.3). Shown in orange are the viscosity predictions where a relation between weight fraction and intensity given in Equation 2.14 was assumed.

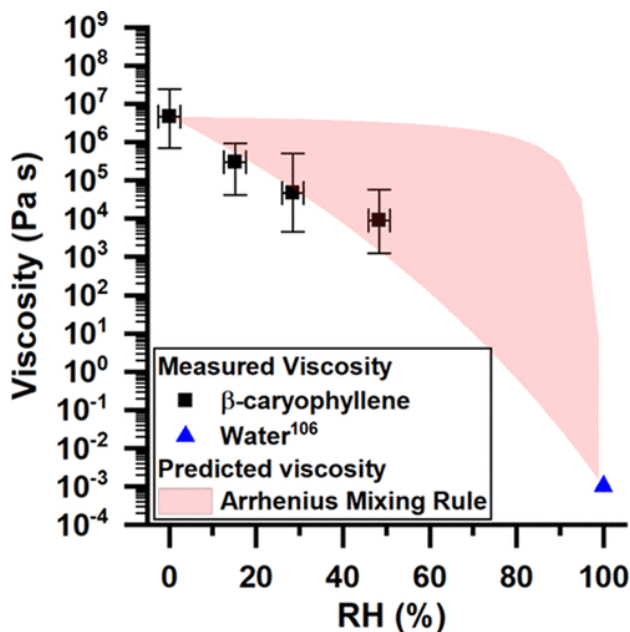
The ultimate dataset for viscosity predictions would be a full roster of the actual (rather than estimated) mass fractions of all SOA compounds. Because of the overwhelmingly large number of SOA compounds and lack of appropriate calibration standards, no existing experimental method can provide such a dataset. However, our analysis suggests that an approximate estimation of mass fractions based on Equation 2.14 can work reasonably well for the purposes of predicting material viscosity. Specifically, we have shown that nano-DESI can be used with Equations 2.1, 2.2, and 2.4-2.7 and the relation between  $w_i$  and  $I_i$  shown in Equation 2.14 to

provide an improved prediction of viscosity for toluene SOA, diesel fuel SOA, and  $\beta$ -caryophyllene SOA compared to using the assumption in Equation 2.3.

### **2.3.5 Viscosity predictions based on mole-fraction based Arrhenius mixing rule**

The viscosities of SOA as a function of RH were also estimated using a mole-fraction based Arrhenius mixing rule (Equation 2.8) and the measured viscosities of pure water and dry SOA. For a viscosity of the dry SOA, we used  $4.6 \times 10^6$  Pa s (which is consistent with our experimental data) and for the viscosity of pure water, we used  $10^{-3}$  Pa s.<sup>168</sup>

The predictions based on this approach overlapped with the measured viscosities (Figure 2.12). This is consistent with the recent studies by Gervasi et al.,<sup>108</sup> who showed that a mole-fraction based mixing rule is the best choice among simple mixing rules for predicting viscosity in binary aqueous systems. These predicted viscosities had large uncertainties for RH values ranging from approximately 30 to 95%, mainly due to the large uncertainty in the  $\kappa$  values used to predict the mole fraction of water in the SOA. The predictions based on the chemical composition and the method from DeRieux et al.<sup>29</sup> (Figure 2.9) also had large uncertainties at similar RH values for the same reason. This highlights that accurate and precise measurements of  $\kappa$  values for SOA are needed for predicting viscosities of SOA as a function of RH.



**Figure 2.12** Measured viscosities and predicted viscosities using a mole-fraction based Arrhenius mixing rule. For the measurements, the  $x$ -error bars correspond to uncertainties in the RH and the  $y$ -error bars represent the upper and lower limits of the simulated viscosities at each RH. The uncertainties in the predictions are due to uncertainties in the hygroscopicity of the SOA. For the hygroscopicity, we used a range of CCN-derived kappa values of 0.04–0.001.<sup>158,159</sup>

## 2.4 Conclusions

Viscosity was measured as a function of RH for SOA generated via the ozonolysis of  $\beta$ -caryophyllene. The viscosity was  $1.3 \times 10^3$  to  $5.6 \times 10^4$  Pa s at 48% RH, and it increased to  $6.9 \times 10^5$  to  $2.4 \times 10^7$  Pa s at 0% RH, where the ranges correspond to measurement and data analysis uncertainties. Diffusion coefficients were calculated from the viscosities using the fractional Stokes–Einstein equation and ranged from  $\sim 4.1 \times 10^{-16}$  m<sup>2</sup> s<sup>-1</sup> at 48% RH to  $\sim 1.8 \times 10^{-18}$  m<sup>2</sup> s<sup>-1</sup> at 0% RH. Mixing times of organic molecules within 200 nm SOA particles were calculated from the diffusion coefficients and ranged from <3 s at 48% RH to 0.2 h at 0% RH. Based on these values, mixing times within 200 nm  $\beta$ -caryophyllene SOA are fast (<1 h) for RH and temperatures typically found in the planetary boundary layer.

The chemical composition of the SOA was determined with nano-DESI mass spectrometry. The most-abundant peaks in the mass spectra were C15 and C14 peaks, corresponding to the first- and second-generation ozonolysis products. Another abundant peak in the mass spectra was a C28 peak, likely the result of dimerization of the  $\beta$ -caryophyllene oxidation products. We note that ESI and nano-ESI favored the detection of smaller compounds compared to nano-DESI, and the fact that relative peak abundances from the three ionization methods do not fully agree with each other highlights the difficulty of estimating relative abundances of SOA compounds using direct infusion methods. In this study, we assumed that nano-DESI provides the most accurate information about SOA composition because it is known to better detect labile compounds.

The viscosity data and the chemical composition from mass spectrometry were used to test the accuracy of the method from DeRieux et al.<sup>29</sup> for predicting the viscosity of  $\beta$ -caryophyllene SOA. Using raw peak nano-DESI abundances in the mass spectra as substitutes of mass fractions led to a drastic overprediction of the viscosity by up to 6 orders of magnitude (depending on the RH). However, when the peak abundances were adjusted to account for the sensitivity of the electrospray ionization to larger molecular weight components using an empirical relationship suggested by Nguyen et al.,<sup>190</sup> the predicted viscosities better overlapped with the measured viscosities. Furthermore, the same method produced better or similar predictions for our previous observations of viscosity of toluene SOA and diesel fuel SOA. These results further highlight the level of sensitivity of viscosity predictions to the method used for relating peak abundances to relative concentrations in direct infusion mass spectra.

We also tested the accuracy of a mole-fraction based Arrhenius mixing rule for predicting viscosity as a function of RH from the viscosity of water and the dry SOA. For this case, the predictions overlapped with the measured data.

## CHAPTER 3

### VISCOSITY AND LIQUID-LIQUID PHASE SEPARATION IN HEALTHY AND STRESSED PLANT SOA

Portions of this chapter were reproduced under the Creative Commons Attribution 4.0 License with permission from the Royal Society of Chemistry:

Smith, N. R.; Crescenzo, G. V.; Huang, Y.; Hettiyadura, A. P. S.; Siemens, K.; Li, Y.; Faiola, C. L.; Laskin, Shiraiwa, M.; Bertram, A. K.; Nizkorodov, S. A.; Viscosity and liquid-liquid phase separation in healthy and stressed plant SOA, *Environmental Science: Atmospheres*, **1** (2021) 140-153.

#### Abstract

Molecular composition, viscosity, and liquid-liquid phase separation (LLPS) were investigated for secondary organic aerosol (SOA) derived from synthetic mixtures of volatile organic compounds (VOC) representing emission profiles for Scots pine trees under healthy and aphid-herbivory stress conditions. Model “healthy plant SOA” and “stressed plant SOA” were generated in a 5 m<sup>3</sup> environmental smog chamber by photooxidation of the mixtures at 50% relative humidity (RH). SOA from photooxidation of  $\alpha$ -pinene was also prepared for comparison. Molecular composition was determined with high resolution mass spectrometry, viscosity was determined with the poke-flow technique, and liquid-liquid phase separation was investigated with optical microscopy. The stressed plant SOA had increased abundance of higher molecular weight species, reflecting greater fraction of sesquiterpenes in the stressed VOC mixture compared to the healthy plant VOC mixture. LLPS occurred in both the healthy and stressed plant SOA; however, stressed plant SOA exhibited phase separation over a broader humidity range than healthy plant SOA, with LLPS persisting down to  $23 \pm 11\%$  RH. At  $\text{RH} \leq 25\%$ , both stressed and healthy plant SOA viscosity exceeded 108 Pa s, value similar to tar pitch. At 40% and 50%

RH, stressed plant SOA had the highest viscosity, followed by healthy plant SOA and then  $\alpha$ -pinene SOA in descending order. The observed peak abundances in the mass spectra were also used to estimate the SOA viscosity as a function of RH and volatility. The predicted viscosity of the healthy plant SOA was lower than that of the stressed plant SOA driven by both the higher glass transition temperatures and lower hygroscopicity of the organic molecules making up stressed plant SOA. These findings suggest that plant stress influences the physicochemical properties of biogenic SOA. Furthermore, a complex mixture of VOCs resulted in a higher SOA viscosity compared to SOA generated from  $\alpha$ -pinene alone at  $\geq 25\%$  RH, highlighting the importance of studying properties of SOA generated from more realistic multi-component VOC mixtures.

### 3.1 Introduction

Secondary organic aerosol (SOA) dominates the total fine particle mass in the atmosphere.<sup>1,192</sup> SOA is formed from the condensation of oxidation products of volatile organic compounds (VOCs). Approximately 100,000 different organic compounds have been measured in the atmosphere,<sup>2</sup> resulting in the highly complex composition of SOA and a wide range of volatility, hygroscopicity, and reactivity.<sup>1</sup> Of the total amount of atmospheric VOCs, roughly 90% come from biogenic sources.<sup>11</sup> Because of the chemical complexity of ambient SOA, only 10% of the total mass of SOA has been speciated in terms of molecular composition.<sup>1</sup> A comprehensive understanding of the formation, properties, and transformation of SOA is essential to understand their impact on atmospheric processes, climate, and human health.<sup>1</sup>

The most abundant biogenic VOCs are isoprene ( $C_5H_8$ ), monoterpenes ( $C_{10}H_{16}$ ), and sesquiterpenes ( $C_{15}H_{24}$ ).<sup>11,12</sup> Because  $\alpha$ -pinene and limonene typically dominate the

monoterpene emission profile in forested areas,<sup>14,15</sup> they have commonly been used as representative monoterpenes in laboratory and modeling studies investigating biogenic SOA. In laboratory studies,<sup>16,17</sup> SOA generated from a single VOC is commonly used because these simpler systems allow for the investigation of their fundamental physical and chemical properties. These single VOC experimental studies provide parameterizations of SOA formation mechanisms for air quality and climate models. However, ambient SOA is produced from a more complex mixture of VOCs. Using complex VOC mixtures can impact the oxidant reactivity and subsequent products formed when compared to selected single VOCs.<sup>193</sup> The discrepancy between laboratory-generated SOA and real atmospheric SOA could lead to errors in the estimation of their impact on climate and air quality, as well as their impact on human health. Therefore, it is pertinent to conduct experiments on SOA formed from realistically complex mixtures of VOCs to better represent ambient scenarios.

Plant health needs to be considered when deciding which VOCs to use to replicate biogenic SOA in a laboratory setting. Plants become stressed due to changing environmental conditions, including biotic and abiotic factors.<sup>22</sup> Some examples of abiotic stress include increased temperature, drought, or low soil nutrient levels.<sup>22</sup> Examples of biotic stress in plants include insect feeding (including defoliators, bark borers, or sap-sucking aphids) known as herbivory, insect egg laying known as oviposition, or pathogen attack.<sup>22,194–196</sup> When plants become stressed, biochemical defense pathways are initiated, which alters their VOC emissions in both quantity and types of compounds being emitted.<sup>23,19</sup> Aphid-herbivory, typically increases sesquiterpene emissions from pine trees.<sup>197</sup> During stress events, different types of compounds such as acyclic sesquiterpenes



are produced.<sup>23</sup> The function of these stress VOC emissions includes increased membrane thermotolerance, antioxidant properties, tri-trophic signaling (e.g., attracting natural enemies of herbivores), and inter- and intra-plant communication.<sup>198-199</sup> In addition, these VOCs can protect plants from further destruction by priming them for the next stress event they may experience, which can lead to quicker recovery times.<sup>24-25</sup> Importantly, changes in healthy and stressed biogenic VOC emissions can alter SOA composition, as well as the distribution of volatilities of SOA compounds, with the potential to alter climate-relevant SOA properties.

Studying how the change in the emission profile of plants impacts SOA properties is important because plant stress is common in ecosystems, and is rapidly increasing in many locations due to a changing climate.<sup>200</sup> Moreover, the SOA formed from stressed plants could impact climate differently than SOA formed from healthy plants due to differences in composition and physical properties. Recent studies have shown that herbivore stress has the potential to decrease or increase SOA mass yields,<sup>19-201</sup> increase SOA mass and cloud condensation nuclei (CCN) number in the boreal forest,<sup>202</sup> decrease hygroscopicity of the resulting particles,<sup>203</sup> and increase the relative proportion of fragmentation vs. functionalization reactions in the gas phase.<sup>23</sup> Therefore, the chemical and physical properties of healthy versus stressed plant SOA should be investigated to parse out if there is a significant difference between the two systems, with implications for changes in aerosol properties in an evolving environment.

SOA particles were commonly assumed to be liquid-like, permitting fast diffusion of molecules through the particle. However, studies of SOA material generated from the oxidation of single biogenic VOCs, including isoprene and various terpenes, have shown

that SOA becomes highly viscous semi-solids or glassy solids under certain environmental conditions such as low temperature and low RH.<sup>16,28,32-43</sup> Increases in viscosity lead to much slower diffusion rates within the SOA, impacting particle growth and evaporation, gas-particle partitioning, size distributions, multiphase chemistry, and the ability of SOA to serve as nuclei for liquid cloud droplets or ice particles.<sup>8,9,31,37,83,85,87-90,94,95,109,204</sup>

The viscosity of SOA material depends on the molecular weight and the degree of oxidation of its chemical constituents.<sup>28,42,205,206</sup> Moreover, the viscosity of SOA is strongly affected by temperature and RH. Water acts as a plasticizer, therefore an increase in RH leads to a decrease in viscosity of amorphous organic materials, allowing for higher diffusion rates of molecules within the SOA.<sup>28\*31\*44</sup> However, an increase in RH may not lead to a decrease in viscosity of organic aerosol with very low hygroscopicity, as seen in previous studies investigating cooking organic aerosol.<sup>207</sup> Viscosity and diffusion are interrelated and it is practical to estimate diffusion rates of large organic molecules within SOA from measured viscosity and the Stokes-Einstein equation.<sup>208\*209</sup> On the other hand, diffusion rates of small organic molecules, water, and oxidants within SOA can be estimated from SOA viscosity using the fractional Stokes-Einstein equation.<sup>98</sup>

Recently, a parameterization was developed for predicting the viscosity of SOA based on its chemical composition; which can be used with chemical transport models to predict viscosity of SOA in the atmosphere.<sup>29\*210\*205</sup> This parameterization, together with high resolution mass spectrometry measurements of chemical composition, has been used successfully to predict the viscosity of several types of SOA formed from isoprene,  $\alpha$ -pinene, toluene and diesel fuel vapors.<sup>16,36,51,106</sup> However, the accuracy of the

parameterization for predicting the viscosity of SOA from a mixture of VOCs has not been evaluated.

As an added layer of complexity, individual SOA particles can undergo liquid-liquid phase separation (LLPS) and form two distinct liquid phases, an inner aqueous-rich phase and an outer organic-rich phase. LLPS in SOA particles was initially observed in mixed particles containing organic and inorganic species.<sup>48,49,211</sup> This LLPS phenomena was thought to be, at least partially, driven by the presence of the inorganic salts, which can cause salting out of organics.<sup>48</sup> More recently, it has been shown that LLPS also occurs in SOA particles in the absence of inorganic salts.<sup>51,212-215</sup> The LLPS events in SOA particles can impact the extent to which gas-particle partitioning of semivolatile compounds may occur,<sup>52-54</sup> the reactive uptake of gasses,<sup>55,56,216</sup> as well as their ability to act as nuclei for cloud droplets and ice particles,<sup>57,213,217,218</sup> making it an important process to study.

In this work, we investigate chemical composition, viscosity, and LLPS in SOA produced from complex mixtures of VOCs representative of emissions from healthy plant (abbreviated as hp-SOA from here on) and stressed plant (sp-SOA) pine trees. We compare the results to SOA generated from  $\alpha$ -pinene to test whether the physicochemical properties of particles made from a single VOC are comparable to more representative SOA formed from complex mixtures of VOCs. The VOC mixtures used in this work are based on the emission profile of healthy and aphid-stressed Scots pine saplings (*Pinus sylvestris* L.) previously reported by Faiola et al.<sup>23</sup> Pine trees (Pinaceae) have a wide spatial distribution<sup>58</sup> and are typically found in boreal forests which cover one-third of the global forested area<sup>219</sup> making them a good representative plant for studying biogenic SOA over boreal forests. In addition, we investigate the accuracy of the parameterization from DeRieux et al.

(2018)<sup>29</sup> by comparing the predicted viscosities of the SOA to the experimentally determined viscosities. Volatility and viscosity are closely related and it was recently reported that SOA with low volatility showed an increased viscosity.<sup>34,43,47</sup> Therefore, we also report the volatility distribution of compounds within the hp-SOA and sp-SOA using parameterization from Li et al. (2016).<sup>210</sup>

We find that SOA produced from the VOC mixtures is more viscous compared to the more commonly studied  $\alpha$ -pinene SOA. Increased farnesene and other sesquiterpene mixing ratios used in the generation of sp-SOA significantly increased the viscosity of the resulting sp-SOA when compared to hp-SOA. In addition, two liquid phases are persistent in sp-SOA over a wider RH range compared to hp-SOA. These findings suggest that consideration of complex plant VOC mixtures and effects of plant stress are important in determining the physicochemical properties of biogenic SOA.

## **3.2 Experimental methods**

### **3.2.1 VOC mixtures**

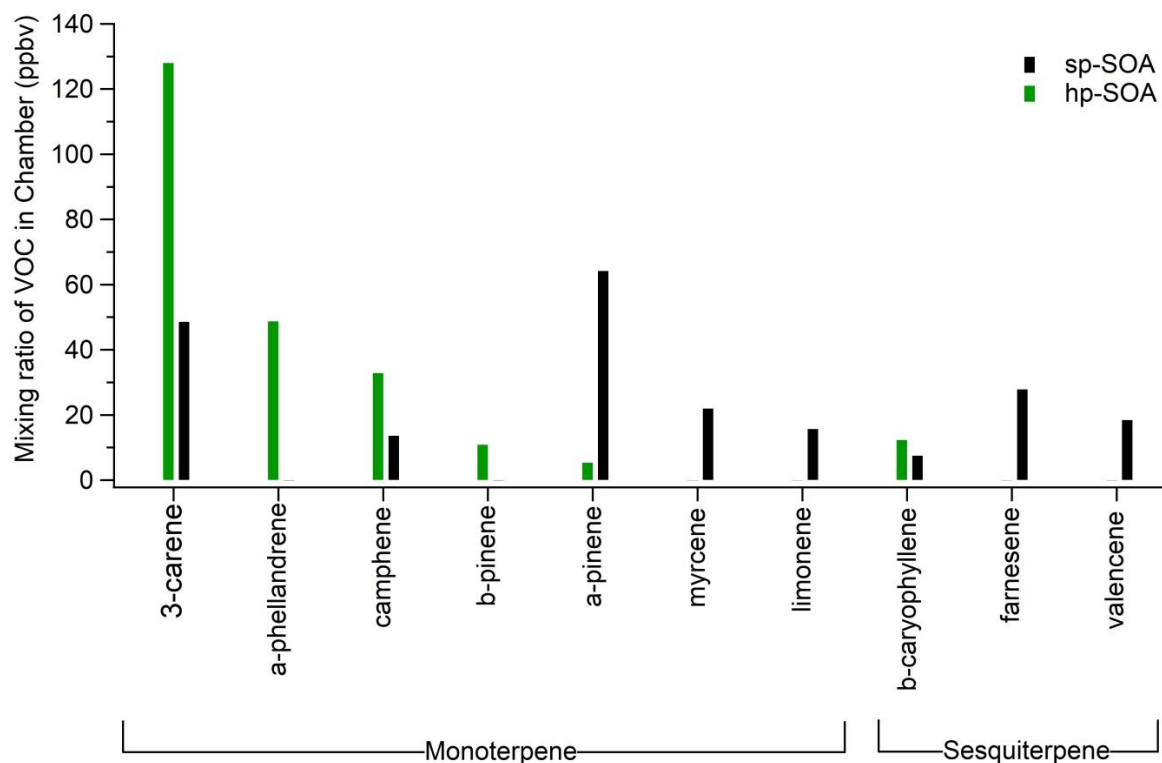
Two VOC mixtures were created from commercially available compounds listed in Table 3.1. The compounds were mixed in molar fractions chosen to represent the VOC profile of compounds emitted from healthy and stressed 8-year old Scots pine (*Pinus sylvestris* L) trees, as reported in Faiola et al. (2019).<sup>23</sup> Valencene was used as a representative cyclic sesquiterpene and a farnesene isomer mixture was used as a proxy for acyclic sesquiterpenes. Ylisirniö et al. (2020) analyzed a similar farnesene isomer mixture to the one used in this study (Sigma Aldrich) and found a significant fractional contribution by bisabolene isomers (40%) and other unidentified sesquiterpenes (20%) in addition to the farnesene isomers.<sup>220</sup>

**Table 3.1** Chemical composition of the VOC mixture used to produce SOA; purity and sources of commercially- available standards used to generate healthy and stressed VOC mixtures; and lifetimes with respect to oxidation in the chamber. Monoterpene is abbreviated as MT and sesquiterpene is abbreviated as SQT. The chemical structures of these VOCs are reported in Appendix A.

VOC type	Chemical Species	Healthy (mol/mol %)	Stressed (mol/mol %)	Purity	Source	Lifetime (h)
MT	$\alpha$ -phellandrene	20.3%	-	$\geq 75\%$ stabilized ( $\leq 0.050\%$ $\alpha$ -tocopherol)	Sigma (CAS:99-83-2)	0.63 <sup>a</sup>
MT	$\beta$ -pinene	4.6%	-	98%	Acros Organics (CAS: 18172-67-3)	2.66 <sup>a</sup>
MT	$\alpha$ -pinene	2.3%	29.4%	98%	Acros Organics (CAS:7785-26-4)	3.78 <sup>a</sup>
MT	3-carene	53.9%	22.3%	90%	Aldrich (CAS: 13466-78-9)	2.25 <sup>a</sup>
MT	camphene	13.8%	6.3%	$\geq 96\%$	Sigma Aldrich (CAS: 79-92-5)	3.73 <sup>a</sup>
MT	myrcene	-	10.0%	$>75\%$ (Contains 1000 ppm of BHT as inhibitor)	Aldrich (CAS:123-35-3)	0.92 <sup>a</sup>
MT	limonene	-	7.3%	97% Stabilized	Alfa Aesar, (CAS:5989-27-5)	1.21 <sup>a</sup>
SQT	b-caryophyllene	5.2%	3.4%	98.5%	Sigma (CAS:87-44-5)	1.00 <sup>a</sup>
SQT	mix of farnesene isomers <sup>c</sup>	-	12.8%	stabilized ( $<0.10\%$ $\alpha$ -tocopherol)	Sigma-Aldrich (Product#: W383902)	1.16 <sup>b</sup>
SQT	valencene	-	8.5%	$\geq 70\%$	Aldrich (CAS:4630-07-3)	N/A

<sup>a</sup> Lifetimes calculated using k-values reported in Atkinson et al. (2003).<sup>18</sup> <sup>b</sup> Calculated using k-values for (E)-b-farnesene reported in Kourtchev et al. (2012).<sup>221</sup> <sup>c</sup> May contain sesquiterpenes, trans- $\beta$ -farnesene, cis- $\alpha$ -farnesene, trans- $\alpha$ -farnesene, and bisabolene.

The mixing ratios of monoterpenes and sesquiterpenes that were evaporated into the chamber were calculated assuming total desorption into the chamber and are shown in Figure 3.1. The farnesene isomers bar in Figure 3.1 contains the bisabolene and other sesquiterpenes observed by Ylisirniö et al. (2020) – we have not performed an explicit analysis of the injected mixture to further classify them. The total VOC mixing ratio was approximately the same across all experiments (200 ppb). The dominant VOC in the



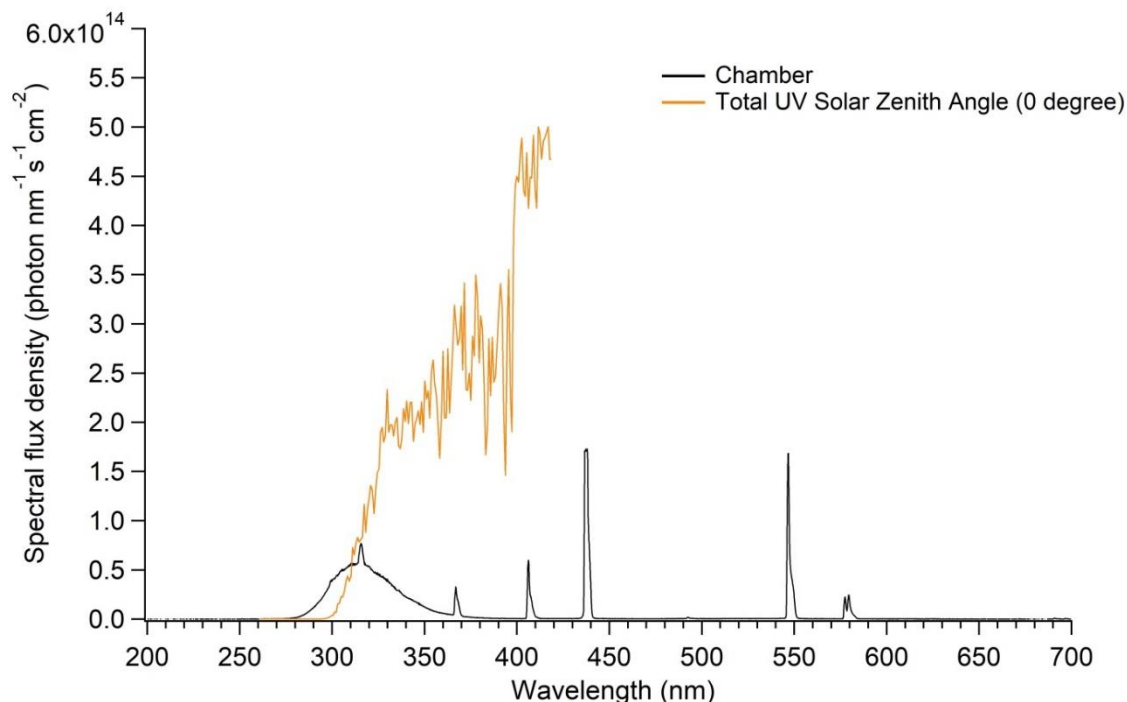
**Figure 3.1** Mixing ratio of each VOC after the injection into the environmental chamber. The relative VOC amounts (Table 3.1) were chosen to replicate the emission profile of healthy (green) and aphid-stressed (black) Scots Pine trees reported in Faiola et al. (2019).

healthy mixture was 3-carene with a mixing ratio of (128 ppb). In the stressed mixture  $\alpha$ -pinene was the most abundant monoterpene and, compared to the healthy mixture, had three sesquiterpenes with farnesene having the highest mixing ratio (28 ppb) of the three.

### 3.2.2 SOA generation

SOA was generated by OH-initiated photooxidation of VOCs in air under low- $\text{NO}_x$  conditions in a 5 m<sup>3</sup> Teflon environmental chamber. The chamber was operated in the batch mode at 50% RH and room temperature (21- 26 °C) for all trials. Seed particles were not used to avoid interference with experimental viscosity and LLPS measurements. Evaporation of 45  $\mu\text{l}$  of 30 wt.%  $\text{H}_2\text{O}_2$  into the chamber via a heated inlet (45 °C) produced approximately 2 ppm of  $\text{H}_2\text{O}_2$  vapor serving as photochemical OH precursor. Following

oxidant injection, 8  $\mu\text{l}$  of either healthy or stressed VOC mixtures were evaporated into the chamber via the same heated inlet, and a bank of UV-B lights was turned on (the UV-B lamp spectral flux density in the chamber is shown in Figure 3.2).



**Figure 3.2** Measured spectral flux density in chamber compared to the solar spectral flux density calculated at a solar zenith angle of 0 degrees.

To verify completeness of injection of the VOCs into the chamber, gas-phase abundance of monoterpenes ( $m/z$  137.1330) and sesquiterpenes ( $m/z$  205.1956) were monitored using a proton-transfer-reaction time-of flight mass spectrometer (PTR-ToF-MS; Ionicon model 8000) with  $\text{H}_3\text{O}^+$  as the reagent ion. The particle size and number concentration were monitored using a scanning mobility particle sizer (SMPS; TSI differential mobility analyzer model 3080 and CPC model 3775). The ozone and  $\text{NO}/\text{NO}_y$  concentrations in the chamber were monitored using an  $\text{O}_3$  analyzer (Thermo Scientific, Model 49i) and a  $\text{NO-DIF-NO}_y$  analyzer (Thermo Scientific, Model 42I-Y), respectively. After three hours of photooxidation, when the particle mass concentration in the chamber

reached approximately  $200 \mu\text{g m}^{-3}$ , the UV-B lights were turned off. The steady-state OH concentration was  $1.4 \times 10^6 \text{ cm}^{-3}$  calculated from the rate of decay of limonene under similar experimental conditions used in this study. At this OH concentration the VOC lifetimes were 0.6-3.8 h (Table 3.1), at least 50% of each VOC was consumed by the end of the irradiation period. The PTR-ToF-MS data suggested that 40-50% of total monoterpenes and sesquiterpenes were consumed.

For the viscosity and LLPS measurements, SOA particles were collected at  $30 \text{ L min}^{-1}$  onto hydrophobic glass substrates placed in stage 9 of a non-rotating microorifice uniform deposit impactor (MOUDI) with all the remaining MOUDI stages removed. Under normal operating conditions, stage 9 collects particles with diameters above 100 nm,<sup>222</sup> however, its operation without other MOUDI stages increases the pressure drop across the stage, thus increasing the jet velocity and decreasing the minimal particle size, but potentially increasing particle bounce. The 50% RH in the chamber should help reduce the bouncing effect compared to what would happen in a dry air case.<sup>223</sup> This method of collection resulted in discrete spots of aggregated SOA particles. By the time of the viscosity or LLPS measurement, the individual submicron SOA particles in some of the spots merged into “macroparticles” with spherical cap geometry and diameters of 30-100  $\mu\text{m}$ . Hydrophobic glass slides were generated by coating plain glass slides (Hampton Research) with Trichloro(1H,1H,2H,2H-perfluorooctyl) silane or FluoroPel 800 (Cytonix USA). Simultaneously, SOA was collected on aluminum foils for high resolution mass spectrometry analysis using the same sampling method. Samples were collected for 2-3 hours. Samples were then placed in protective plastic enclosures, sealed with a vacuum



food sealer, and stored in a freezer at -20 °C until analysis (except for 24 h transit time when the samples had to be shipped to other participating laboratories on ice at 0 °C).

### 3.2.3 High-resolution mass spectrometry

The high-resolution mass spectrometry data were obtained using a high-resolution Q Exactive HF-X Orbitrap mass spectrometer (Thermo Scientific) with a mass resolving power of  $2.4 \times 10^5$  (at  $m/z$  200) outfitted with a nano-desorption electrospray ionization source (nano-DESI-HRMS).<sup>183</sup> Nano-DESI-HRMS was performed in negative and positive modes for the collected SOA samples similar to previous work.<sup>224</sup> The spray voltage was set to 3.5 kV, the capillary temperature was 250 °C and the S-lens ion funnel RF level was 80. The solvent consisted of a 1:1 (v/v) mixture of LC-MS grade acetonitrile and water. The sample was line-scanned starting from the area free of the analyte. Then, all peaks that rose above a signal to noise ratio of 3 were considered as analyte related.<sup>183</sup> In addition to the samples, a solvent blank was prepared following the same procedure above, but using a control substrate without analyte. Molecular formulas were assigned similarly to previous work.<sup>224,152</sup> Briefly, the peaks were extracted from the mass spectra, and peaks containing  $^{13}\text{C}$  isotopes were removed. All peaks were assigned to the formulas  $\text{C}_x\text{H}_y\text{O}_z$  with an accuracy of  $\pm 0.001$   $m/z$  units while containing the assignments to closed-shell ions with even nominal masses and constraining H/C to 0.30-2.25 and O/C to 0.00-2.30. The assigned ion formulas were corrected for the ionization mechanism, and all the HRMS results below are reported as formulas of neutral SOA compounds. The assumed ionization mechanisms were formation of adducts with  $\text{H}^+$  or  $\text{Na}^+$  for positive ions and deprotonation for negative ions.

### 3.2.4 Liquid-liquid phase separation

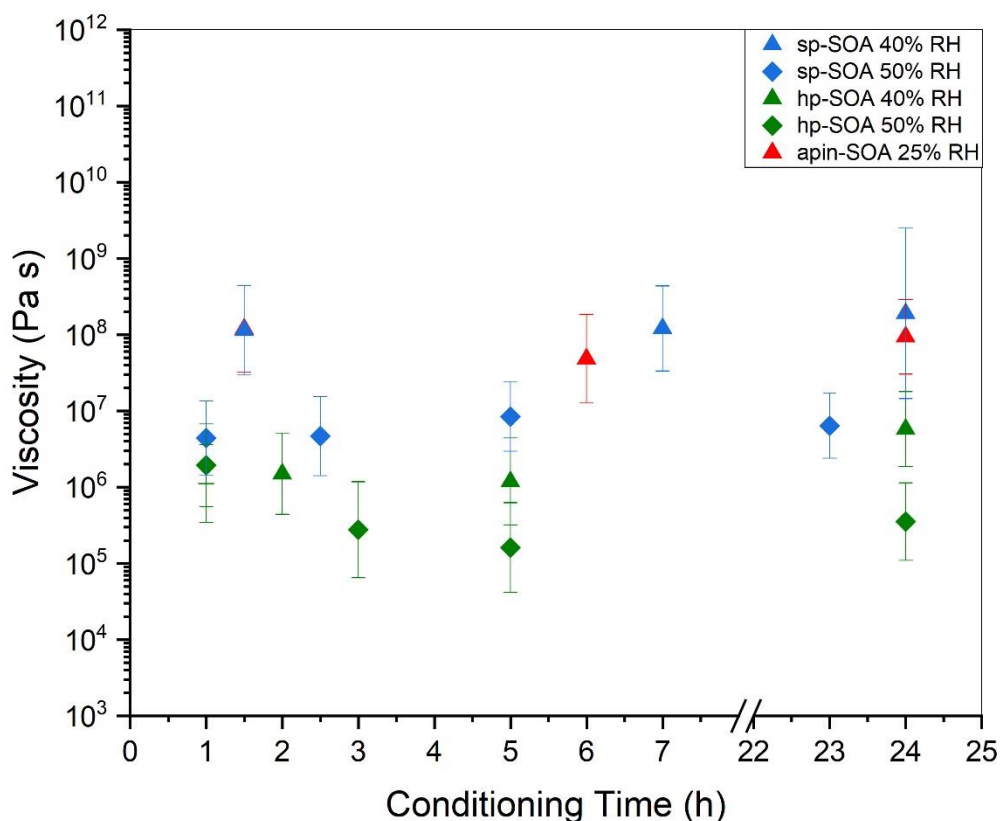
Events of LLPS in substrate deposited samples of SOA material were measured for all samples using an optical microscope equipped with a CCD (charge-coupled device) camera by our collaborators at University of British Columbia. The procedure for LLPS has been described by Song et al. (2019).<sup>51</sup> In short, the hydrophobic glass slides containing the SOA samples were placed in a RH and temperature-controlled flow cell (experimental setup shown in Appendix B). The RH was monitored using a chilled-mirror dew point hygrometer (General Eastern M4/E4 dew point monitor, Canada). The SOA particles were initially conditioned at 98% RH in the flow cell for 10 minutes. At this RH, particles already exhibited LLPS. The RH was decreased at a rate of 1% RH min<sup>-1</sup> until LLPS was no longer visible. A picture was taken every 10 s throughout the duration of the experiment via the CCD. Afterwards, the RH was quickly dropped down to 0% to confirm LLPS did not reappear at lower RH. Three trials were performed for each SOA generation condition.

### **3.2.5 Viscosity measurements**

Viscosities of SOA were determined by our collaborators at the University of British Columbia using the poke-flow technique described elsewhere.<sup>16,32</sup> This method relies on observing the flow of material under an optical microscope after deforming it with a blunt object.<sup>225</sup> After collecting SOA on the hydrophobic slides, the slides were placed into a flow-cell mounted onto a polarizing metallurgical inverted microscope (AMScope). Dry or humidified nitrogen passed through the cell and the RH of the outgoing gas flow was measured continuously with an optical chilled mirror hygrometer (1311DR, Chilled Mirror Hygrometer, General Eastern). The hygrometer RH was calibrated with respect to the deliquescence relative humidity (DRH) of potassium carbonate (43% DRH). The temperature was continuously monitored with a thermocouple (Omega HH200A) attached

to the top of the flow cell. All experiments were performed at 291-295 K. Before any experiments were performed, the slides with SOA were conditioned at the desired RH (approximately 0%, 10%, 25%, 40% or 50%) for 1.5 h. Longer conditioning times of up to 24 h were later investigated for each SOA type to see if the measured viscosity was sensitive to the conditioning time; however, there was no significant change as shown in Figure 3.3.

For the poke-flow experiments, a hydrophobically coated (OilSlip 110, Cytonix USA)



**Figure 3.3** Particle viscosity as a function of conditioning time in poke-flow cell at humidity of interest. Vertical bars represent the calculated lower and upper limits of viscosity (83% confidence interval) based on COMSOL simulations (see Table 3.2 for input parameters).

needle was mounted to a micromanipulator arm that could move it in XYZ directions. The

needle was placed directly above an SOA “macroparticle” (diameter of 30-50  $\mu\text{m}$ ), and then moved downwards vertically to penetrate the particle surface and contact the surface of the hydrophobic glass slide. Upon removal of the needle, a visible hole was left behind resulting in the formation of a particle with half-torus geometry. The poked particle was allowed to flow until the area of the hole (A) had recovered to one quarter of the original area of the poke hole ( $\frac{1}{4}A$ ). If allowed long enough, particles would recover to their original, energetically favorable state of spherically capped geometry. The time of the  $\frac{1}{4}A$  recovery will be referred to as the experimental flow time ( $\tau_{\text{exp, flow}}$ ).

**Table 3.2** COMSOL parameters used for simulating the upper and lower limits of viscosity of the collected SOA by poke-flow.

SOA type		Surface tension ( $\text{mN m}^{-1}$ )	Slip length (m)	Contact angle ( $^{\circ}$ )
Healthy plant SOA	Range of values	25.3 <sup>a</sup> -45 <sup>b</sup>	$5 \times 10^{-9}$ - $1 \times 10^{-6}$ <sup>c</sup>	50.9-60.0 <sup>d</sup>
Stressed plant SOA	Range of values	23.0 <sup>e</sup> -45 <sup>b</sup>	$5 \times 10^{-9}$ - $1 \times 10^{-6}$ <sup>c</sup>	54.2-63.8 <sup>d</sup>
$\alpha$ -pinene SOA	Range of values	25.3 <sup>z</sup> -45 <sup>b</sup>	$5 \times 10^{-9}$ - $1 \times 10^{-6}$ <sup>c</sup>	52.7-67.7

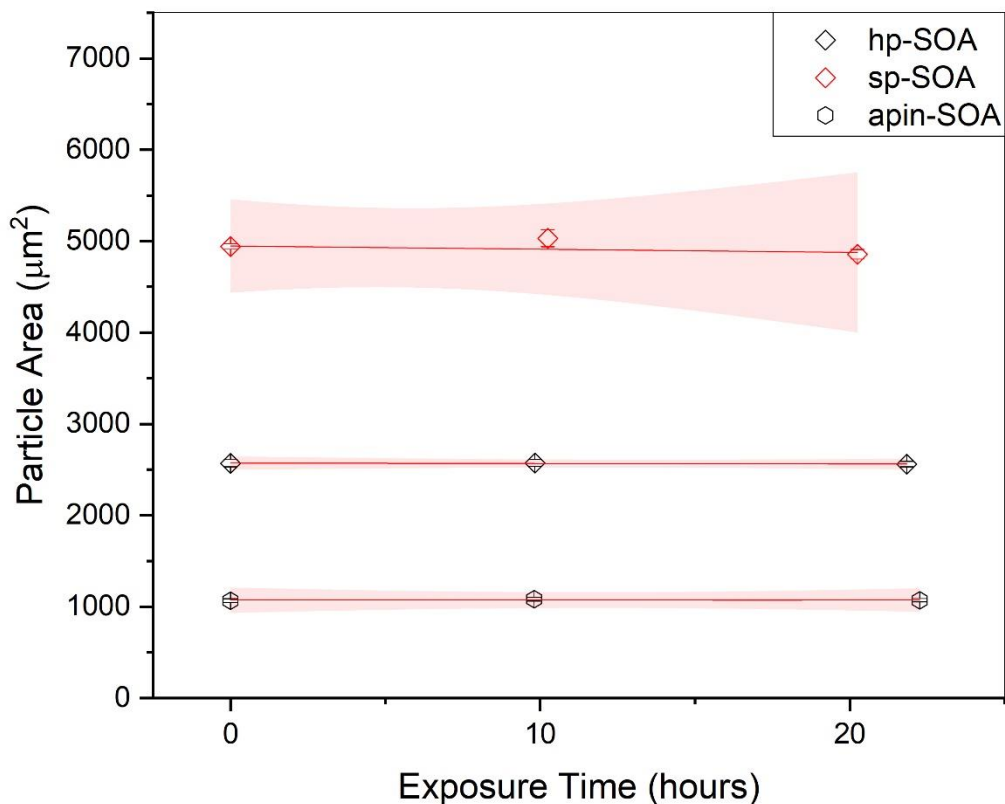
<sup>a</sup> As a conservative lower limit to the surface tension of the healthy plant SOA, we used the surface tension of liquid 3-carene. <sup>b</sup> 3-Carene has the lowest surface tension of all the VOCs used to model healthy plant emissions. Surface tension of liquid  $\alpha$ -pinene. Surface tensions were determined with the ACD/Labs Percepta Platform-PhysChem Module, retrieved from Chemspider July 12, 2019. <sup>b</sup> This upper limit is consistent with surface tension measurements of SOA at RH  $\leq$  65% RH and surface tensions reported for alcohols, organic acids, esters, and ketones, as well as surface tension measurements of water solutions containing SOA products. <sup>c</sup> Range based on measurements of the slip length of organic compounds and water on hydrophobic surfaces.<sup>226-238</sup> <sup>d</sup> The contact angle was determined by measuring the height and radii of individual droplets using a confocal microscope. Note: the simulated viscosities depend only weakly on the contact angle. Changing the contact angle by  $\pm 10\%$  changes the simulated viscosity on average by  $\pm 15\%$ , which is small compared to the overall uncertainties associated with the simulated viscosities. <sup>e</sup> As a conservative lower limit to the surface tension of the stressed plant SOA, we used the surface tension of liquid myrcene. Myrcene has the lowest surface tension of all the VOCs used to model stressed plant emissions. Surface tensions were determined with the ACD/Labs Percepta Platform-PhysChem Module, retrieved from Chemspider July 12, 2019.

Viscosity of the SOA were determined from  $\tau_{\text{exp, flow}}$  and fluid dynamics simulations, performed using the Microfluidics module within *COMSOL Multiphysics*.<sup>16,17</sup> The initial configuration in the simulations was half-torus geometry with dimensions consistent with

the dimensions in the experiment. The simulations required surface tension, slip length, density, and contact angle. Conservative upper and lower limits were used in the simulations, resulting in conservative upper and lower limits for the simulated viscosities. In the simulations, the material flowed and the hole in the half-torus geometry decreased to minimize the surface energy of the system, consistent with the experiments. From the simulations, we determined the time for the diameter of the hole in the half-torus geometry to decrease to  $\frac{1}{4}A$  referred to as  $\tau_{\text{model, flow}}$ . To determine viscosity from  $\tau_{\text{exp,flow}}$ , the viscosity in the simulations was adjusted until  $\tau_{\text{model, flow}}$  was within 1% of  $\tau_{\text{exp,flow}}$ .

For some conditions, for example at 0% RH, the poked particles did not visibly flow over the course of the observation (6 h for hp-SOA and 19 hours for sp-SOA). In these cases, lower limits to viscosity were obtained from the simulations by assuming the fluid flowed by  $\leq 0.5\mu\text{m}$  (the spatial resolution of the microscope) within the observation time in the experiments.

In the poke flow experiments, SOA “macroparticles” were exposed to flow of  $\text{N}_2$  gas for several hours (1.5-24 h). During this time, semivolatile compounds could potentially evaporate from the SOA, resulting in a change in composition and possibly in viscosity.<sup>82</sup> To determine if evaporation of semivolatile compounds was significant in the poke-flow experiments, new SOA samples were exposed to a dry ( $< 0.5\%$  RH) flow of  $\text{N}_2$  gas in the poke-flow apparatus for 24 h, while monitoring the cross-sectional area of the “macroparticles” (Figure 3.4).



**Figure 3.4** Particle area as a function of exposure time to dry (< 0.5% RH) nitrogen gas flow, shaded red regions indicates the 95% confidence bands. The lack of change suggests that particles are stable with respect to evaporation over the experimental time scale.

The flow rate of the dry N<sub>2</sub> gas was the same as the rate used for the measurements because this could affect the evaporation of the SOA particles. These tests showed that the area of the particles changed by less than 2%. Hence, evaporation of semivolatile compounds was regarded as a minor effect in our experiments, at least for dry conditions (< 0.5% RH). Even though semivolatile compounds did not evaporate under dry conditions, they could still have evaporated at higher RH values when the viscosity was lower and diffusion within the particles was faster.<sup>82,131,239,240</sup> The loss of semivolatile

compounds should lead to an increase in viscosity.<sup>82,130,131</sup> The fact that the viscosity did not significantly change using conditioning times ranging from 1.5 h to 24 h in the poke-flow experiments, even at 50% RH (Figure 3.3) suggests that any loss of semivolatile compounds in our experiment did not significantly affect the viscosity of the particles, even at the highest RH values used in our studies.

The mixing times for water in our hp-SOA and sp-SOA “macroparticles” were calculated using the fractional Stokes-Einstein equation at a given RH and temperature. Mixing times of water within SOA were determined for a 50  $\mu\text{m}$  particle at 293 K, which corresponds to the approximate size of particles and temperature at which experiments were performed for the hp-SOA and sp-SOA in this study. The fractional stokes-Einstein equation was used to determine diffusion coefficients for water as a function of RH and temperature<sup>208,209,241</sup>:

$$D_{H_2O}(RH, T) = D_0(T) * \left(\frac{\eta_0(T)}{\eta(RH, T)}\right)^\xi \quad (3.1)$$

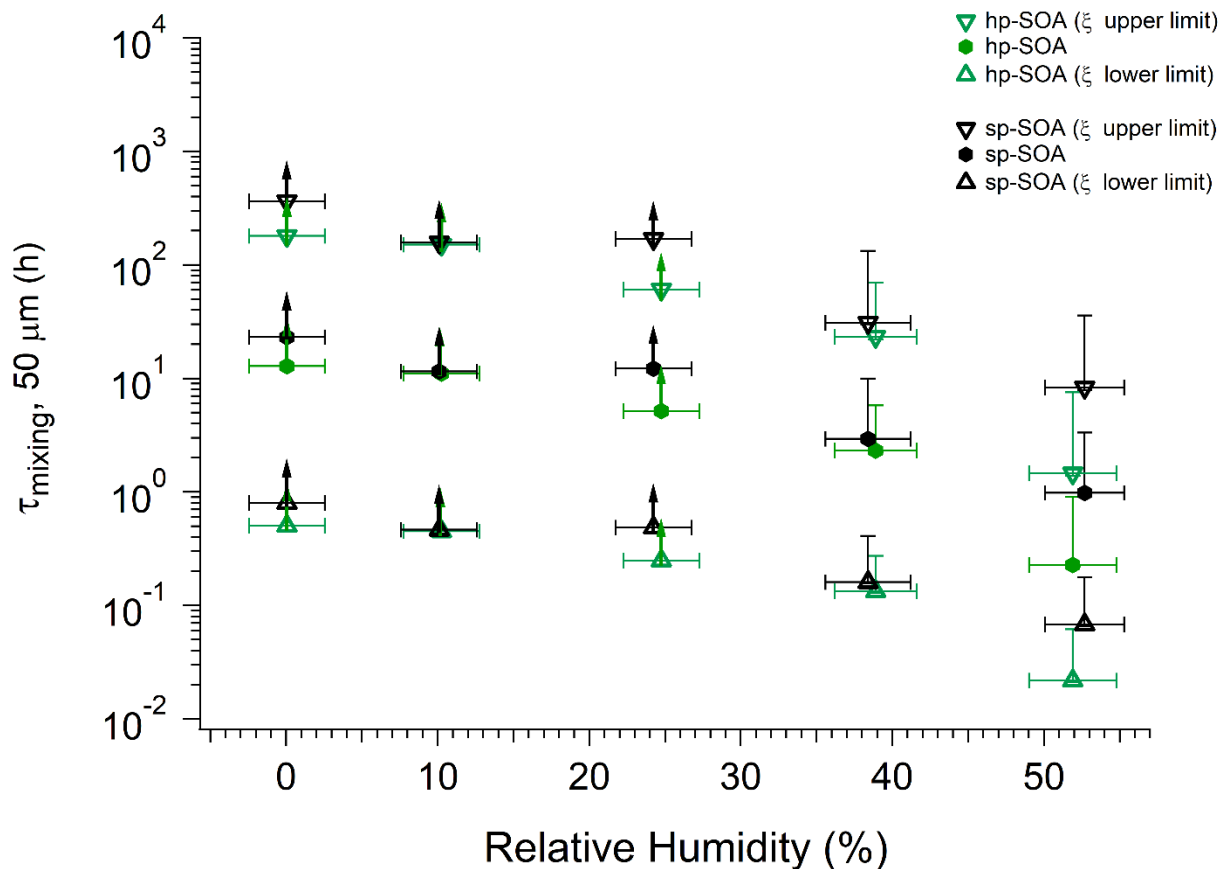
where  $D_{H_2O}(RH, T)$  is the RH and temperature dependent diffusion coefficient of water in SOA,  $D_0(T)$  is the temperature dependent diffusion coefficient of water in pure water (calculated using Equation. (3.3)),  $\xi$  is the fractional exponent,  $\eta_0(T)$  is the temperature-dependent viscosity of pure water at 293 K, and  $\eta(RH, T)$  is the calculated viscosity of the hp-SOA or sp-SOA at a specific RH and 293 K. The temperature-dependent viscosity data for pure water was taken from Hallett (1963) and Crittenden et al. (2012).<sup>168,242</sup>  $D_0(T)$  was evaluated using the Stokes-Einstein equation and assuming a radius for pure water of 0.1 nm<sup>209</sup>. The value of the fractional exponent was calculated using the equation below<sup>241</sup>:

$$\xi = 1 - \left[ A \exp\left(-B \frac{R_{diff}}{R_{matrix}}\right) \right] \quad (3.2)$$

where A and B are coefficients with values of  $0.73 \pm 0.12$  and  $1.79 \pm 0.29$ , respectively. To evaluate the fractional exponent, we assumed  $R_{\text{diff}} = 0.1$  nm and  $R_{\text{matrix}} = 0.4$  nm to be consistent with the size of organic molecules discussed above. The fractional Stokes-Einstein equation is able to predict 98 % of the published diffusion coefficients of small molecules, including water, within the uncertainties of the measurements for organic-water mixtures.<sup>241</sup> Once  $D_{\text{H}_2\text{O}}(\text{RH}, \text{T})$  was determined using the equations above, we then calculated mixing times of water within the SOA using an equation similar to Equation. (3.4) . The results of this calculation are shown in Figure 3.5.

For the hp-SOA and sp-SOA at  $\leq 25\%$  RH, we cannot be sure that equilibrium is established with the surrounding at 1.5 hours. Therefore, these particles may have had a higher water content than expected based on equilibrium with gas-phase water at  $\leq 25\%$  RH, and hence may have higher viscosity, consistent with the lower limit we report. At 40 and 50% RH, equilibrium established in 1.5 hours is within uncertainty of our calculations (Figure 3.5).





**Figure 3.5** Results from the poke-flow experiments for hp-SOA (green hexagons), sp-SOA (black hexagons) mixing times of water within a  $50 \mu\text{m}$  sized particle ( $\tau_{\text{mixing}, 50 \mu\text{m}}$ ). Error in the RH measurement was  $\pm 2.5\%$ . Upward arrows indicate lower limits. Vertical bars represent the calculated lower and upper limits of  $\tau_{\text{mixing}, 50 \mu\text{m}}$  (83% confidence interval) based on COMSOL simulations (see Table 3.2 for input parameters).  $\tau_{\text{mixing}, 50 \mu\text{m}}$  was also calculated using upper ( $A=0.61$ ,  $B=2.08$ ) and lower limits ( $A=0.85$ ,  $B=1.50$ ) for uncertainty in the fractional exponent ( $\xi$ ).

To investigate mixing times of organic molecules within the SOA by molecular diffusion, we first converted the measured viscosity into a diffusion coefficient ( $D$ ) using the Stokes-Einstein equation:

$$D = \frac{k_B T}{6\pi\eta r} \quad (3.3)$$

where  $k_B$  is the Boltzmann constant,  $T$  is temperature in Kelvin,  $\eta$  is the viscosity in Pa s, and  $r$  is the hydrodynamic radius. When calculating diffusion coefficients, we assumed a hydrodynamic radius of 0.38 nm for diffusing SOA molecules.<sup>244</sup>

Next  $D$  was converted into the characteristic mixing time within the particle using the following equation:

$$\tau_{mixing} = \frac{d_p^2}{4\pi^2 D} \quad (3.4)$$

For the purposes of this estimation, the particle diameter was set to  $d_p = 200$  nm, which is roughly the median diameter in the volume distribution of ambient SOA-containing particles.<sup>175–178</sup> For reference, accumulation mode particles typically range in diameters from 100 to 1000 nm.

### 3.2.6 Volatility predictions

The assigned molecular formulas from the HRMS data were used to determine the volatility distribution of compounds found within the hp-SOA and sp-SOA. The volatility was calculated based on parameterizations of pure compound saturation mass concentration ( $C_0$ ) by elemental composition reported in Li et al. (2016) for CHO compounds using equation (3.5),

$$\log_{10} C_0 = (n_C^0 - n_C) b_C - n_O b_O - 2 \frac{n_C n_O}{n_C + n_O} b_{CO} \quad (3.5)$$

where  $n_C^0$  is the reference carbon number, and  $n_C$  and  $n_O$  represent the number of carbon and oxygen atoms, respectively. The values for parameters  $n_C^0$ ,  $b_C$ ,  $b_O$ , and  $b_{CO}$  were 22.6, 0.4481, 1.656, and -0.779, respectively, as determined for reference CHO compounds in Li et al. (2016).<sup>210</sup>

### 3.2.7 Viscosity predictions

Viscosity were predicted using the method described by DeRieux et al. (2018).<sup>29</sup> Briefly, the glass transition temperature ( $T_{g,i}$ ), at which a phase transition between amorphous solid and semi-solid states occurs,<sup>28</sup> can be predicted as a function of molecular composition for a single compound:<sup>29</sup>

$$T_{g,i} = (n_C^0 + \ln(n_C)) b_C + \ln(n_H) b_H + \ln(n_C) \ln(n_H) b_{CH} + \ln(n_O) b_O + \ln(n_C) \ln(n_O) b_{CO} \quad (3.6)$$

$n_C$ ,  $n_H$ , and  $n_O$  are the number of carbon, hydrogen, and oxygen atoms, respectively. Values of the coefficients [ $n_C^0$ ,  $b_C$ ,  $b_H$ ,  $b_{CH}$ ,  $b_O$ , and  $b_{CO}$ ] are [12.13, 10.95, -41.82, 21.61, 118.96, -24.38] for CHO compounds.<sup>29</sup> The glass transition temperature of the SOA under dry conditions ( $T_{g,org}$ ) was estimated using the Gordon-Taylor equation, assuming the Gordon-Taylor constant ( $k_{GT}$ ) of 1 for each organic mixture component:<sup>206</sup>

$$T_{g,org} = \sum_i w_i T_{g,i} \quad (3.7)$$

where  $w_i$  is the mass fraction of an organic compound  $i$ .<sup>206</sup> We estimated  $w_i$  using two different methods. In the first method  $w_i$  values were assumed to be proportional to the observed peak abundances in the mass spectra. In the second method the relative abundance of each compound [ $A_i$ ] was converted from the peak abundance ( $I_i$ ) considering the effect of molecular weight ( $M_i$ ) and the degree of unsaturation (represented by the  $[H/C]_i$  ratio) on ionization efficiency following the method in Nguyen et al. (2013):<sup>245</sup>

$$[A_i] = \frac{I_i}{(H/C)_i \times M_i} \quad (3.8)$$

where  $(H/C)_i \times M_i$  is known as adjusted mass (AM).<sup>245</sup> Note that we assumed the effective limit of detection (LOD) used in Nguyen et al. (2013) to be zero. This is a reasonable approximation based on the results in Nguyen et al. (2013) that LOD decreased quickly at high AM. In our study more than 90% of the detected compounds have an AM value higher than 200 Da, resulting in a small LOD.

Under humid conditions, the water content in SOA was estimated using the effective hygroscopicity parameter ( $\kappa$ ).<sup>246</sup> The  $\kappa$  values derived from cloud condensation nuclei measurements by Zhao et al. (2017)<sup>203</sup> of 0.15 and 0.07 were used for hp-SOA and sp-SOA, respectively. This was based on the assumption that hp-SOA were formed from monoterpene-dominated emissions and sp-SOA were formed from sesquiterpene-dominated emissions, with a high proportion of farnesenes and bisabolene, which is consistent with the synthetic profiles studied in this work.<sup>203</sup> These  $\kappa$  values are likely upper limits for these types of SOA. The true water content at 50% RH may be lower but likely will still follow the same trend as reported here.  $T_g$  of organic-water mixtures ( $T_{g,mix}$ ) was then calculated by the Gordon-Taylor equation using a Gordon-Taylor constant ( $k_{GT}$ ) of 2.5:<sup>28,155</sup>

$$T_{g,mix} = \frac{(1-w_{org})T_{g,H_2O} + \frac{1}{k_{GT}}w_{org}T_{g,org}}{(1-w_{org}) + \frac{1}{k_{GT}}w_{org}} \quad (3.9)$$

Where  $T_{g,H_2O}$  and  $T_{g,org}$  are the glass transition temperatures of water and SOA organics, and  $w_{org}$  is the mass fraction of the organic compounds in the particle. The mass concentration of water ( $m_{H_2O}$ ) and SOA ( $m_{SOA}$ ) can be used to estimate  $w_{org}$  as  $w_{org} =$

$m_{SOA}/(m_{SOA} + m_{H2O})$ , and  $m_{H2O}$  can be estimated using the effective hygroscopicity factor ( $\kappa$ ):<sup>246</sup>

$$m_{H2O} = \frac{\kappa \rho_w m_{SOA}}{\rho_{SOA} \left( \frac{1}{a_w} - 1 \right)} \quad (3.10)$$

where the density of water ( $\rho_w$ ) is  $1 \text{ g cm}^{-3}$ , the density of SOA particles ( $\rho_{SOA}$ ) is assumed to be  $1.4 \text{ g cm}^{-3}$ , and  $a_w$  is the water activity calculated as  $a_w = RH/100$ .<sup>247</sup>

Using the calculated  $T_{g,mix}$ , the temperature-dependence of viscosity was calculated applying the Vogel-Tammann-Fulcher (VTF) equation:

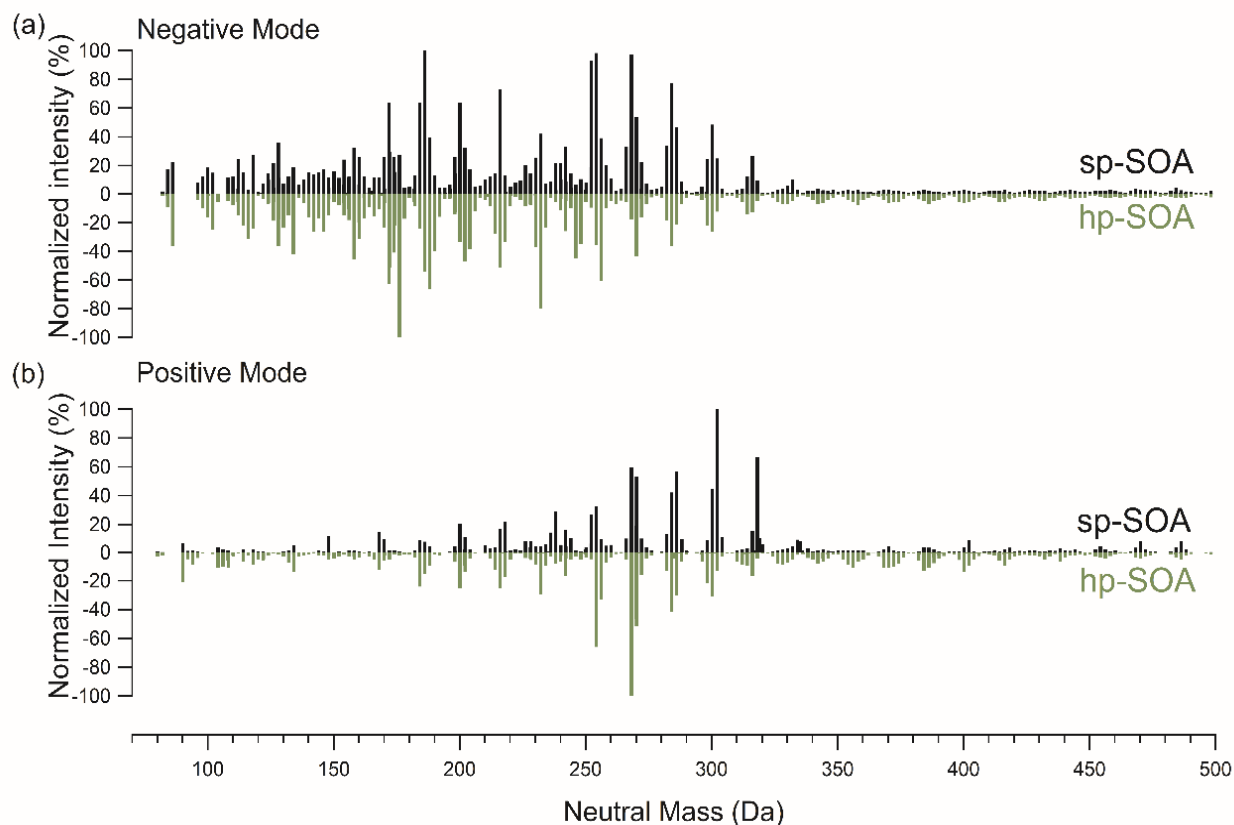
$$\log(\eta) = -5 + 0.434 \frac{T_0 D_f}{T - T_0} \quad (3.11)$$

Where  $T_0$  is the Vogel temperature calculated as  $T_0 = \frac{39.17 T_g}{D_f + 39.17}$ , which is deduced from an assumed viscosity of  $10^{12} \text{ Pa s}$  at the glass transition temperature,<sup>161</sup> and  $T$  is the temperature at which the viscosity measurements were conducted (291 K). The fragility parameter ( $D_f$ ), which characterizes deviation of the temperature dependence of viscosity from the Arrhenius behavior<sup>29,160</sup> was assumed to be 10 based on our previous study.<sup>29</sup> The viscosity was predicted assuming one phase, despite the LLPS observations at higher RH as we do not know composition in the different phases.

### 3.3 Results and Discussion

#### 3.3.1 Molecular composition of SOA particles

The high-resolution mass spectra obtained for the hp-SOA and sp-SOA in positive and negative modes are shown in Figure 3.6. While the mass spectra indicate similar features, the mass spectrum of the sp-SOA has a larger summed peak abundance for species with molecular weight (MW) above 250 Da (43% for negative mode and 73% for positive mode) than that of the hp-SOA (37% for negative mode and 69% for positive mode). We define high molecular mass as >250 Da because this usually designates a transition region between monomers and dimers products in monoterpene SOA.<sup>248,131</sup> This difference between the two mass spectra is expected because the stressed plant VOC mixture contained more sesquiterpene species compared to the



**Figure 3.6** Nano-DESI mass spectra in a) negative mode and b) positive mode for healthy (green) and stressed (black) plant SOA as a function of the molecular weight of the detected neutral compound.

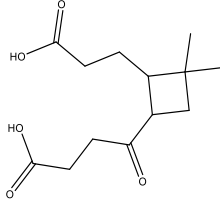
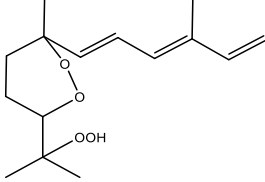
healthy plant VOC mixture. The average O:C ratios (average  $\pm$  1SD) calculated from the high-

resolution mass spectrometry data of the hp-SOA and sp-SOA were  $0.51 \pm 0.20$  and  $0.41 \pm 0.18$ , respectively. The H:C ratios were  $1.52 \pm 0.19$  and  $1.52 \pm 0.18$  for the hp-SOA and sp-SOA, respectively. The lower value of O:C in the sp-SOA means that the compounds are on average less oxidized and supports our choice of lower  $\kappa$  to model hygroscopicity of sp-SOA. The most abundant peak in the negative mode mass spectrum for sp-SOA corresponded to  $C_9H_{14}O_4$ , whereas in the hp-SOA the largest peak was  $C_7H_{12}O_5$ . The top 4 peaks in each ionization mode and their reported formulas, names, and plausible structures based on previous studies are listed in Table 3.3. It should be noted the exact m/z reported in Table 3.3 represent various isomers for each sum formula and the exact dominant structures corresponding to each peak have not been confirmed. These compounds include previously reported photooxidation products for both monoterpenes and sesquiterpenes.<sup>65,249–251</sup>

**Table 3.3** The most abundant formulas detected by nano-DESI-HRMS. All of these compounds appear in both (+) and (-) ESI modes; the second column lists the ionization mode in which they have higher relative peak abundance. References for previously reported structures identified as a monoterpene oxidation product (MTOX) or sesquiterpene oxidation product (SQTOX) that have the same neutral molecular formula and mass as those found in this study are listed in the last column.

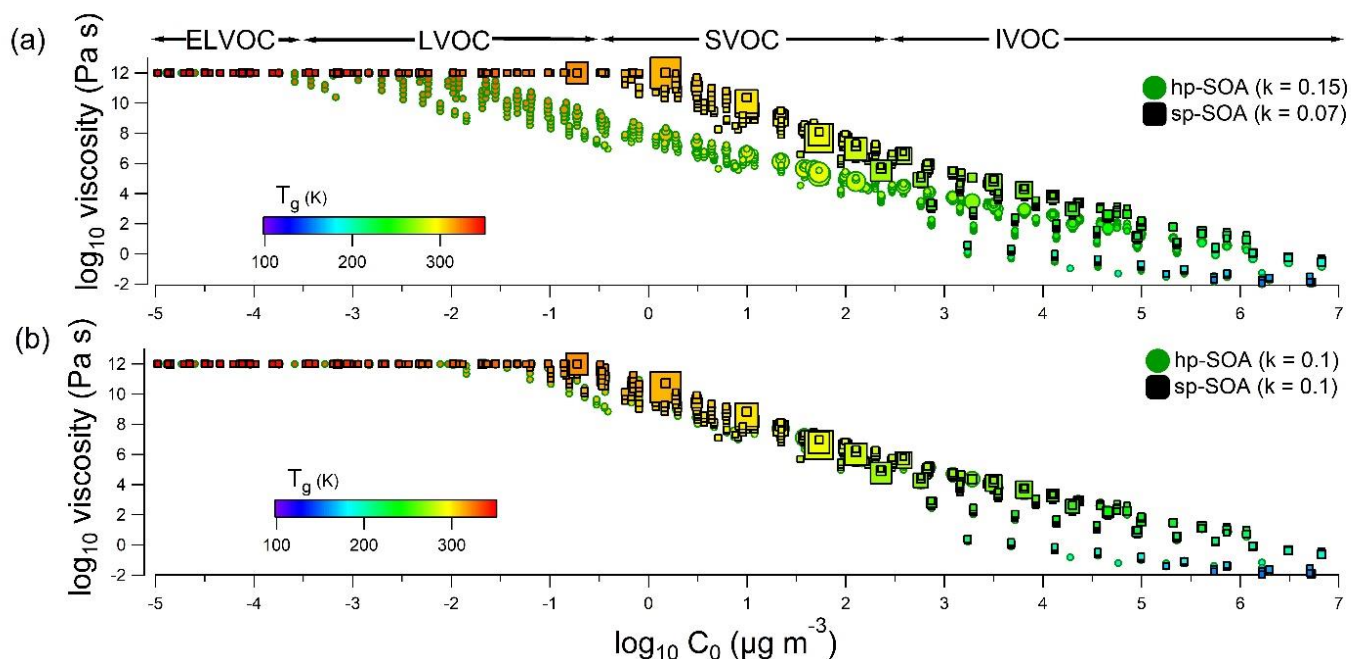
Neutral Mass (Da)	Prominent Ionization Mode (-/+ ) and sample	Neutral molecular Formula	Name	Previously Reported Structures <sup>a</sup>	References
176.07	(-) hp-SOA	C <sub>7</sub> H <sub>12</sub> O <sub>5</sub>	3-hydroxy-2,2-dimethyl glutaric acid		MTOX (Haddad et al 2011) <sup>249</sup>
186.09	(-) sp-SOA	C <sub>9</sub> H <sub>14</sub> O <sub>4</sub>	Pinic acid limonic acid		MTOX (Yee et al 2018) <sup>65</sup> (Jaoui et al 2006) <sup>250</sup> (Fang et al 2017) <sup>251</sup>
188.07	(-) hp-SOA	C <sub>8</sub> H <sub>12</sub> O <sub>5</sub>	Ketolimonic acid		MTOX (Jaoui et al 2006) <sup>250</sup>
232.09	(-) hp-SOA	C <sub>10</sub> H <sub>16</sub> O <sub>6</sub>	Diaterpenylic acid acetate		MTOX (Yee et al 2018) <sup>65</sup>
252.17	(-) sp-SOA	C <sub>15</sub> H <sub>24</sub> O <sub>3</sub>	β-caryophyllonic acid		SQTOX (Yee et al 2018) <sup>65</sup>
254.15	(-) sp-SOA (+) hp-SOA	C <sub>14</sub> H <sub>22</sub> O <sub>4</sub>	β-caryophyllinic acid		SQTOX (Yee et al 2018) <sup>65</sup>



256.13	(+/-) hp-SOA	C <sub>13</sub> H <sub>20</sub> O <sub>5</sub>	β-nocaryophyllinic acid		SQTOX (Yee et al 2018) <sup>65</sup>
268.17	(+/-) sp-SOA (+) hp-SOA	C <sub>15</sub> H <sub>24</sub> O <sub>4</sub>	----- (Conjugated triene hydroperoxide)		SQTOX (Jaoui et al 2016) <sup>252</sup>
302.17	(+) sp-SOA	C <sub>15</sub> H <sub>26</sub> O <sub>6</sub>	-----		
318.17	(+) sp-SOA	C <sub>15</sub> H <sub>26</sub> O <sub>7</sub>	-----		

<sup>a</sup> Tentatively assigned structures as MS/MS has not been performed.

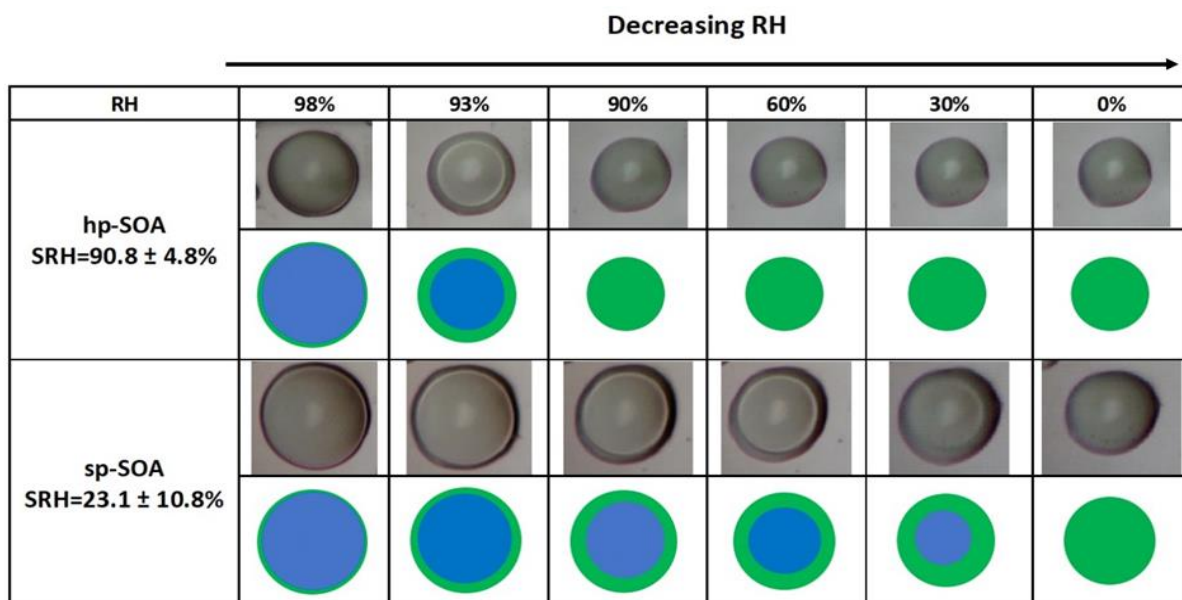
The total organic mass concentration for each system was approximately  $200 \mu\text{g m}^{-3}$  and there were several molecules with predicted volatilities in excess of that value, as seen in the Intermediate Volatility Organic (IVOC;  $300 < C_0 < 3 \times 10^6 \mu\text{g m}^{-3}$ ) region in Figure 3.7. The abundance of these low molecular weight, intermediate volatility molecules, particularly in the negative ion mode mass spectra, is surprising because they should be too volatile to partition into the condensed phase and contribute significantly to the particle mass under our experimental conditions. There are several possible explanations for the presence of these higher volatility species. First, although ESI-based methods are typically regarded as “soft”, some in-source fragmentation may be occurring. Second, it is possible that these volatile species could be physically entrapped in the particles during the particle growth phase. For example, Vander Wall et al. (2019) identified a burying mechanism in which semivolatile compounds became trapped in viscous SOA, preventing them from escaping back into the gas phase.<sup>253</sup> Third, these compounds could be formed after the particles are collected by spontaneous decomposition of larger organic compounds such as peroxides,<sup>254,255</sup> with the decomposition products still remaining in the particles due to the high viscosity. At this time, we cannot rule out any of these explanations.



**Figure 3.7** (a) viscosity of individual SOA compounds at 50% RH and 291 K as a function of  $C_0$  in healthy ( $\kappa = 0.15$ ) and stressed ( $\kappa = 0.07$ ) plant SOA. (b) Viscosity of individual SOA compounds at 50% RH and 291 K as a function of  $C_0$  with  $\kappa = 0.1$  applied to both healthy and stressed plant SOA. In each panel, the warmer the color, the higher the glass transition temperature. The larger the circle or square marker size, the larger the relative abundance of the species based on the HRMS analysis.

### 3.3.2 LLPS

LLPS occurred in both the healthy and stressed plant SOA samples as shown in Figure 3.8. The light-colored circle in the center of the particle is an optical effect of light scattering from a hemispherical uniform particle.<sup>256</sup> For the hp-SOA, the particle was phase separated at 98% RH. As the relative humidity decreased, the inner aqueous-rich phase



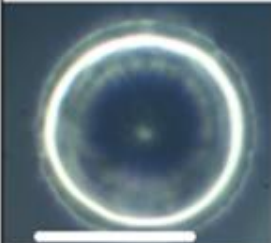

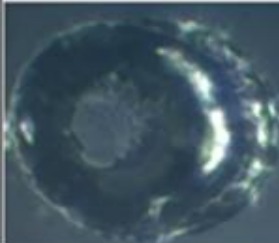
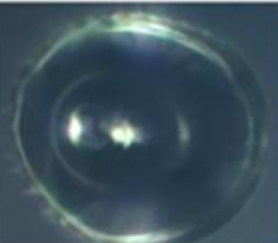
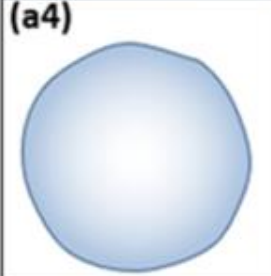
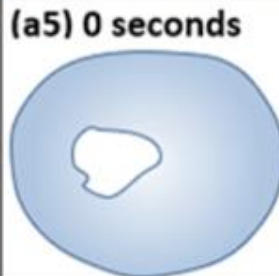
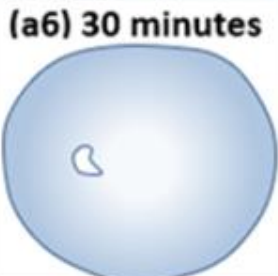
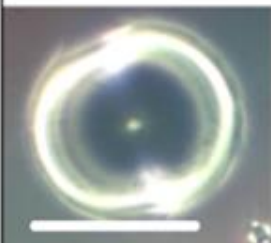
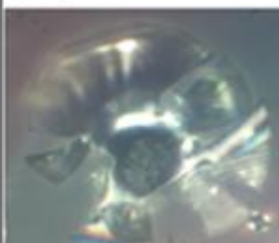
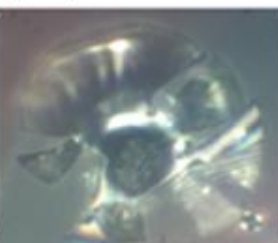
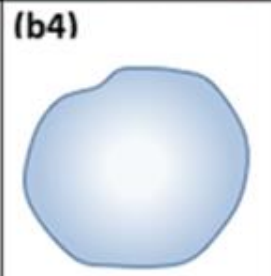
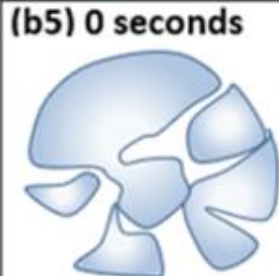

**Figure 3.8** Optical images and illustrations of stressed and healthy plant SOA particles taken while decreasing relative humidity. The green represents the organic-rich phase and blue represents the aqueous-rich phase. The relative error of the SRH was obtained by using twice the standard deviation from the four measurement results plus an uncertainty of the hydrometer (~2.5%). The diameter of the particles was between 50-80  $\mu\text{m}$ .

started to shrink until it reached a critical RH, called the separation relative humidity (SRH), at  $91 \pm 5\%$  RH where LLPS completely disappeared. Upon further RH reduction, only a single organic-rich phase remained. The sp-SOA particle exhibited phase separation over a broader humidity range than the hp-SOA, with LLPS persisting down to  $23 \pm 11\%$  RH.



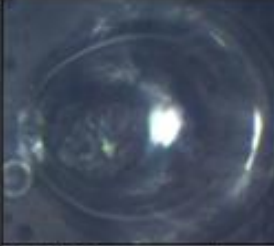

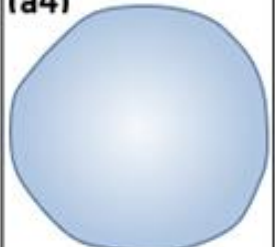

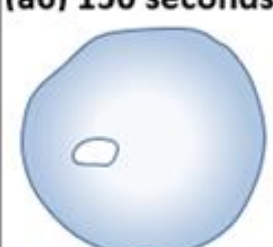
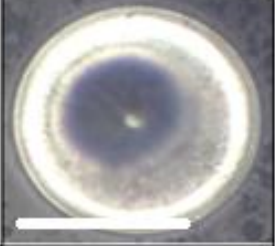
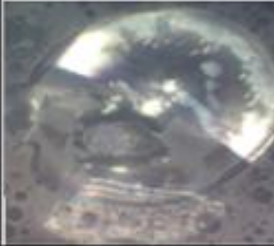
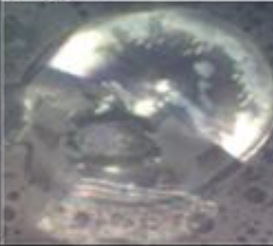
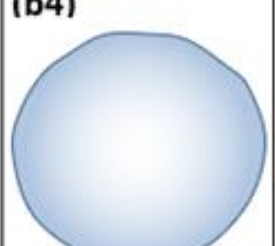
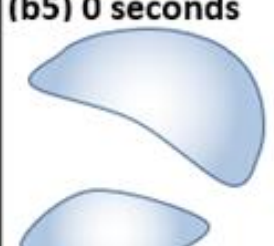
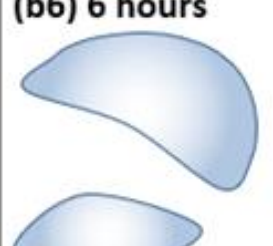
Several previous studies have investigated LLPS in SOA from the ozonolysis of single biogenic VOC precursors. In these cases LLPS was observed only at RH values above 90% RH.<sup>212–214</sup> The existence of LLPS in a purely organic SOA particle below 90% RH has only been observed previously for SOA generated by the photooxidation of diesel fuel vapors.<sup>51</sup> The presence of LLPS down to as low as 20% RH for sp-SOA, suggests that LLPS could be more common in organic SOA systems than previously thought.

### 3.3.3 Experimental viscosity and mixing

Figures 3.9 and 3.10 show images of particles during the poke flow experiments for sp-SOA and hp-SOA, respectively. At 50% RH the holes formed by the needle closed on a time scale of 100–5000 s. In contrast, the “macroparticles” shattered under dry conditions and the particle fragments remained largely unchanged on a timescale of the experiment. The experimental flow time ( $\tau_{\text{exp, flow}}$ ) of hp-SOA, sp-SOA, and  $\alpha$ -pinene SOA are shown in Figure 3.11a. At RH  $\leq$  10%,  $\tau_{\text{exp, flow}}$  was  $\geq 10^4$  seconds for all three SOA. At RH = 25%,  $\tau_{\text{exp, flow}}$  was  $\geq 10^4$  seconds for hp-SOA and sp-SOA, but  $1\text{--}6 \times 10^3$  s for  $\alpha$ -pinene SOA. As RH increased the  $\tau_{\text{exp, flow}}$  decreased, leading to lower viscosity at higher RH. Over the RHs investigated, the  $\tau_{\text{exp, flow}}$  values had the following order: sp-SOA > hp-SOA >  $\alpha$ -pinene SOA. This order suggests that stressed plant SOA had the highest viscosity, followed by healthy plant SOA and then  $\alpha$ -pinene SOA in descending order. We attribute this difference, at least in part, to the relative temperatures and lower hygroscopicity. Figure 3.11b shows viscosity values calculated

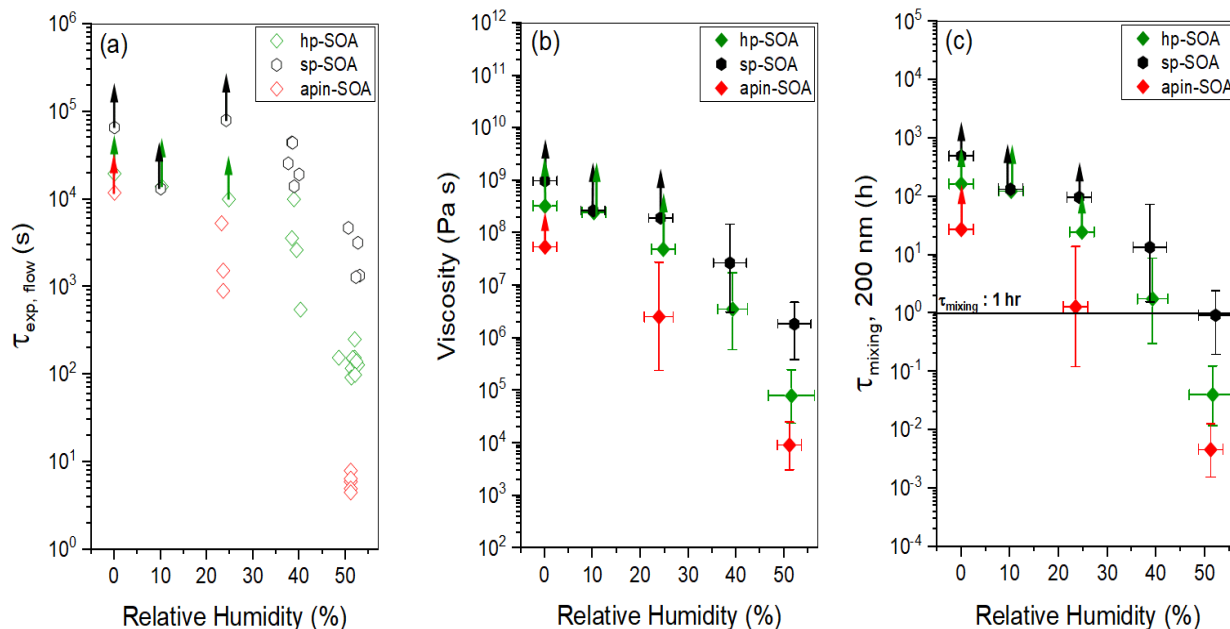
Relative humidity	Pre-poking	Poking	First frame post-poking	Post-poking
(a) 50%	(a1) 		(a2) 0 seconds 	(a3) 30 minutes 
	(a4) 		(a5) 0 seconds 	(a6) 30 minutes 
(b) 0%	(b1) 		(b2) 0 seconds 	(b3) 19 hours 
	(b4) 		(b5) 0 seconds 	(b6) 19 hours 

**Figure 3.9** Optical images of SOA particles produced from photooxidation with VOCs from stressed trees during a poke-flow experiment at a) 50%, and b) 0% RH. Images a1), and b1) are pre-poking images. a4), and b4) are demonstrative diagrams of pre-poking. a2), and b2) are the first frame post-poking. a5), and b5) are demonstrative diagrams of the first frame post-poking. a3), and b3) are the post-poking images. a6), and b6) are demonstrative diagrams of post-poking. The white scale bars correspond to 50  $\mu\text{m}$ .

Relative humidity	Pre-poking	Poking	First frame post-poking	Post-Poking
(a) 50%	(a1) 		(a2) 0 seconds 	(a3) 150 seconds 
	(a4) 		(a5) 0 seconds 	(a6) 150 seconds 
(b) 0%	(b1) 		(b2) 0 seconds 	(b3) 6 hours 
	(b4) 		(b5) 0 seconds 	(b6) 6 hours 

**Figure 3.10** Optical images of SOA particles produced from photooxidation of VOCs from healthy trees during a poke-flow experiment at a) 50%, and b) 0% RH. Images a1) and b1) are pre-poking images. a4) and b4) are demonstrative diagrams of pre-poking. a2) and b2) are the first frame post-poking. a5) and b5) are demonstrative diagrams of the first frame post-poking. a3) and b3) are the post-poking images at 150 s and 6 hrs. a6) and b6) are demonstrative diagrams of post-poking at 150 s and 6 h. The white scale bars correspond to 50  $\mu$ m.



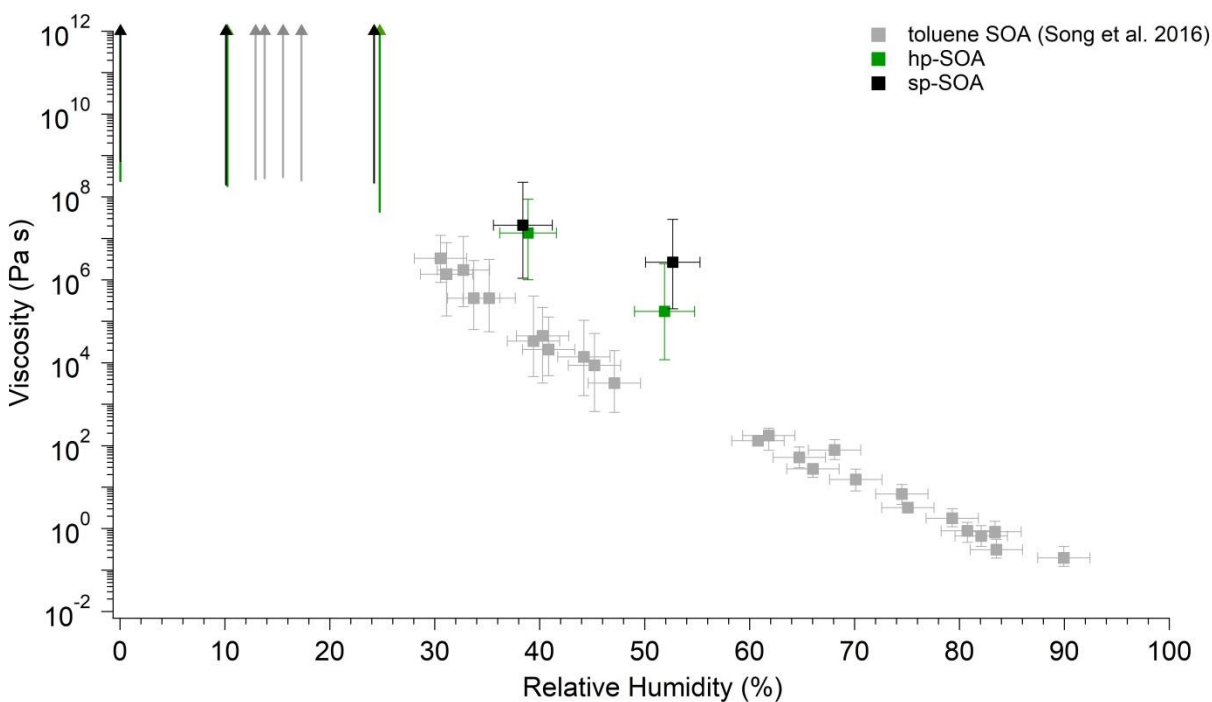


**Figure 3.11** Results from the poke-flow experiments for hp-SOA (green diamonds), sp-SOA (black hexagons), and apin-SOA (red diamonds): (a) experimental flow time,  $\tau_{\text{exp, flow}}$ ; (b) viscosity; (c) mixing times of organic molecules within a 200 nm sized particle ( $\tau_{\text{mixing, 200 nm}}$ ). In panel (a) error in the RH measurement was  $\pm 2.5\%$ . In panel (c), horizontal  $\tau_{\text{mixing}}$  bars correspond to the 1 h mixing band, which is roughly the mixing time assumed in chemical transport models. Upward arrows indicate lower limits. Vertical bars represent the calculated lower and upper limits of viscosity and  $\tau_{\text{mixing, 200 nm}}$  (83% confidence interval) based on COMSOL simulations (see Table 3.2 for input parameters).

(for reference the viscosity of tar pitch is similar to  $10^8$  Pa s). At  $\text{RH} > 25\%$ , the viscosity decreases as the RH increased. This decrease is expected because the viscosity of water is much less than the viscosity of the condensed organic material and as RH increases the water content of SOA also increases. At 40 and 50% RH the sp-SOA contain two phases: an aqueous-rich and organic-rich phase. When calculating the viscosity of these particles we did not take into account the presence of two phases in the particles. Hence, the measured viscosity is due to a combination of both phases. The aqueous-rich phase likely has a lower viscosity than the measured viscosity due to the plasticizing effect of water, and conversely the organic-rich phase likely has a higher viscosity than the measured viscosity. At 50% RH the viscosity of hp-SOA and sp-SOA was  $\geq 10^4$  Pa s (for reference, the viscosity of peanut butter is roughly  $10^3$  Pa s). This high viscosity at



50% RH can be explained, in part, by the low hygroscopicity of the SOA samples generated from sesquiterpenes. For example, Varutbangkul et al. (2006) reported the growth factor of only  $\sim 1.01$  for sesquiterpene high- $\text{NO}_x$  SOA at 50% RH,<sup>257</sup> resulting in a volume fraction of water of only a few percent, probably insufficient for making the SOA material softer. For comparison, the viscosity values of the hp-SOA and sp-SOA are higher than toluene SOA (anthropogenic SOA proxy) at 40% and 50% RH (Figure 3.12). At 0% RH, the viscosity of  $\alpha$ -pinene SOA, hp-SOA, and sp-SOA was in all cases in excess of  $10^8$  Pa s – lower limit afforded by the measurement uncertainty. However, at 40% and 50% RH, sp-SOA had the highest viscosity, followed by hp-SOA and then  $\alpha$ -pinene SOA in descending order. The elevated viscosity observed in the plant SOA over  $\alpha$ -pinene SOA is likely due to the influence of the sesquiterpenes on the MW of the



**Figure 3.12** Experimentally determined viscosity of toluene photooxidation SOA reproduced from Song et al. (2016) compared to healthy and stressed photooxidation SOA over various relative humidities determined by the poke-flow method. Vertical bars represent the calculated lower and upper limits of viscosity using the COMSOL simulations (see Table 3.2 for input parameters). Horizontal bars represent the uncertainty in the relative humidity measurement. The upward arrows indicate lower limits of viscosity.

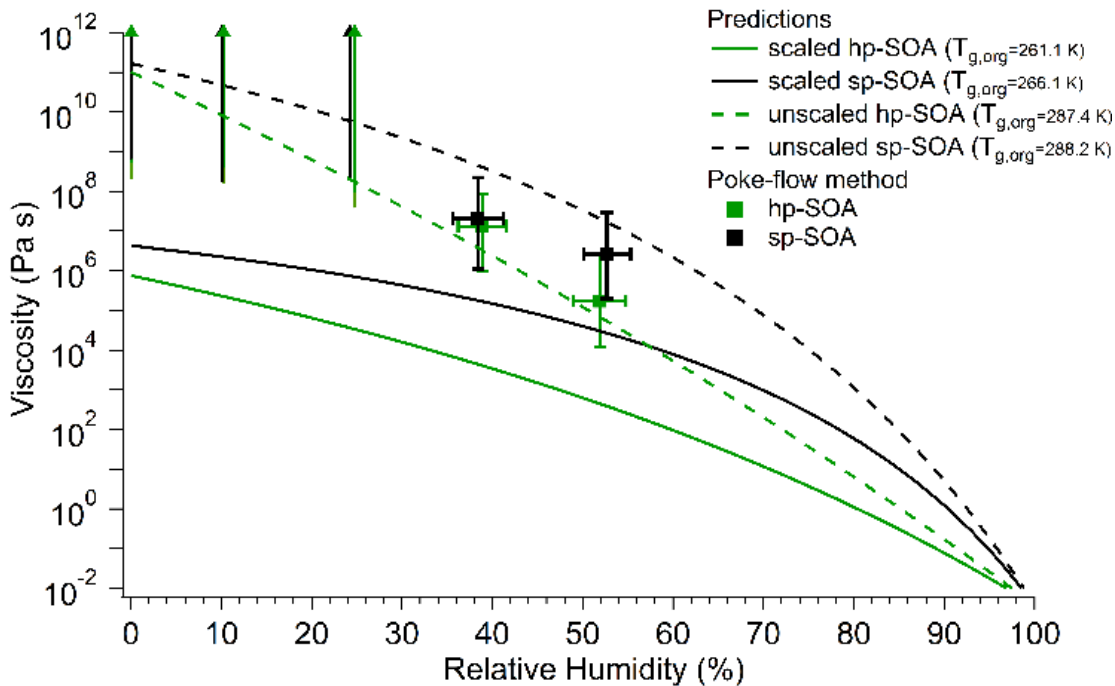
SOA products. The results from this study are consistent with previous studies of rebound of SOA particles generated from Scots pine tree emissions.<sup>258</sup>

Current chemical transport models assume mixing times of organic molecules by molecular diffusion within SOA is less than 1 h, meaning they are well mixed. Mixing times calculated from diffusion based on the viscosity measurements and the Stokes-Einstein equation are shown in Figure 3.11c. From the mixing times inferred from the experiments for hp-SOA and sp-SOA, it was found that samples at 0-25% RH had mixing times greater than 10 h, suggesting strong diffusive limitations for condensed-phase transport of particle components. At 40% RH, the median mixing times were still >10 h and 1 h for sp-SOA hp-SOA, respectively. The hp-SOA samples were observed to have mixing times of < 1 h at 50% RH, meaning they can be regarded as well mixed. The mixing times for  $\alpha$ -pinene photooxidation SOA had lower mixing time compared to hp-SOA or sp-SOA. Our results indicate that particles produced from realistic mixtures of VOCs have longer mixing time scales in comparison to the 1 h well-mixed assumption at <40% RH. The well-mixed assumption for biogenic SOA, produced under healthy and stressed conditions, is therefore incorrect below 40% RH.

### 3.3.4 Viscosity predictions

The viscosity predictions for the hp-SOA and sp-SOA are shown in Figure 3.13 along with the experimental viscosity values determined *via* poke-flow method. The predicted viscosity values were calculated using relative peak abundances in a combined mass spectrum that included compounds observed in both positive and negative ion modes. Specifically, peak abundances were normalized to 1 in both positive and negative mass spectra, and the relative peak abundances for the same formula were from the two

ionization modes we added. The predictions were done after scaling the peak abundances by the adjusted mass based on Eq. 3.3, as well as with unscaled peak abundances similar to our previous studies.<sup>29,51</sup> Figure 3.13 shows that the predicted viscosity values from unscaled peak abundances are approximately two orders of magnitude higher than the predictions for the scaled intensities at ~50% RH, confirming the expectation that predicted viscosities depend strongly on the assumed relative abundance of detected compounds. The experimentally determined viscosities correlate better with the prediction from the unscaled peak abundances. In theory, the mass scaled approach should correlate better with the experimentally determined viscosities because the ionization efficiency for electrospray is greater for higher molecular weight species, which could lead to an



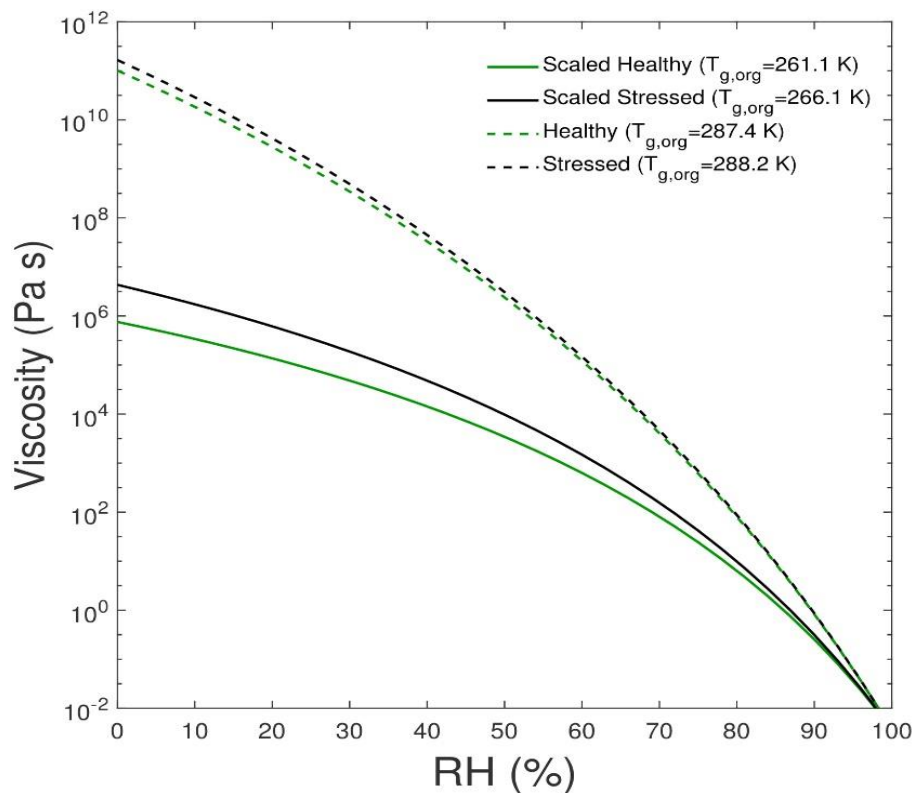
**Figure 3.13** Predicted viscosity as a function of RH compared to the experimental values determined by the poke-flow method. Vertical bars represent the calculated lower and upper limits of viscosity using the COMSOL simulations (see Table 3.2 for input parameters). Horizontal bars represent the uncertainty in the relative humidity measurement. The upward arrows indicate lower limits of the viscosity. Predicted viscosities were calculated for healthy and stressed plant SOA using either scaled (solid lines) or unscaled (dashed lines) peak abundances in the mass spectra that combined both positive and negative ion mode peaks.

overestimation of SOA viscosity determined from molecular formula assignments.<sup>189</sup> However, possible in-source fragmentation (see molecular composition of SOA section) could balance out this effect leading to the unscaled approach correlating with the data better.

Regardless of the peak abundance scaling method, the sp-SOA is predicted to have higher viscosity than the hp-SOA. The predicted  $T_{g,org}$  values are higher for the sp-SOA, resulting in differences in viscosities of a factor of 2-10 for the predicted viscosity under dry conditions (Figure 3.13). The difference between the viscosity predictions of hp-SOA and sp-SOA becomes larger around 50% RH which we suspected was due to the higher assumed hygroscopicity parameter used for the hp-SOA. To test this hypothesis, a sensitivity test was done to investigate the impact the assumed hygroscopicity parameter has on the predicted viscosity. Figure 3.7a shows the viscosity values that individual SOA compounds would have at 50% RH and 291 K, calculated with  $\kappa = 0.15$  for the healthy and  $\kappa = 0.07$  for the stressed plant SOA. Shown in Figure 3.7b are the predicted viscosities at 50% RH assuming the same hygroscopicity parameter ( $\kappa = 0.1$ ) for both hp-SOA and sp-SOA. A comparison of Figure 3.7a and 3.7b indicates the viscosity prediction is dependent on the hygroscopicity parameter used and is the main factor controlling the increased difference in the predicted viscosity between hp-SOA and sp-SOA as RH increases. Figure 3.14 shows the predicted viscosity for both data sets assuming  $\kappa = 0.1$ . Compared to the predictions shown in Figure 3.13, Figure 3.14 shows a smaller difference in overall particle viscosity (approximately an order of magnitude) between the two data sets over all RHs instead of several orders of magnitude as shown in Figure 3.13. The overall predicted particle viscosity at >50% RH was larger for hp-SOA when  $\kappa = 0.1$

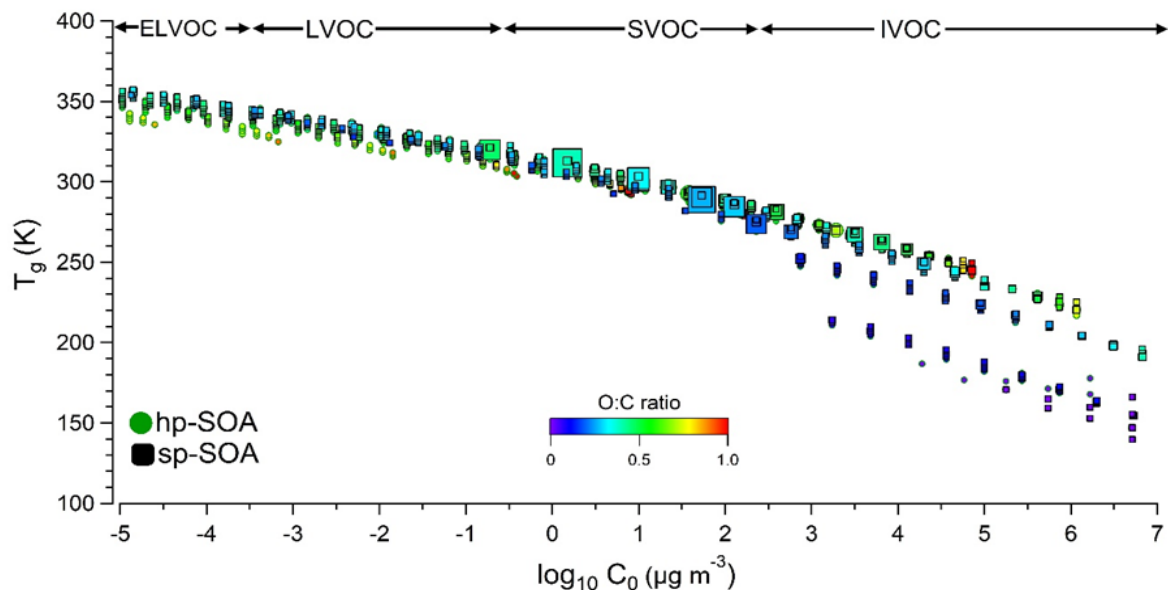
compared to when  $\kappa = 0.15$  and was lower for sp-SOA when  $\kappa = 0.1$  compared to when  $\kappa = 0.07$ . We suggest that hygroscopicity of SOA produced by mixtures should be explicitly measured to minimize this source of uncertainty in the viscosity predictions. We also should note that factors other than hygroscopicity could play a role in controlling the predicted viscosity values. The predictions are also sensitive to the fragility parameter  $D_f$ , which is assumed to be the same for hp-SOA and sp-SOA in the absence of more reliable information. Future work should focus on explicit measurements of  $D_f$  for realistic SOA models.

To gain additional insight into the factors controlling the SOA viscosity, Figure 3.15 shows predicted  $T_{g,org}$  and viscosity for individual SOA compounds in the hp-SOA and sp-SOA samples under dry conditions, plotted as a function of compound-specific saturation mass concentration ( $C_0$ ) calculated from Eq. 3. Figure 6 shows the regions representing extremely low volatility organic compounds (ELVOC;  $C_0 < 3 \times 10^{-4} \mu\text{g m}^{-3}$ ), low-volatility organic compounds (LVOC;  $3 \times 10^{-4} < C_0 < 0.3 \mu\text{g m}^{-3}$ ), semivolatile organic compounds (SVOC;  $0.3 < C_0 < 300 \mu\text{g m}^{-3}$ ), and intermediate volatility organic compounds (IVOC;  $300 < C_0 < 3 \times 10^6 \mu\text{g m}^{-3}$ ).<sup>47</sup> Because smaller MW compounds are more volatile<sup>259</sup> and less viscous,<sup>260,261</sup>  $T_{g,org}$  steadily decreases as  $C_0$  increases. The  $T_{g,org}$  values for the observed healthy and stressed compounds are similar under dry conditions. However, there are individual species identified within the SVOC regime that are larger in abundance in the sp-SOA. The larger abundance of lower volatility species in the sp-SOA with large  $T_{g,org}$  values could drive the difference in particle viscosity between the sp-SOA and hp-SOA. The results of this work indicated the addition of SOA products from sesquiterpenes



**Figure 3.14** Predicted viscosity as a function of RH using  $\kappa = 0.1$  calculated for both healthy and stressed plant SOA using either scaled (solid lines) or unscaled (dashed lines) peak abundances in the mass spectra that combined both positive and negative ion mode peaks.

generally increases SOA particle viscosity. This work also revealed that physicochemical properties of SOA produced from realistic mixtures of biogenic VOCs cannot always be accurately modeled by SOA formed from a single VOC.



**Figure 3.15** Glass transition temperature ( $T_g$ ) of hp-SOA and sp-SOA under dry conditions as a function of saturation mass concentration of individual compounds ( $C_0$ ).  $T_g$  is predicted according to DeRieux et al., (2018) and  $C_0$  is estimated according to Li et al., 2016. The warmer is the color, the higher is the O/C ratio. The larger the circle or square marker size, the larger the relative abundance of the species based on the HRMS analysis.

We recently reported similar viscosity and LLPS measurements for SOA prepared by the ozonolysis of  $\beta$ -caryophyllene,<sup>262</sup> which had 1-2 orders of magnitude lower viscosity than both hp-SOA and sp-SOA even at 50% RH. Since  $\beta$ -caryophyllene is a cyclic compound, its ozonolysis does not lead to an extensive fragmentation of the molecular backbone,<sup>263</sup> thus resulting in compounds with similar molecular weights as from oxidation with OH.<sup>264</sup> Therefore, higher viscosity of sp-SOA and hp-SOA compared to that of  $\beta$ -caryophyllene SOA points to additional, presently unknown, factors that affect viscosity of SOA produced from complex mixtures. It is possible a simpler combination of a monoterpene and sesquiterpene could replicate real plant photooxidation SOA, but comparable measurements of this kind have not been reported.

### 3.4 Conclusions

This work demonstrates that products from sesquiterpenes oxidation increase viscosity of SOA prepared from simulated mixtures of plant volatiles. It follows that physical properties of biogenic SOA cannot be modeled by parameters developed for SOA generated from a single-component VOC. Guenther et al., (2012) estimated the sesquiterpene: monoterpene emission ratio from boreal needleleaf trees to be ~16% even for healthy plants<sup>11</sup> and this ratio is expected to be even higher for stressed plants. These values are comparable across the different “emission types” previously investigated, therefore, sesquiterpenes could be playing a larger role in SOA properties than is currently assumed. In this study, molar fractions of sesquiterpenes were ~5% and 25% for healthy and stressed mixtures, respectively, which are reasonable mixtures for a boreal forest environment. In addition, the boreal forest covers extensive area of land that is particularly sensitive to climate, so real-world sp-SOA could have even higher viscosity than that investigated in this study. The characteristic mixing times for a typical 200 nm diameter particle of the hp-SOA and sp-SOA were greater than 1 h for  $RH \leq 25\%$ , and considerably longer than the corresponding mixing times for  $\alpha$ -pinene photooxidation SOA. The results indicated that these healthy and stressed pine tree SOA at low relative humidities may be misrepresented within air quality/climate models that treat biogenic SOA as a mixture of SOA formed from isoprene, monoterpenes, and sesquiterpenes yet neglect viscosity and LLPS as parameters.<sup>265</sup>



## CHAPTER 4

### INSECT INFESTATION INCREASES VISCOSITY OF BIOGENIC SECONDARY ORGANIC AEROSOL

#### **Abstract**

Plant stress alters volatile emission and SOA chemistry. However, little is known about how this could influence climate-relevant properties of SOA, particularly from complex volatile mixtures like real plant emissions. In this study, the molecular composition and viscosity were investigated for SOA generated from real healthy and aphid-stressed Canary Island pine (*Pinus canariensis*) trees, which are commonly used plants for landscaping in Southern California. Healthy Canary Island pine (HCIP) and stressed Canary Island pine (SCIP) aerosols were generated in a 5 m<sup>3</sup> environmental chamber at 50% relative humidity. SCIP aerosols were more viscous compared to HCIP SOA. The largest differences in particle viscosity were observed at 50% RH where the viscosity of SCIP SOA was approximately a factor of 10 larger than HCIP SOA. The increased viscosity for the stressed pine trees was attributed to the increased fraction of sesquiterpenes in the emission profile. This is the first study using real pine emissions for experimental determination of SOA viscosity. In addition, the comparison of viscosity for real healthy and stressed Canary Island pine SOA is novel. The real pine SOA were more viscous than  $\alpha$ -pinene SOA meaning that a single monoterpene cannot reproduce the physicochemical properties of tree SOA. However, the synthetic mixtures of the major compounds used to generate “mimic SOA” can reproduce the viscosities of SOA observed from the very complex real plant emissions.

## 4.1 Introduction

Plants and vegetation produce a majority of the total volatile organic compounds (VOCs) found in the atmosphere.<sup>14</sup> For example, many pine trees have high emission rates of terpenes including 2-methyl-3-buten-2-ol (MBO), numerous isomers of monoterpenes ( $C_{10}H_{16}$ ) and sesquiterpenes ( $C_{15}H_{24}$ ) of various reactivities and structures.<sup>14,15</sup> Terpenes undergo atmospheric oxidation, which produces low volatility species that condense to form secondary organic aerosol (SOA) particles.<sup>18</sup> These SOA particles play a role in influencing climate, health, and visibility.<sup>1</sup>

Plant VOC emission profiles are very complex, with over 1,700 different compounds identified across ninety plant families.<sup>266</sup> Even a single plant specimen can be highly complex with respect to its VOC emission profile. Recent literature has identified approximately 20-30 terpenes emitted from an individual pine tree.<sup>27,267</sup> To add further complexity, plant VOC emission profiles change seasonally and diurnally, corresponding to changes in metabolic processes and photosynthetic activity.<sup>268</sup> Additionally, plant VOC emission profiles shift in response to environmental and biotic stressors such as temperature extremes and insect infestation.<sup>23,196,200,269</sup> For example, plant stress induced by insect-herbivory increases emission rates of sesquiterpenes from pine trees which are produced through a biochemical defense pathway that functions in plant defense processes.<sup>23,270</sup> Plants are enduring longer and more severe periods of stress due to climate change.<sup>271</sup> Specifically, insect-infestations are expected to increase in frequency and duration as a result of increasing temperature.<sup>272</sup> In a study by Bergström et al. (2014) it was estimated that plant VOC emissions induced by insect-herbivory could account for 50% of all organic aerosol mass in Europe.<sup>273</sup> In addition to altering the total amount of SOA produced, slight modifications to the VOC profile can result in significant changes to SOA chemical composition, mass yield, and volatility due to differences in reactivity and oxidation

products between terpenoid compounds.<sup>19,23</sup> Previous studies have stated that chemical changes in the VOC profile result in significant changes to climate-relevant SOA properties with implications for the radiation budget. However, few studies exist on this topic and this study aims to bridge the gap in knowledge of how plant stress influences climate-relevant properties of SOA such as viscosity.

Viscosity is an important physical property of SOA and is highly influenced by particle chemical composition.<sup>29,31,274</sup> An increase in viscosity can lead to much slower diffusion rates of compounds within the particles, impacting particle growth and evaporation, gas-particle partitioning,<sup>76,275</sup> heterogeneous chemistry, particle-phase photochemistry, and the ability of SOA particles to act as nuclei for liquid cloud droplets<sup>276</sup> or ice particles.<sup>277</sup> Smith et al. (2021), discussed in chapter 3, recently reported that synthetic mixtures of VOCs representing the volatile profile of healthy boreal forest (Scots pine) trees produce highly viscous photooxidation SOA ( $>10^7$  Pa s) at relative humidities  $<40$  % RH.<sup>278</sup> Synthetic mixtures of VOCs representing the volatile profile of aphid-stressed trees produce SOA with an order of magnitude higher viscosity under the same RH conditions.<sup>278</sup> This difference was attributed, at least in part, to the relative amount of sesquiterpenes used to generate the SOA, since sesquiterpenes produce SOA compounds with higher molecular weights, and therefore, higher glass transition temperatures and lower hygroscopicities.<sup>278</sup> The importance of sesquiterpene oxidation products for SOA formation in a springtime hemiboreal forest was investigated by Barreira et al. (2021) and they found that even though the mass concentration of sesquiterpene oxidation products were low in the gas-phase ( $0.07 \mu\text{g m}^{-3}$ ), it contributed significantly to the particle phase mass concentration ( $1.6 \mu\text{g m}^{-3}$  of sesquiterpene oxidation products in the particle phase).<sup>279</sup> They also reported lower volatilities of compounds in the particle phase during a sesquiterpene dominated period compared

to a monoterpene dominated period.<sup>279</sup> A substantial contribution of sesquiterpenes to hemiboreal SOA formation during spring-time, suggests that both atmospheric measurements and models that focus on monoterpene oxidation may overlook a potentially large fraction of SOA particulate mass.<sup>279</sup> However, the viscosity of SOA produced from real pine trees was not investigated and therefore viscosity measurements are needed in order to bridge the knowledge gap of what is happening to SOA particle properties during periods of stress events.

Previous studies investigating the properties of real plant SOA have focused on boreal forest trees such as Scots pine,<sup>278,280</sup> due to their large geospatial abundance in the Northern Hemisphere.<sup>23,58,59</sup> However, VOC profiles between pine species can be very different, so it is important to expand SOA studies to other types of prominent pine trees. There are few works investigating the chemical and physical properties of SOA generated from VOC emissions of plants commonly used in landscaping which are becoming increasingly prevalent with the expansion of urban greening programs. *Pinus canariensis* is a sub-tropical conifer species native to the western Canary Islands, off the coast of North Africa, leading to its common name Canary Island pine. This species grows well in Mediterranean climates and is frequently used in landscaping throughout California due to their drought and thermo-tolerant properties.<sup>281,282</sup> The rising popularity and use of this tree type for the purpose of landscaping makes it an interesting specimen to study, especially in terms of their SOA particle properties in a changing environment. These findings promote interest for understanding the formation, chemical composition, and properties of SOA produced from biogenic volatiles released from plants and vegetation found throughout California.

The goal of this work is to compare the viscosity of SOA particles generated from photooxidation of real healthy and aphid-stressed Canary Island pine tree VOCs. This project

builds off previous laboratory studies that reported higher SOA viscosity from stressed pine SOA compared to healthy pine SOA using complex synthetic VOC mixtures to represent healthy and stressed boreal pine emissions (reported in Smith et al., 2021), but this has not been demonstrated using real plant emissions that are much more complex than synthetic mixtures. Stressed plant SOA is expected to have a greater viscosity than healthy plant SOA due to an increase in emissions of sesquiterpenes that may lead to high molecular weight and low volatility compounds. In this study, Canary Island pine trees (*Pinus canariensis*) were chosen as the VOC source to generate *real* healthy Canary Island pine (HCIP) and aphid-stressed Canary Island pine (SCIP) SOA. The SOA was generated by photooxidation of the VOCs in an environmental chamber under humid conditions. To our knowledge, this study is the first of its kind investigating the viscosity of Canary Island pine tree SOA and will be key in understanding the influence of climate change on the complex relationship between plant emissions, aerosols, and climate.

## **4.2 Experimental**

### **4.2.1 Tree Enclosure**

Canary Island pine saplings (*Pinus canariensis*) were used as the sole source of VOCs for the experiments outlined below. To capture VOCs emitted by the pine trees, a 2 m<sup>3</sup> Teflon plant enclosure was used to contain the pine tree. The tree enclosure was hermetically sealed on all sides except the bottom, which was zip-tied at the base of the tree trunk, excluding the pot of soil. The pot of soil was not included in the pine enclosure to remove any contribution of VOCs coming from air-soil exchange, which is not the focus of this study. Clean humidified air (scrubbed of VOCs and particulate matter, but not scrubbed for CO<sub>2</sub>) flowed into the plant enclosure at a rate of 4.5 L min<sup>-1</sup>. A small piece of PTFE tubing was used at the outlet (installed Teflon port at the side) of the pine enclosure and was connected to a heated stainless-steel tube

(50 °C) attached to a Teflon diaphragm pump (N9 KP18, M&C). This pump was used to actively pull air (containing VOCs) from the tree enclosure and pump into the 5 m<sup>3</sup> batch environmental chamber with the lights off at a rate of 3.5 L min<sup>-1</sup>, until the desired mixing ratio of terpenes was reached as monitored by a proton-transfer-reaction time-of-flight mass spectrometer (discussed below). The desired total mixing ratio was approximately 30 ppb in order to mimic cleaner biogenic environments, but still be able to produce enough particle mass for viscosity experiments.

#### 4.2.2 PTR-ToF-MS

A proton-transfer-reaction time-of-flight mass spectrometer (PTR-ToF-MS; Ionicon model 8000) with H<sub>3</sub>O<sup>+</sup> as the reagent ion was used to monitor the VOC mixing ratio inside the 5 m<sup>3</sup> batch environmental chamber. Mass calibration for the PTR-ToF-MS was performed using *m/z* 21.0226, H<sub>3</sub><sup>18</sup>O<sup>+</sup>; 33.9941, <sup>18</sup>O<sup>16</sup>O<sup>+</sup>; and 39.0332, (H<sub>2</sub><sup>18</sup>O)H<sub>3</sub><sup>16</sup>O<sup>+</sup>. The gas-phase abundance of monoterpenes (*m/z* 137) and sesquiterpenes (*m/z* 205) were monitored over time. When the total monoterpene mixing ratio reached approximately 30-80 ppb (after 22 h) the pine enclosure was disconnected from the environmental chamber and VOC injection was stopped.

#### 4.2.3 TD-GC-MS

Prior to aerosol generation via photooxidation, two cartridges (Markes, Tenax TA adsorbent) were collected at a rate of 450 cm<sup>3</sup> min<sup>-1</sup> for 5 min following the injection of VOCs into the chamber and prior to the addition of oxidant, at the heated outlet (50 °C) of the chamber. A thermal-desorption (TD-100 XR: Markes International) gas chromatograph- mass spectrometer (Agilent 7890B Gas Chromatograph, Agilent 5975 Mass Spectrometer) equipped with an HP-5 (30 m X 320 μm x 0.25 μm, Agilent) column was utilized offline to assess the initial mixing ratio of individual VOC isomers (primarily monoterpenes, oxygenated monoterpenes, and

sesquiterpenes) in the batch chamber that were present prior to SOA generation. The standards used to generate calibration curves are listed in the supplemental information (Table 4.1). VOCs were identified by their mass spectral pattern which was cross referenced with the built-in NIST database along with the standards. Only compounds that had a mass spectral match quality  $\geq 80$  compared to the reference spectra from the NIST database were included in our analysis. In cases where compounds had match qualities  $\geq 80$  compared to reference spectra but were identified as compounds other than those listed in Table 4.1, which we had calibration curves for, proxy compounds were used for quantitation instead. For example,  $\alpha$ -pinene was used for quantitation of monoterpenoids and oxygenated monoterpenes that we did not have specified standards for. For sesquiterpenes other than those listed in Table 4.1, which had molecular weight of 204 and match qualities  $\geq 80$  compared to NIST reference mass spectra, the calibration curve obtained from  $\beta$ -caryophyllene was used as a proxy standard for quantitation.

**Table 4.1** Purity and sources of commercially available standards used to generate calibration curves for TD-GC-MS quantification.

VOC Standard	Purity	Source
$\alpha$ -pinene	98 %	Acros Organics (CAS: 7785-26-4)
$\beta$ -pinene	98 %	Acros Organics (CAS: 18172-67- 3)
$\beta$ -myrcene	>75% (Contains 1000 ppm of BHT as inhibitor)	Aldrich (CAS: 123-35-3)
$\Delta^3$ -carene	90 %	Aldrich (CAS: 13466-78- 9)
camphene	$\geq 96\%$	Sigma Aldrich (CAS: 79-92-5)
limonene	97% Stabilized	Alfa Aesar, (CAS: 5989-27-5)
$\beta$ -caryophyllene	98.5%	Sigma (CAS: 87-44-5)
mix of farnesene isomers	stabilized ( $<0.10\%$ $\alpha$ -tocopherol)	Sigma-Aldrich (Product#: W383902)

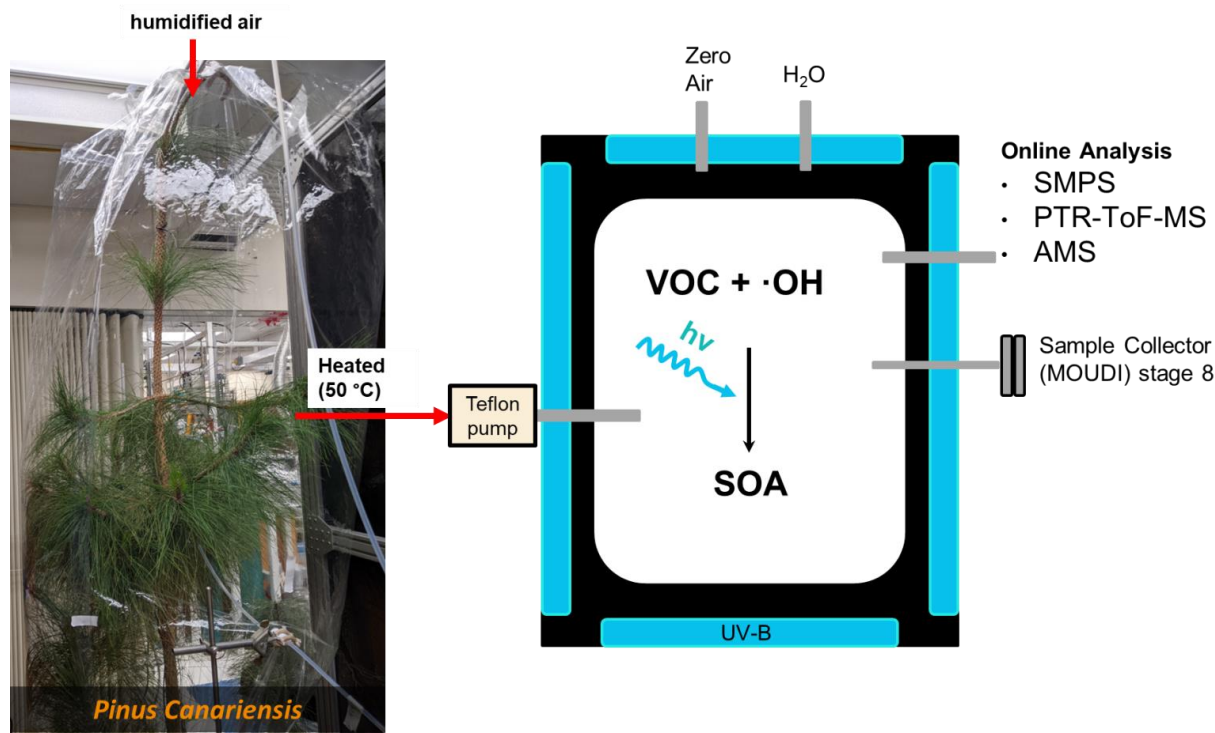
#### 4.2.4 HR-ToF-MS

The chemical composition of SOA particles was monitored using an online High-Resolution Time-of-Flight Aerosol Mass Spectrometer (HR-ToF-AMS or AMS; Aerodyne, Billerica, MA, USA) operated online in V-mode. Particles were vaporized at 600 °C and ionized using electron impact ionization at 70 eV. The AMS data was processed using Squirrel, version 1.62A for unit mass resolution (UMR) data and Pika, version 1.22A for high resolution peak fitting. The improved-ambient method mentioned in Canagaratna et al. (2015) was used to generate elemental ratios for the experimental data, including O:C and H:C ratios.<sup>283</sup>

#### 4.2.5 SOA Generation



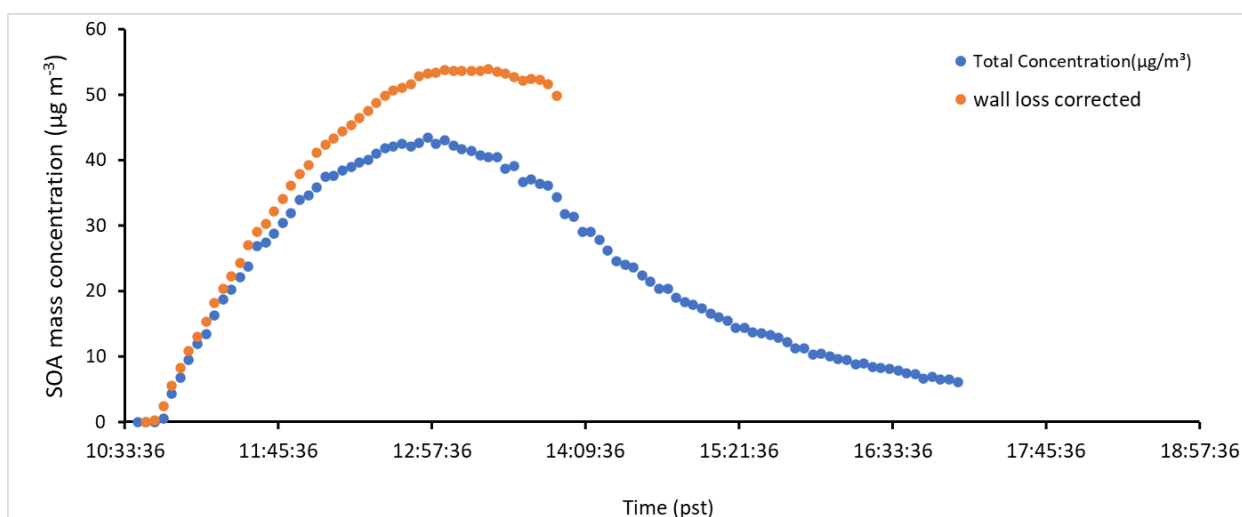
A diagram of the SOA generation setup is shown in Figure 4.1. After the TD-GC-MS cartridges were collected, 45  $\mu\text{L}$  (2 ppm) of aqueous  $\text{H}_2\text{O}_2$  (30 wt.%, Fisher Scientific) was injected into the chamber through the heated inlet (50  $^\circ\text{C}$ ). The chamber was maintained roughly at 30-85 % RH and 21-23  $^\circ\text{C}$ . The bank of UV-B lights was turned on to initiate photooxidation of the VOCs and they were allowed to react for 2 hours. The OH steady-state concentration in the chamber was previously reported as  $1.4 \times 10^6 \text{ cm}^{-3}$  using the same approach.<sup>278</sup> No seed particles were used in these experiments in order to avoid interference during the viscosity measurements in which a common inorganic seed such as ammonium sulfate would result in a core-shell morphology that would be difficult to probe with the poke-flow technique. Particle mass concentration was measured by a scanning mobility particle sizer (SMPS; TSI 3080) equipped with a condensation particle counter CPC; TSI 3775). An experimentally determined particle wall



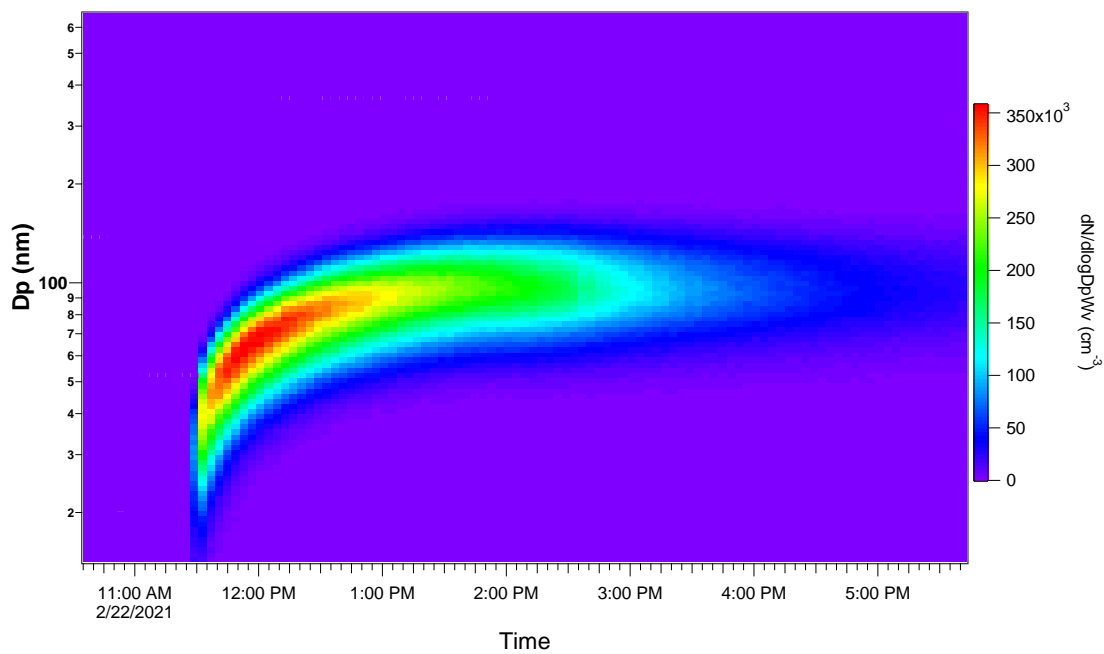
**Figure 4.1** Experimental Setup for SOA generation in a 5 m<sup>3</sup> environmental chamber with 2 m<sup>3</sup> Teflon pine enclosure used a source of VOCs containing a Canary Island pine (*Pinus Canariensis*).

loss rate was identified using the slope of the loss rate after SOA formation was completed. A

particle wall loss correction (loss rate of  $K_w = 0.0028 \text{ s}^{-1}$ ) was applied to the data set, an example of this correction is shown in Figure 4.2. A single nucleation event occurred for all trials, indicating particle formation only occurred at the onset of VOC addition from the Canary Island pine trees, a sample “banana plot” for HCIP1 is shown in Figure 4.3. SOA particles were then collected onto hydrophobically coated glass slides on a single stage 8 non-rotating micro-orifice uniform deposit impactor (MOUDI; MSP Corp. model 110-R). The SOA samples were then hermetically sealed and kept in a freezer until they were shipped on ice for further experiments. A summary of the experimental conditions for each trial is outlined in Table 4.2. A trial in the table refers to a single photooxidation chamber experiment using an individual pine tree as the SOA precursor. The trees were classified as either healthy or stressed Canary Island pine trees based on their VOC mixing ratio profile in combination with physical evidence of aphid-infestation on the trees. No physical evidence of aphid-herbivory was noted for the first three trials, which are referred to hereafter as healthy Canary Island pines (HCIP1-3). For the last two trials, aphid infestations were seen on the trees as shown in Figure 4.4. These aphid infested plants are referred to hereafter as aphid-stressed Canary Island pines (SCIP4 and SCIP5).



**Figure 4.2** Example particle wall loss correction ( $K_w = 0.0028 \text{ s}^{-1}$ ) applied to healthy plant SOA trial



**Figure 4.3** Particle formation as a function of time determined from SMPS data for SOA generated from HCIP1.

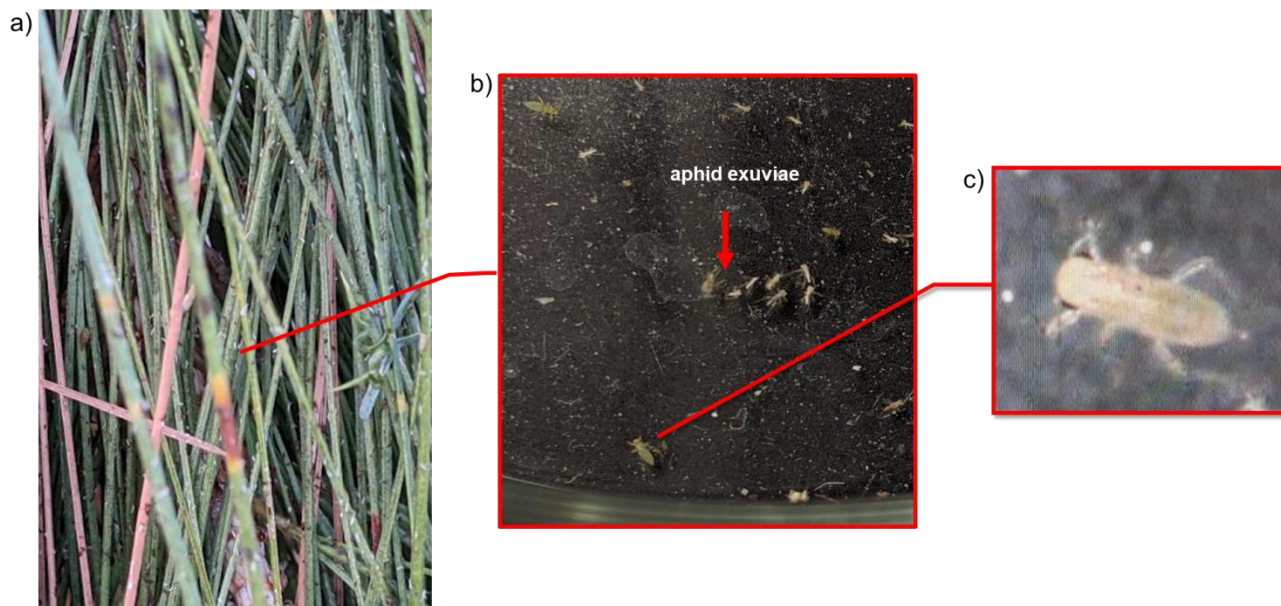
**Table 4.2** Experimental conditions for SOA particles generated in the chamber from different Canary Island pine trees (1-5). The VOC concentration used was the total VOC contribution from terpenes monoterpene (MT<sub>i</sub>), oxygenated monoterpene (OMT<sub>i</sub>), and sesquiterpenes (SQT<sub>i</sub>) identified using GC-MS. HCIP abbreviation designates healthy Canary Island pine trees and SCIP designates stressed Canary Island pine trees.

Pine tree ID	RH (%)	MT <sub>i</sub> <sup>a</sup> (ppb)	OMT <sub>i</sub> <sup>a</sup> (ppb)	SQT <sub>i</sub> <sup>a</sup> (ppb)	ΔSOA <sup>b</sup> (μg m <sup>-3</sup> )	ΔVOC <sub>no OMT</sub> (μg m <sup>-3</sup> )	ΔVOC <sub>all OMT</sub> (μg m <sup>-3</sup> )	SOA Yield <sup>c</sup> (%)
HCIP1	55	29.64	0.18	0.02	56	150	161	35-38
HCIP2	54	30.90	0.14	0.06	71	155	156	45-46
HCIP3	35	23.77	0.19	-	72	118	127	57-61
SCIP4	84	25.94	0.66	0.56	112	132	138	81-85
SCIP5	60	88.87	0.27	1.89	93	274	276	34

<sup>a</sup> MT<sub>i</sub>, OMT<sub>i</sub>, SQT<sub>i</sub> refer to initial mixing ratio measured in the chamber before oxidation was initiated.

<sup>b</sup> SOA mass concentration was corrected for particle wall losses (Figure 4.2).

<sup>c</sup> SOA mass yield calculation and description is reported below.



**Figure 4.4** a) picture of aphid-infested tree (SCIP4). b) Sample of aphid and aphid exuviae (exoskeleton) collected from pine needles onto a petri dish. C) Close up of collected aphid, identified as a light green pine needle aphid (*Eulachnus brevipilosus*).

#### 4.2.6 SOA yield calculation

The SOA yield was calculated for each trial (CIP1-5) using the equation below.

$$SOA\ Yield\ (\%) = \frac{\Delta SOA}{\Delta VOC_{MT+OMT+SQT}} \times 100 \quad (4.1)$$

The change in SOA mass concentration ( $\Delta SOA$ ) was determined from the SMPS data and was corrected for particle wall losses (Figure 4.2). The SOA density in the SMPS was assumed to be  $1.2\text{ g cm}^{-3}$ . The change in VOC mass concentration ( $\Delta VOC$ ) was determined using a combination of PTR-ToF-MS data and TD-GC-MS data for the summed total mass concentration difference for monoterpene, oxygenated monoterpene, and sesquiterpene. The percent of reacted VOC was determined using PTR-ToF-MS data for total monoterpenes ( $m/z\ 137$ ) and sesquiterpenes ( $m/z\ 205$ ). A range of reactivity was assumed for the oxygenated monoterpenes (OMT). The low range for the SOA mass yield was determined assuming none of the OMT identified in the TD-GC-MS reacted away as a result of

photooxidation whereas the high range for the SOA mass yield assumes that all (100%) of the OMT reacted away over the course of oxidation. To convert percent reacted monoterpene, oxygenated monoterpene and sesquiterpenes into mass concentration to be used in Equation 4.1, the percent reacted monoterpene, oxygenated monoterpene, and sesquiterpene was multiplied by the total mass concentration of these individual terpene categories based on the TD-GC-MS data.

SOA yield results are reported in Table 4.2. SICP4 had the highest yield followed by HCIP3, HCIP2, HCIP1, and SCIP5. The yield of  $\alpha$ -pinene photooxidation was previously reported as  $26.7 \pm 2.5$  % for SOA by generation through photooxidation with no seeds with a mass concentration of SOA of  $66.8 \pm 6.0 \mu\text{g m}^{-3}$  at low RH.<sup>284</sup> Most of the trials in this study had SOA yields  $>30\%$ , meaning that  $\alpha$ -pinene alone can not replicate the SOA yield from real pine trees. Trials with high SOA yield correlated well with trees that had higher contribution of oxygenated monoterpene in the initial VOC profile in the chamber (Table 4.3), with SCIP4 having the largest followed by HCIP3, HCIP1, HCIP2, and HCIP5. However, it is worth noting that due to our assumptions with calculating the change in VOC mass concentration, it is possible there are some errors in our estimations of VOC yield and further investigation of how oxygenated monoterpene influences SOA yield from mixtures of biogenic volatiles is recommended. The high SOA yield for SCIP4 could also be attributed to increased fraction of germacrene D which is expected to have a higher yield due to more double bonds within the structure that are capable of oxidizing and forming lower volatility products. The yield for SCIP5 is not as high because the main stress SQT in this VOC system was farnesene, an acyclic sesquiterpene that could undergo fragmentation under photooxidation.<sup>285</sup> This is consistent with high-resolution mass spectra in the literature for

farnesene photooxidation SOA made in an environmental chamber. This theory is further supported by Faiola et al. (2019) SOA in which they reported that the biggest change in plant volatiles was farnesene in the stressed plant samples, however the plant volatile mixtures with more farnesene did not appreciably change SOA production from photooxidation (healthy 10.8-23.2% and stressed 17.8-26.8%).<sup>23</sup>

**Table 4.3** Percent of total VOC identified with TD-GC-MS for each experiment. P-values were determined using a two-tailed, Student’s t-test for the comparison of the average healthy (HCIP1-3) and stressed (SCIP4-5) trees.

VOC Name	HCIP1 (% total)	HCIP2 (% total)	HCIP3 (% total)	SCIP4 (% total)	SCIP5 (% total)	p-value
α-pinene	77.99	82.49	80.00	69.43	78.02	0.17
β-pinene	7.26	8.89	7.56	7.04	14.49	0.39
d-limonene	2.91	1.58	3.16	3.49	2.22	0.73
β-myrcene	1.05	5.16	0.25	2.51	1.30	0.39
camphene	2.15	0.50	1.84	2.21	0.52	0.89
Other MT	7.97	0.74	6.35	10.83	1.08	0.85
Oxy-T	0.59	0.44	0.81	2.44	0.30	0.42
caryophyllene	0.04	0.07	0.01	0.21	0.10	0.10
Stress SQT	0.02	0.01	-	1.17	1.93	0.01*
Other SQT	0.01	0.12	0.01	0.66	0.05	0.27
<b>Total MT</b>	99.33	99.35	99.17	95.52	97.62	
<b>Total OMT</b>	0.59	0.44	0.81	2.44	0.30	
<b>Total SQT</b>	0.08	0.21	0.02	2.05	2.08	

\*denotes p-values that are statistically significant assuming a threshold of significance of  $p \leq 0.01$ .

#### 4.2.7 Experimental Viscosity

Viscosities of SOA were determined by our collaborators at the University of British Columbia using the poke-flow method as previously described.<sup>16,17,278</sup> Briefly, the poke-flow method relies on observing the flow of material under an optical microscope after deformation with a blunt object.<sup>125</sup> In our study, a needle was used to poke a supermicron single particle suspended on the glass slide substrate (supermicron particles were generated by impacting many submicron particles on the glass slide followed by coagulation of the submicron particles). Removing the needle resulted in a visible hole and left behind a half-torus shaped deformation on the spherical cap supermicron particle. The poked particle was allowed to flow until the area of the hole ( $A$ ) had recovered to one quarter of the original area of the poke hole ( $\frac{1}{4}A$ ). Given enough time, particles would recover to their original spherically capped geometry which is energetically favorable. The time of the  $\frac{1}{4}A$  recovery is referred to as the experimental flow time ( $\tau_{\text{exp,flow}}$ ). Viscosity of the SOA was determined from  $\tau_{\text{exp,flow}}$  and fluid dynamics simulations, performed using the Microfluidics module within COMSOL Multiphysics.<sup>25,26</sup> The simulations were similar to those previously reported in Smith et al. (2021).<sup>278</sup> Under low relative humidity conditions, such as 0% RH, the HCIP and SCIP SOA did not visibly flow over the duration of the experiment. In this case, adjustments to the COMSOL Multiphysics model were made similar to those reported in Smith et al. (2021) and a lower limit to viscosity were obtained by assuming the SOA material flowed by  $\leq 0.5 \mu\text{m}$  (the spatial resolution of the microscope) within the observation time in the experiments.<sup>278</sup> The simulations required inputs of surface tension, slip length, density, and contact angle. The experimental flow times ( $\tau_{\text{exp,flow}}$ ) were then used in COMSOL Multiphysics fluid dynamic model with conservative upper and lower limits for the parameters outlined (Table 4.4). Conservative upper and lower limits for these parameters resulted in conservative upper and



lower limits for the simulated SOA viscosities. Prior to poking the particles, the particles were conditioned to the surrounding RH for times ranging from 1 h to 24 h. Within the uncertainties of the measurements, the viscosities were independent of the conditioning times (Figure 4.5). Particle evaporation tests were also performed for both systems to verify that there was no significant change in the size of the particles in the poke-flow experiments due to evaporation. For times up to 25 h, which is the maximum length of time of the poke-flow experiments, the change in the size of the particles due to evaporation was less than the uncertainty of the measurements (Figure 4.6).

**Table 4.4** COMSOL parameters used for simulating the upper and lower limits of viscosity of the collected SOA by poke-flow at 292 K.

SOA type		Surface tension (mN m <sup>-1</sup> )	Slip length (m)	Contact angle (°)
HCIP1	Range of values	25.3 <sup>a</sup> -45 <sup>b</sup>	5x10 <sup>-9</sup> -1x10 <sup>-6</sup> <sup>c</sup>	45.7-60.7 <sup>d</sup>
HCIP2	Range of values	25.3 <sup>a</sup> -45 <sup>b</sup>	5x10 <sup>-9</sup> -1x10 <sup>-6</sup> <sup>c</sup>	56.2-61.7 <sup>d</sup>
HCIP3	Range of values	25.3 <sup>a</sup> -45 <sup>b</sup>	5x10 <sup>-9</sup> -1x10 <sup>-6</sup> <sup>c</sup>	53.4-58.8 <sup>d</sup>
SCIP4/SCIP5	Range of values	23.0 <sup>a</sup> -45 <sup>b</sup>	5x10 <sup>-9</sup> -1x10 <sup>-6</sup> <sup>c</sup>	22.5-35.1 <sup>d</sup>

<sup>a</sup> As a conservative lower limit to the surface tension of the SOA, the lowest surface tension of the pure liquid was used based on the distributions of molecules emitted by the saplings. Surface tensions were determined with the ACD/Labs Percepta Platform-PhysChem Module, retrieved from ChemSpider August 27, 2021. <sup>b</sup> This upper limit is consistent with surface tension measurements of SOA at RH  $\lesssim$  65% RH and surface tensions reported for alcohols, organic acids, esters, and ketones, as well as surface tension measurements of water solutions containing SOA products <sup>286-289</sup>. <sup>c</sup> Range based on measurements of the slip length of organic compounds and water on hydrophobic surfaces <sup>290-302</sup>. <sup>d</sup> Contact angles determined by measuring the height and radii of individual droplets using a confocal microscope following the method of <sup>303</sup>. Note: the simulated viscosities depend only weakly on the contact angle. Changing the contact angle by  $\pm$ 10% changes the simulated viscosity on average by  $\pm$ 15%, which is small compared to the overall uncertainties associated with the simulated viscosities.

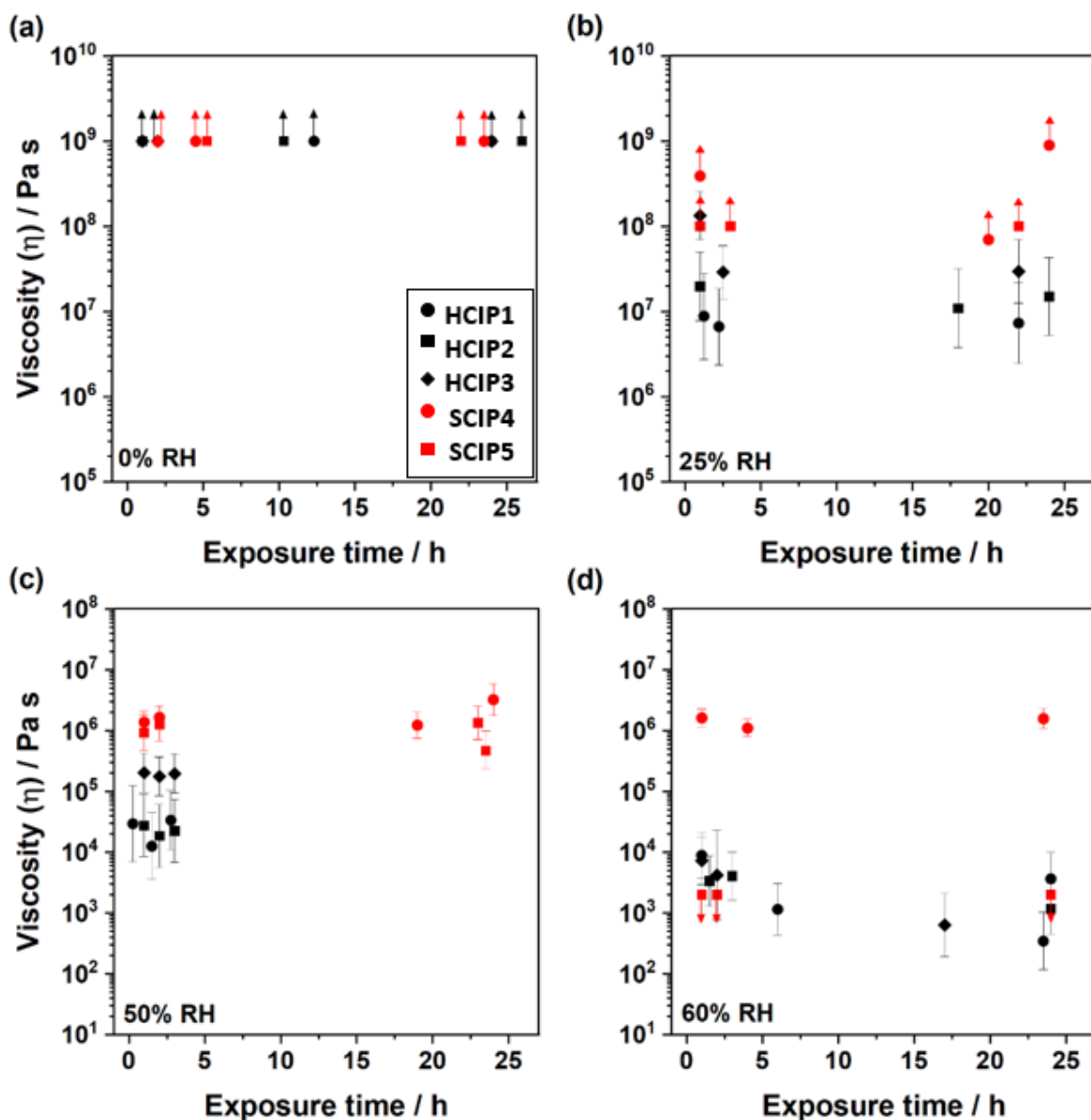
Diffusion coefficients (D) of organic molecules within the SOA were calculated from the experimental viscosities ( $\eta$ , in units of Pa s) using the Stokes-Einstein Equation:

$$D (RH, T) = \frac{K_B T}{6\pi\eta(RH,T)r_{diff}} \quad (4.2)$$

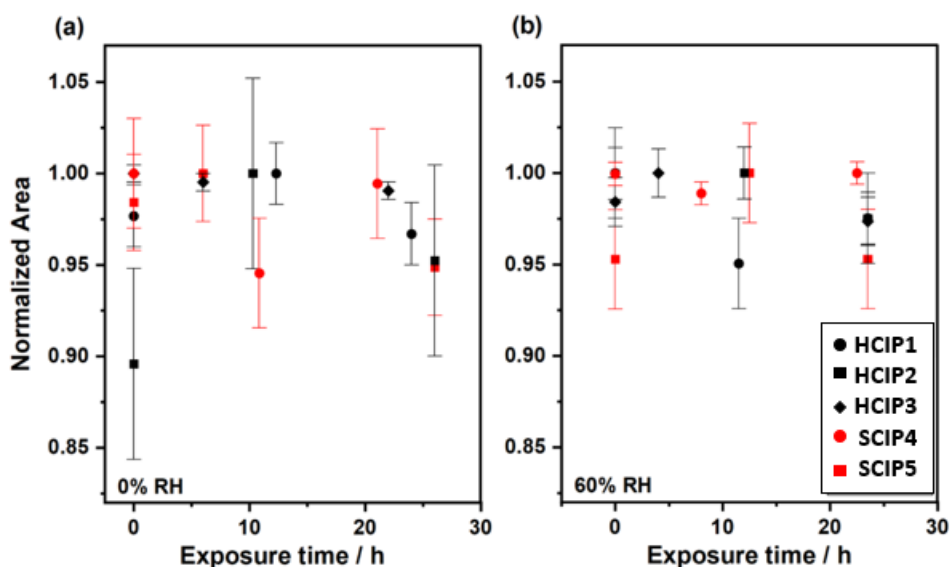
where  $K_B$  refers to the Boltzmann constant and T represents the temperature in Kelvin, and  $r_{diff}$  refers to the hydrodynamic radius which was assumed to be 0.38 nm for diffusing SOA molecules.<sup>244</sup> The characteristic mixing time ( $\tau_{mixing}$ ) within SOA particles in the atmosphere was then calculated from the diffusion coefficients using the following equation:

$$\tau_{mixing} (RH,T) = \frac{d_p^2}{4\pi^2 D (RH,T)} \quad (4.3)$$

where  $d_p$  represents the particle diameter. For this study, the particle diameter was assumed to be 200 nm, which corresponds to roughly the median diameter in the volume distribution of ambient SOA-containing particles and falls within the accumulation mode which can range from 100 – 1000 nm in diameter.<sup>175–178</sup>



**Figure 4.5** The dependence of viscosity on exposure time was monitored for all SOA types. A poke-flow experiment was performed at various exposure times up to 24 h at (a) 0%, (b) 25%, (c) 50%, and (d) 60% RH to ensure that the particles were at equilibrium. Black points correspond to those of healthy plant SOA and red points correspond to stressed plant SOA.



**Figure 4.6** Particle evaporation tests performed within the flow cell of a poke-flow experiment. The area of a SOA particle was monitored for each SOA type over the course of up to 27 h. The particles were exposed to (a)  $\approx 0\%$  RH and (b)  $60\%$  RH within the flow cell. Error bars correspond to the standard deviation of repeated measurements of the area of the particle at a given time point. Black points correspond to those of healthy plant SOA and red points correspond to stressed plant SOA.

## 4.3 Results and Discussion

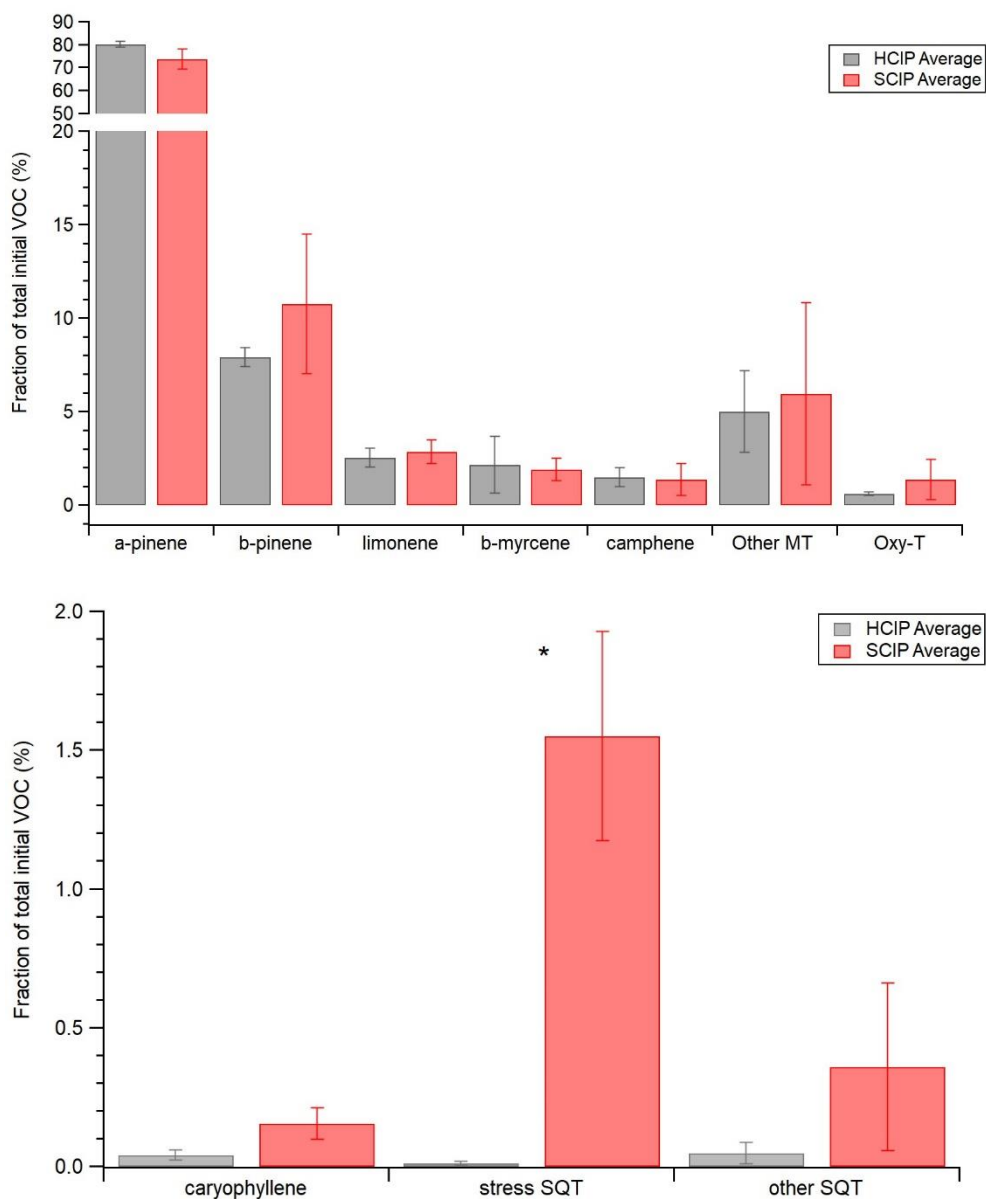
### 4.3.1 Gas-phase composition

The percent contribution to the total VOC mixing ratio profile determined from TD-GC-MS for the individual tree trials is listed in Table S3. For a more visual comparison, the percent contributions to the total initial VOC mixing ratio for the average of the healthy trees (HCIP1-3) and the average of the aphid-stressed trees (SCIP4-5) are shown in Figure 4.7. In all five trials,  $\alpha$ -pinene contributed to approximately 70-80% of the total initial VOC mixing ratio in the chamber prior to photooxidation. This is expected as evergreen trees typically have high emission rates of  $\alpha$ -pinene, as seen in studies investigating terpene concentrations in and above forested environments.<sup>69,304</sup> The other monoterpenoid category (Other OMT) included monoterpenoids

such as tricyclene (C<sub>10</sub>H<sub>16</sub>), Δ<sup>3</sup>-carene (C<sub>10</sub>H<sub>16</sub>), o- and p-cymene (C<sub>10</sub>H<sub>14</sub>), and isopropenyltoluene (C<sub>10</sub>H<sub>12</sub>). Terpinolene (C<sub>10</sub>H<sub>16</sub>) was only identified in the two stressed tree samples (SCIP4 and SCIP5). The oxygenated terpene volatiles identified are represented in the Oxy-T category. Emissions from all trees contained bornyl acetate. All trials except SCIP5 contained verbenone, whereas camphor and borneol were only identified in SCIP4. Additionally, sesquiterpenes were identified and the stress SQT category corresponds to the combined contribution of farnesene and germacrene D, which have previously been linked to volatiles induced by insect-herbivory.<sup>68</sup> SCIP4 stress SQT was predominantly germacrene D whereas SCIP5 was primarily α-farnesene. The Other SQT category includes other cyclic sesquiterpenes with molecular weight 204, besides germacrene D or β-caryophyllene, such as copaene, cadinene, muurolene, etc.

Figure 4.4a shows a close-up of the pine needles on SCIP4 that contains both live green aphids and aphid exuviae, which is the exoskeleton that an aphid sheds over the course of its life. Figure 4.4b shows a close up of a petri dish containing the aphid exuviae and live aphids that had been shaken off from a group of pine needles on the tree. The live aphid (Figure 4.4b) was identified as a light green pine needle aphid (*Eulachnus brevipilosus*). Aphids had slowly migrated into the greenhouse where these plants were being stored over the course of the experimental trials. It is unclear exactly when the aphid infestation started, however, once the infestation was identified these plants were quarantined into a different room of the greenhouse to prevent induction of stress onto the remaining trees through plant-plant communication through changes in volatile emissions. The minimum time between aphids first observed and the first stressed SOA trial was roughly 1 week.

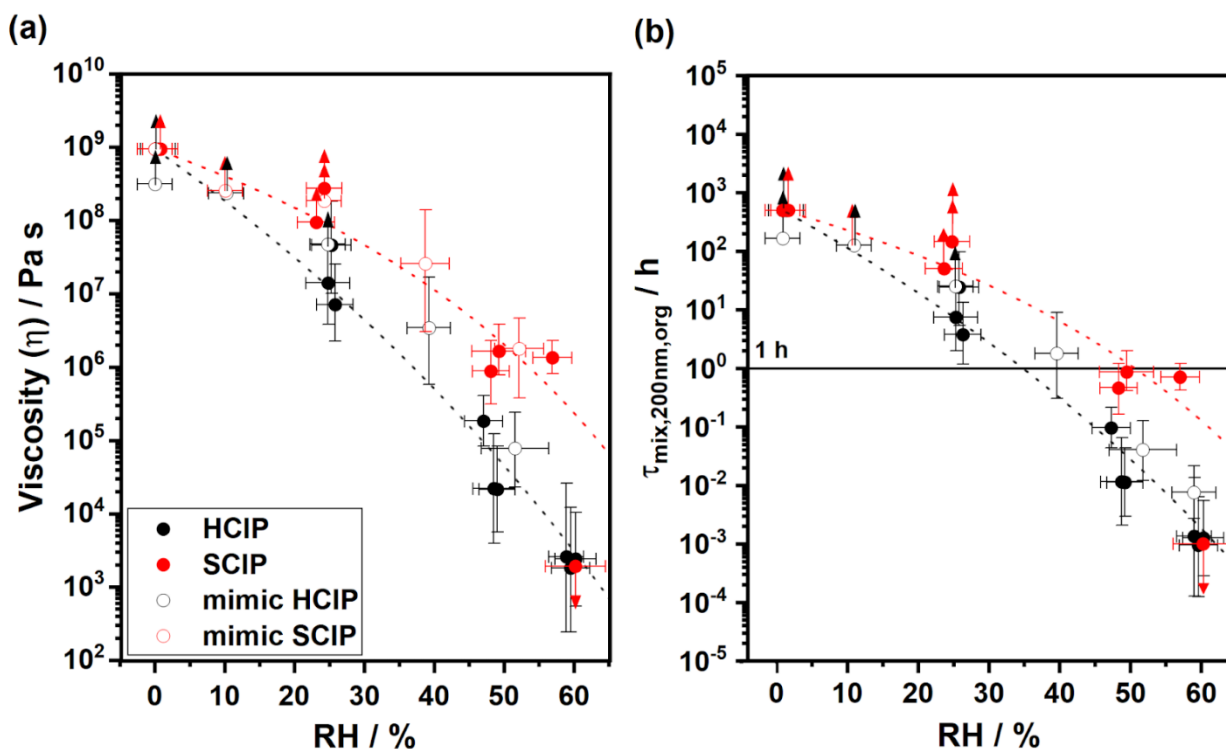
Our work has confirmed previous observations that insect infestations can alter the quantity and types of VOCs being emitted by the plant.<sup>278</sup> Overall, the SCIP trees had a statistically significant increase in fractional contribution of stress SQT compared to the HCIP trees, as determined by using a Student's t-test with a significance threshold of  $p \leq 0.01$ . Individual p-values from this test are reported in Table S3. The increase in stress SQT was attributed to the aphid infestations occurring on these two trees. The emission of farnesene and germacrene D, which comprise the stress SQT category have been previously reported as indicators of stressed induced volatiles, specifically stress hormones produced by pine trees as a result of aphid- herbivory.<sup>68</sup> In a study by Helmig et al. (2007),  $\beta$ -farnesene and  $\beta$ -caryophyllene were the most abundant sesquiterpenes identified over a pine forest, which is consistent with the volatile profile for SCIP trees in this study.<sup>68</sup> Apart from the stress SQT category, all other terpene contributions were approximately similar between the HCIP and SCIP systems. Even though the difference in average oxygenated monoterpenes between the HCIP and SCIP trees were not statistically significant, the presence of oxygenated monoterpenes within the individual samples could lead to changes in the SOA chemical composition within the condensed phase particles.



**Figure 4.7** Average fraction of total initial VOC mixing ratio in the chamber at the start of the experiment for the healthy (HCIP1-3) and aphid-stressed (HCIP4-5) experiments. Other MT category refers to other monoterpenoids. The Oxy-T category refers to oxygenated monoterpenes. The stress SQT category contains farnesene and germacrene. An asterisk (\*) denotes statistical significance ( $p \leq 0.01$ ) with a Student's t-test (reported in Table S3). Error bars are standard error of the mean.

### 4.3.2 Experimental Viscosity

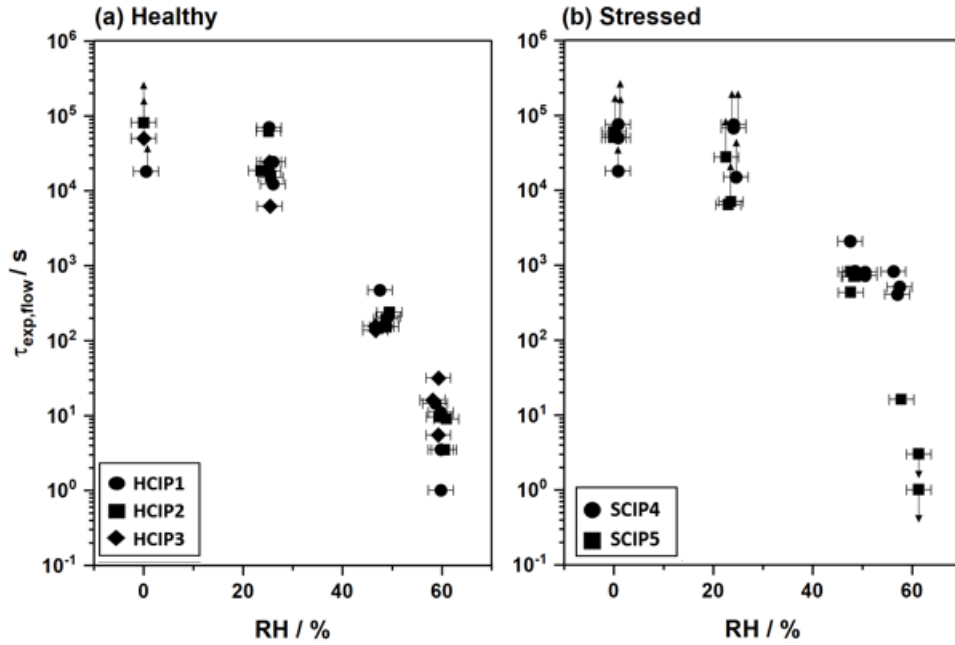
The RH-dependent viscosity of the SOA particles generated from the real healthy trees (HCIP1-3) are shown in red in Figure 4.8 and referred to as HCIP. Similarly, the two aphid-stressed tree SOA trials (SCIP4 and SCIP5) are shown in black in Figure 4.8 and referred to as SCIP along with the healthy (mimic HCIP) and stressed plant mimic SOA (mimic SCIP) previously reported by Smith et al. (2021), as a reference.<sup>278</sup> As the relative humidity increased, the  $\tau_{\text{exp,flow}}$  decreased corresponding to lowered viscosity due to the plasticizing effect water has on SOA.<sup>28,31,44</sup> The experimental flow times ( $\tau_{\text{exp,flow}}$ ) for the individual HCIP1-3 and SCIP4-5



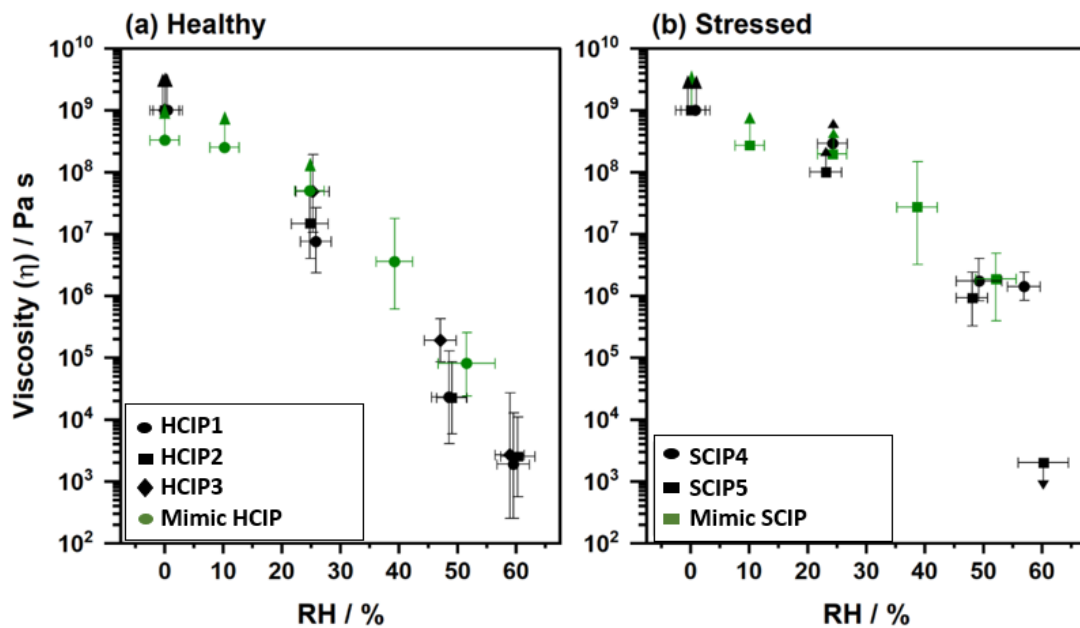
**Figure 4.8** (a) Viscosity and (b) mixing times of organic molecules ( $\tau_{\text{mix},200\text{nm,org}}$ ) obtained from poke-flow measurements of healthy and stressed plant SOA as a function of relative humidity at room temperature (292 K). Error bars in the y-direction correspond to the upper and lower bounds of viscosity and mixing times determined from the range of input parameters used in the COMSOL simulations. The error bars in the x-direction correspond to the error in relative humidity from the measurement of dewpoints using a chilled mirror hygrometer. Upward arrows correspond to lower limits, and downwards arrows correspond to upper limits. Open black circles (mimic HCIP SOA) correspond to data from Smith et al. (2021) and Maclean et al. (2021)<sup>278,280</sup>, red open circles (mimic SCIP SOA) correspond to data from Smith et al. (2021).<sup>278</sup> The dashed lines are fits to the experimental data.



SOA trials are reported in Figure 4.9 a and b, respectively. The relative humidity dependent viscosity, derived from  $\tau_{\text{exp,flow}}$  for the individual trials (reported in Table 4.2) is shown in Figure 4.10.



**Figure 4.9** Experimental flow times ( $\tau_{\text{exp,flow}}$ ) as a function of relative humidity of poke-flow experiments obtained at room temperature (292 K). Panel (a) corresponds to those of healthy plant SOA (HCIP1-3) and panel (b) corresponds to those of stressed plant SOA (SCIP4-5). The error bars in the x-direction correspond to the error in relative humidity from the measurement of dewpoints using a chilled mirror hygrometer. Upward arrows correspond to lower limits, and downward arrows correspond to upper limits.



**Figure 4.10** Viscosity as a function of RH of poke-flow experiments obtained at room temperature (292 K). Panel (a) corresponds to those of healthy plant SOA (CIP1-3) and panel (b) corresponds to those of stressed plant SOA (TA3 and TB2). Green circles (hp-proxy SOA) correspond to data from Smith et al. (2021) and Maclean et al. (2021)<sup>305,306</sup>, green squares (sp-proxy SOA) correspond to data from Smith et al. (2021).<sup>305</sup>

HCIP and SCIP SOA viscosity are represented well by mimic HCIP and SCIP, respectively (Figure 4.8). The HCIP SOA viscosity was within experimental uncertainties of the mimic HCIP SOA viscosity reported by Smith et al. (2021) over the entire RH range investigated. The real SCIP SOA closely followed the trend in viscosity as a function of RH for the mimic SCIP SOA system reported by Smith et al. (2021). The HCIP SOA particles (black) had lower viscosity than the SCIP SOA particles (red) between 0-60% RH, consistent with the trend reported by Smith et al. (2021). The difference in SOA particle viscosity between the two system was largest at 50% RH where the HCIP SOA had an average viscosity between  $10^5$  -  $10^6$  Pa s compared to that of the SCIP SOA particles which had a viscosity between  $10^4$  -  $10^5$  Pa s and approximately an order of magnitude higher viscosity than for just  $\alpha$ -pinene photooxidation SOA ( $10^3$ - $10^4$ ),

previously reported.<sup>278</sup> At  $\leq 10\%$  RH, all systems had viscosities  $\geq 10^8$  Pa s which is greater than that of tar pitch which is highly viscous ( $10^8$  Pa s).

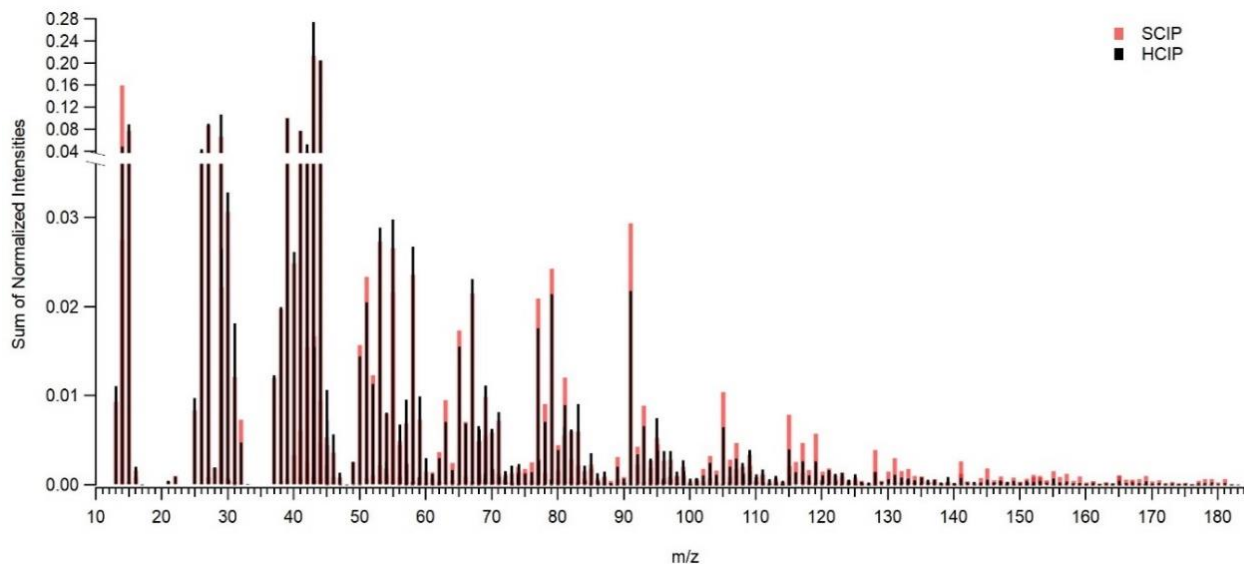
Large differences in viscosity were observed with very small changes in the VOC profile. Although the *real* and mimic SCIP SOA systems were dominated by monoterpenes (~80%), they contained a slightly larger fraction of sesquiterpenes relative to their healthy counterpart systems. The mimic SCIP SOA had 20% more sesquiterpenes in the initial total VOC profile compared to the mimic HCIP SOA and likewise the real SCIP system exhibited a 3% increase in sesquiterpenes compared to that of the real HCIP system. The real SCIP SOA sesquiterpene profile was comprised of caryophyllene, germacrene D,  $\alpha$ -farnesene, and a small fraction of “other” sesquiterpenes such as copaene, whereas the mimic SCIP SOA sesquiterpene profile consisted of only caryophyllene, isomers of farnesene, and valencene. This increased fraction of sesquiterpenes in the real stressed sample versus the real healthy sample could explain its higher SOA viscosity, due to generation of lower volatility species which would have higher glass transition temperatures, consistent with previous studies.<sup>220,278</sup>

Chemical transport models often assume semivolatile compounds become well mixed within SOA particles on timescales less than one hour.<sup>1</sup> Figure 4.8b shows mixing times of organics within a particle of 200 nm in diameter as a function of RH for the four SOA systems. At  $\leq 40\%$  RH, all the SOA systems had mixing times greater than 1 h, contrary to assumptions in chemical transport models. For fast processes, equilibrium partitioning of SVOCs is the dominant growth pathway. However, if gas-particle equilibration time is slow, specifically for viscous particles, then the dominant SOA growth pathway will switch from equilibrium partitioning to kinetic uptake. In this case, models based on equilibrium partitioning will underpredict SOA mass concentration in the atmosphere.<sup>307</sup> Shiraiwa and Seinfeld (2012) estimated that SOA mass

concentrations could be incorrectly predicted by an order of magnitude using a kinetic flux model (KM-GAP) when organic aerosol is semi-solid<sup>77</sup> and would also result in incorrectly predicted SOA particle size.<sup>78</sup> The mixing time of real biogenic SOA that get transported into the upper troposphere and lower stratosphere, which have very low humidity and temperature, could have mixing times  $\geq 10$  h. These longer mixing times should be considered when investigating long-range transport processes for these types of SOA because this would result in longer SOA lifetimes due to slower photodegradation rates observed within viscous SOA.<sup>308,309</sup>

### 4.3.3 Particle phase composition (AMS)

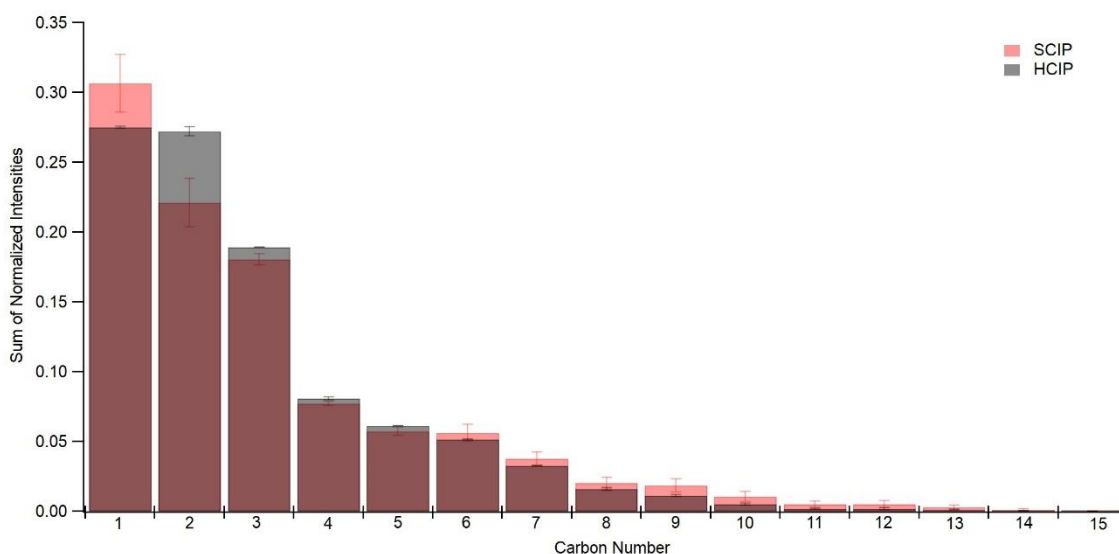
The AMS particle mass spectra were dominated by organic compounds as no seed particles were used in these experiments. The inorganic species such as nitrate, sulfate and ammonium did not contribute to particle mass. The average elemental ratios were determined for trials HCIP 2-3 and SCIP 4-5 based on the HR-ToF-AMS data. HR-ToF-AMS data was not recorded for HCIP1. The average O:C ratio (average  $\pm$  1SD) over 30 minutes coinciding with peak SOA mass concentration in the chamber at the end of photooxidation was  $0.55 \pm 0.01$  and



**Figure 4.11** High resolution mass spectra normalized to the sum of normalized intensities for HCIP2-3 (HCIP, black) and SCIP4-5 (SCIP, red) from AMS data.

$0.50 \pm 0.01$  for HCIP 2-3. The average O:C for the stressed plants SCIP 4 - 5 were  $0.50 \pm 0.01$  and  $0.46 \pm 0.01$ , respectively. The healthy and stressed plant SOA had roughly the same level of oxidation. The average H:C ratio was  $1.63 \pm 0.01$  and  $1.69 \pm 0.01$  for HCIP 2 - 3, respectively. The average H:C ratio was  $1.46 \pm 0.03$  and  $1.66 \pm 0.01$  for SCIP 4 - 5, respectively. Previous literature has reported a wide range of H:C and O:C ratios for SOA generated from different terpenes.<sup>34</sup> The differences in elemental ratios observed within this study is likely attributed to variations in individual terpene abundance at the start of each trial.

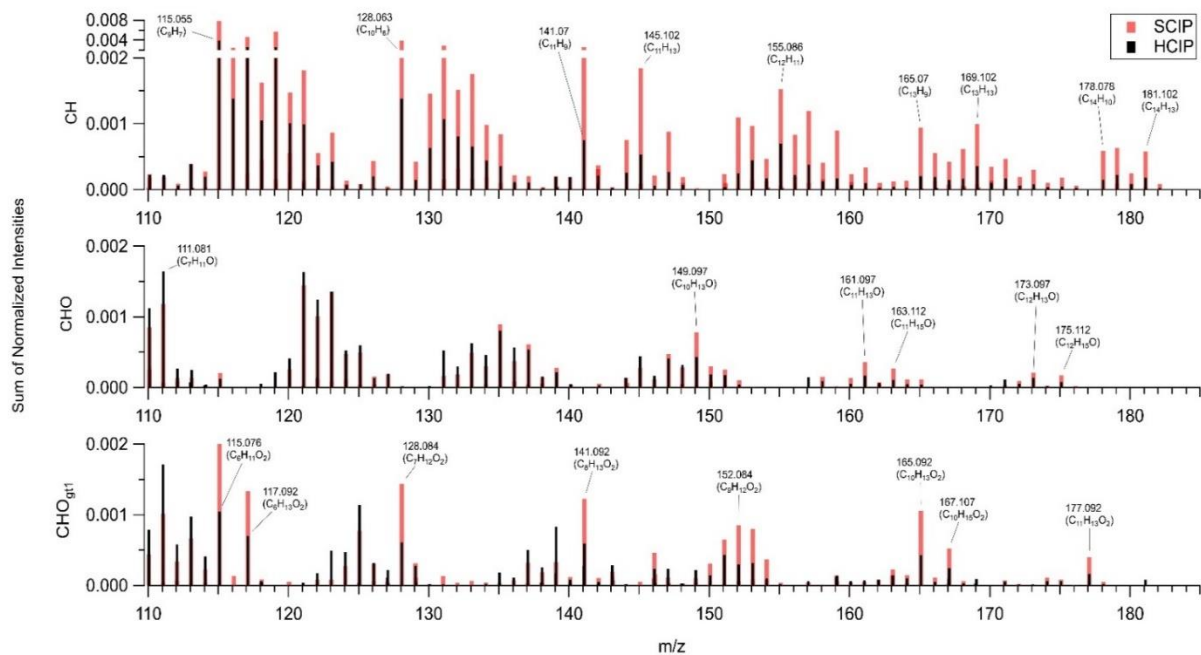
The unit mass resolution of the average of healthy (HCIP 2-3, black) and stressed (SCIP 4-5, red) SOA determined from AMS data is reported in Figure 4.11 and was normalized to the sum of total intensities between the two systems for direct comparison. Figure 4.11 is only showing the unit mass resolution for the organic families consisting of CH ( $C_xH_y^+$ ), CHO ( $C_xH_yO^+$ ), and CHO<sub>gt1</sub> ( $C_xH_yO_{z>1}^+$ ) fragments. The relative contribution of CH, CHO, and CHO<sub>gt1</sub> to HCIP was 48%, 38%, and 13%, whereas for SCIP CH, CHO, CHO<sub>gt1</sub> contributed to 51%, 36%, and 13%, respectively. The AMS data only showed signal for ions  $\leq 180$  m/z, likely due to



**Figure 4.12** Sum of normalized intensities as a function of carbon number based on organic families for HCIP2-3 (HCIP, black) and SCIP 4-5 (SCIP, red) from AMS data.

increased fragmentation from the SOA particles being vaporized at 600 °C inside the HR-ToF-AMS during ionization. The SCIP SOA had increased abundance of compounds with >10 carbon compared to the HCIP SOA (Figure 4.12). The increased signal of compounds with > 10 carbons for the stressed plant system is attributed to the increased abundance of sesquiterpenes identified in the initial VOC profile for the stressed SOA system, which would produce SOA products of higher molecular weight and therefore lead to overall higher particle viscosity compared to a healthy SOA system.

Figure 4.13 shows a breakdown of the organic ion fragments identified at  $m/z > 110$  for the CH, CHO, and CHO<sub>gt1</sub> families. Most of the organic intensity for both the HCIP and SCIP SOA was attributed to CH family fragments, as seen in Figure 4.13. Compared to the HCIP SOA, SCIP SOA had higher intensity in the CH and CHO<sub>gt1</sub> families within this range compared to the



**Figure 4.13** High resolution mass spectra normalized to the sum of normalized intensities for HCIP2-3 (HCIP, black) and SCIP4-5 (SCIP, red) from AMS data, with respect to chemical family CH ( $C_xH_y^+$ ), CHO ( $C_xH_yO^+$ ), CHO<sub>gt1</sub> ( $C_xH_yO_{z>1}^+$ ).

HCIP and some minute differences within the CHO family.

Fragments with >10 carbons in larger quantities in the SCIP case are labeled in Figure 4.13. Fragments such as  $C_{14}H_{13}$ ,  $C_{13}H_{13}$ , and  $C_{11}H_{13}O_2$  indicate these may be fragments of sesquiterpene oxidation products because they have >10 carbon. The SCIP spectra in Figure 4.11 also shows a large peak for fragment 91  $m/z$  (referred to as f91) which has been previously noted to be high for sesquiterpene SOA systems such as  $\beta$ -caryophyllene, a cyclic sesquiterpene with similar structure to germacrene D which dominated the SCIP4 SOA.<sup>310</sup> In previous ambient and plant chamber studies, the  $m/z$  91 peak in cToF-AMS data has been attributed to the tropylium ion ( $C_7H_7^+$ )<sup>310-312</sup>, concurrent with this study. The increased abundance of  $m/z$  91 for the SCIP compared to the HCIP can be explained by the higher fraction of sesquiterpenes in the initial VOC profile used to generate the SCIP SOA. However, the AMS spectra show a shift towards higher molecular weight fragments which correlate with larger molecules that are expected to have higher glass transition temperatures and therefore higher viscosity compared to smaller molecules.

#### 4.4 Conclusion

Plant stress can drastically alter the physical properties of SOA generated from VOCs emitted by plants. This increase in sesquiterpene emitted into the atmosphere, even in relatively small quantities, leads to significant changes in the resulting SOA particle properties. This study reports novel humidity-dependent viscosity for *real* healthy and aphid-stressed Canary Island pine tree SOA. We have demonstrated that real pine trees experiencing aphid-herbivory generate SOA particle with higher viscosity compared to SOA generated from healthy trees of the same species. This confirms the results of our previous study in which SOA generated from proxy mixtures of VOCs representing the emission profile of real and aphid-stressed pine trees showed that

including a small fraction of sesquiterpenes to a mixture of monoterpenes produced highly viscous particles at low relative humidity.

Our results have broader atmospheric implications because real SOA produced from trees have mixing times of organics > 1 h under room temperature and <40% RH conditions, which has been previously suggested based on SOA generated from terpene mixtures but has not been verified with real tree SOA until now. Mixing times > 1 h is significant since chemical transport models often assume mixing times shorter than 1 h when predicting SOA properties such as mass and size. In addition, this study verifies that a single monoterpene, such as  $\alpha$ -pinene, cannot accurately represent the physicochemical properties of real biogenic SOA and mixtures of terpenes containing a range of cyclic and acyclic, monoterpenes and sesquiterpenes should be used when investigating the fundamental properties of biogenic SOA systems in a laboratory setting. These findings are important as they suggest that in a changing environment where plant stress due to aphid-herbivory is expected to increase, there will be higher emission rates of sesquiterpenes by plants which will lead to chemically and physically different SOA than is assumed for healthy or only monoterpene-containing SOA. More studies investigating the physical properties of stressed SOA are recommended to accurately assess their impact on climate and health. Since the results of this study closely follow those from Smith et al. (2021) it is also expected that the SCIP SOA in this study will exhibit liquid-liquid phase separation down to lower relative humidities compared the HCIP system which can impact processes such as cloud nucleation and long-range transport of the SOA and this phenomenon will be investigated in future studies.



## REFERENCES

- (1) Hallquist, M.; Wenger, J. C.; Baltensperger, U.; Rudich, Y.; Simpson, D.; Claeys, M.; Dommen, J.; Donahue, N. M.; George, C.; Goldstein, A. H.; Hamilton, J. F.; Herrmann, H.; Hoffmann, T.; Iinuma, Y.; Jang, M.; Jenkin, M. E.; Jimenez, J. L.; Kiendler-Scharr, A.; Maenhaut, W.; McFiggans, G.; Mentel, T. F.; Monod, A.; Prévôt, A. S. H.; Seinfeld, J. H.; Surratt, J. D.; Szmigielski, R.; Wildt, J. The Formation, Properties and Impact of Secondary Organic Aerosol: Current and Emerging Issues. *Atmos. Chem. Phys.* **2009**, *9*, 5155–5236. <https://doi.org/10.5194/acp-9-5155-2009>.
- (2) Goldstein, A. H.; Galbally, I. E. Known and Unexplored Organic Constituents in the Earth's Atmosphere. *Environ. Sci. Technol* **2007**, *41*, 1514–1521.
- (3) Harrison, R. M.; Yin, J. Particulate Matter in the Atmosphere: Which Particle Properties Are Important for Its Effects on Health? *Science of the Total Environment* **2000**, *249* (1–3), 85–101. [https://doi.org/10.1016/S0048-9697\(99\)00513-6](https://doi.org/10.1016/S0048-9697(99)00513-6).
- (4) Pope III, C. A.; Dockery, D. W. Health Effects of Fine Particulate Air Pollution: Lines That Connect. *J. Air Waste Manage.* **2006**, *56*, 709–742.
- (5) Dockery, D. W.; Pope, C. A.; Xu, X.; Spengler, J. D.; Ware, J. H.; Fay, M. E.; Ferris, B. G. Jr.; Speizer, F. E. An Association between Air Pollution and Mortality in Six U.S. Cities. <http://dx.doi.org/10.1056/NEJM199312093292401> **2010**, *329* (24), 1753–1759. <https://doi.org/10.1056/NEJM199312093292401>.
- (6) *AR4 Climate Change 2007: The Physical Science Basis — IPCC; 2007.*
- (7) Aman, N.; Manomaiphiboon, K.; Suwattiga, P.; Assareh, N.; Limpaseni, W.; Suwanathada, P.; Soonsin, V.; Wang, Y. Visibility, Aerosol Optical Depth, and Low-Visibility Events in Bangkok during the Dry Season and Associated Local Weather and Synoptic Patterns. *Environ Monit Assess* **2022**, *194* (4), 322. <https://doi.org/10.1007/S10661-022-09880-2>.
- (8) Zelenyuk, A.; Imre, D.; Beránek, J.; Abramson, E.; Wilson, J.; Shrivastava, M. Synergy between Secondary Organic Aerosols and Long-Range Transport of Polycyclic Aromatic Hydrocarbons. *Environ Sci Technol* **2012**, *46* (22), 12459–12466. <https://doi.org/10.1021/es302743z>.
- (9) Shrivastava, M.; Lou, S.; Zelenyuk, A.; Easter, R. C.; Corley, R. A.; Thrall, B. D.; Rasch, P. J.; Fast, J. D.; Simonich, S. L. M.; Shen, H.; Tao, S. Global Long-Range Transport and Lung Cancer Risk from Polycyclic Aromatic Hydrocarbons Shielded by Coatings of Organic Aerosol. *Proc Natl Acad Sci U S A* **2017**, *114* (6), 1246–1251. <https://doi.org/10.1073/pnas.1618475114>.
- (10) Kulshrestha, U.; Mishra, M. Atmospheric Chemistry in Asia: Need of Integrated Approach. *Asian Atmospheric Pollution: Sources, Characteristics and Impacts* **2022**, 55–74. <https://doi.org/10.1016/B978-0-12-816693-2.00002-0>.
- (11) Guenther, A. B.; Jiang, X.; Heald, C. L.; Sakulyanontvittaya, T.; Duhl, T.; Emmons, L. K.; Wang, X. The Model of Emissions of Gases and Aerosols from Nature Version 2.1 (MEGAN2.1): An

- Extended and Updated Framework for Modeling Biogenic Emissions. *Geosci Model Dev* **2012**, *5* (6), 1471–1492. <https://doi.org/10.5194/gmd-5-1471-2012>.
- (12) Marais, E. A.; Jacob, D. J.; Turner, J. R.; Mickley, L. J. Evidence of 1991–2013 Decrease of Biogenic Secondary Organic Aerosol in Response to SO<sub>2</sub> Emission Controls. *Environmental Research Letters* **2017**, *12* (5), 054018. <https://doi.org/10.1088/1748-9326/aa69c8>.
- (13) Ioannou, E.; Koutsaviti, A.; Tzakou, O.; Roussis, V. The Genus Pinus: A Comparative Study on the Needle Essential Oil Composition of 46 Pine Species. *Phytochemistry Reviews* **2014**, *13* (4), 741–768. <https://doi.org/10.1007/S11101-014-9338-4/TABLES/4>.
- (14) Guenther, A.; Hewitt, C. N.; Erickson, D.; Fall, R.; Geron, C.; Graedel, T.; Harley, P.; Klinger, L.; Lerdau, M.; McKay, W. A.; Pierce, T.; Scholes, B.; Steinbrecher, R.; Tallamraju, R.; Taylor, J.; Zimmerman, P. A Global Model of Natural Volatile Organic Compound Emissions. *J Geophys Res* **1995**, *100* (D5), 8873. <https://doi.org/10.1029/94JD02950>.
- (15) María Yáñez-Serrano, A.; Nölscher, C.; Bourtsoukidis, E.; Gomes Alves, E.; Ganzeveld, L.; Bonn, B.; Wolff, S.; Sa, M.; Yamasoe, M.; Williams, J.; Andreae, M. O.; Kesselmeier, J. Monoterpene Chemical Speciation in a Tropical Rainforest: Variation with Season, Height, and Time of Day at the Amazon Tall Tower Observatory (ATTO). *Atmos. Chem. Phys* **2018**, *18*, 3403–3418. <https://doi.org/10.5194/acp-18-3403-2018>.
- (16) Renbaum-Wolff, L.; Grayson, J. W.; Bateman, A. P.; Kuwata, M.; Sellier, M.; Murray, B. J.; Shilling, J. E.; Martin, S. T.; Bertram, A. K. Viscosity of  $\alpha$ -Pinene Secondary Organic Material and Implications for Particle Growth and Reactivity. *Proceedings of the National Academy of Sciences* **2013**, *110* (20), 8014–8019. <https://doi.org/10.1073/pnas.1219548110>.
- (17) Grayson, J. W.; Song, M.; Sellier, M.; Bertram, A. K. Validation of the Poke-Flow Technique Combined with Simulations of Fluid Flow for Determining Viscosities in Samples with Small Volumes and High Viscosities. *Atmos Meas Tech* **2015**, *8* (6), 2463–2472. <https://doi.org/10.5194/amt-8-2463-2015>.
- (18) Atkinson, R.; Arey, J. Atmospheric Degradation of Volatile Organic Compounds. *Chem Rev* **2003**, *103*, 4605–4638. <https://doi.org/10.1021/cr0206420>.
- (19) Faiola, C. L.; Buchholz, A.; Kari, E.; Yli-Pirilä, P.; Holopainen, J. K.; Kivimäenpää, M.; Miettinen, P.; Worsnop, D. R.; Lehtinen, K. E. J.; Guenther, A. B.; Virtanen, A. Terpene Composition Complexity Controls Secondary Organic Aerosol Yields from Scots Pine Volatile Emissions. *Sci Rep* **2018**, *8* (1), 3053. <https://doi.org/10.1038/s41598-018-21045-1>.
- (20) Holopainen, J. K.; Kivimäenpää, M.; Nizkorodov, S. A. Plant-Derived Secondary Organic Material in the Air and Ecosystems. *Trends Plant Sci* **2017**, *22* (9), 744–753. <https://doi.org/10.1016/J.TPLANTS.2017.07.004>.
- (21) Watne, Å. K.; Westerlund, J.; Hallquist, Å. M.; Brune, W. H.; Hallquist, M. Ozone and OH-Induced Oxidation of Monoterpenes: Changes in the Thermal Properties of Secondary Organic Aerosol (SOA). *J Aerosol Sci* **2017**, *114*, 31–41. <https://doi.org/10.1016/J.JAEROSCI.2017.08.011>.

- (22) Holopainen, J. K.; Gershenzon, J. Multiple Stress Factors and the Emission of Plant VOCs. *Trends Plant Sci* **2010**, *15* (3), 176–184. <https://doi.org/10.1016/j.tplants.2010.01.006>.
- (23) Faiola, C. L.; Pullinen, I.; Buchholz, A.; Khalaj, F.; Ylisirniö, A.; Kari, E.; Miettinen, P.; Holopainen, J. K.; Kivimäenpää, M.; Schobesberger, S.; Yli-Juuti, T.; Virtanen, A. Secondary Organic Aerosol Formation from Healthy and Aphid-Stressed Scots Pine Emissions. *ACS Earth Space Chem* **2019**, *3* (9), 1756–1772. <https://doi.org/10.1021/acsearthspacechem.9b00118>.
- (24) Engelberth, J.; Alborn, H. T.; Schmelz, E. A.; Tumlinson, J. H. Airborne Signals Prime Plants against Insect Herbivore Attack. *Proc Natl Acad Sci U S A* **2004**, *101* (6), 1781–1785. <https://doi.org/10.1073/pnas.0308037100>.
- (25) Frost, C. J.; Appel, H. M.; Carlson, J. E.; De Moraes, C. M.; Mescher, M. C.; Schultz, J. C. Within-Plant Signalling via Volatiles Overcomes Vascular Constraints on Systemic Signalling and Primes Responses against Herbivores. *Ecol Lett* **2007**, *10* (6), 490–498. <https://doi.org/10.1111/j.1461-0248.2007.01043.x>.
- (26) McFiggans, G.; Mentel, T. F.; Wildt, J.; Pullinen, I.; Kang, S.; Kleist, E.; Schmitt, S.; Springer, M.; Tillmann, R.; Wu, C.; Zhao, D.; Hallquist, M.; Faxon, C.; Le Breton, M.; Hallquist, Å. M.; Simpson, D.; Bergström, R.; Jenkin, M. E.; Ehn, M.; Thornton, J. A.; Alfarra, M. R.; Bannan, T. J.; Percival, C. J.; Priestley, M.; Topping, D.; Kiendler-Scharr, A. Secondary Organic Aerosol Reduced by Mixture of Atmospheric Vapours. *Nature* **2019**, *565* (7741), 587–593. <https://doi.org/10.1038/s41586-018-0871-y>.
- (27) Ylisirniö, A.; Buchholz, A.; Mohr, C.; Li, Z.; Barreira, L.; Lambe, A.; Faiola, C.; Kari, E.; Yli-Juuti, T.; Nizkorodov, S. A.; Worsnop, D. R.; Virtanen, A.; Schobesberger, S. Composition and Volatility of Secondary Organic Aerosol (SOA) Formed from Oxidation of Real Tree Emissions Compared to Simplified Volatile Organic Compound (VOC) Systems. *Atmos. Chem. Phys* **2020**, *20*, 5629–5644. <https://doi.org/10.5194/acp-20-5629-2020>.
- (28) Koop, T.; Bookhold, J.; Shiraiwa, M.; Pöschl, U. Glass Transition and Phase State of Organic Compounds: Dependency on Molecular Properties and Implications for Secondary Organic Aerosols in the Atmosphere. *Phys. Chem. Chem. Phys* **2011**, *13* (43), 19238–19255. <https://doi.org/10.1039/c1cp22617g>.
- (29) Wong Derieux, W.-S.; Li, Y.; Lin, P.; Laskin, J.; Laskin, A.; Bertram, A. K.; Nizkorodov, S. A.; Shiraiwa, M. Predicting the Glass Transition Temperature and Viscosity of Secondary Organic Material Using Molecular Composition. *Atmos Chem Phys* **2018**, *18* (9), 2017–1066. <https://doi.org/10.5194/acp-2017-1066>.
- (30) Virtanen, A.; Joutsensaari, J.; Koop, T.; Kannosto, J.; Yli-Pirilä, P.; Leskinen, J.; Mäkelä, J. M.; Holopainen, J. K.; Pöschl, U.; Kulmala, M.; Worsnop, D. R.; Laaksonen, A. An Amorphous Solid State of Biogenic Secondary Organic Aerosol Particles. *Nature* **2010**, *467* (7317), 824–827. <https://doi.org/10.1038/nature09455>.
- (31) Reid, J. P.; Bertram, A. K.; Topping, D. O.; Laskin, A.; Martin, S. T.; Petters, M. D.; Pope, F. D.; Rovelli, G. The Viscosity of Atmospherically Relevant Organic Particles. *Nat Commun* **2018**, *9* (10), 1–14. <https://doi.org/10.1038/s41467-018-03027-z>.

- (32) Grayson, J. W.; Zhang, Y.; Mutzel, A.; Renbaum-Wolff, L.; Böge, O.; Kamal, S.; Herrmann, H.; Martin, S. T.; Bertram, A. K. Effect of Varying Experimental Conditions on the Viscosity of  $\alpha$ -Pinene Derived Secondary Organic Material. *Atmos Chem Phys* **2016**, *16* (10), 6027–6040. <https://doi.org/10.5194/acp-16-6027-2016>.
- (33) Ullmann, D. A.; Hinks, M. L.; MacLean, A. M.; Butenhoff, C. L.; Grayson, J. W.; Barsanti, K.; Jimenez, J. L.; Nizkorodov, S. A.; Kamal, S.; Bertram, A. K. Viscosities, Diffusion Coefficients, and Mixing Times of Intrinsic Fluorescent Organic Molecules in Brown Limonene Secondary Organic Aerosol and Tests of the Stokes-Einstein Equation. *Atmos Chem Phys* **2019**, *19* (3), 1491–1503. <https://doi.org/10.5194/acp-19-1491-2019>.
- (34) Champion, W. M.; Rothfuss, N. E.; Petters, M. D.; Grieshop, A. P. Volatility and Viscosity Are Correlated in Terpene Secondary Organic Aerosol Formed in a Flow Reactor. *Environ Sci Technol Lett* **2019**, *6*, 513–519. <https://doi.org/10.1021/acs.estlett.9b00412>.
- (35) Järvinen, E.; Ignatius, K.; Nichman, L.; Kristensen, T. B.; Fuchs, C.; Hoyle, C. R.; Höppel, N.; Corbin, J. C.; Craven, J.; Duplissy, J.; Ehrhart, S.; El Haddad, I.; Frege, C.; Gordon, H.; Jokinen, T.; Kallinger, P.; Kirkby, J.; Kiselev, A.; Naumann, K. H.; Petäjä, T.; Pinterich, T.; Prevot, A. S. H.; Saathoff, H.; Schiebel, T.; Sengupta, K.; Simon, M.; Slowik, J. G.; Tröstl, J.; Virtanen, A.; Vochezer, P.; Vogt, S.; Wagner, A. C.; Wagner, R.; Williamson, C.; Winkler, P. M.; Yan, C.; Baltensperger, U.; Donahue, N. M.; Flagan, R. C.; Gallagher, M.; Hansel, A.; Kulmala, M.; Stratmann, F.; Worsnop, D. R.; Möhler, O.; Leisner, T.; Schnaiter, M. Observation of Viscosity Transition in  $\alpha$ -Pinene Secondary Organic Aerosol. *Atmos Chem Phys* **2016**, *16* (7), 4423–4438. <https://doi.org/10.5194/acp-16-4423-2016>.
- (36) Song, M.; Liu, P. F.; Hanna, S. J.; Li, Y. J.; Martin, S. T.; Bertram, A. K. Relative Humidity-Dependent Viscosities of Isoprene-Derived Secondary Organic Material and Atmospheric Implications for Isoprene-Dominant Forests. *Atmos Chem Phys* **2015**, *15* (9), 5145–5159. <https://doi.org/10.5194/acp-15-5145-2015>.
- (37) Li, Y. J.; Liu, P.; Gong, Z.; Wang, Y.; Bateman, A. P.; Bergoend, C.; Bertram, A. K.; Martin, S. T. Chemical Reactivity and Liquid/Nonliquid States of Secondary Organic Material. *Environ Sci Technol* **2015**, *49* (22), 13264–13274. <https://doi.org/10.1021/acs.est.5b03392>.
- (38) Li, Y.; Shiraiwa, M. Timescales of Secondary Organic Aerosols to Reach Equilibrium at Various Temperatures and Relative Humidities. *Atmos Chem Phys* **2019**, *19* (9), 5959–5971. <https://doi.org/10.5194/acp-19-5959-2019>.
- (39) Ye, Q.; Upshur, M. A.; Robinson, E. S.; Geiger, F. M.; Sullivan, R. C.; Thomson, R. J.; Donahue, N. M. Following Particle-Particle Mixing in Atmospheric Secondary Organic Aerosols by Using Isotopically Labeled Terpenes. *Chem* **2018**, *4* (2), 318–333. <https://doi.org/10.1016/j.chempr.2017.12.008>.
- (40) Pajunoja, A.; Lambe, A. T.; Hakala, J.; Rastak, N.; Cummings, M. J.; Brogan, J. F.; Hao, L.; Paramonov, M.; Hong, J.; Prisle, N. L.; Malila, J.; Romakkaniemi, S.; Lehtinen, K. E. J.; Laaksonen, A.; Kulmala, M.; Massoli, P.; Onasch, T. B.; Donahue, N. M.; Riipinen, I.; Davidovits, P.; Worsnop, D. R.; Petäjä, T.; Virtanen, A. Adsorptive Uptake of Water by Semisolid Secondary Organic

- Aerosols In the Atmosphere. *Geophys Res Lett* **2015**, *42* (8), 3063–3068.  
<https://doi.org/10.1002/2015GL063142>. Received.
- (41) Pajunoja, A.; Malila, J.; Hao, L.; Joutsensaari, J.; Lehtinen, K. E. J.; Virtanen, A. Estimating the Viscosity Range of SOA Particles Based on Their Coalescence Time. *Aerosol Science and Technology* **2014**, *48* (2). <https://doi.org/10.1080/02786826.2013.870325>.
- (42) Saukko, E.; Lambe, A. T.; Massoli, P.; Koop, T.; Wright, J. P.; Croasdale, D. R.; Pedernera, D. A.; Onasch, T. B.; Laaksonen, A.; Davidovits, P.; Worsnop, D. R.; Virtanen, A. Humidity-Dependent Phase State of SOA Particles from Biogenic and Anthropogenic Precursors. *Atmos Chem Phys* **2012**, *12* (16), 7517–7529. <https://doi.org/10.5194/acp-12-7517-2012>.
- (43) Zhang, Y.; Nichman, L.; Spencer, P.; Jung, J. I.; Lee, A.; Heffernan, B. K.; Gold, A.; Zhang, Z.; Chen, Y.; Canagaratna, M. R.; Jayne, J. T.; Worsnop, D. R.; Onasch, T. B.; Surratt, J. D.; Chandler, D.; Davidovits, P.; Kolb, C. E. The Cooling Rate- And Volatility-Dependent Glass-Forming Properties of Organic Aerosols Measured by Broadband Dielectric Spectroscopy. *Environ Sci Technol* **2019**, *53* (21), 12366–12378. <https://doi.org/10.1021/acs.est.9b03317>.
- (44) Mikhailov, E.; Vlasenko, S.; Martin, S. T.; Koop, T.; Pöschl, U. Amorphous and Crystalline Aerosol Particles Interacting with Water Vapor: Conceptual Framework and Experimental Evidence for Restructuring, Phase Transitions and Kinetic Limitations. *Atmos Chem Phys* **2009**, *9* (24), 9491–9522. <https://doi.org/10.5194/acp-9-9491-2009>.
- (45) Song, Y.-C.; Lilek, J.; Lee, J. B.; Chan, M. N.; Wu, Z.; Zuend, A.; Song, M. Viscosity and Phase State of Aerosol Particles Consisting of Sucrose Mixed with Inorganic Salts. *Atmos. Chem. Phys* **2021**, *21*, 10215–10228. <https://doi.org/10.5194/acp-21-10215-2021>.
- (46) Petters, S. S.; Kreidenweis, S. M.; Grieshop, A. P.; Ziemann, P. J.; Petters, M. D. Temperature- and Humidity-Dependent Phase States of Secondary Organic Aerosols. *Geophys Res Lett* **2019**, *46* (2), 1005–1013. <https://doi.org/10.1029/2018GL080563>.
- (47) Li, Y.; Day, D. A.; Stark, H.; Jimenez, J. L.; Shiraiwa, M. Predictions of the Glass Transition Temperature and Viscosity of Organic Aerosols from Volatility Distributions. *Atmos. Chem. Phys* **2020**, *20*, 8103–8122. <https://doi.org/10.5194/acp-20-8103-2020>.
- (48) You, Y.; Smith, M. L.; Song, M.; Martin, S. T.; Bertram, A. K. Liquid–Liquid Phase Separation in Atmospherically Relevant Particles Consisting of Organic Species and Inorganic Salts. *Int Rev Phys Chem* **2014**, *33* (1), 43–77. <https://doi.org/10.1080/0144235X.2014.890786>.
- (49) You, Y.; Renbaum-Wolff, L.; Carreras-Sospedra, M.; Hanna, S. J.; Hiranuma, N.; Kamal, S.; Smith, M. L.; Zhang, X.; Weber, R. J.; Shilling, J. E.; Dabdub, D.; Martin, S. T.; Bertram, A. K. Images Reveal That Atmospheric Particles Can Undergo Liquid-Liquid Phase Separations. *Proc Natl Acad Sci U S A* **2012**, *109* (33), 13188–13193. <https://doi.org/10.1073/pnas.1206414109>.
- (50) Renbaum-Wolff, L.; Song, M.; Marcolli, C.; Zhang, Y.; Liu, P. F.; Grayson, J. W.; Geiger, F. M.; Martin, S. T.; Bertram, A. K. Observations and Implications of Liquid-Liquid Phase Separation at High Relative Humidities in Secondary Organic Material Produced by  $\alpha$ -Pinene Ozonolysis without Inorganic Salts. *Atmos Chem Phys* **2016**, *16* (12), 7969–7979. <https://doi.org/10.5194/acp-16-7969-2016>.

- (51) Song, M.; Maclean, A. M.; Huang, Y.; Smith, N. R.; Blair, S. L.; Laskin, J.; Laskin, A.; DeRieux, W.-S. W.; Li, Y.; Shiraiwa, M.; Nizkorodov, S. A.; Bertram, A. K. Liquid–Liquid Phase Separation and Viscosity within Secondary Organic Aerosol Generated from Diesel Fuel Vapors. *Atmos Chem Phys* **2019**, *19* (19), 12515–12529. <https://doi.org/10.5194/acp-19-12515-2019>.
- (52) Seinfeld, J. H.; Erdakos, G. B.; Asher, W. E.; Pankow, J. F. Modeling the Formation of Secondary Organic Aerosol (SOA). 2. The Predicted Effects of Relative Humidity on Aerosol Formation in the Alpha-Pinene-, Beta-Pinene-, Sabinene-, Delta 3-Carene-, and Cyclohexene-Ozone Systems. *Environ Sci Technol* **2001**, *35* (9), 1806–1817. <https://doi.org/10.1021/es001765+>.
- (53) Zuend, A.; Marcolli, C.; Peter, T.; Seinfeld, J. H. Computation of Liquid-Liquid Equilibria and Phase Stabilities: Implications for RH-Dependent Gas/Particle Partitioning of Organic-Inorganic Aerosols. *Atmos Chem Phys* **2010**, *10* (16), 7795–7820. <https://doi.org/10.5194/acp-10-7795-2010>.
- (54) Chang, E. I.; Pankow, J. F. Prediction of Activity Coefficients in Liquid Aerosol Particles Containing Organic Compounds, Dissolved Inorganic Salts, and Water-Part 2: Consideration of Phase Separation Effects by an X-UNIFAC Model. *Atmos Environ* **2006**, *40* (33), 6422–6436. <https://doi.org/10.1016/j.atmosenv.2006.04.031>.
- (55) Thornton, J. A.; Braban, C. F.; Abbatt, J. P. D. N<sub>2</sub>O<sub>5</sub> Hydrolysis on Sub-Micron Organic Aerosols: The Effect of Relative Humidity, Particle Phase, and Particle Size. *Physical Chemistry Chemical Physics* **2003**, *5*, 4593–4603. <https://doi.org/10.1039/b307498f>.
- (56) McNeill, V. F.; Patterson, J.; Wolfe, G. M.; Thornton, J. A. The Effect of Varying Levels of Surfactant on the Reactive Uptake of N<sub>2</sub>O<sub>5</sub> to Aqueous Aerosol. *Atmos Chem Phys* **2006**, *6* (6), 1635–1644. <https://doi.org/10.5194/acp-6-1635-2006>.
- (57) Schill, G. P.; Tolbert, M. A. Heterogeneous Ice Nucleation on Phase-Separated Organic-Sulfate Particles: Effect of Liquid vs. Glassy Coatings. *Atmos Chem Phys* **2013**, *13* (9), 4681–4695. <https://doi.org/10.5194/acp-13-4681-2013>.
- (58) Hämet-Ahti, L.; Palmén, A.; Alanko, P.; Tigerstedt, P. M. A. *Woody Flora of Finland*; University Press: Helsinki, 1992.
- (59) Gauthier, S.; Bernier, P.; Kuuluvainen, T.; Shvidenko, A. Z.; Schepaschenko, D. G.; S. Trumbore, P. Brando, H. H. Forest Health and Global Change. *Science*. American Association for the Advancement of Science August 21, 2015, pp 814–818. <https://doi.org/10.1126/science.aaa9092>.
- (60) Ervens, B.; Turpin, B. J.; Weber, R. J. Secondary Organic Aerosol Formation in Cloud Droplets and Aqueous Particles (AqSOA): A Review of Laboratory, Field and Model Studies. *Atmos Chem Phys* **2011**, *11* (21), 11069–11102. <https://doi.org/10.5194/ACP-11-11069-2011>.
- (61) Spracklen, D. v.; Jimenez, J. L.; Carslaw, K. S.; Worsnop, D. R.; Evans, M. J.; Mann, G. W.; Zhang, Q.; Canagaratna, M. R.; Allan, J.; Coe, H.; McFiggans, G.; Rap, A.; Forster, P. Aerosol Mass Spectrometer Constraint on the Global Secondary Organic Aerosol Budget. *Atmos Chem Phys* **2011**, *11* (23), 12109–12136. <https://doi.org/10.5194/ACP-11-12109-2011>.

- (62) Kanakidou, M.; Seinfeld, J. H.; Pandis, S. N.; Barnes, I.; Dentener, F. J.; Facchini, M. C.; van Dingenen, R.; Ervens, B.; Nenes, A.; Nielsen, C. J.; Swietlicki, E.; Putaud, J. P.; Balkanski, Y.; Fuzzi, S.; Horth, J.; Moortgat, G. K.; Winterhalter, R.; Myhre, C. E. L.; Tsigaridis, K.; Vignati, E.; Stephanou, E. G.; Wilson, J. Organic Aerosol and Global Climate Modelling: A Review. *Atmos Chem Phys* **2005**, *5* (4), 1053–1123. <https://doi.org/10.5194/ACP-5-1053-2005>.
- (63) Khan, M. A. H.; Jenkin, M. E.; Foulds, A.; Derwent, R. G.; Percival, C. J.; Shallcross, D. E. A Modeling Study of Secondary Organic Aerosol Formation from Sesquiterpenes Using the STOCHEM Global Chemistry and Transport Model. *Journal of Geophysical Research: Atmospheres* **2017**, *122* (8), 4426–4439. <https://doi.org/10.1002/2016JD026415>.
- (64) Sakulyanontvittaya, T.; Guenther, A.; Helmig, D.; Milford, J.; Wiedinmyer, C. Secondary Organic Aerosol from Sesquiterpene and Monoterpene Emissions in the United States. *Environ Sci Technol* **2008**, *42* (23), 8784–8790. [https://doi.org/10.1021/ES800817R/SUPPL\\_FILE/ES800817R\\_SI\\_001.PDF](https://doi.org/10.1021/ES800817R/SUPPL_FILE/ES800817R_SI_001.PDF).
- (65) Yee, L. D.; Isaacman-Vanwertz, G.; Wernis, R. A.; Meng, M.; Rivera, V.; Kreisberg, N. M.; Hering, S. V.; Bering, M. S.; Glasius, M.; Upshur, M. A.; Bé, A. G.; Thomson, R. J.; Geiger, F. M.; Offenberg, J. H.; Lewandowski, M.; Kourtchev, I.; Kalberer, M.; De Sá, S.; Martin, S. T.; Alexander, M. L.; Palm, B. B.; Hu, W.; Campuzano-Jost, P.; Day, D. A.; Jimenez, J. L.; Liu, Y.; McKinney, K. A.; Artaxo, P.; Viegas, J.; Manzi, A.; Oliveira, M. B.; De Souza, R.; Machado, L. A. T.; Longo, K.; Goldstein, A. H. Observations of Sesquiterpenes and Their Oxidation Products in Central Amazonia during the Wet and Dry Seasons. *Atmos. Chem. Phys* **2018**, *18*, 10433–10457. <https://doi.org/10.5194/acp-18-10433-2018>.
- (66) Ying, Q.; Li, J.; Kota, S. H. Significant Contributions of Isoprene to Summertime Secondary Organic Aerosol in Eastern United States. *Environ Sci Technol* **2015**, *49* (13), 7834–7842. [https://doi.org/10.1021/ACS.EST.5B02514/SUPPL\\_FILE/ES5B02514\\_SI\\_001.PDF](https://doi.org/10.1021/ACS.EST.5B02514/SUPPL_FILE/ES5B02514_SI_001.PDF).
- (67) Bouvier-Brown, N. C.; Goldstein, A. H.; Gilman, J. B.; Kuster, W. C.; de Gouw, J. A. In-Situ Ambient Quantification of Monoterpenes, Sesquiterpenes and Related Oxygenated Compounds during BEARPEX 2007: Implications for Gas- And Particle-Phase Chemistry. *Atmos Chem Phys* **2009**, *9* (15), 5505–5518. <https://doi.org/10.5194/ACP-9-5505-2009>.
- (68) Helmig, D.; Ortega, J.; Duhl, T.; Tanner, D.; Guenther, A.; Harley, P.; Wiedinmyer, C.; Milford, J.; Sakulyanontvittaya, T. Sesquiterpene Emissions from Pine Trees - Identifications, Emission Rates and Flux Estimates for the Contiguous United States. *Environ Sci Technol* **2007**, *41* (5), 1545–1553. <https://doi.org/10.1021/ES0618907/ASSET/IMAGES/LARGE/ES0618907F00003.JPEG>.
- (69) Guenther, A. B.; Jiang, X.; Heald, C. L.; Sakulyanontvittaya, T.; Duhl, T.; Emmons, L. K.; Wang, X. The Model of Emissions of Gases and Aerosols from Nature Version 2.1 (MEGAN2.1): An Extended and Updated Framework for Modeling Biogenic Emissions. *Geosci. Model Dev* **2012**, *5* (6), 1471–1492. <https://doi.org/10.5194/gmd-5-1471-2012>.
- (70) Seinfeld, J. H.; Pandis, S. N. *Atmospheric Chemistry and Physics*, 2nd Ed.; John Wiley and Sons: Hoboken, NJ, 2006.

- (71) Stocker, T. F.; Quin, D.; Plattner, G. K.; Tignor, M. M. B.; Allen, S. K.; Boschung, J.; Nauels, A.; Xia, Y.; Bex, V.; Midgley, P. M. *Climate Change 2013 - The Physical Science Basis*; Intergovernmental Panel on Climate Change, Ed.; Cambridge University Press: Cambridge, 2013.  
<https://doi.org/10.1017/CBO9781107415324>.
- (72) Finlayson-Pitts, B. J.; Pitts, J. N. *Chemistry of the Upper and Lower Atmosphere*; Academic Press: San Diego, 2000.
- (73) Knopf, D. A.; Alpert, P. A.; Wang, B. The Role of Organic Aerosol in Atmospheric Ice Nucleation: A Review. *ACS Earth Space Chem* **2018**, *2* (3), 168–202.  
[https://doi.org/10.1021/ACSEARTHSPACECHEM.7B00120/ASSET/IMAGES/LARGE/SP-2017-001202\\_0015.JPEG](https://doi.org/10.1021/ACSEARTHSPACECHEM.7B00120/ASSET/IMAGES/LARGE/SP-2017-001202_0015.JPEG).
- (74) Shiraiwa, M.; Ueda, K.; Pozzer, A.; Lammel, G.; Kampf, C. J.; Fushimi, A.; Enami, S.; Arangio, A. M.; Fröhlich-Nowoisky, J.; Fujitani, Y.; Furuyama, A.; Lakey, P. S. J.; Lelieveld, J.; Lucas, K.; Morino, Y.; Pöschl, U.; Takahama, S.; Takami, A.; Tong, H.; Weber, B.; Yoshino, A.; Sato, K. Aerosol Health Effects from Molecular to Global Scales. *Environ Sci Technol* **2017**, *51* (23), 13545–13567. [https://doi.org/10.1021/ACS.EST.7B04417/ASSET/IMAGES/LARGE/ES-2017-04417P\\_0004.JPEG](https://doi.org/10.1021/ACS.EST.7B04417/ASSET/IMAGES/LARGE/ES-2017-04417P_0004.JPEG).
- (75) Lelieveld, J.; Evans, J. S.; Fnais, M.; Giannadaki, D.; Pozzer, A. The Contribution of Outdoor Air Pollution Sources to Premature Mortality on a Global Scale. *Nature* **2015**, *525* (7569), 367–371.  
<https://doi.org/10.1038/nature15371>.
- (76) Shiraiwa, M.; Ammann, M.; Koop, T.; Pöschl, U. Gas Uptake and Chemical Aging of Semisolid Organic Aerosol Particles. *Proc Natl Acad Sci U S A* **2011**, *108* (27), 11003–11008.  
<https://doi.org/10.1073/pnas.1103045108>.
- (77) Shiraiwa, M.; Seinfeld, J. H. Equilibration Timescale of Atmospheric Secondary Organic Aerosol Partitioning. *Geophys Res Lett* **2012**, *39* (24), 2012GL054008.  
<https://doi.org/10.1029/2012GL054008>.
- (78) Zaveri, R. A.; Easter, R. C.; Shilling, J. E.; Seinfeld, J. H. Modeling Kinetic Partitioning of Secondary Organic Aerosol and Size Distribution Dynamics: Representing Effects of Volatility, Phase State, and Particle-Phase Reaction. *Atmos Chem Phys* **2014**, *14* (10), 5153–5181.  
<https://doi.org/10.5194/ACP-14-5153-2014>.
- (79) Zaveri, R. A.; Shilling, J. E.; Zelenyuk, A.; Liu, J.; Bell, D. M.; D'Ambro, E. L.; Gaston, C. J.; Thornton, J. A.; Laskin, A.; Lin, P.; Wilson, J.; Easter, R. C.; Wang, J.; Bertram, A. K.; Martin, S. T.; Seinfeld, J. H.; Worsnop, D. R. Growth Kinetics and Size Distribution Dynamics of Viscous Secondary Organic Aerosol. *Environ Sci Technol* **2018**, *52* (3), 1191–1199.  
<https://doi.org/10.1021/acs.est.7b04623>.
- (80) Shiraiwa, M.; Yee, L. D.; Schilling, K. A.; Loza, C. L.; Craven, J. S.; Zuend, A.; Ziemann, P. J.; Seinfeld, J. H. Size Distribution Dynamics Reveal Particle-Phase Chemistry in Organic Aerosol Formation. *Proc Natl Acad Sci U S A* **2013**, *110* (29), 11746–11750.  
[https://doi.org/10.1073/PNAS.1307501110/SUPPL\\_FILE/PNAS.201307501SI.PDF](https://doi.org/10.1073/PNAS.1307501110/SUPPL_FILE/PNAS.201307501SI.PDF).



- (81) Kim, Y.; Sartelet, K.; Couvidat, F. Modeling the Effect of Non-Ideality, Dynamic Mass Transfer and Viscosity on SOA Formation in a 3-D Air Quality Model. *Atmos Chem Phys* **2019**, *19* (2), 1241–1261. <https://doi.org/10.5194/acp-19-1241-2019>.
- (82) Yli-Juuti, T.; Pajunoja, A.; Tikkanen, O. P.; Buchholz, A.; Faiola, C.; Väisänen, O.; Hao, L.; Kari, E.; Peräkylä, O.; Garmash, O.; Shiraiwa, M.; Ehn, M.; Lehtinen, K.; Virtanen, A. Factors Controlling the Evaporation of Secondary Organic Aerosol from  $\alpha$ -Pinene Ozonolysis. *Geophys Res Lett* **2017**, *44* (5), 2562–2570. <https://doi.org/10.1002/2016GL072364>.
- (83) Zhang, Y.; Chen, Y.; Lei, Z.; Olson, N. E.; Riva, M.; Koss, A. R.; Zhang, Z.; Gold, A.; Jayne, J. T.; Worsnop, D. R.; Onasch, T. B.; Kroll, J. H.; Turpin, B. J.; Ault, A. P.; Surratt, J. D. Joint Impacts of Acidity and Viscosity on the Formation of Secondary Organic Aerosol from Isoprene Epoxydiols (IEPOX) in Phase Separated Particles. *ACS Earth Space Chem* **2019**, *3* (12), 2646–2658. <https://doi.org/10.1021/acsearthspacechem.9b00209>.
- (84) Keyte, I. J.; Harrison, R. M.; Lammel, G. Chemical Reactivity and Long-Range Transport Potential of Polycyclic Aromatic Hydrocarbons – a Review. *Chem Soc Rev* **2013**, *42* (24), 9333–9391. <https://doi.org/10.1039/C3CS60147A>.
- (85) Mu, Q.; Shiraiwa, M.; Octaviani, M.; Ma, N.; Ding, A.; Su, H.; Lammel, G.; Pöschl, U.; Cheng, Y. Temperature Effect on Phase State and Reactivity Controls Atmospheric Multiphase Chemistry and Transport of PAHs. *Sci Adv* **2018**, *4* (3), eaap7314. <https://doi.org/10.1126/sciadv.aap7314>.
- (86) Friedman, C. L.; Pierce, J. R.; Selin, N. E. Assessing the Influence of Secondary Organic versus Primary Carbonaceous Aerosols on Long-Range Atmospheric Polycyclic Aromatic Hydrocarbon Transport. *Environ Sci Technol* **2014**, *48* (6), 3293–3302. [https://doi.org/10.1021/ES405219R/SUPPL\\_FILE/ES405219R\\_SI\\_001.PDF](https://doi.org/10.1021/ES405219R/SUPPL_FILE/ES405219R_SI_001.PDF).
- (87) Steimer, S. S.; Lampimäki, M.; Coz, E.; Grzanic, G.; Ammann, M. The Influence of Physical State on Shikimic Acid Ozonolysis: A Case for in Situ Microspectroscopy. *Atmos Chem Phys* **2014**, *14* (19), 10761–10772. <https://doi.org/10.5194/acp-14-10761-2014>.
- (88) Li, Z.; Smith, K. A.; Cappa, C. D. Influence of Relative Humidity on the Heterogeneous Oxidation of Secondary Organic Aerosol. *Atmos Chem Phys* **2018**, *18* (19), 14585–14608. <https://doi.org/10.5194/acp-18-14585-2018>.
- (89) Hinks, M. L.; Brady, M. V.; Lignell, H.; Song, M.; Grayson, J. W.; Bertram, A. K.; Lin, P.; Laskin, A.; Laskin, J.; Nizkorodov, S. A. Effect of Viscosity on Photodegradation Rates in Complex Secondary Organic Aerosol Materials. *Physical Chemistry Chemical Physics* **2016**, *18* (13), 8785–8793. <https://doi.org/10.1039/c5cp05226b>.
- (90) Berkemeier, T.; Steimer, S. S.; Krieger, U. K.; Peter, T.; Pöschl, U.; Ammann, M.; Shiraiwa, M. Ozone Uptake on Glassy, Semi-Solid and Liquid Organic Matter and the Role of Reactive Oxygen Intermediates in Atmospheric Aerosol Chemistry. *Physical Chemistry Chemical Physics* **2016**, *18* (18), 12662–12674. <https://doi.org/10.1039/c6cp00634e>.
- (91) Li, J.; Forrester, S. M.; Knopf, D. A. Heterogeneous Oxidation of Amorphous Organic Aerosol Surrogates by O<sub>3</sub>, NO<sub>3</sub>, and OH at Typical Tropospheric Temperatures. *Atmos Chem Phys* **2020**, *20* (10), 6055–6080. <https://doi.org/10.5194/ACP-20-6055-2020>.

- (92) Zhao, Z.; Tolentino, R.; Lee, J.; Vuong, A.; Yang, X.; Zhang, H. Interfacial Dimerization by Organic Radical Reactions During Heterogeneous Oxidative Aging of Oxygenated Organic Aerosols. *Journal of Physical Chemistry A* **2019**, *123* (50), 10782–10792. <https://doi.org/10.1021/ACS.JPCA.9B10779>/ASSET/IMAGES/LARGE/JP9B10779\_0005.JPEG.
- (93) Zhou, S.; Shiraiwa, M.; McWhinney, R. D.; Pöschl, U.; Abbatt, J. P. D. Kinetic Limitations in Gas-Particle Reactions Arising from Slow Diffusion in Secondary Organic Aerosol. *Faraday Discuss* **2013**, *165* (0), 391–406. <https://doi.org/10.1039/C3FD00030C>.
- (94) Liu, P.; Li, Y. J.; Wang, Y.; Bateman, A. P.; Zhang, Y.; Gong, Z.; Bertram, A. K.; Martin, S. T.; Paulson, J. A.; Chan, T. H. Highly Viscous States Affect the Browning of Atmospheric Organic Particulate Matter. *ACS Cent Sci* **2018**, *4* (2), 207–215. <https://doi.org/10.1021/acscentsci.7b00452>.
- (95) Houle, F. A.; Hinsberg, W. D.; Wilson, K. R. Oxidation of a Model Alkane Aerosol by OH Radical: The Emergent Nature of Reactive Uptake. *Physical Chemistry Chemical Physics* **2015**, *17* (6), 4412–4423. <https://doi.org/10.1039/c4cp05093b>.
- (96) Chenyakin, Y.; Ullmann, A. D.; Evoy, E.; Renbaum-Wolff, L.; Kamal, S.; Bertram, K. A. Diffusion Coefficients of Organic Molecules in Sucrose-Water Solutions and Comparison with Stokes-Einstein Predictions. *Atmos Chem Phys* **2017**, *17* (3), 2423–2435. <https://doi.org/10.5194/ACP-17-2423-2017>.
- (97) Evoy, E.; Maclean, A. M.; Rovelli, G.; Li, Y.; Tsimpidi, A. P.; Karydis, V. A.; Kamal, S.; Lelieveld, J.; Shiraiwa, M.; Reid, J. P.; Bertram, A. K. Predictions of Diffusion Rates of Large Organic Molecules in Secondary Organic Aerosols Using the Stokes–Einstein and Fractional Stokes–Einstein Relations. *Atmos Chem Phys* **2019**, *19* (15), 10073–10085. <https://doi.org/10.5194/acp-19-10073-2019>.
- (98) Evoy, E.; Kamal, S.; Patey, G. N.; Martin, S. T.; Bertram, A. K. Unified Description of Diffusion Coefficients from Small to Large Molecules in Organic–Water Mixtures. *J Phys Chem A* **2020**, *124* (11), 2301–2308. <https://doi.org/10.1021/acs.jpca.9b11271>.
- (99) Kiland, K. J.; Maclean, A. M.; Kamal, S.; Bertram, A. K. Diffusion of Organic Molecules as a Function of Temperature in a Sucrose Matrix (a Proxy for Secondary Organic Aerosol). *J. Phys. Chem. Lett* **2019**, *10*, 5902–5908. <https://doi.org/10.1021/acs.jpcllett.9b02182>.
- (100) Ullmann, D. A.; Hinks, M. L.; MacLean, A. M.; Butenhoff, C. L.; Grayson, J. W.; Barsanti, K.; Jimenez, J. L.; Nizkorodov, S. A.; Kamal, S.; Bertram, A. K. Viscosities, Diffusion Coefficients, and Mixing Times of Intrinsic Fluorescent Organic Molecules in Brown Limonene Secondary Organic Aerosol and Tests of the Stokes-Einstein Equation. *Atmos Chem Phys* **2019**, *19* (3), 1491–1503. <https://doi.org/10.5194/acp-19-1491-2019>.
- (101) Abramson, E.; Imre, D.; Beránek, J.; Wilson, J.; Zelenyuk, A. Experimental Determination of Chemical Diffusion within Secondary Organic Aerosol Particles. *Physical Chemistry Chemical Physics* **2013**, *15* (8), 2983–2991. <https://doi.org/10.1039/C2CP44013J>.
- (102) Price, H. C.; Mattsson, J.; Murray, B. J. Sucrose Diffusion in Aqueous Solution. *Physical Chemistry Chemical Physics* **2016**, *18* (28), 19207–19216.

- (103) Zhao, Y.; Wingen, L. M.; Perraud, V.; Finlayson-Pitts, B. J. Phase, Composition, and Growth Mechanism for Secondary Organic Aerosol from the Ozonolysis of  $\alpha$ -Cedrene. *Atmos Chem Phys* **2016**, *16* (5), 3245–3264. <https://doi.org/10.5194/acp-16-3245-2016>.
- (104) Booth, A. M.; Murphy, B.; Riipinen, I.; Percival, C. J.; Topping, D. O. Connecting Bulk Viscosity Measurements to Kinetic Limitations on Attaining Equilibrium for a Model Aerosol Composition. *Environ Sci Technol* **2014**, *48* (16), 9298–9305. <https://doi.org/10.1021/ES501705C>.
- (105) Hosny, N. A.; Fitzgerald, C.; Tong, C.; Kalberer, M.; Kuimova, M. K.; Pope, F. D. Fluorescent Lifetime Imaging of Atmospheric Aerosols: A Direct Probe of Aerosol Viscosity. *Faraday Discuss* **2013**, *165* (0), 343–356. <https://doi.org/10.1039/C3FD00041A>.
- (106) Song, M.; Liu, P. F.; Hanna, S. J.; Zaveri, R. A.; Potter, K.; You, Y.; Martin, S. T.; Bertram, A. K. Relative Humidity-Dependent Viscosity of Secondary Organic Material from Toluene Photo-Oxidation and Possible Implications for Organic Particulate Matter over Megacities. *Atmos Chem Phys* **2016**, *16*, 8817–8830. <https://doi.org/10.5194/acp-16-8817-2016>.
- (107) Shiraiwa, M.; Li, Y.; Tsimpidi, A. P.; Karydis, V. A.; Berkemeier, T.; Pandis, S. N.; Lelieveld, J.; Koop, T.; Pöschl, U. Global Distribution of Particle Phase State in Atmospheric Secondary Organic Aerosols. *Nat Commun* **2017**, *8*, 15002. <https://doi.org/10.1038/ncomms15002>.
- (108) Gervasi, N. R.; Topping, D. O.; Zuend, A. A Predictive Group-Contribution Model for the Viscosity of Aqueous Organic Aerosol. *Atmos Chem Phys* **2020**, *20* (5), 2987–3008. <https://doi.org/10.5194/ACP-20-2987-2020>.
- (109) Schmedding, R.; Rasool, Q. Z.; Zhang, Y.; Pye, H. O. T.; Zhang, H.; Chen, Y.; Surratt, J. D.; Lopez-Hilfiker, F. D.; Thornton, J. A.; Goldstein, A. H.; Vizuete, W. Predicting Secondary Organic Aerosol Phase State and Viscosity and Its Effect on Multiphase Chemistry in a Regional-Scale Air Quality Model. *Atmos Chem Phys* **2020**, *20* (13), 8201–8225. <https://doi.org/10.5194/acp-20-8201-2020>.
- (110) Ditto, J. C.; Joo, T.; Khare, P.; Sheu, R.; Takeuchi, M.; Chen, Y.; Xu, W.; Bui, A. A. T.; Sun, Y.; Ng, N. L.; Gentner, D. R. Effects of Molecular-Level Compositional Variability in Organic Aerosol on Phase State and Thermodynamic Mixing Behavior. *Environ Sci Technol* **2019**. [https://doi.org/10.1021/ACS.EST.9B02664/SUPPL\\_FILE/ES9B02664\\_SI\\_001.PDF](https://doi.org/10.1021/ACS.EST.9B02664/SUPPL_FILE/ES9B02664_SI_001.PDF).
- (111) Schum, S. K.; Zhang, B.; Dzepina, K.; Fialho, P.; Mazzoleni, C.; Mazzoleni, L. R. Molecular and Physical Characteristics of Aerosol at a Remote Free Troposphere Site: Implications for Atmospheric Aging. *Atmos Chem Phys* **2018**, *18* (19), 14017–14036. <https://doi.org/10.5194/ACP-18-14017-2018>.
- (112) Slade, J. H.; Ault, A. P.; Bui, A. T.; Ditto, J. C.; Lei, Z.; Bondy, A. L.; Olson, N. E.; Cook, R. D.; Desrochers, S. J.; Harvey, R. M.; Erickson, M. H.; Wallace, H. W.; Alvarez, S. L.; Flynn, J. H.; Boor, B. E.; Petrucci, G. A.; Gentner, D. R.; Griffin, R. J.; Shepson, P. B. Bouncer Particles at Night: Biogenic Secondary Organic Aerosol Chemistry and Sulfate Drive Diel Variations in the Aerosol Phase in a Mixed Forest. *Environ Sci Technol* **2019**, *53* (9), 4977–4987. <https://doi.org/10.1021/acs.est.8b07319>.
- (113) Riva, M.; Chen, Y.; Zhang, Y.; Lei, Z.; Olson, N. E.; Boyer, H. C.; Narayan, S.; Yee, L. D.; Green, H. S.; Cui, T.; Zhang, Z.; Baumann, K.; Fort, M.; Edgerton, E.; Budisulistiorini, S. H.; Rose, C. A.;

- Ribeiro, I. O.; Oliveira, R. L. E.; dos Santos, E. O.; Machado, C. M. D.; Szopa, S.; Zhao, Y.; Alves, E. G.; de Sá, S. S.; Hu, W.; Knipping, E. M.; Shaw, S. L.; Duvoisin Junior, S.; de Souza, R. A. F.; Palm, B. B.; Jimenez, J. L.; Glasius, M.; Goldstein, A. H.; Pye, H. O. T.; Gold, A.; Turpin, B. J.; Vizuete, W.; Martin, S. T.; Thornton, J. A.; Dutcher, C. S.; Ault, A. P.; Surratt, J. D. Increasing Isoprene Epoxydiol-to-Inorganic Sulfate Aerosol Ratio Results in Extensive Conversion of Inorganic Sulfate to Organosulfur Forms: Implications for Aerosol Physicochemical Properties. *Environ Sci Technol* **2019**, *53* (15), 8682–8694. [https://doi.org/10.1021/ACS.EST.9B01019/ASSET/IMAGES/LARGE/ES-2019-01019G\\_0004.JPEG](https://doi.org/10.1021/ACS.EST.9B01019/ASSET/IMAGES/LARGE/ES-2019-01019G_0004.JPEG).
- (114) Wolf, M. J.; Coe, A.; Dove, L. A.; Zawadowicz, M. A.; Dooley, K.; Biller, S. J.; Zhang, Y.; Chisholm, S. W.; Cziczo, D. J. Investigating the Heterogeneous Ice Nucleation of Sea Spray Aerosols Using *Prochlorococcus* as a Model Source of Marine Organic Matter. *Environ Sci Technol* **2019**, *53* (3), 1139–1149. [https://doi.org/10.1021/ACS.EST.8B05150/ASSET/IMAGES/LARGE/ES-2018-051503\\_0006.JPEG](https://doi.org/10.1021/ACS.EST.8B05150/ASSET/IMAGES/LARGE/ES-2018-051503_0006.JPEG).
- (115) Pratap, V.; Chen, Y.; Yao, G.; Nakao, S. Temperature Effects on Multiphase Reactions of Organic Molecular Markers: A Modeling Study. *Atmos Environ* **2018**, *179*, 40–48. <https://doi.org/10.1016/J.ATMOENV.2018.02.009>.
- (116) Centeno, G.; Sánchez-Reyna, G.; Ancheyta, J.; Muñoz, J. A. D.; Cardona, N. Testing Various Mixing Rules for Calculation of Viscosity of Petroleum Blends. *Fuel* **2011**, *90* (12), 3561–3570. <https://doi.org/10.1016/J.FUEL.2011.02.028>.
- (117) Rovelli, G.; Song, Y. C.; MacLean, A. M.; Topping, D. O.; Bertram, A. K.; Reid, J. P. Comparison of Approaches for Measuring and Predicting the Viscosity of Ternary Component Aerosol Particles. *Anal Chem* **2019**, *91* (8), 5074–5082. [https://doi.org/10.1021/ACS.ANALCHEM.8B05353/ASSET/IMAGES/LARGE/AC-2018-053533\\_0005.JPEG](https://doi.org/10.1021/ACS.ANALCHEM.8B05353/ASSET/IMAGES/LARGE/AC-2018-053533_0005.JPEG).
- (118) Song, Y. C.; Haddrell, A. E.; Bzdek, B. R.; Reid, J. P.; Bannan, T.; Topping, D. O.; Percival, C.; Cai, C. Measurements and Predictions of Binary Component Aerosol Particle Viscosity. *Journal of Physical Chemistry A* **2016**, *120* (41), 8123–8137. [https://doi.org/10.1021/ACS.JPCA.6B07835/ASSET/IMAGES/LARGE/JP-2016-078358\\_0011.JPEG](https://doi.org/10.1021/ACS.JPCA.6B07835/ASSET/IMAGES/LARGE/JP-2016-078358_0011.JPEG).
- (119) Parsons, M. T.; Sydoryk, I.; Lim, A.; McIntyre, T. J.; Tulip, J.; Jäger, W.; McDonald, K. Real-Time Monitoring of Benzene, Toluene, and p-Xylene in a Photoreaction Chamber with a Tunable Mid-Infrared Laser and Ultraviolet Differential Optical Absorption Spectroscopy. *Appl Opt* **2011**, *50* (4), A90–A99. <https://doi.org/10.1364/AO.50.000A90>.
- (120) King, S. M.; Rosenoern, T.; Shilling, J. E.; Chen, Q.; Martin, S. T. Increased Cloud Activation Potential of Secondary Organic Aerosol for Atmospheric Mass Loadings. *Atmos Chem Phys* **2009**, *9* (9), 2959–2971. <https://doi.org/10.5194/ACP-9-2959-2009>.
- (121) King, S. M.; Rosenoern, T.; Shilling, J. E.; Chen, Q.; Martin, S. T. Cloud Condensation Nucleus Activity of Secondary Organic Aerosol Particles Mixed with Sulfate. *Geophys Res Lett* **2007**, *34* (24), 24806. <https://doi.org/10.1029/2007GL030390>.

- (122) Kleindienst, T. E.; Smith, D. F.; Li, W.; Edney, E. O.; Driscoll, D. J.; Speer, R. E.; Weathers, W. S. Secondary Organic Aerosol Formation from the Oxidation of Aromatic Hydrocarbons in the Presence of Dry Submicron Ammonium Sulfate Aerosol. *Atmos Environ* **1999**, *33* (22), 3669–3681. [https://doi.org/10.1016/S1352-2310\(99\)00121-1](https://doi.org/10.1016/S1352-2310(99)00121-1).
- (123) Shilling, J. E.; Chen, Q.; King, S. M.; Rosenoern, T.; Kroll, J. H.; Worsnop, D. R.; McKinney, K. A.; Martin, S. T. Particle Mass Yield in Secondary Organic Aerosol Formed by the Dark Ozonolysis of  $\alpha$ -Pinene. *Atmos Chem Phys* **2008**, *8* (7), 2073–2088. <https://doi.org/10.5194/ACP-8-2073-2008>.
- (124) Kroll, J. H.; Donahue, N. M.; Cee, V. J.; Demerjian, K. L.; Anderson, J. G. Gas-Phase Ozonolysis of Alkenes: Formation of OH from Anti Carbonyl Oxides. *J Am Chem Soc* **2002**, *124* (29), 8518–8519. [https://doi.org/10.1021/JA0266060/SUPPL\\_FILE/JA0266060\\_S1.PDF](https://doi.org/10.1021/JA0266060/SUPPL_FILE/JA0266060_S1.PDF).
- (125) Murray, B. J.; Haddrell, A. E.; Peppe, S.; Davies, J. F.; Reid, J. P.; O’Sullivan, D.; Price, H. C.; Kumar, R.; Saunders, R. W.; Plane, J. M. C.; Umo, N. S.; Wilson, T. W. Glass Formation and Unusual Hygroscopic Growth of Iodic Acid Solution Droplets with Relevance for Iodine Mediated Particle Formation in the Marine Boundary Layer. *Atmos Chem Phys* **2012**, *12* (18), 8575–8587. <https://doi.org/10.5194/acp-12-8575-2012>.
- (126) Martin, S. T. Phase Transitions of Aqueous Atmospheric Particles. *Chem Rev* **2000**, *100* (9), 3403–3453. <https://doi.org/10.1021/CR990034T/ASSET/IMAGES/MEDIUM/CR990034TF00034.GIF>.
- (127) Greenspan, L. Humidity Fixed Points of Binary Saturated Aqueous Solutions. *JOURNAL OF RESEARCH of the National Bureau of Standards-A. Physics and Chemistry* **81** (1).
- (128) Reist, P. C. *Aerosol Science and Technology*, 2nd ed.; McGraw-Hill Professional: New York, NY, USA, 1992.
- (129) Schneider, C. A.; Rasband, W. S.; Eliceiri, K. W. NIH Image to ImageJ: 25 Years of Image Analysis. *Nature Methods* **2012**, *9* (7), 671–675. <https://doi.org/10.1038/nmeth.2089>.
- (130) Wilson, J.; Imre, D.; Beránek, J.; Shrivastava, M.; Zelenyuk, A. Evaporation Kinetics of Laboratory-Generated Secondary Organic Aerosols at Elevated Relative Humidity. *Environ Sci Technol* **2015**, *49* (1), 243–249. <https://doi.org/10.1021/es505331d>.
- (131) Buchholz, A.; Lambe, A. T.; Ylisirniö, A.; Li, Z.; Tikkanen, O.-P.; Faiola, C.; Kari, E.; Hao, L.; Luoma, O.; Huang, W.; Mohr, C.; Worsnop, D. R.; Nizkorodov, S. A.; Yli-Juuti, T.; Schobesberger, S.; Virtanen, A. Insights into the O : C-Dependent Mechanisms Controlling the Evaporation of  $\alpha$ -Pinene Secondary Organic Aerosol Particles. *Atmos Chem Phys* **2019**, *19* (6), 4061–4073. <https://doi.org/10.5194/acp-19-4061-2019>.
- (132) Gorkowski, K.; Donahue, N. M.; Sullivan, R. C. Aerosol Optical Tweezers Constrain the Morphology Evolution of Liquid-Liquid Phase-Separated Atmospheric Particles. *Chem* **2020**, *6* (1), 204–220. <https://doi.org/10.1016/J.CHEMPR.2019.10.018>.
- (133) Hritz, A. D.; Raymond, T. M.; Dutcher, D. D. A Method for the Direct Measurement of Surface Tension of Collected Atmospherically Relevant Aerosol Particles Using Atomic Force Microscopy. *Atmos Chem Phys* **2016**, *16* (15), 9761–9769. <https://doi.org/10.5194/ACP-16-9761-2016>.

- (134) Demond, A. H.; Lindner, A. S. Estimation of Interfacial Tension between Organic Liquids and Water. *Environ Sci Technol* **1993**, *27* (12), 2318–2331. [https://doi.org/10.1021/ES00048A004/ASSET/ES00048A004.FP.PNG\\_V03](https://doi.org/10.1021/ES00048A004/ASSET/ES00048A004.FP.PNG_V03).
- (135) Gray Bé, A.; Upshur, M. A.; Liu, P.; Martin, S. T.; Geiger, F. M.; Thomson, R. J. Cloud Activation Potentials for Atmospheric  $\alpha$ -Pinene and  $\beta$ -Caryophyllene Ozonolysis Products. *ACS Cent Sci* **2017**, *3* (7), 715–725. [https://doi.org/10.1021/ACSCENTSCI.7B00112/ASSET/IMAGES/LARGE/OC-2017-00112Q\\_0005.JPEG](https://doi.org/10.1021/ACSCENTSCI.7B00112/ASSET/IMAGES/LARGE/OC-2017-00112Q_0005.JPEG).
- (136) Zhu, L.; Attard, P.; Neto, C. Reconciling Slip Measurements in Symmetric and Asymmetric Systems. *Langmuir* **2012**, *28* (20), 7768–7774. <https://doi.org/10.1021/la301040d>.
- (137) Craig, V. S. J.; Neto, C.; Williams, D. R. M. Shear-Dependent Boundary Slip in an Aqueous Newtonian Liquid. *Phys Rev Lett* **2001**, *87* (5), 054504. <https://doi.org/10.1103/PhysRevLett.87.054504>.
- (138) Baudry, J.; Charlaix, E.; Tonck, A.; Mazuyer, D. Experimental Evidence for a Large Slip Effect at a Nonwetting Fluid-Solid Interface. *Langmuir* **2001**, *17* (17), 5232–5236. <https://doi.org/10.1021/LA0009994/ASSET/IMAGES/LARGE/LA0009994F00004.JPEG>.
- (139) Tretheway, D. C.; Meinhart, C. D. Apparent Fluid Slip at Hydrophobic Microchannel Walls. *Physics of Fluids* **2002**, *14* (3), L9. <https://doi.org/10.1063/1.1432696>.
- (140) Joseph, P.; Tabeling, P. Direct Measurement of the Apparent Slip Length. *Phys Rev E Stat Nonlin Soft Matter Phys* **2005**, *71* (3), 035303. <https://doi.org/10.1103/PHYSREVE.71.035303/FIGURES/5/MEDIUM>.
- (141) Churaev, N. v.; Sobolev, V. D.; Somov, A. N. Slippage of Liquids over Lyophobic Solid Surfaces. *J Colloid Interface Sci* **1984**, *97* (2), 574–581. [https://doi.org/10.1016/0021-9797\(84\)90330-8](https://doi.org/10.1016/0021-9797(84)90330-8).
- (142) Vinogradova, O. I.; Koynov, K.; Best, A.; Feuillebois, F. Direct Measurements of Hydrophobic Slippage Using Double-Focus Fluorescence Cross-Correlation. *Phys Rev Lett* **2009**, *102* (11), 118302. <https://doi.org/10.1103/PHYSREVLETT.102.118302/FIGURES/4/MEDIUM>.
- (143) McBride, S. P.; Law, B. M. Viscosity-Dependent Liquid Slip at Molecularly Smooth Hydrophobic Surfaces. *Phys Rev E Stat Nonlin Soft Matter Phys* **2009**, *80* (6), 060601. <https://doi.org/10.1103/PHYSREVE.80.060601/FIGURES/2/MEDIUM>.
- (144) Jing, D.; Bhushan, B. Boundary Slip of Superoleophilic, Oleophobic, and Superoleophobic Surfaces Immersed in Deionized Water, Hexadecane, and Ethylene Glycol. *Langmuir* **2013**, *29* (47), 14691–14700. [https://doi.org/10.1021/LA4030876/ASSET/IMAGES/LA-2013-030876\\_M006.GIF](https://doi.org/10.1021/LA4030876/ASSET/IMAGES/LA-2013-030876_M006.GIF).
- (145) Cottin-Bizonne, C.; Jurine, S.; Baudry, J.; Crassous, J.; Restagno, F.; Charlaix, É. Nanorheology: An Investigation of the Boundary Condition at Hydrophobic and Hydrophilic Interfaces. *The European Physical Journal E* **2002**, *9* (1), 47–53. <https://doi.org/10.1140/EPJE/I2001-10112-9>.

- (146) Cottin-Bizonne, C.; Cross, B.; Steinberger, A.; Charlaix, E. Boundary Slip on Smooth Hydrophobic Surfaces: Intrinsic Effects and Possible Artifacts. *Phys Rev Lett* **2005**, *94* (5), 056102. <https://doi.org/10.1103/PHYSREVLETT.94.056102/FIGURES/2/MEDIUM>.
- (147) Cho, J. H. J.; Law, B. M.; Rieutord, F. Dipole-Dependent Slip of Newtonian Liquids at Smooth Solid Hydrophobic Surfaces. *Phys Rev Lett* **2004**, *92* (16), 166102. <https://doi.org/10.1103/PHYSREVLETT.92.166102/FIGURES/3/MEDIUM>.
- (148) Bhushan, B.; Wang, Y.; Maali, A. Boundary Slip Study on Hydrophilic, Hydrophobic, and Superhydrophobic Surfaces with Dynamic Atomic Force Microscopy. *Langmuir* **2009**, *25* (14), 8117–8121. [https://doi.org/10.1021/LA900612S/ASSET/IMAGES/LARGE/LA-2009-00612S\\_0005.JPEG](https://doi.org/10.1021/LA900612S/ASSET/IMAGES/LARGE/LA-2009-00612S_0005.JPEG).
- (149) Tasoglou, A.; Pandis, S. N. Formation and Chemical Aging of Secondary Organic Aerosol during the  $\beta$ -Caryophyllene Oxidation. *Atmos Chem Phys* **2015**, *15* (11), 6035–6046. <https://doi.org/10.5194/ACP-15-6035-2015>.
- (150) Song, M.; Liu, P. F.; Hanna, S. J.; Li, Y. J.; Martin, S. T.; Bertram, A. K. Relative Humidity-Dependent Viscosities of Isoprene-Derived Secondary Organic Material and Atmospheric Implications for Isoprene-Dominant Forests. **2015**, *15* (9), 5145–5159. <https://doi.org/10.5194/acp-15-5145-2015>.
- (151) Roach, P. K.; Laskin, J.; Laskin, A. Nanospray Desorption Electrospray Ionization: An Ambient Method for Liquid-Extraction Surface Sampling in Mass Spectrometry. *The Royal Society of Chemistry* **2010**, *135* (9), 2161–2452. <https://doi.org/DOI:10.1039/c0an00312c>.
- (152) Nizkorodov, S. A.; Laskin, J.; Laskin, A. Molecular Chemistry of Organic Aerosols through the Application of High Resolution Mass Spectrometry. *Physical Chemistry Chemical Physics* **2011**, *13* (9), 3612–3629. <https://doi.org/10.1039/c0cp02032j>.
- (153) Leenheer, J. A.; Rostad, C. E.; Gates, P. M.; Furlong, E. T.; Ferrer, I. Molecular Resolution and Fragmentation of Fulvic Acid by Electrospray Ionization/Multistage Tandem Mass Spectrometry. *Anal Chem* **2001**, *73* (7), 1461–1471. <https://doi.org/10.1021/AC0012593>.
- (154) Willoughby, S. E.; Mitrovich, S. A. *Global View of LC/MS*; Global View Publishing: Pittsburg, 1998.
- (155) Zobrist, B.; Marcolli, C.; Pedernera, D. A.; Koop, T. Do Atmospheric Aerosols Form Glasses? *Atmos Chem Phys* **2008**, *8* (17), 5221–5244. <https://doi.org/10.5194/acp-8-5221-2008>.
- (156) Kohl, I.; Bachmann, L.; Hallbrucker, A.; Mayer, E.; Loerting, T. Liquid-like Relaxation in Hyperquenched Water at  $\leq 140$  K. *Physical Chemistry Chemical Physics* **2005**, *7* (17), 3210–3220. <https://doi.org/10.1039/B507651J>.
- (157) Petters, M. D.; Kreidenweis, S. M. A Single Parameter Representation of Hygroscopic Growth and Cloud Condensation Nucleus Activity. *Atmos. Chem. Phys.* **2007**, *7* (8), 1961–1971. <https://doi.org/10.5194/acp-7-1961-2007>.
- (158) Asa-Awuku, A.; Engelhart, G. J.; Lee, B. H.; Pandis, S. N.; Nenes, A. Relating CCN Activity, Volatility, and Droplet Growth Kinetics of  $\beta$ -Caryophyllene Secondary Organic Aerosol. *Atmos Chem Phys* **2009**, *9* (3), 795–812. <https://doi.org/10.5194/ACP-9-795-2009>.

- (159) Frosch, M.; Bilde, M.; Nenes, A.; Praplan, A. P.; Jurányi, Z.; Dommen, J.; Gysel, M.; Weingartner, E.; Baltensperger, U. CCN Activity and Volatility of  $\beta$ -Caryophyllene Secondary Organic Aerosol. *Atmos Chem Phys* **2013**, *13* (4), 2283–2297. <https://doi.org/10.5194/ACP-13-2283-2013>.
- (160) Angell, C. A. Relaxation in Liquids, Polymers and Plastic Crystals - Strong/Fragile Patterns and Problems. *J Non Cryst Solids* **1991**, *131–133* (PART 1), 13–31. [https://doi.org/10.1016/0022-3093\(91\)90266-9](https://doi.org/10.1016/0022-3093(91)90266-9).
- (161) Angell, C. A. Liquid Fragility and the Glass Transition in Water and Aqueous Solutions. *Chem Rev* **2002**, *102* (8), 2627–2650. <https://doi.org/10.1021/cr000689q>.
- (162) Rothfuss, N. E.; Petters, M. D. Influence of Functional Groups on the Viscosity of Organic Aerosol. *Environ Sci Technol* **2017**, *51* (1), 271–279. [https://doi.org/10.1021/ACS.EST.6B04478/SUPPL\\_FILE/ES6B04478\\_SI\\_001.PDF](https://doi.org/10.1021/ACS.EST.6B04478/SUPPL_FILE/ES6B04478_SI_001.PDF).
- (163) Marsh, A.; Petters, S. S.; Rothfuss, N. E.; Rovelli, G.; Song, Y. C.; Reid, J. P.; Petters, M. D. Amorphous Phase State Diagrams and Viscosity of Ternary Aqueous Organic/Organic and Inorganic/Organic Mixtures. *Physical Chemistry Chemical Physics* **2018**, *20* (22), 15086–15097. <https://doi.org/10.1039/C8CP00760H>.
- (164) Rothfuss, N. E.; Petters, M. D. Characterization of the Temperature and Humidity-Dependent Phase Diagram of Amorphous Nanoscale Organic Aerosols. *Physical Chemistry Chemical Physics* **2017**, *19* (9), 6532–6545. <https://doi.org/10.1039/c6cp08593h>.
- (165) Longinotti, M. P.; Corti, H. R. Viscosity of Concentrated Sucrose and Trehalose Aqueous Solutions Including the Supercooled Regime. *J Phys Chem Ref Data* **2008**, *37* (3), 1503. <https://doi.org/10.1063/1.2932114>.
- (166) Kasparoglu, S.; Li, Y.; Shiraiwa, M.; Petters, M. D. Toward Closure between Predicted and Observed Particle Viscosity over a Wide Range of Temperatures and Relative Humidity. *Atmos Chem Phys* **2021**, *21* (2), 1127–1141. <https://doi.org/10.5194/ACP-21-1127-2021>.
- (167) Zhumd, B. Viscosity Blending Equations. *Lube Magazine* **2014**, *121*, 22–27.
- (168) Crittenden, J. C.; Trussel, R. R.; Hand, D. W.; Howe, K. J.; Tchobanoglous, G. *MWH's Water Treatment*; John Wiley and Sons, 2012.
- (169) Hildebrandt Ruiz, L.; Paciga, A. L.; Cerully, K. M.; Nenes, A.; Donahue, N. M.; Pandis, S. N. Formation and Aging of Secondary Organic Aerosol from Toluene: Changes in Chemical Composition, Volatility, and Hygroscopicity. *Atmos Chem Phys* **2015**, *15* (14), 8301–8313. <https://doi.org/10.5194/ACP-15-8301-2015>.
- (170) Easteal, A. J. Tracer Diffusion in Aqueous Sucrose and Urea Solutions. *Can. J. CHEM* **1990**, *68* (9), 1611–1615. <https://doi.org/10.1139/V90-248>.
- (171) Li, Y. J.; Chen, Q.; Guzman, M. I.; Chan, C. K.; Martin, S. T. Second-Generation Products Contribute Substantially to the Particle-Phase Organic Material Produced by  $\beta$ -Caryophyllene Ozonolysis. *Atmos. Chem. Phys* **2011**, *11*, 121–132. <https://doi.org/10.5194/acp-11-121-2011>.



- (172) Cheng, Y.; Su, H.; Koop, T.; Mikhailov, E.; Pöschl, U. Size Dependence of Phase Transitions in Aerosol Nanoparticles. *Nature Communications* 2015 6:1 **2015**, 6 (1), 1–7. <https://doi.org/10.1038/ncomms6923>.
- (173) Mattsson, J.; Forrest, J. A.; Börjesson, L. Quantifying Glass Transition Behavior in Ultrathin Free-Standing Polymer Films. *Phys. Rev. E: Stat. Phys., Plasmas, Fluids, Relat. Interdiscip. Top.* **2000**, 62, 5187–5200.
- (174) Alcoutlabi, M.; McKenna, G. B. Effects of Confinement on Material Behaviour at the Nanometre Size Scale. *J. Phys.: Condens. Matter* **2005**, 17, R461–E524. <https://doi.org/10.1088/0953-8984/17/15/R01>.
- (175) Martin, S. T.; Andreae, M. O.; Althausen, D.; Artaxo, P.; Baars, H.; Borrmann, S.; Chen, Q.; Farmer, D. K.; Guenther, A.; Gunthe, S. S.; Jimenez, J. L.; Karl, T.; Longo, K.; Manzi, A.; Müller, T.; Pauliquevis, T.; Petters, M. D.; Prenni, A. J.; Pöschl, U.; Rizzo, L. v.; Schneider, J.; Smith, J. N.; Swietlicki, E.; Tota, J.; Wang, J.; Wiedensohler, A.; Zorn, S. R. An Overview of the Amazonian Aerosol Characterization Experiment 2008 (AMAZE-08). *Atmos Chem Phys* **2010**, 10 (23), 11415–11438. <https://doi.org/10.5194/acp-10-11415-2010>.
- (176) Pöschl, U.; Martin, S. T.; Sinha, B.; Chen, Q.; Gunthe, S. S.; Huffman, J. A.; Borrmann, S.; Farmer, D. K.; Garland, R. M.; Helas, G.; Jimenez, J. L.; King, S. M.; Manzi, A.; Mikhailov, E.; Pauliquevis, T.; Petters, M. D.; Prenni, A. J.; Roldin, P.; Rose, D.; Schneider, J.; Su, H.; Zorn, S. R.; Artaxo, P.; Andreae, M. O. Rainforest Aerosols as Biogenic Nuclei of Clouds and Precipitation in the Amazon. *Science (1979)* **2010**, 329 (5998), 1513–1516. <https://doi.org/10.1126/science.1191056>.
- (177) Riipinen, I.; Pierce, J. R.; Yli-Juuti, T.; Nieminen, T.; Häkkinen, S.; Ehn, M.; Junninen, H.; Lehtipalo, K.; Petäjä, T.; Slowik, J.; Chang, R.; Shantz, N. C.; Abbatt, J.; Leaitch, W. R.; Kerminen, V.-M.; Worsnop, D. R.; Pandis, S. N.; Donahue, N. M.; Kulmala, M. Organic Condensation: A Vital Link Connecting Aerosol Formation to Cloud Condensation Nuclei (CCN) Concentrations. *Atmos Chem Phys* **2011**, 11 (8), 3865–3878. <https://doi.org/10.5194/acp-11-3865-2011>.
- (178) Maclean, A. M.; Butenhoff, C. L.; Grayson, J. W.; Barsanti, K.; Jimenez, J. L.; Bertram, A. K. Mixing Times of Organic Molecules within Secondary Organic Aerosol Particles: A Global Planetary Boundary Layer Perspective. *Atmos. Chem. Phys* **2017**, 17, 13037–13048. <https://doi.org/10.5194/acp-17-13037-2017>.
- (179) Raatikainen, T.; Vaattovaara, P.; Tiitta, P.; Miettinen, P.; Rautiainen, J.; Ehn, M.; Kulmala, M.; Laaksonen, A.; Worsnop, D. R. Physicochemical Properties and Origin of Organic Groups Detected in Boreal Forest Using an Aerosol Mass Spectrometer. *Atmos Chem Phys* **2010**, 10 (4), 2063–2077. <https://doi.org/10.5194/ACP-10-2063-2010>.
- (180) Jain, S.; Fischer, K. B.; Petrucci, G. A. The Influence of Absolute Mass Loading of Secondary Organic Aerosols on Their Phase State. *Atmosphere* 2018, Vol. 9, Page 131 **2018**, 9 (4), 131. <https://doi.org/10.3390/ATMOS9040131>.

- (181) Donahue, N. M.; Robinson, A. L.; Pandis, S. N. Atmospheric Organic Particulate Matter: From Smoke to Secondary Organic Aerosol. *Atmos Environ* **2009**, *43* (1), 94–106. <https://doi.org/10.1016/J.ATMOENV.2008.09.055>.
- (182) Ye, Q.; Upshur, M. A.; Robinson, E. S.; Geiger, F. M.; Sullivan, R. C.; Thomson, R. J.; Donahue, N. M. Following Particle-Particle Mixing in Atmospheric Secondary Organic Aerosols by Using Isotopically Labeled Terpenes. *Chem* **2018**, *4* (2), 318–333. <https://doi.org/10.1016/j.chempr.2017.12.008>.
- (183) Roach, P. J.; Laskin, J.; Laskin, A. Molecular Characterization of Organic Aerosols Using Nanospray-Desorption/ Electro spray Ionization-Mass Spectrometry. *Anal Chem* **2010**, *82* (19), 7979–7986. <https://doi.org/10.1021/ac101449p>.
- (184) Laskin, J.; Laskin, A.; Roach, P. J.; Slysz, G. W.; Anderson, G. A.; Nizkorodov, S. A.; Bones, D. L.; Nguyen, L. Q. High-Resolution Desorption Electro spray Ionization Mass Spectrometry for Chemical Characterization of Organic Aerosols. *Anal Chem* **2010**, *82* (5), 2048–2058. [https://doi.org/10.1021/AC902801F/ASSET/IMAGES/MEDIUM/AC-2009-02801F\\_0008.GIF](https://doi.org/10.1021/AC902801F/ASSET/IMAGES/MEDIUM/AC-2009-02801F_0008.GIF).
- (185) Klodt, A.; Romonosky, D.; Lin, P.; Laskin, J.; Laskin, A.; Nizkorodov, S. A. Aqueous Photochemistry of Secondary Organic Aerosol of  $\alpha$ -Pinene and  $\alpha$ -Humulene in the Presence of Hydrogen Peroxide or Inorganic Salts. *ACS Earth Space Chem* **2019**, acsearthspacechem.9b00222. <https://doi.org/10.1021/acsearthspacechem.9b00222>.
- (186) Romonosky, D. E.; Li, Y.; Shiraiwa, M.; Laskin, A.; Laskin, J.; Nizkorodov, S. A. Aqueous Photochemistry of Secondary Organic Aerosol of  $\alpha$ -Pinene and  $\alpha$ -Humulene Oxidized with Ozone, Hydroxyl Radical, and Nitrate Radical. *Journal of Physical Chemistry A* **2017**, *121* (6), 1298–1309. [https://doi.org/10.1021/ACS.JPCA.6B10900/SUPPL\\_FILE/JP6B10900\\_SI\\_001.XLSX](https://doi.org/10.1021/ACS.JPCA.6B10900/SUPPL_FILE/JP6B10900_SI_001.XLSX).
- (187) Jaoui, M.; Kamens, R. M. Gas and Particulate Products Distribution from the Photooxidation of  $\alpha$ -Humulene in the Presence of NO<sub>x</sub>, Natural Atmospheric Air and Sunlight. *Journal of Atmospheric Chemistry* **2003**, *46* (1), 29–54. <https://doi.org/10.1023/A:1024843525968>.
- (188) Richters, S.; Herrmann, H.; Berndt, T. Different Pathways of the Formation of Highly Oxidized Multifunctional Organic Compounds (HOMs) from the Gas-Phase Ozonolysis of  $\beta$ -Caryophyllene. *Atmos Chem Phys* **2016**, *16* (15), 9831–9845. <https://doi.org/10.5194/ACP-16-9831-2016>.
- (189) Kenseth, C. M.; Hafeman, N. J.; Huang, Y.; Dalleska, N. F.; Stoltz, B. M.; Seinfeld, J. H. Synthesis of Carboxylic Acid and Dimer Ester Surrogates to Constrain the Abundance and Distribution of Molecular Products in  $\alpha$ -Pinene and  $\beta$ -Pinene Secondary Organic Aerosol. *Environ Sci Technol* **2020**. <https://doi.org/10.1021/acs.est.0c01566>.
- (190) Nguyen, T. B.; Nizkorodov, S. A.; Laskin, A.; Laskin, J. An Approach toward Quantification of Organic Compounds in Complex Environmental Samples Using High-Resolution Electro spray Ionization Mass Spectrometry. *Anal. Methods* **2013**, *5* (1), 72–80. <https://doi.org/10.1039/C2AY25682G>.
- (191) Hinks, M. L.; Montoya-Aguilera, J.; Ellison, L.; Lin, P.; Laskin, A.; Laskin, J.; Shiraiwa, M.; Dabdub, D.; Nizkorodov, S. A. Effect of Relative Humidity on the Composition of Secondary Organic

- Aerosol from the Oxidation of Toluene. *Atmos. Chem. Phys* **2018**, *18*, 1643–1652. <https://doi.org/10.5194/acp-18-1643-2018>.
- (192) Shrivastava, M.; Cappa, C. D.; Fan, J.; Goldstein, A. H.; Guenther, A. B.; Jimenez, J. L.; Kuang, C.; Laskin, A.; Martin, S. T.; Ng, N. L.; Petaja, T.; Pierce, J. R.; Rasch, P. J.; Roldin, P.; Seinfeld, J. H.; Shilling, J.; Smith, J. N.; Thornton, J. A.; Volkamer, R.; Wang, J.; Worsnop, D. R.; Zaveri, R. A.; Zelenyuk, A.; Zhang, Q. Recent Advances in Understanding Secondary Organic Aerosol: Implications for Global Climate Forcing. *Reviews of Geophysics* **2017**, *55* (2), 509–559. <https://doi.org/10.1002/2016RG000540>.
- (193) McFiggans, G.; Mentel, T. F.; Wildt, J.; Pullinen, I.; Kang, S.; Kleist, E.; Schmitt, S.; Springer, M.; Tillmann, R.; Wu, C.; Zhao, D.; Hallquist, M.; Faxon, C.; Le Breton, M.; Hallquist, Å. M.; Simpson, D.; Bergström, R.; Jenkin, M. E.; Ehn, M.; Thornton, J. A.; Alfarra, M. R.; Bannan, T. J.; Percival, C. J.; Priestley, M.; Topping, D.; Kiendler-Scharr, A. Secondary Organic Aerosol Reduced by Mixture of Atmospheric Vapours. *Nature* **2019**, *565* (7741), 587–593. <https://doi.org/10.1038/s41586-018-0871-y>.
- (194) Niinemets, Ü.; Kännaste, A.; Copolovici, L. Quantitative Patterns between Plant Volatile Emissions Induced by Biotic Stresses and the Degree of Damage. *Front Plant Sci* **2013**, *4* (July), 1–15. <https://doi.org/10.3389/fpls.2013.00262>.
- (195) Niinemets, Ü.; Arneth, A.; Kuhn, U.; Monson, R. K.; Peñuelas, J.; Staudt, M. The Emission Factor of Volatile Isoprenoids: Stress, Acclimation, and Developmental Responses. *Biogeosciences* **2010**, *7* (7), 2203–2223. <https://doi.org/10.5194/bg-7-2203-2010>.
- (196) Loreto, F.; Schnitzler, J. P. Abiotic Stresses and Induced BVOCs. *Trends in Plant Science*. Elsevier Current Trends March 1, 2010, pp 154–166. <https://doi.org/10.1016/j.tplants.2009.12.006>.
- (197) Kivimäenpää, M.; Babalola, A. B.; Joutsensaari, J.; Holopainen, J. K. Methyl Salicylate and Sesquiterpene Emissions Are Indicative for Aphid Infestation on Scots Pine. *Forests* **2020**, *11* (5), 573. <https://doi.org/10.3390/F11050573>.
- (198) Holopainen, J. K. Multiple Functions of Inducible Plant Volatiles. *Trends Plant Sci* **2004**, *9* (11), 529–533. <https://doi.org/10.1016/j.tplants.2004.09.006>.
- (199) Vickers, C. E.; Gershenzon, J.; Ler dau, M. T.; Loreto, F. A Unified Mechanism of Action for Volatile Isoprenoids in Plant Abiotic Stress. *Nature Chemical Biology*. Nature Publishing Group April 17, 2009, pp 283–291. <https://doi.org/10.1038/nchembio.158>.
- (200) Loreto, F.; Dicke, M.; Schnitzler, J. P.; Turlings, T. C. J. Plant Volatiles and the Environment. *Plant Cell Environ* **2014**, *37* (8), 1905–1908. <https://doi.org/10.1111/pce.12369>.
- (201) Mentel, Th. F.; Kleist, E.; Andres, S.; Dal Maso, M.; Hohaus, T.; Kiendler-Scharr, A.; Rudich, Y.; Springer, M.; Tillmann, R.; Uerlings, R.; Wahner, A.; Wildt, J. Secondary Aerosol Formation from Stress-Induced Biogenic Emissions and Possible Climate Feedbacks. *Atmos Chem Phys* **2013**, *13* (17), 8755–8770. <https://doi.org/10.5194/acp-13-8755-2013>.
- (202) Joutsensaari, J.; Yli-Pirilä, P.; Korhonen, H.; Arola, A.; Blande, J. D.; Heijari, J.; Kivimäenpää, M.; Mikkonen, S.; Hao, L.; Miettinen, P.; Lyytikäinen-Saarenmaa, P.; Faiola, C. L.; Laaksonen, A.;

- Holopainen, J. K. Biotic Stress Accelerates Formation of Climate-Relevant Aerosols in Boreal Forests. *Atmos Chem Phys* **2015**, *15* (21), 12139–12157. <https://doi.org/10.5194/acp-15-12139-2015>.
- (203) Zhao, D. F.; Buchholz, A.; Tillmann, R.; Kleist, E.; Wu, C.; Rubach, F.; Kiendler-Scharr, A.; Rudich, Y.; Wildt, J.; Mentel, T. F. Environmental Conditions Regulate the Impact of Plants on Cloud Formation. *Nat Commun* **2017**, *8* (1), 14067. <https://doi.org/10.1038/ncomms14067>.
- (204) Zaveri, R. A.; Shilling, J. E.; Zelenyuk, A.; Liu, J.; Bell, D. M.; D'Ambro, E. L.; Gaston, C. J.; Thornton, J. A.; Laskin, A.; Lin, P.; Wilson, J.; Easter, R. C.; Wang, J.; Bertram, A. K.; Martin, S. T.; Seinfeld, J. H.; Worsnop, D. R. Growth Kinetics and Size Distribution Dynamics of Viscous Secondary Organic Aerosol. *Environ Sci Technol* **2018**, *52* (3), 1191–1199. <https://doi.org/10.1021/acs.est.7b04623>.
- (205) Shiraiwa, M.; Li, Y.; Tsimpidi, A. P.; Karydis, V. A.; Berkemeier, T.; Pandis, S. N.; Lelieveld, J.; Koop, T.; Pöschl, U. Global Distribution of Particle Phase State in Atmospheric Secondary Organic Aerosols. *Nat Commun* **2017**, *8* (1), 1–7. <https://doi.org/10.1038/ncomms15002>.
- (206) Dette, H. P.; Qi, M.; Schröder, D. C.; Godt, A.; Koop, T. Glass-Forming Properties of 3-Methylbutane-1,2,3-Tricarboxylic Acid and Its Mixtures with Water and Pinonic Acid. *Journal of Physical Chemistry A* **2014**, *118* (34), 7024–7033. <https://doi.org/10.1021/jp505910w>.
- (207) Li, Y.; Tasoglou, A.; Liangou, A.; Cain, K. P.; Jahn, L.; Gu, P.; Kostenidou, E.; Pandis, S. N. Cloud Condensation Nuclei Activity and Hygroscopicity of Fresh and Aged Cooking Organic Aerosol. *Atmos Environ* **2018**, *176*, 103–109. <https://doi.org/10.1016/j.atmosenv.2017.11.035>.
- (208) Evoy, E.; Maclean, A. M.; Rovelli, G.; Li, Y.; Tsimpidi, A. P.; Karydis, V. A.; Kamal, S.; Lelieveld, J.; Shiraiwa, M.; Reid, J. P.; Bertram, A. K. Predictions of Diffusion Rates of Large Organic Molecules in Secondary Organic Aerosols Using the Stokes-Einstein and Fractional Stokes-Einstein Relations. *Atmos Chem Phys* **2019**, *19* (15), 10073–10085. <https://doi.org/10.5194/acp-19-10073-2019>.
- (209) Price, H. C.; Mattsson, J.; Murray, B. J. Sucrose Diffusion in Aqueous Solution. *Physical Chemistry Chemical Physics* **2016**, *18* (28), 19207–19216. <https://doi.org/10.1039/c6cp03238a>.
- (210) Li, Y.; Pöschl, U.; Shiraiwa, M. Molecular Corridors and Parameterizations of Volatility in the Chemical Evolution of Organic Aerosols. *Atmos. Chem. Phys* **2016**, *16*, 3327–3344. <https://doi.org/10.5194/acp-16-3327-2016>.
- (211) Freedman, M. A. Phase Separation in Organic Aerosol. *Chemical Society Reviews*. Royal Society of Chemistry December 21, 2017, pp 7694–7705. <https://doi.org/10.1039/c6cs00783j>.
- (212) Renbaum-Wolff, L.; Song, M.; Marcolli, C.; Zhang, Y.; Liu, P. F.; Grayson, J. W.; Geiger, F. M.; Martin, S. T.; Bertram, A. K. Observations and Implications of Liquid-Liquid Phase Separation at High Relative Humidities in Secondary Organic Material Produced by  $\alpha$ -Pinene Ozonolysis without Inorganic Salts. *Atmos Chem Phys* **2016**, *16* (12), 7969–7979. <https://doi.org/10.5194/acp-16-7969-2016>.

- (213) Liu, P.; Song, M.; Zhao, T.; Gunthe, S. S.; Ham, S.; He, Y.; Qin, Y. M.; Gong, Z.; Amorim, J. C.; Bertram, A. K.; Martin, S. T. Resolving the Mechanisms of Hygroscopic Growth and Cloud Condensation Nuclei Activity for Organic Particulate Matter. *Nat Commun* **2018**, *9* (1), 1–10. <https://doi.org/10.1038/s41467-018-06622-2>.
- (214) Song, M.; Liu, P.; Martin, S. T.; Bertram, A. K. Liquid–Liquid Phase Separation in Particles Containing Secondary Organic Material Free of Inorganic Salts. *Atmos Chem Phys* **2017**, *17* (18), 11261–11271. <https://doi.org/10.5194/acp-17-11261-2017>.
- (215) Rastak, N.; Pajunoja, A.; Acosta Navarro, J. C.; Ma, J.; Song, M.; Partridge, D. G.; Kirkevåg, A.; Leong, Y.; Hu, W. W.; Taylor, N. F.; Lambe, A.; Cerully, K.; Bougiatioti, A.; Liu, P.; Krejci, R.; Petäjä, T.; Percival, C.; Davidovits, P.; Worsnop, D. R.; Ekman, A. M. L.; Nenes, A.; Martin, S.; Jimenez, J. L.; Collins, D. R.; Topping, D. O.; Bertram, A. K.; Zuend, A.; Virtanen, A.; Riipinen, I. Microphysical Explanation of the RH-Dependent Water Affinity of Biogenic Organic Aerosol and Its Importance for Climate. *Geophys Res Lett* **2017**, *44* (10), 5167–5177. <https://doi.org/10.1002/2017GL073056>.
- (216) Schmedding, R.; Ma, M.; Zhang, Y.; Farrell, S.; Pye, H. O. T.; Chen, Y.; Wang, C.; Rasool, Q. Z.; Budisulistiorini, S. H.; Ault, A. P.; Surratt, J. D.; Vizuete, W.  $\alpha$ -Pinene-Derived Organic Coatings on Acidic Sulfate Aerosol Reduce Secondary Organic Aerosol Formation from Isoprene in a Box Model. *Atmos. Environ.* **2019**, *213*, 456–462.
- (217) Davies, J. F.; Zuend, A.; Wilson, K. R. Technical Note: The Role of Evolving Surface Tension in the Formation of Cloud Droplets. *Atmos Chem Phys* **2019**, *19* (5), 2933–2946. <https://doi.org/10.5194/acp-19-2933-2019>.
- (218) Ovadnevaite, J.; Zuend, A.; Laaksonen, A.; Sanchez, K. J.; Roberts, G.; Ceburnis, D.; Decesari, S.; Rinaldi, M.; Hodas, N.; Facchini, M. C.; Seinfeld, J. H.; O’Dowd, C. Surface Tension Prevails over Solute Effect in Organic-Influenced Cloud Droplet Activation. *Nature* **2017**, *546* (7660), 637–641. <https://doi.org/10.1038/nature22806>.
- (219) Gauthier, S.; Bernier, P.; Kuuluvainen, T.; Shvidenko, A. Z.; Schepaschenko, D. G. Boreal Forest Health and Global Change. *Science (1979)* **2015**, *349* (6250), 819–822. <https://doi.org/10.1126/science.aaa9092>.
- (220) Ylisirniö, A.; Buchholz, A.; Mohr, C.; Li, Z.; Barreira, L.; Lambe, A.; Faiola, C.; Kari, E.; Yli-Juuti, T.; Nizkorodov, S. A.; Worsnop, D. R.; Virtanen, A.; Schobesberger, S. Composition and Volatility of SOA Formed from Oxidation of Real Tree Emissions Compared to Single VOC-Systems. *Atmos. Chem. Phys* **2020**, *20*, 5629–5644. <https://doi.org/10.5194/acp-2019-939>.
- (221) Kourtchev, I.; Bejan, I.; Sodeau, J. R.; Wenger, J. C. Gas Phase Reaction of OH Radicals with (E)- $\beta$ -Farnesene at  $296 \pm 2$  K: Rate Coefficient and Carbonyl Products. *Atmos Environ* **2012**, *46*, 338–345. <https://doi.org/10.1016/j.atmosenv.2011.09.061>.
- (222) Marple, V. A.; Rubow, K. L.; Behm, S. M. A Microorifice Uniform Deposit Impactor (Moudi): Description, Calibration, and Use. *Aerosol Science and Technology* **1991**, *14* (4), 434–436. <https://doi.org/10.1080/02786829108959504>.

- (223) Bateman, A. P.; Bertram, A. K.; Martin, S. T. Hygroscopic Influence on the Semisolid-to-Liquid Transition of Secondary Organic Materials. *Journal of Physical Chemistry A* **2015**, *119* (19), 4386–4395. <https://doi.org/10.1021/jp508521c>.
- (224) Fleming, L. T.; Lin, P.; Laskin, A.; Laskin, J.; Weltman, R.; Edwards, R. D.; Arora, N. K.; Yadav, A.; Meinardi, S.; Blake, D. R.; Pillarisetti, A.; Smith, K. R.; Nizkorodov, S. A. Molecular Composition of Particulate Matter Emissions from Dung and Brushwood Burning Household Cookstoves in Haryana, India. *Atmos Chem Phys* **2018**, *18* (4), 2461–2480. <https://doi.org/10.5194/acp-18-2461-2018>.
- (225) Murray, B. J.; Haddrell, A. E.; Peppe, S.; Davies, J. F.; Reid, J. P.; O’Sullivan, D.; Price, H. C.; Kumar, R.; Saunders, R. W.; Plane, J. M. C.; Umo, N. S.; Wilson, T. W. Glass Formation and Unusual Hygroscopic Growth of Iodic Acid Solution Droplets with Relevance for Iodine Mediated Particle Formation in the Marine Boundary Layer. *Atmos Chem Phys* **2012**, *12* (18), 8575–8587. <https://doi.org/10.5194/acp-12-8575-2012>.
- (226) Baudry, J.; Charlaix, E.; Tonck, A.; Mazuyer, D. Experimental Evidence for a Large Slip Effect at a Nonwetting Fluid-Solid Interface. *Langmuir* **2001**, *17* (17), 5232–5236. <https://doi.org/10.1021/la0009994>.
- (227) Bhushan, B.; Wang, Y.; Maali, A. Boundary Slip Study on Hydrophilic, Hydrophobic, and Superhydrophobic Surfaces with Dynamic Atomic Force Microscopy. *Langmuir* **2009**, *25* (14), 8117–8121. <https://doi.org/10.1021/la900612s>.
- (228) Cho, J. H. J.; Law, B. M.; Rieutord, F. Dipole-Dependent Slip of Newtonian Liquids at Smooth Solid Hydrophobic Surfaces. *Phys Rev Lett* **2004**, *92* (16), 166102. <https://doi.org/10.1103/PhysRevLett.92.166102>.
- (229) Churaev, N. V.; Sobolev, V. D.; Somov, A. N. Slippage of Liquids over Lyophobic Solid Surfaces. *J Colloid Interface Sci* **1984**, *97* (2), 574–581. [https://doi.org/10.1016/0021-9797\(84\)90330-8](https://doi.org/10.1016/0021-9797(84)90330-8).
- (230) Cottin-Bizonne, C.; Jurine, S.; Baudry, J.; Crassous, J.; Restagno, F.; Charlaix, É. Nanorheology: An Investigation of the Boundary Condition at Hydrophobic and Hydrophilic Interfaces. *European Physical Journal E* **2002**, *9* (1), 47–53. <https://doi.org/10.1140/epje/i2001-10112-9>.
- (231) Cottin-Bizonne, C.; Cross, B.; Steinberger, A.; Charlaix, E. Boundary Slip on Smooth Hydrophobic Surfaces: Intrinsic Effects and Possible Artifacts. *Phys Rev Lett* **2005**, *94* (5), 1–4. <https://doi.org/10.1103/PhysRevLett.94.056102>.
- (232) Craig, V. S. J.; Neto, C.; Williams, D. R. M. Shear-Dependent Boundary Slip in an Aqueous Newtonian Liquid. *Phys Rev Lett* **2001**, *87* (5), 05450414. <https://doi.org/10.1103/PhysRevLett.87.054504>.
- (233) Jing, D.; Bhushan, B. Boundary Slip of Superoleophilic, Oleophobic, and Superoleophobic Surfaces Immersed in Deionized Water, Hexadecane, and Ethylene Glycol. *Langmuir* **2013**, *29* (47), 14691–14700. <https://doi.org/10.1021/la4030876>.
- (234) Joseph, P.; Tabeling, P. Direct Measurement of the Apparent Slip Length. *Phys Rev E Stat Nonlin Soft Matter Phys* **2005**, *71* (3), 1–4. <https://doi.org/10.1103/PhysRevE.71.035303>.

- (235) McBride, S. P.; Law, B. M. Viscosity Dependent Liquid Slip at Molecularly Smooth Hydrophobic Surfaces. *Phys Rev E* **2009**, *80*, 060601. <https://doi.org/10.1103/PhysRevE.80.060601>.
- (236) Tretheway, D. C.; Meinhart, C. D. Apparent Fluid Slip at Hydrophobic Microchannel Walls. *Physics of Fluids* **2002**, *14* (3), L9–L12. <https://doi.org/10.1063/1.1432696>.
- (237) Vinogradova, O. I.; Koynov, K.; Best, A.; Feuillebois, F. Direct Measurements of Hydrophobic Slippage Using Double-Focus Fluorescence Cross-Correlation. *Phys Rev Lett* **2009**, *102* (11), 118302. <https://doi.org/10.1103/PhysRevLett.102.118302>.
- (238) Zhu, L.; Attard, P.; Neto, C. Reconciling Slip Measurements in Symmetric and Asymmetric Systems. *Langmuir* **2012**, *28* (20), 7768–7774. <https://doi.org/10.1021/la301040d>.
- (239) Zaveri, R. A.; Shilling, J. E.; Zelenyuk, A.; Zawadowicz, M. A.; Suski, K.; China, S.; Bell, D. M.; Veghte, D.; Laskin, A. Particle-Phase Diffusion Modulates Partitioning of Semivolatile Organic Compounds to Aged Secondary Organic Aerosol. *Environ Sci Technol* **2020**, *54* (5), 2595–2605. <https://doi.org/10.1021/acs.est.9b05514>.
- (240) Li, Z.; Tikkanen, O. P.; Buchholz, A.; Hao, L.; Kari, E.; Yli-Juuti, T.; Virtanen, A. Effect of Decreased Temperature on the Evaporation of  $\alpha$ -Pinene Secondary Organic Aerosol Particles. *ACS Earth Space Chem* **2019**, *3* (12), 2775–2785. <https://doi.org/10.1021/acsearthspacechem.9b00240>.
- (241) Evoy, E.; Kamal, S.; Patey, G. N.; Martin, S. T.; Bertram, A. K. Unified Description of Diffusion Coefficients from Small to Large Molecules in Organic-Water Mixtures. *J Phys Chem A* **2020**, *124* (11), 2301–2308. <https://doi.org/10.1021/acs.jpca.9b11271>.
- (242) Hallett, J. The Temperature Dependence of the Viscosity of Supercooled Water. *Proceedings of the Physical Society* **1963**, *82* (6), 1046–1050. <https://doi.org/10.1088/0370-1328/82/6/326>.
- (243) Crittenden, J. C.; Trussel, R. R.; Hand, D. W.; Howe, K. J.; Tchobanoglous, G. *MWH's Water Treatment*; John Wiley and Sons, 2012.
- (244) Huff Hartz, K. E.; Rosenørn, T.; Ferchak, S. R.; Raymond, T. M.; Bilde, M.; Donahue, N. M.; Pandis, S. N. Cloud Condensation Nuclei Activation of Monoterpene and Sesquiterpene Secondary Organic Aerosol. *Journal of Geophysical Research: Atmospheres* **2005**, *110* (D14), n/a-n/a. <https://doi.org/10.1029/2004JD005754>.
- (245) Nguyen, T. B.; Nizkorodov, S. A.; Laskin, A.; Laskin, J. An Approach toward Quantification of Organic Compounds in Complex Environmental Samples Using High-Resolution Electrospray Ionization Mass Spectrometry. *Analytical Methods* **2013**, *5* (1), 72–80. <https://doi.org/10.1039/c2ay25682g>.
- (246) Petters, M. D.; Kreidenweis, S. M. A Single Parameter Representation of Hygroscopic Growth and Cloud Condensation Nucleus Activity. *Atmos Chem Phys* **2007**, *7* (8), 1961–1971. <https://doi.org/10.5194/acp-7-1961-2007>.
- (247) Kuwata, M.; Martin, S. T. Phase of Atmospheric Secondary Organic Material Affects Its Reactivity. *Proc Natl Acad Sci U S A* **2012**, *109* (43), 17354–17359. <https://doi.org/10.1073/pnas.1209071109>.

- (248) Romonosky, D. E.; Laskin, A.; Laskin, J.; Nizkorodov, S. A. High-Resolution Mass Spectrometry and Molecular Characterization of Aqueous Photochemistry Products of Common Types of Secondary Organic Aerosols. *J Phys Chem A* **2015**, *119* (11), 2594–2606. <https://doi.org/10.1021/jp509476r>.
- (249) Haddad, I. El; Marchand, N.; Temime-Roussel, B.; Wortham, H.; Piot, C.; Besombes, J.-L.; Baduel, C.; Voisin, D.; Armengaud, A.; Jaffrezo, J.-L. Atmospheric Chemistry and Physics Insights into the Secondary Fraction of the Organic Aerosol in a Mediterranean Urban Area: Marseille. *Atmos. Chem. Phys* **2011**, *11*, 2059–2079. <https://doi.org/10.5194/acp-11-2059-2011>.
- (250) Jaoui, M.; Corse, E.; Kleindienst, T. E.; Offenber, J. H.; Lewandowski, M.; Edney, E. O. Analysis of Secondary Organic Aerosol Compounds from the Photooxidation of D-Limonene in the Presence of NO<sub>x</sub> and Their Detection in Ambient PM<sub>2.5</sub>. *Environ Sci Technol* **2006**, *40* (12), 3819–3828. <https://doi.org/10.1021/es052566z>.
- (251) Fang, W.; Gong, L.; Sheng, L. Online Analysis of Secondary Organic Aerosols from OH-Initiated Photooxidation and Ozonolysis of  $\alpha$ -Pinene,  $\beta$ -Pinene,  $\Delta$  3-Carene, and d-Limonene by Thermal Desorption-Photoionisation Aerosol Mass Spectrometry. *Environ. Chem* **2017**, *14*, 75–90. [https://doi.org/10.1071/EN16128\\_AC](https://doi.org/10.1071/EN16128_AC).
- (252) Jaoui, M.; Lewandowski, M.; Docherty, K. S.; Corse, E. W.; Lonneman, W. A.; Offenber, J. H.; Kleindienst, T. E. Photooxidation of Farnesene Mixtures in the Presence of NO<sub>x</sub>: Analysis of Reaction Products and Their Implication to Ambient PM<sub>2.5</sub>. *Atmos Environ* **2016**, *130*, 190–201. <https://doi.org/10.1016/j.atmosenv.2015.10.091>.
- (253) Vander Wall, A. C.; Perraud, V.; Wingen, L. M.; Finlayson-Pitts, B. J. Evidence for a Kinetically Controlled Burying Mechanism for Growth of High Viscosity Secondary Organic Aerosol. *Environ Sci Process Impacts* **2020**, *22* (1), 66–83. <https://doi.org/10.1039/c9em00379g>.
- (254) Krapf, M.; El Haddad, I.; Bruns, E. A.; Molteni, U.; Daellenbach, K. R.; Prévôt, A. S. H.; Baltensperger, U.; Dommen, J. Labile Peroxides in Secondary Organic Aerosol. *Chem* **2016**, *1* (4), 603–616. <https://doi.org/10.1016/j.chempr.2016.09.007>.
- (255) Li, H.; Chen, Z.; Huang, L.; Huang, D. Organic Peroxides' Gas-Particle Partitioning and Rapid Heterogeneous Decomposition on Secondary Organic Aerosol. *Atmos. Chem. Phys* **2016**, *16*, 1837–1848. <https://doi.org/10.5194/acp-16-1837-2016>.
- (256) Bertram, A. K.; Martin, S. T.; Hanna, S. J.; Smith, M. L.; Bodsworth, A.; Chen, Q.; Kuwata, M.; Liu, A.; You, Y.; Zorn, S. R. Predicting the Relative Humidities of Liquid-Liquid Phase Separation, Efflorescence, and Deliquescence of Mixed Particles of Ammonium Sulfate, Organic Material, and Water Using the Organic-to-Sulfate Mass Ratio of the Particle and the Oxygen-to-Carbon Elemental Ratio of the Organic Component. *Atmos Chem Phys* **2011**, *11* (21), 10995–11006. <https://doi.org/10.5194/acp-11-10995-2011>.
- (257) Varutbangkul, V.; Brechtel, F. J.; Bahreini, R.; Ng, N. L.; Keywood, M. D.; Kroll, J. H.; Flagan, R. C.; Seinfeld, J. H.; Lee, A.; Goldstein, A. H. Hygroscopicity of Secondary Organic Aerosols Formed by Oxidation of Cycloalkenes, Monoterpenes, Sesquiterpenes, and Related Compounds. *Atmos Chem Phys* **2006**, *6* (9), 2367–2388. <https://doi.org/10.5194/acp-6-2367-2006>.



- (258) Virtanen, A.; Kannosto, J.; Kuuluvainen, H.; Arffman, A.; Joutsensaari, J.; Saukko, E.; Hao, L.; Yli-Pirilä, P.; Tiitta, P.; Holopainen, J. K.; Keskinen, J.; Worsnop, D. R.; Smith, J. N.; Laaksonen, A. Bounce Behavior of Freshly Nucleated Biogenic Secondary Organic Aerosol Particles. *Atmos. Chem. Phys* **2011**, *11*, 8759–8766. <https://doi.org/10.5194/acp-11-8759-2011>.
- (259) Shiraiwa, M.; Berkemeier, T.; Schilling-Fahnestock, K. A.; Seinfeld, J. H.; Pöschl, U. Molecular Corridors and Kinetic Regimes in the Multiphase Chemical Evolution of Secondary Organic Aerosol. *Atmos Chem Phys* **2014**, *14* (16), 8323–8341. <https://doi.org/10.5194/acp-14-8323-2014>.
- (260) Thomas, L. H.; Meatyard, R.; Smith, H.; Davis, G. H. Viscosity Behavior of Associated Liquids at Lower Temperatures and Vapor Pressures. *J Chem Eng Data* **1979**, *24* (3), 161–164. <https://doi.org/10.1021/je60082a011>.
- (261) Rothfuss, N. E.; Petters, M. D. Influence of Functional Groups on the Viscosity of Organic Aerosol. *Environ Sci Technol* **2017**, *51* (1), 271–279. <https://doi.org/10.1021/acs.est.6b04478>.
- (262) Maclean, A. M.; Smith, N. R.; Li, Y.; Huang, Y.; Hettiyadura, A. P. S.; Crescenzo, G. V.; Shiraiwa, M.; Laskin, A.; Nizkorodov, S. A.; Bertram, A. K. Humidity-Dependent Viscosity of Secondary Organic Aerosol from Ozonolysis of  $\beta$ -Caryophyllene: Measurements, Predictions, and Implications. *ACS Earth Space Chem* **2021**. <https://doi.org/10.1021/acsearthspacechem.0c00296>.
- (263) Jaoui, M.; Leungsakul, S.; Kamens, R. M. *Gas and Particle Products Distribution from the Reaction of  $\beta$ -Caryophyllene with Ozone*; 2003; Vol. 45.
- (264) Lee, A.; Goldstein, A. H.; Kroll, J. H.; Ng, N. L.; Varutbangkul, V.; Flagan, R. C.; Seinfeld, J. H. Gas-Phase Products and Secondary Aerosol Yields from the Photooxidation of 16 Different Terpenes. *J Geophys Res* **2006**, *111* (D17), D17305. <https://doi.org/10.1029/2006JD007050>.
- (265) Shrivastava, M.; Andreae, M. O.; Artaxo, P.; Barbosa, H. M. J.; Berg, L. K.; Brito, J.; Ching, J.; Easter, R. C.; Fan, J.; Fast, J. D.; Feng, Z.; Fuentes, J. D.; Glasius, M.; Goldstein, A. H.; Alves, E. G.; Gomes, H.; Gu, D.; Guenther, A.; Jathar, S. H.; Kim, S.; Liu, Y.; Lou, S.; Martin, S. T.; McNeill, V. F.; Medeiros, A.; de Sá, S. S.; Shilling, J. E.; Springston, S. R.; Souza, R. A. F.; Thornton, J. A.; Isaacman-VanWertz, G.; Yee, L. D.; Ynoue, R.; Zaveri, R. A.; Zelenyuk, A.; Zhao, C. Urban Pollution Greatly Enhances Formation of Natural Aerosols over the Amazon Rainforest. *Nat Commun* **2019**, *10* (1), 1–12. <https://doi.org/10.1038/s41467-019-08909-4>.
- (266) Knudsen, J. T.; Eriksson, R.; Gershenzon, J.; Ståhl, B. Diversity and Distribution of Floral Scent. *The Botanical Review* **2006**, *72* (1), 1–120.
- (267) Clark, E. L.; Carroll, A. L.; Huber, D. P. W. Differences in the Constitutive Terpene Profile of Lodgepole Pine across a Geographical Range in British Columbia, and Correlation with Historical Attack by Mountain Pine Beetle. *Can. Entomol* **2010**, *142*, 557–573. <https://doi.org/10.4039/n10-022>.
- (268) Räisänen, T.; Ryyppö, A.; Kellomäki, S. Monoterpene Emission of a Boreal Scots Pine (*Pinus Sylvestris* L.) Forest. *Agric For Meteorol* **2009**, *149* (5), 808–819. <https://doi.org/10.1016/J.AGRFORMET.2008.11.001>.

- (269) Vickers, C. E.; Gershenzon, J.; Lerda, M. T.; Loreto, F. A Unified Mechanism of Action for Volatile Isoprenoids in Plant Abiotic Stress. *Nature Chemical Biology*. Nature Publishing Group April 17, 2009, pp 283–291. <https://doi.org/10.1038/nchembio.158>.
- (270) Kari, E.; Faiola, C. L.; Isokääntä, S.; Miettinen, P.; Yli-Pirilä, P.; Buchholz, A.; Kivimäenpää, M.; Mikkonen, S.; Holopainen, J. K.; Virtanen, A. Time-Resolved Characterization of Biotic Stress Emissions from Scots Pines Being Fed upon by Pine Weevil by Means of PTR-ToF-MS. **2019**, *2469* (June), 25–49.
- (271) Peñuelas, J.; Staudt, M. BVOCs and Global Change. *Trends Plant Sci* **2010**, *15* (3), 133–144. <https://doi.org/10.1016/J.TPLANTS.2009.12.005>.
- (272) Wu, Y.; Li, J.; Liu, H.; Qiao, G.; Huang, X. Investigating the Impact of Climate Warming on Phenology of Aphid Pests in China Using Long-Term Historical Data. *Insects* **2020**, *11* (3). <https://doi.org/10.3390/INSECTS11030167>.
- (273) Bergström, R.; Hallquist, M.; Simpson, D.; Wildt, J.; Mentel, T. F. Biotic Stress: A Significant Contributor to Organic Aerosol in Europe? *Atmos Chem Phys* **2014**, *14* (24), 13643–13660. <https://doi.org/10.5194/ACP-14-13643-2014>.
- (274) Rothfuss, N. E.; Petters, M. D. Influence of Functional Groups on the Viscosity of Organic Aerosol. *Environ Sci Technol* *51* (1), 271–279. <https://doi.org/10.1021/acs.est.6b04478>.
- (275) Li, Y.; Shiraiwa, M. Timescales of Secondary Organic Aerosols to Reach Equilibrium at Various Temperatures and Relative Humidities. *Atmos Chem Phys* **2019**, *19* (9), 5959–5971. <https://doi.org/10.5194/acp-19-5959-2019>.
- (276) Zaveri, R. A.; Wang, J.; Fan, J.; Zhang, Y.; Shilling, J. E.; Zelenyuk, A.; Mei, F.; Newsom, R.; Pekour, M.; Tomlinson, J.; Comstock, J. M.; Shrivastava, M.; Fortner, E.; Machado, L. A. T.; Artaxo, P.; Martin, S. T. Rapid Growth of Anthropogenic Organic Nanoparticles Greatly Alters Cloud Life Cycle in the Amazon Rainforest. *Sci Adv* **2022**, *8* (2), 329. [https://doi.org/10.1126/SCIADV.ABJ0329/SUPPL\\_FILE/SCIADV.ABJ0329\\_SM.PDF](https://doi.org/10.1126/SCIADV.ABJ0329/SUPPL_FILE/SCIADV.ABJ0329_SM.PDF).
- (277) Wolf, M. J.; Zhang, Y.; Zawadowicz, M. A.; Goodell, M.; Froyd, K.; Freney, E.; Sellegri, K.; Rösch, M.; Cui, T.; Winter, M.; Lacher, L.; Axisa, D.; DeMott, P. J.; Levin, E. J. T.; Gute, E.; Abbatt, J.; Koss, A.; Kroll, J. H.; Surratt, J. D.; Cziczo, D. J. A Biogenic Secondary Organic Aerosol Source of Cirrus Ice Nucleating Particles. *Nature Communications* *2020 11:1* **2020**, *11* (1), 1–9. <https://doi.org/10.1038/s41467-020-18424-6>.
- (278) Smith, N. R.; Crescenzo, G. v.; Huang, Y.; Hettiyadura, A. P. S.; Siemens, K.; Li, Y.; Faiola, C. L.; Laskin, A.; Shiraiwa, M.; Bertram, A. K.; Nizkorodov, S. A. Viscosity and Liquid–Liquid Phase Separation in Healthy and Stressed Plant SOA. *Environmental Science: Atmospheres* **2021**, *1* (3), 140–153. <https://doi.org/10.1039/D0EA00020E>.
- (279) Barreira, L. M. F.; Ylisirniö, A.; Pullinen, I.; Buchholz, A.; Li, Z.; Lipp, H.; Junninen, H.; Hörrak, U.; Noe, S. M.; Krasnova, A.; Krasnov, D.; Kask, K.; Talts, E.; Niinemets, Ü.; Ruiz-Jimenez, J.; Schobesberger, S. The Importance of Sesquiterpene Oxidation Products for Secondary Organic Aerosol Formation in a Springtime Hemiboreal Forest. *Atmos. Chem. Phys* **2021**, *21*, 11781–11800. <https://doi.org/10.5194/acp-21-11781-2021>.

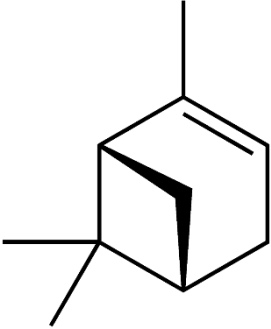
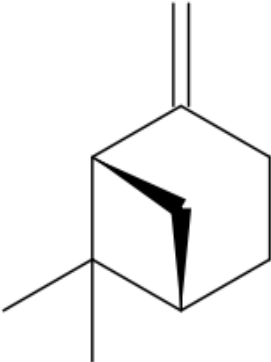
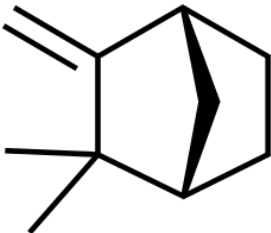
- (280) Maclean, A. M.; Li, Y.; Crescenzo, G. v.; Smith, N. R.; Karydis, V. A.; Tsimpidi, A. P.; Butenhoff, C. L.; Faiola, C. L.; Lelieveld, J.; Nizkorodov, S. A.; Shiraiwa, M.; Bertram, A. K. Global Distribution of the Phase State and Mixing Times within Secondary Organic Aerosol Particles in the Troposphere Based on Room-Temperature Viscosity Measurements. *ACS Earth Space Chem* **2021**, *5* (12), 3458–3473. <https://doi.org/10.1021/acsearthspacechem.1c00296>.
- (281) López, R.; Rodríguez-Calcerrada, J.; Gil, L. Physiological and Morphological Response to Water Deficit in Seedlings of Five Provenances of *Pinus Canariensis*: Potential to Detect Variation in Drought-Tolerance. *Trees - Structure and Function* **2009**, *23* (3), 509–519. <https://doi.org/10.1007/S00468-008-0297-5/FIGURES/5>.
- (282) Ramírez-Valiente, J. A.; Santos del Blanco, L.; Alía, R.; Robledo-Arnuncio, J. J.; Climent, J. Adaptation of Mediterranean Forest Species to Climate: Lessons from Common Garden Experiments. *Journal of Ecology* **2021**, *00*, 1–21. <https://doi.org/10.1111/1365-2745.13730>.
- (283) Canagaratna, M. R.; Jimenez, J. L.; Kroll, J. H.; Chen, Q.; Kessler, S. H.; Massoli, P.; Hildebrandt Ruiz, L.; Fortner, E.; Williams, L. R.; Wilson, K. R.; Surratt, J. D.; Donahue, N. M.; Jayne, J. T.; Worsnop, D. R. Elemental Ratio Measurements of Organic Compounds Using Aerosol Mass Spectrometry: Characterization, Improved Calibration, and Implications. *Atmos Chem Phys* **2015**, *15* (1), 253–272. <https://doi.org/10.5194/acp-15-253-2015>.
- (284) Eddingsaas, N. C.; Loza, C. L.; Yee, L. D.; Chan, M.; Schilling, K. A.; Chhabra, P. S.; Seinfeld, J. H.; Wennberg, P. O. Atmospheric Chemistry and Physics  $\alpha$ -Pinene Photooxidation under Controlled Chemical Conditions-Part 2: SOA Yield and Composition in Low-and High-NO<sub>x</sub> Environments. *Atmos. Chem. Phys* **2012**, *12*, 7413–7427. <https://doi.org/10.5194/acp-12-7413-2012>.
- (285) Kiland, K. J.; Marroquin, K. L.; Smith, N. R.; Xu, S.; Nizkorodov, S. A.; Bertram, A. K. A New Hot-Stage Microscopy Technique for Measuring Temperature-Dependent Viscosities of Aerosol Particles and Its Application to Farnesene Secondary Organic Aerosol. <https://doi.org/10.5194/amt-2022-151>.
- (286) Demond, A. H.; Lindner, A. S. Estimation of Interfacial Tension between Organic Liquids and Water. *Environ Sci Technol* **1993**, *27* (12), 2318–2331. <https://doi.org/10.1021/es00048a004>.
- (287) Gray Bé, A.; Upshur, M. A.; Liu, P.; Martin, S. T.; Geiger, F. M.; Thomson, R. J. Cloud Activation Potentials for Atmospheric  $\alpha$ -Pinene and  $\beta$ -Caryophyllene Ozonolysis Products. *ACS Cent Sci* **2017**, *3* (7), 715–725. <https://doi.org/10.1021/acscentsci.7b00112>.
- (288) Hritz, A. D.; Raymond, T. M.; Dutcher, D. D. A Method for the Direct Measurement of Surface Tension of Collected Atmospherically Relevant Aerosol Particles Using Atomic Force Microscopy. *Atmos Chem Phys* **2016**, *16* (15), 9761–9769. <https://doi.org/10.5194/acp-16-9761-2016>.
- (289) Gorkowski, K.; Donahue, N. M.; Sullivan, R. C. Aerosol Optical Tweezers Constrain the Morphology Evolution of Liquid-Liquid Phase-Separated Atmospheric Particles. *Chem* **2020**, *6* (1), 204–220. <https://doi.org/10.1016/j.chempr.2019.10.018>.
- (290) Churaev, N. V.; Sobolev, V. D.; Somov, A. N. Slippage of Liquids over Lyophobic Solid Surfaces. *J Colloid Interface Sci* **1984**, *97* (2), 574–581. [https://doi.org/10.1016/0021-9797\(84\)90330-8](https://doi.org/10.1016/0021-9797(84)90330-8).

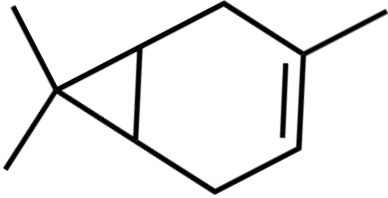
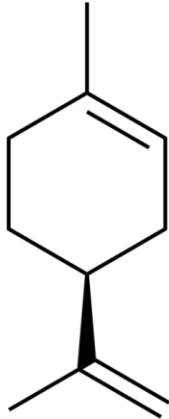

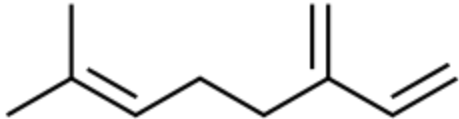
- (291) Zhu, L.; Attard, P.; Neto, C. Reconciling Slip Measurements in Symmetric and Asymmetric Systems. *Langmuir* **2012**, *28* (20), 7768–7774. <https://doi.org/10.1021/la301040d>.
- (292) Baudry, J.; Charlaix, E.; Tonck, A.; Mazuyer, D. Experimental Evidence for a Large Slip Effect at a Nonwetting Fluid-Solid Interface. *Langmuir* **2001**, *17* (17), 5232–5236. <https://doi.org/10.1021/la0009994>.
- (293) Joseph, P.; Tabeling, P. Direct Measurement of the Apparent Slip Length. *Phys Rev E Stat Nonlin Soft Matter Phys* **2005**, *71* (3), 1–4. <https://doi.org/10.1103/PhysRevE.71.035303>.
- (294) Vinogradova, O. I.; Koynov, K.; Best, A.; Feuillebois, F. Direct Measurements of Hydrophobic Slippage Using Double-Focus Fluorescence Cross-Correlation. *Phys Rev Lett* **2009**, *102* (11), 1–4. <https://doi.org/10.1103/PhysRevLett.102.118302>.
- (295) Tretheway, D. C.; Meinhart, C. D. Apparent Fluid Slip at Hydrophobic Microchannel Walls. *Physics of Fluids* **2002**, *14* (3). <https://doi.org/10.1063/1.1432696>.
- (296) McBride, S. P.; Law, B. M. Viscosity-Dependent Liquid Slip at Molecularly Smooth Hydrophobic Surfaces. *Phys Rev E Stat Nonlin Soft Matter Phys* **2009**, *80* (6), 2–5. <https://doi.org/10.1103/PhysRevE.80.060601>.
- (297) Jing, D.; Bhushan, B. Boundary Slip of Superoleophilic, Oleophobic, and Superoleophobic Surfaces Immersed in Deionized Water, Hexadecane, and Ethylene Glycol. *Langmuir* **2013**, *29* (47), 14691–14700. <https://doi.org/10.1021/la4030876>.
- (298) Craig, V. S. J.; Neto, C.; Williams, D. R. M. Shear-Dependent Boundary Slip in an Aqueous Newtonian Liquid. *Phys Rev Lett* **2001**, *87* (5), 54504-1-54504-4. <https://doi.org/10.1103/PhysRevLett.87.054504>.
- (299) Cottin-Bizonne, C.; Jurine, S.; Baudry, J.; Crassous, J.; Restagno, F.; Charlaix, É. Nanorheology: An Investigation of the Boundary Condition at Hydrophobic and Hydrophilic Interfaces. *European Physical Journal E* **2002**, *9* (1), 47–53. <https://doi.org/10.1140/epje/i2001-10112-9>.
- (300) Cottin-Bizonne, C.; Cross, B.; Steinberger, A.; Charlaix, E. Boundary Slip on Smooth Hydrophobic Surfaces: Intrinsic Effects and Possible Artifacts. *Phys Rev Lett* **2005**, *94* (5), 1–4. <https://doi.org/10.1103/PhysRevLett.94.056102>.
- (301) Cho, J. H. J.; Law, B. M.; Rieutord, F. Dipole-Dependent Slip of Newtonian Liquids at Smooth Solid Hydrophobic Surfaces. *Phys Rev Lett* **2004**, *92* (16), 1–4. <https://doi.org/10.1103/PhysRevLett.92.166102>.
- (302) Bhushan, B.; Wang, Y.; Maali, A. Boundary Slip Study on Hydrophilic, Hydrophobic, and Superhydrophobic Surfaces with Dynamic Atomic Force Microscopy. *Langmuir* **2009**, *25* (14), 8117–8121. <https://doi.org/10.1021/la900612s>.
- (303) Chesna, J. W.; Wiedmaier, B. F.; Wang, J.; Samara, A.; Leach, R. K.; Her, T. H.; Smith, S. T. Aerial Wetting Contact Angle Measurement Using Confocal Microscopy. *Meas Sci Technol* **2016**, *27* (12). <https://doi.org/10.1088/0957-0233/27/12/125202>.

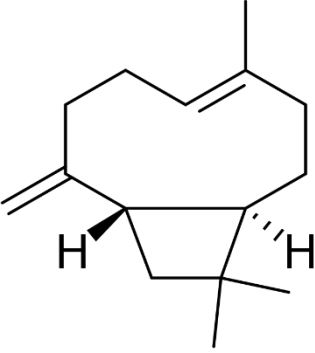
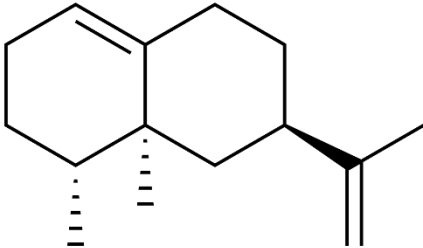
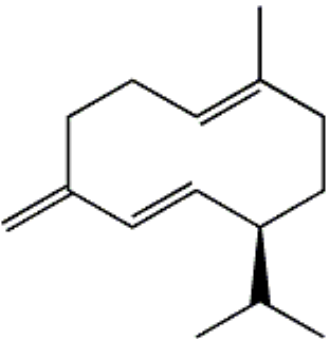
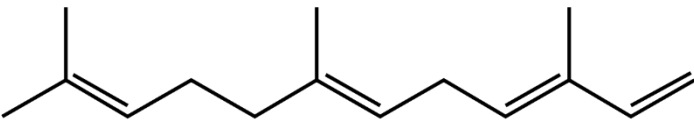
- (304) Janson, R. Monoterpene Concentrations in and Above a Forest of Scots Pine. *J Atmos Chem* **1992**, *14*, 385–394.
- (305) Smith, N. R.; Crescenzo, G. v.; Huang, Y.; Hettiyadura, A. P. S.; Siemens, K.; Li, Y.; Faiola, C. L.; Laskin, A.; Shiraiwa, M.; Bertram, A. K.; Nizkorodov, S. A. Viscosity and Liquid–Liquid Phase Separation in Healthy and Stressed Plant SOA. *Environmental Science: Atmospheres* **2021**, 140–153. <https://doi.org/10.1039/d0ea00020e>.
- (306) Maclean, A. M.; Li, Y.; Crescenzo, G. v.; Smith, N. R.; Karydis, V. A.; Tsimpidi, A. P.; Butenhoff, C. L.; Faiola, C. L.; Lelieveld, J.; Nizkorodov, S. A.; Shiraiwa, M.; Bertram, A. K. Global Distribution of the Phase State and Mixing Times within Secondary Organic Aerosol Particles in the Troposphere Based on Room-Temperature Viscosity Measurements. *ACS Earth Space Chem* **2021**, *5* (12), 3458–3473. <https://doi.org/10.1021/acsearthspacechem.1c00296>.
- (307) Perraud, V.; Bruns, E. A.; Ezell, M. J.; Johnson, S. N.; Yu, Y.; Alexander, M. L.; Zelenyuk, A.; Imre, D.; Chang, W. L.; Dabdub, D.; Pankow, J. F.; Finlayson-Pitts, B. J. Nonequilibrium Atmospheric Secondary Organic Aerosol Formation and Growth. *Proc Natl Acad Sci U S A* **2012**, *109* (8), 2836–2841. <https://doi.org/10.1073/PNAS.1119909109/ASSET/7E5BF052-6712-4A7E-97CC-45401AB49279/ASSETS/GRAPHIC/PNAS.1119909109EQ7.GIF>.
- (308) Hinks, M. L.; Brady, M. v.; Lignell, H.; Song, M.; Grayson, J. W.; Bertram, A. K.; Lin, P.; Laskin, A.; Laskin, J.; Nizkorodov, S. A. Effect of Viscosity on Photodegradation Rates in Complex Secondary Organic Aerosol Materials. *Physical Chemistry Chemical Physics* **2016**, *18* (13), 8785–8793. <https://doi.org/10.1039/C5CP05226B>.
- (309) Dalton, A. B.; Nizkorodov, S. A. Photochemical Degradation of 4-Nitrocatechol and 2,4-Dinitrophenol in a Sugar-Glass Secondary Organic Aerosol Surrogate. *Environ Sci Technol* **2021**, *55* (21), 14586–14594. [https://doi.org/10.1021/ACS.EST.1C04975/ASSET/IMAGES/LARGE/ES1C04975\\_0004.JPEG](https://doi.org/10.1021/ACS.EST.1C04975/ASSET/IMAGES/LARGE/ES1C04975_0004.JPEG).
- (310) Lee, A. K. Y.; Abbatt, J. P. D.; Leaitch, W. R.; Li, S.-M.; Sjostedt, S. J.; Wentzell, J. J. B.; Liggio, J.; Macdonald, A. M. Substantial SOA Formation in a Coniferous Forest Substantial Secondary Organic Aerosol Formation in a Coniferous Forest: Observations of Both Day and Night Time Chemistry Substantial SOA Formation in a Coniferous Forest. *Atmos. Chem. Phys. Discuss* **2015**, *15*, 28005–28035. <https://doi.org/10.5194/acpd-15-28005-2015>.
- (311) Chen, Q.; Farmer, D. K.; Rizzo, L. v; Pauliquevis, T.; Kuwata, M.; Karl, T. G.; Guenther, A.; Allan, J. D.; Coe, H.; Andreae, M. O.; Pöschl, U.; Jimenez, J. L.; Artaxo, P.; Martin, S. T. Submicron Particle Mass Concentrations and Sources in the Amazonian Wet Season (AMAZE-08). *Atmos. Chem. Phys* **2015**, *15*, 3687–3701. <https://doi.org/10.5194/acp-15-3687-2015>.
- (312) Kiendler-Scharr, A.; Zhang, Q.; Hohaus, T.; Kleist, E.; Mensah, A.; Mentel, T. F.; Spindler, C.; Uerlings, R.; Tillmann, R.; Wildt, J. Aerosol Mass Spectrometric Features of Biogenic SOA: Observations from a Plant Chamber and in Rural Atmospheric Environments. *Environ Sci Technol* **2009**, *43* (21), 8166–8172. [https://doi.org/10.1021/ES901420B/SUPPL\\_FILE/ES901420B\\_SI\\_001.PDF](https://doi.org/10.1021/ES901420B/SUPPL_FILE/ES901420B_SI_001.PDF).

## APPENDIX A

### STRUCTURES OF TERPENE PRECURSORS

Class of Compound	Name of Compound	Chemical Structure
Monoterpene (C <sub>10</sub> H <sub>16</sub> )	$\alpha$ -pinene	 The structure of $\alpha$ -pinene is a bicyclic monoterpene. It consists of a six-membered ring fused to a five-membered ring. The six-membered ring has a double bond between the two carbons that are not part of the fusion. There is a methyl group attached to the carbon adjacent to the double bond in the six-membered ring, and another methyl group attached to the carbon adjacent to the fusion point in the same ring.
	$\beta$ -pinene	 The structure of $\beta$ -pinene is a bicyclic monoterpene. It consists of a six-membered ring fused to a five-membered ring. The six-membered ring has a double bond between the two carbons that are not part of the fusion. There is a methyl group attached to the carbon adjacent to the fusion point in the six-membered ring, and a methylene group (=CH <sub>2</sub> ) attached to the carbon adjacent to the double bond in the same ring.
	Camphene	 The structure of camphene is a bicyclic monoterpene. It consists of a six-membered ring fused to a five-membered ring. The six-membered ring has a double bond between the two carbons that are not part of the fusion. There is a methyl group attached to the carbon adjacent to the fusion point in the six-membered ring, and a methylene group (=CH <sub>2</sub> ) attached to the carbon adjacent to the double bond in the same ring.

	3-Carene	
	Limonene	
	$\alpha$ -phellandrene	
	Myrcene	

Sesquiterpene (C <sub>15</sub> H <sub>24</sub> )	β-caryophyllene	
	Valencene	
	Germacrene D	
	Farnesene	



## APPENDIX B

### DIAGRAM OF POKE-FLOW EXPERIMENTAL SETUP

